NUMERICAL MODELING OF A GEOTHERMAL SITE UNDER DEVELOPMENT: A CASE STUDY IN BÜYÜK MENDERES GRABEN

A THESIS SUBMITTED TO
THE GRADUATE SCHOOL OF NATURAL AND APPLIED SCIENCES
OF
MIDDLE EAST TECHNICAL UNIVERSITY

BY

GÖZDE PINAR YAL ÖNDER

IN PARTIAL FULFILLMENT OF THE REQUIREMENTS
FOR
THE DEGREE OF DOCTOR OF PHILOSOPHY
IN
GEOLOGICAL ENGINEERING

JANUARY 2025

Approval of the thesis:

NUMERICAL MODELING OF A GEOTHERMAL SITE UNDER DEVELOPMENT: A CASE STUDY IN BÜYÜK MENDERES GRABEN

submitted by **GÖZDE PINAR YAL ÖNDER** in partial fulfillment of the requirements for the degree of **Doctor of Philosophy** in **Geological Engineering, Middle East Technical University** by,

Prof. Dr. Naci Emre Altun
Dean, Graduate School of **Natural and Applied Sciences** ________________

Prof. Dr. Erdin Bozkurt
Head of the Department, **Geological Engineering** ________________

Prof. Dr. Haluk Akgün
Supervisor, **Geological Engineering, METU** ________________

Examining Committee Members:

Prof. Dr. Candan Gökçeoğlu
Geological Engineering, Cappadocia University ________________

Prof. Dr. Haluk Akgün
Geological Engineering, METU ________________

Prof. Dr. Uğur Murat Leloğlu
Astronautical Engineering, TAAU ________________

Assoc. Dr. Mustafa Kerem Koçkar
Civil Engineering, Hacettepe University ________________

Prof. Dr. Kaan Sayıt
Geological Engineering, METU ________________

Date: 31.01.2025

Name Last name : Gözde Pınar Yal Önder

Signature :

ABSTRACT

NUMERICAL MODELING OF A GEOTHERMAL SITE UNDER DEVELOPMENT: A CASE STUDY IN BÜYÜK MENDERES GRABEN

Yal Önder, Gözde Pınar
Doctor of Philosophy, Geological Engineering
Supervisor: Prof. Dr. Haluk Akgün

January 2025, 251 pages

The purpose of this study is to construct a hydrological and mechanical model that best represents the geothermal reservoir in the study area to determine the effectiveness of mechanical enhancement strategies.

The mechanical response of the reservoir to pressurized water injection was assessed by considering the possible activation of natural fractures through shear failure. The impact of the activation of the fractures on fluid flow and reservoir permeability was assessed.

In order to determine the parameters required for the model, field study encompassing scan-line surveying, photogrammetric image acquisition from reservoir rock outcrops, fault kinematic analysis, and collection of rock samples to conduct geomechanical tests has been performed. A geologically constrained discrete fracture network along with a hydrological and mechanical model has been generated. It was observed that mechanical enhancement techniques can effectively improve reservoir productivity and/or injectivity in fracture-controlled reservoirs and that, the extent of mechanical failure achievable with standard pumps is limited

and highly dependent on the orientation of fractures relative to the principal stress direction.

Keywords: Fracture network, Geothermal, Reservoir enhancement.

ÖZ

GELİŞTİRİLMEKTE OLAN BİR JEOTERMAL SAHANIN SAYISAL MODELLEMESİ: BÜYÜK MENDERES GRABENİNDE BİR ÖRNEK ÇALIŞMA

Yal Önder, Gözde Pınar
Doktora, Jeoloji Mühendisliği
Tez Yöneticisi: Prof. Dr. Haluk Akgün

Ocak 2025, 251 sayfa

Bu çalışmanın amacı, mekanik iyileştirme stratejilerinin etkinliğini belirlemek için çalışma bölgesindeki jeotermal rezervuarı en iyi şekilde temsil eden bir hidrolik ve mekanik model oluşturmaktır.

Rezervuarın basınçlı su enjeksiyonuna mekanik tepkisi, doğal kırıkların kesme kırılması yoluyla olası aktivasyonunun dikkate alınması ile değerlendirilmiştir. Kırıkların aktivasyonunun akışkan hareketi ve rezervuar geçirgenliği üzerindeki etkisi incelenmiştir.

Model için gerekli parametreleri belirlemek amacıyla, hat etüdleri, rezervuar kaya kütlesi mostralarından fotogrametrik görüntü edinimi, fay kinematik analizi ve jeomekanik testler yapılmak üzere kaya örneklerinin toplanmasını içeren bir saha çalışması gerçekleştirilmiştir. Jeolojik olarak sınırlı ayrık kırık ağı oluşturulmuş ve hidrolik ile mekanik modeller geliştirilmiştir. Mekanik iyileştirme tekniklerinin, kırık kontrollü rezervuarların üretkenliğini ve/veya enjeksiyon kapasitesini etkin bir şekilde artırabileceği sonucuna varılmıştır. Bununla birlikte, standart pompalarla gerçekleştirilebilecek mekanik kırılma derecesinin sınırlı olduğu ve kırıkların ana stres yönelimine göre yönlendirilmesine büyük ölçüde bağlı olduğu gözlemlenmiştir.

Anahtar Kelimeler: Kırık ağı, Jeotermal, Rezervuar iyileştirme

Dedication

To my son

May he be destined for fulfilling endeavours.

ACKNOWLEDGMENTS

The author wishes to express his deepest gratitude to his supervisor Prof. Dr. Haluk Akgün, for his guidance, advice, criticism, encouragement and insight throughout the research.

The author would also like to thank Assoc. Prof. Mustafa Kerem Koçkar who supported this study.

Invaluable comments and contributions of the former and current Thesis Examination Committee members Prof. Dr. Asuman Günal Türkmenoğlu, Prof. Dr. Uğur Murat Leloğlu, Prof.Dr. Candan Gökçeoğlu and Prof. Dr. Kaan Sayit are gratefully acknowledged.

The author is also deeply grateful to her family Erkan Önder, Merih Yal, Erdal Yal and Ural Yal and friends, Beril Boyacıoğlu, Selim Cambazoglu, Ayten Koç, and Mert Eker, whose unwavering support, encouragement, and friendship have been a strength throughout this journey. Their practical and emotional contributions were invaluable in bringing this work to completion.

I would like to express my profound gratitude to İrfan Acar and Osman Şen for their invaluable support and guidance and for permitting to use the data collected from the study area for this thesis, which has been essential to the success of this research.

This work was partially funded by the Middle East Technical University Scientific Research Projects Coordination Unit under grant number GAP-10185 and the TUBITAK 1001 project under grant number 119Y535.

Finally, I would like to extend my deepest gratitude to my family, whose unwavering support, love, and encouragement have been a constant source of strength throughout this journey. Their belief in me, even during the most challenging times, has been invaluable in completing this work. This achievement would not have been possible

without their continuous support, and I am forever grateful for their presence in my life.

TABLE OF CONTENTS

LIST OF TABLES

TABLES

LIST OF FIGURES

FIGURES

CHAPTER 1

INTRODUCTION

This thesis has primarily focused on understanding the mechanical processes that govern the behavior of a fracture-controlled geothermal reservoir in the Kuyucak Geothermal Field, situated within the Büyük Menderes Graben. As of 2023, the Büyük Menderes Graben stands as Turkey's most significant geothermal region, with an installed power capacity exceeding 1000 MW (megawatts).

The primary objective was to develop optimized strategies for efficient reservoir enhancement and performance in the Kuyucak Geothermal Field, while also contributing to a broader understanding of flow mechanisms in fracture-controlled reservoirs. This thesis presents a methodology for guiding the development stage of geothermal reservoirs, highlighting the critical importance of integrating field and legacy data prior to incurring high investment costs. Such an approach substantially improves the understanding of flow controls, enabling the design of strategies to optimize reservoir development.

In fracture-controlled reservoirs, incorporating fracture networks into reservoir models is essential for accurately representing fluid flow dynamics, which differ significantly from models considering only porous media flow. Fractures provide preferential pathways for fluid movement, leading to a more heterogeneous flow behaviour that traditional porous media models cannot capture. Understanding the impact of fracture enhancement through shear and tensile failure is crucial, as it directly influences permeability and reservoir performance. By simulating these failure mechanisms, the models can better predict reservoir behaviour under different stress conditions.

In order to understand the mechanical process, obtaining information on the current stress regime, fracture network, reservoir properties and geometry, and geomechanical properties of the reservoir rock is crucial. For this purpose, analysis and evaluation of geophysical investigations, deep geothermal wells, fault kinematic measurements, scan-line surveys, geomechanical tests on reservoir rock samples, and well test analyses has been conducted. These data have been collectively analyzed to characterise the geothermal system.

The notion that failure mechanisms significantly influence flow controls and can guide enhancement strategies originated from the irregular results observed during injection tests. These irregularities were attributed to injection-induced shear failure within the fractured reservoir. To explore this, data from previous studies conducted in the area, along with data collected as part of this thesis, were utilized to construct mechanical and fluid models. These models demonstrate the positive effects of mechanically induced failures on reservoir productivity through increased permeability.

In this thesis, initially all data collected and used to characterize the geothermal reservoir is presented including the data coverage, data collection strategies, and data analysis methodologies. It then evolves into the development of mechanical and fluid models, followed by the discussion of the results. The thesis finally concludes with insights derived from the findings and recommendations for future research.

CHAPTER 2

STUDY AREA

The study area is located at the northern flank of Büyük Menderes Graben in Kuyucak district of Aydın province, Türkiye (Figure 2.1). In this chapter, the structural and general geology of the study area, with references to the geothermal system, is presented.

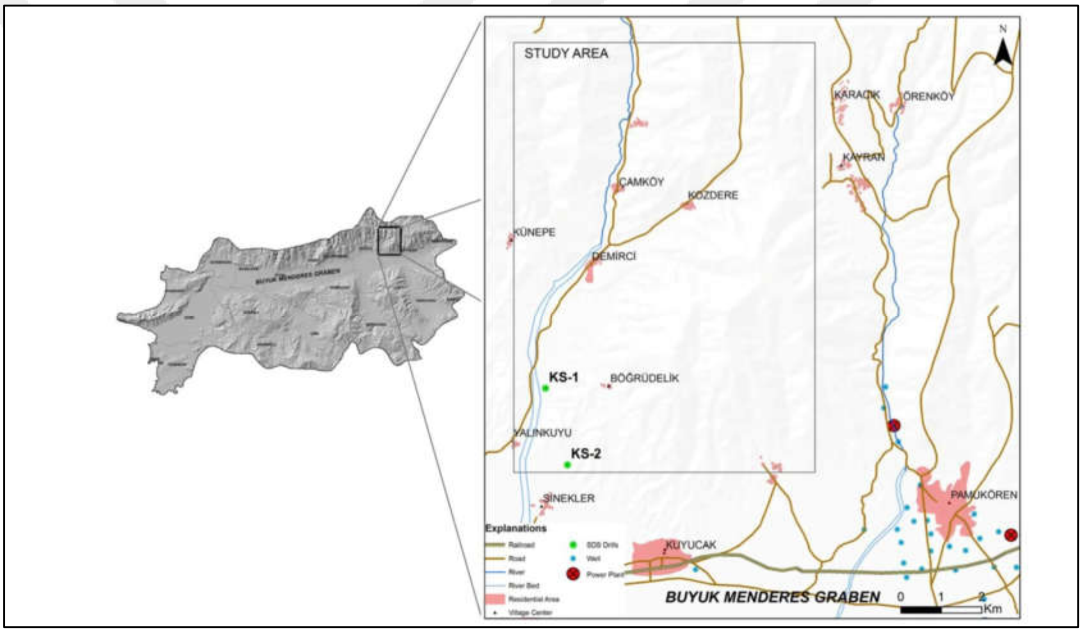

Figure 2.1. Study area

2.1 Geology of the Study Area

The source, nature, and geometry of the geothermal reservoirs in the study can only be understood by a detailed investigation of the regional geological and structural history. The study area is located in the Büyük Menderes Graben, where the geothermal system is regarded as having a magmatic origin caused by the N-S extension of the region due to young tectonic activity. The mechanics behind the formation of the geothermal reservoirs in the study area were utterly controlled by the regional tectonics and its structural consequences. This chapter reviews Paleo-Neo tectonics, regional stratigraphy and current structural settings by specifying their role in the geothermal layout.

2.2 Tectonics

Türkiye is located in the Alpine-Himalayan orogenic belt. Türkiye has experienced compressional and extensional tectonics during the paleotectonic and neotectonic periods, which are associated with the evolution of the Tethys. The relative motion between the tectonic plates indicates the south-westward retreat of Anatolia, which was caused by the roll-back of the slab beneath Anatolia (Le Pichon and Angelier, 1979; Royden, 1993; Govers and Fichtner, 2016). The study area is located in the northern flanks of the Büyük Menderes Graben in Western Anatolia. Western Anatolian is mainly characterized by the N-S extension and E-W trending graben-horst systems. There are four theories on the tectonic origin of the West Anatolian Horst Graben System. The first theory is the Westward escape of the Anatolian plate model, where the westward movement of the Anatolian Plate has been associated with the northward movement of the Arabian Plate and the resultant collision along the Bitlis-Zagros suture along the bounding North and East Anatolian Faults (Şengör, 1979; Şengör and Kidd, 1979; Dewey and Şengör, 1979).

The second theory is the back-arc spreading model, where the steepening of the Hellenic subduction zone is identified as the cause of the N-S-directed extension. This slab pull has been evidenced by the south-westward migration of the volcanism from the Miocene arc to the Aegean arc (McKenzie, 1970, 1972, 1978; Jackson and McKenzie, 1988; Le Pichon and Angelier, 1981; Meijer and Wortel, 1997; Jolivet et al., 2003, 2013; Philippon et al., 2014).

The third theory is the orogenic collapse model where the spreading and over-thickened crust is associated with the collision and ongoing uplift followed by crustal thinning, causing the orogenic collapse and the subsequent N-S extension and uplift (Dewey, 1988; Şengör et al., 1984; Rimmele et al., 2003, Dewey and Şengör, 1979; Şengör, 1979; Dewey, 1988; Dewey et al., 1973).

The fourth theory is the episodic two-stage graben model that suggests an initial episode of extension due to orogenic collapse, followed by a compression stage due to brief variations in the movement of Arabian and Eurasian plates, which was ended by the westward escape of the Anatolian plate initiating the currently on going N-S extension stage (Bozkurt and Park, 1994; Koçyiğit et al., 1999; Bozkurt, 2002; Yılmaz et al., 2000; Koçyiğit and Özacar, 2003; Bozkurt and Sözbilir, 2004; Purvis and Robertson, 2004, 2005; Bozkurt and Rojay, 2005; Koçyiğit, 2005; Yılmaz, 2017).

1.3. Structural Geology

The brittle tectonics nature of the Menderes Massif caused the formation of normal and normal-oblique-slip faults that construct the horst and graben system. The N-S extension first initiated in the Late Oligocene in Büyük Menderes, mainly through Neogene to Quaternary, has caused the formation of NW and NE trending sub-vertical oblique normal faults with dip values ranging from 50˚ to 70˚. These oblique faultsthat are dissected by N-S trending strike-slip faults have been interpreted as transfer faults (Çitçi et al., 2011) that serve as lateral ramps (Kaya, 2015) and E-W trending low-angle fault, the Miocene aged Büyük Menderes Detachment fault and secondary listric high-angle faults as the synthetic and antithetic splays of the mainly S-dipping (40-65°) Büyük Menderes Detachment Fault (Gürer et al., 2009). The E-W trending high angle normal faults are responsible for the formation of the step-wise topography of the Büyük Menderes graben and the formation of blocks that are younger towards the basin. The N-S trending strike-slip faults are mapped north of Nazilli and north of Kuyucak by Çiftçi (2011), which are categorized as cross faults.

The first large-scale extension of the continental crust due to tectonic exhumation of the Menderes Massif started during Late Oligocene-Miocene and lasted till the second extension during Quaternary. (Bozkurt, 1996, 2000; Bozkurt & Park, 1997a, Bozkurt & Park, 1999; Bozkurt, Park, & Winchester, 1993; Bozkurt & Satır, 2000; Bozkurt, Winchester, & Park, 1995). The current structural settings that include the well-developed horst graben system, the widespread granitic rocks, and the shallow Curie point depths of 8-11.5 km at the Menderes Massif (Aydın et al., 2005; Dolmaz et al., 2005) is the evidence of the extension and thinning of the crust. These high thermal anomalies that resulted from asthenospheric upwelling in natural response to lithospheric extension (Koçyiğit, 2015) act as the heat source of the geothermal system in the Büyük Menderes Graben. Thus, the heat source is associated with young tectonic activity in the region. In this system, deeply penetrating faults act as the fluid pathways to the geothermal fluids and actualize an efficient heat transfer from the deep crust (Faulds et al., 2009). The major normal faults and/or intersecting normal and strike-slip to oblique-slip fault zones are one of the major features of the structural setting in the Büyük Menderes Graben system responsible for the transfer of hot geothermal fluids to the exploitable upper levels of the crust. Normal and strike-slip faults in the Kuyucak geothermal region create a favorable environment for the upwelling of geothermal fluids in the deep-seated geothermal reservoir (Figure 1). The tectonic complexity due to the cross-cutting of the faults in the region also forms highly fractured shear zones that harbor geothermal fluids.

2.3 Stratigraphy

The basement rock of the study area is the Menderes Massif. The core assemblage of theMenderes massif aged Late Precambrian and Early Cambrian (Gessner et al., 2001; Hetzel & Reischmann, 1996; Loos & Reischmann, 1999) is composed of augen gneiss, metagranite, schist and metagabro (Candan,1995; Satır & Friedrichsen, 1986). The cover assemblage aged Permian–Middle Paleocene (Çağlayan et al., 1980; Konak et al., 1987) consists of a series of low-grade metasediments comprising metapelites, amphibolite with dolomitic marble intercalations, marble-dominated recrystallised sedimentary sequence. The Menderes Massif was formed due to the main Menderes metamorphism (MMM), which resulted in the deep burial of the massif beneath the Lycian Nappes (Bozkurt, 1996, 2004). The tectonic load of the nappe caused a regional metamorphism (MMM) during the Eocene (Şengör et al., 1984; Şengör & Yılmaz, 1981).

Tertiary sedimentary rocks are deposited over the metamorphic basement, including coarse- and fine-grained sandstones, siltstones, and well-cemented conglomerates. These Neogene formations serve as the cap rock of the deep-seated geothermal system at places in the study area. On top of the Neogene sediments lies the alluvium deposits composed of lateral alluvial and axial graben floor sediments. W-trending high-angle normal faults initiated from N-S directed streams (Çiftçi, 2011).

The geological map of the study area can be seen in Figure 2.2. The area formations are divided into two primary categories: older metamorphic basement rocks and younger non-metamorphosed sedimentary rocks or graben fills.

2.3.1 Basement Rocks

The Menderes Massif, an elongated and dome-shaped core complex, dominates the basement. The Massif comprises two major metamorphic rock assemblages. The first includes high-pressure/high-temperature metamorphic rocks, known as the Core, consisting mainly of augen gneiss, metagranite, schist, and metagabbro. These rocks date back to the Late Precambrian and Early Cambrian periods. The second assemblage, the Cover, consists of low-grade metasediments, including metapelites, amphibolite, marble, and metabauxite, with Permian to Middle Palaeocene age.

Several theories exist regarding the nature of the contact between the Core and Cover rocks, including a regional unconformity to a south-facing extensional shear zone or a thrust fault. The Menderes Massif underwent significant metamorphism during the Eocene, caused by tectonic burial and later exhumation during the Oligocene-Miocene period. The rocks in the study area, especially the augen gneisses, are highly fractured and potentially serve as reservoir rocks for geothermal fluids.

2.3.2 Graben Fills

The graben fills are primarily Miocene to Quaternary in age, deposited in fluvial-lacustrine environments under the influence of normal faulting. These deposits can be divided into three main rock-stratigraphic units: the Kızılburun group, the Tosunlar formation, and the Feslek formation.

2.3.2.1 Kızılburun Group

The Kızılburun Group comprises basal clastics and upper coal-bearing lacustrine sediments. The basal clastics consist of poorly sorted conglomerates with clasts derived from the underlying basement rocks. These conglomerates show transition into finer-grained sandstones, siltstones, and lacustrine limestones, shifting from alluvial fans to lacustrine environments. The group was likely deposited in a supra-detachment basin and is dated from the Early to late Middle Miocene.

2.3.2.2 Tosunlar formation

This formation is another thick, unsorted conglomerate layer found along the northern margin of the Büyük Menderes Graben. It is characterized by poorly lithified boulders and sedimentary breccias that are uplifted and deformed by tectonic processes. The Tosunlar formation lies unconformably over the Kızılburun

Group and represents deposits from a high-energy environment, that is most likely formed by debris flows along the graben margins.

2.3.2.3 Feslek formation

Feslek formation, is a geological unit located in the Büyük Menderes Graben area, particularly along its northern margin. It comprises about 400 meters of weakly lithified, loose sedimentary deposits formed during the Late Quaternary period. The formation is primarily found in E–W trending linear depressions and N–S transverse drainage systems like the Kestel, Kayrandere, Asmalıdere, and Feslek streams. The Feslek formation is characterized by an angular unconformity with the underlying Miocene Kızılburun Group and exhibits both erosional and gradational contacts with the Lower Quaternary Tosunlar formation.

2.4 Geothermal Geology of the Study Area

The geological map of the study area can be seen in Figure 2.2. As can be seen from the geological map of the study area, the Neogene units and alluvial cover are not exposed in the northern parts of the study area, which mostly serve as the cap rock in the Buyuk Menderes Graben. However, Menderes Massif rocks are well-exposed over an extensive area along the northern margins of the Büyük Menderes Graben, where the study area is located. However, the geothermal reservoir in the study area is represented by the highly fractured augen gneisses, quartzites, and marbles of the Menderes Massif, which is in the Buyuk Menderes graben system. In contrast, the schists, such as mica and chlorite schists, represent the cap rocks of the geothermal system in and around the study area. The augen gneisses, along with the quartzites and marbles, having high porosity due to their highly fractured nature, act as the reservoir rocks of the geothermal system, while the fine-grained and thinly foliated schists, such as the mica and chlorite schists act as the cap rock of the geothermal system (Koçyiğit, 2015). These large fissures and fracture zones that developed during neotectonic activity in the Menderes Massif rocks, and quartz veins and calcite and chlorite veins that occur in swarms are related to deep-seated intrusive bodies (Karamanderesi, 2013).

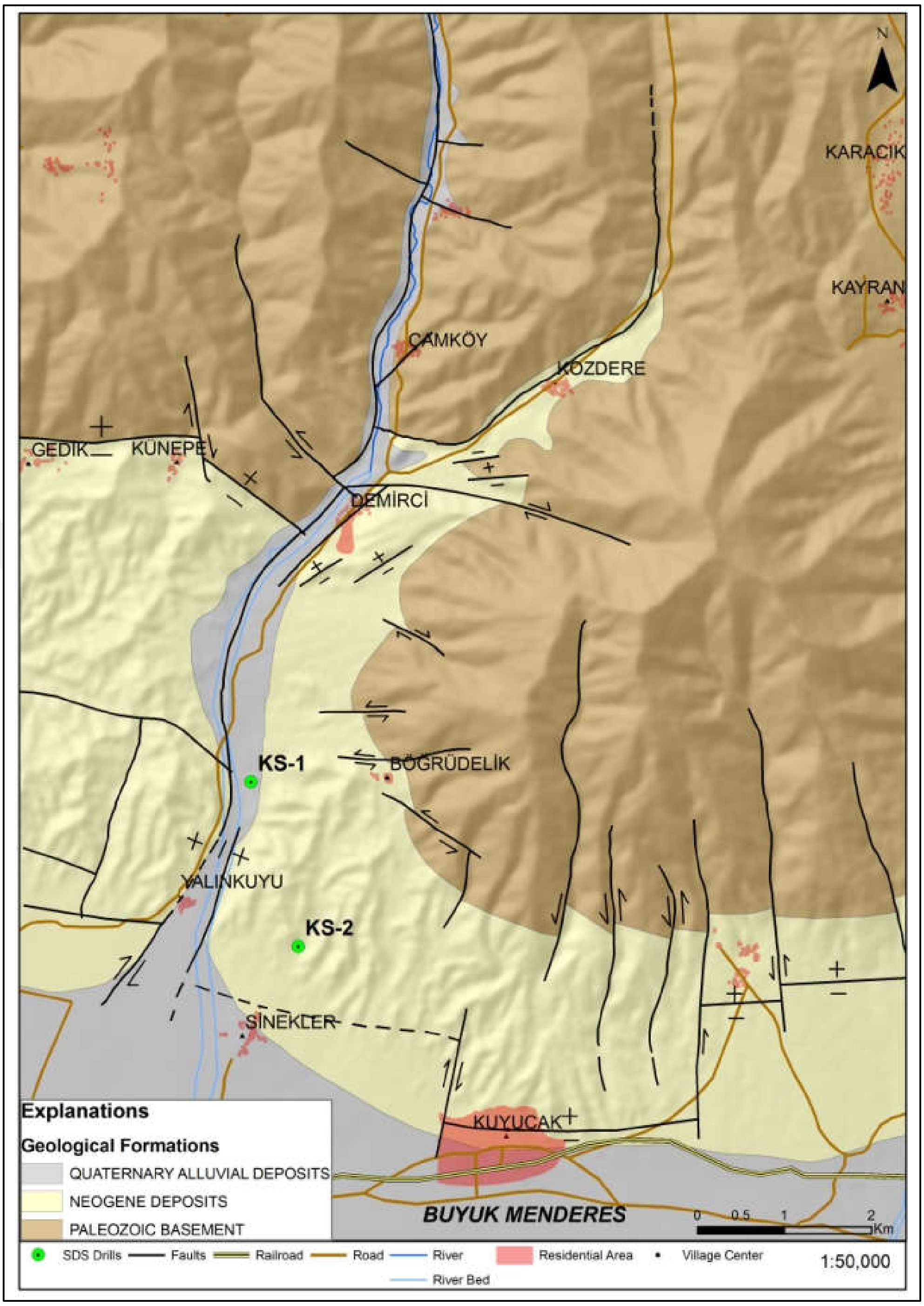

Figure 2.2. Geological map of the study area.

CHAPTER 3

INTERPRETATIONS OF PREVIOUS DATA

In this chapter, the studies conducted prior to the initiation of the studies in the scope of this thesis are presented, including the data collection, processing methodologies and interpretation of the results. These studies entail geophysical investigations, namely Magnetotelluric (MT) surveys and deep geothermal drillings.

3.1 Geophysical Investigations: MT Surveys

Geophysical exploration of geothermal resources involves measuring physical parameters that vary with depth and laterally due to changes in the Earth's properties. This exploration helps derive fundamental rock and fluid properties, focusing on high-enthalpy geothermal resources where temperatures and fluid contents are crucial. The main goals include delineating and characterizing geothermal resources, locating aquifers, identifying structures controlling fluid flow and heat transfer, and determining the optimal locations for future wells. Essential parameters in geothermal systems are temperature, porosity, permeability, fluid chemistry, and pressure.

While most of these parameters cannot be directly measured by conventional geophysical methods, other related parameters such as temperature, electrical resistivity, magnetization, density, seismic velocity, seismic activity, thermal conductivity, and streaming potential can be measured.

Magnetotellurics (MT) is an effective method for exploring electrical resistivity at depths ranging from tens of meters to several kilometers. In MT surveys, electric and magnetic field components are measured simultaneously on the Earth's surface to gather data.

The MT method is applied to determine the geothermal system's location and structure, which is an effective method for systems represented by faulted and fractured zones containing geothermal fluids.

Geothermal fluids often have high concentrations of dissolved salts, which increase conductivity as temperatures rise. These salts act as conducting electrolytes within the rock matrix and fractures. In high-enthalpy geothermal resources, the highly mineralized waters create significant variations in subsurface electrical resistivity. It makes resistivity a crucial parameter for imaging the subsurface structure of a geothermal system and determining its characteristics, particularly in convection-dominated magmatic environments.

3D inversion modeling was carried out using the code described by Mackie and Madden (1993), subsequently developed and implemented by Schlumberger. Such code exploits a regularization operator whose parameters are tuned to produce a smoothly varying resistivity volume consistent with the gradual resistivity changes expected within a geothermal system.

3.1.1 Data Collection and Methodology

As part of the geothermal exploration program undertaken by SDS Energy, magnetotelluric (MT) measurements were conducted in the Kuyucak geothermal field (Schlumberger, 2015). The survey area was approximately 11 km by 7 km, where the MT data was acquired at 83 stations with an average spacing of 250 m on an irregular grid. Schlumberger has conducted the full tensor 3D MT inversion of the MT stations, and the methodology used for analyzing the MT data is outlined in this chapter. While a detailed discussion of MT data processing falls outside the scope of this thesis, a concise overview is provided to inform readers and ensure they do not miss the key methods employed in the analysis.

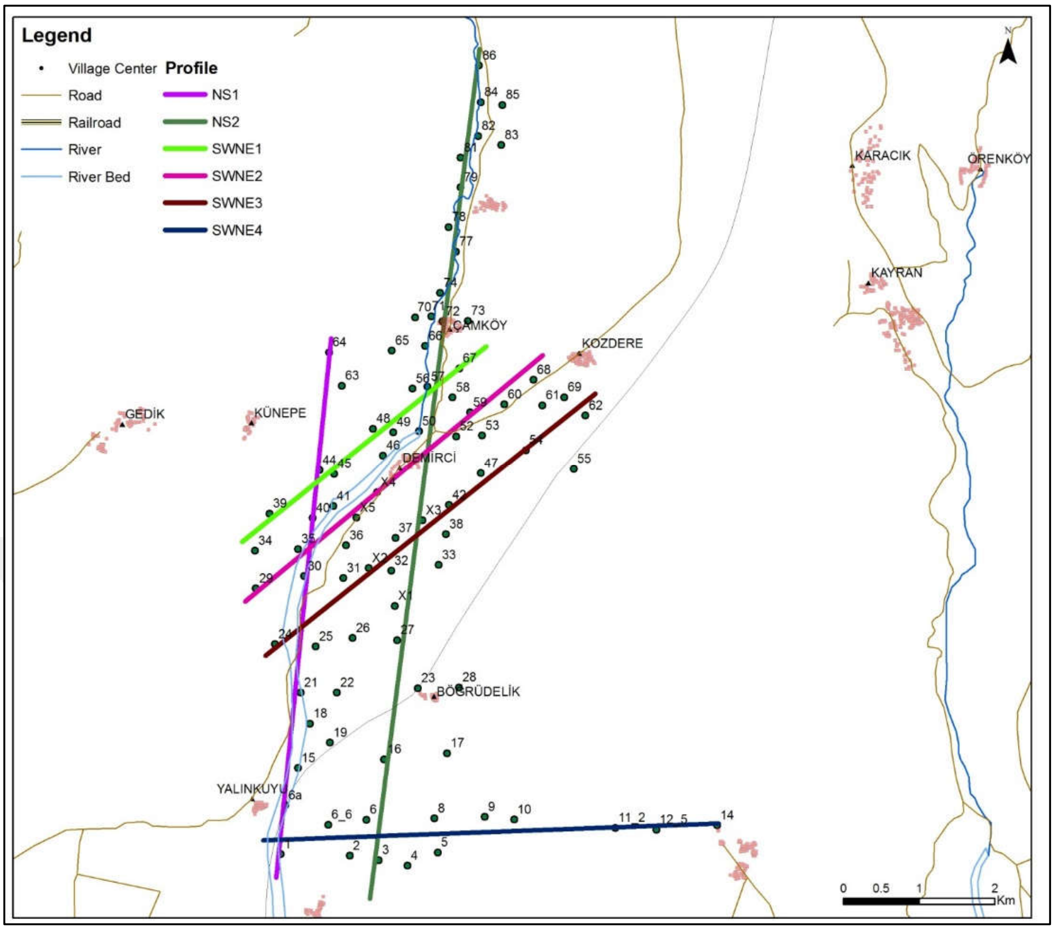

Figure 3.1. Magnetotelluric measurement profiles.

3.1.2 Data characteristics and editing

The analysis of the Magnetotelluric (MT) soundings revealed several issues with data quality. The soundings generally suffered from a poor signal-to-noise ratio and static shift effects. Distortions were observed in both the XY and YX components, particularly at high (>100 Hz) and low (<0.01 Hz) frequencies. High-frequency distortions led to inconsistent apparent resistivity versus phase behaviour, while low-frequency distortions caused scattered and unrealistic trends in the sounding curves. Some sites also exhibited distortion in the mid-frequency range (0.01 to 100 Hz), suggesting possible processing errors such as reversed polarity. Static shift effects were common across many sites, impacting one or both modes.

Initially, the sources of error, including noise, static shift, distortion and processing, were addressed. Sites with significant distortion were muted within the affected frequency bands to preserve the integrity of the data curves. Sites suspected of processing errors were excluded from further analysis. After editing, about 50% of the soundings contained data across 4 to 4.5 decades of frequency, 30% covered 3 to 3.5 decades, and 20% had data for 2.5 decades or fewer. The Tipper measurements were often absent or of poor quality and hence, were excluded from the interpretation and inversion processes.

Following quality control, 78 soundings were included in the final 3D inversion. The pseudo-sections revealed a resistivity pattern with increased complexity in the northern part of the survey area, most likely due to topographic influences. The resistivity and phase maps demonstrated increasing resistivity in the northern section, consistent with the underlying geology and topography.

Prior to the 3D modeling, 1D models were used for quality control and to estimate the deep resistive structure. The 1D models, which used both smooth and layered approaches, indicated that static shift effects impacted the results, particularly in the northern sites. The 3D inversion aimed to address these issues by incorporating static shift corrections and fine topographic cells into the model.

The 3D inversion workflow involved testing various model parameters to achieve a stable result with minimal RMS misfit. The final RMS value reached 1.55 after 30 iterations, reflecting overall data fit quality. The comparisons between observed and computed data indicated that while some sites had higher misfit values due to noisy data, the inversion generally provided a good fit.

In the 3D inversion results in Figure 3.2 and Figure 3.3, a conductive layer is bounded by two resistive zones, with its elevation ranging from 250 m a.s.l. to -750 m a.s.l. A significant deep conductor is evident around -3000 m a.s.l., which is visible in all cross-sections.

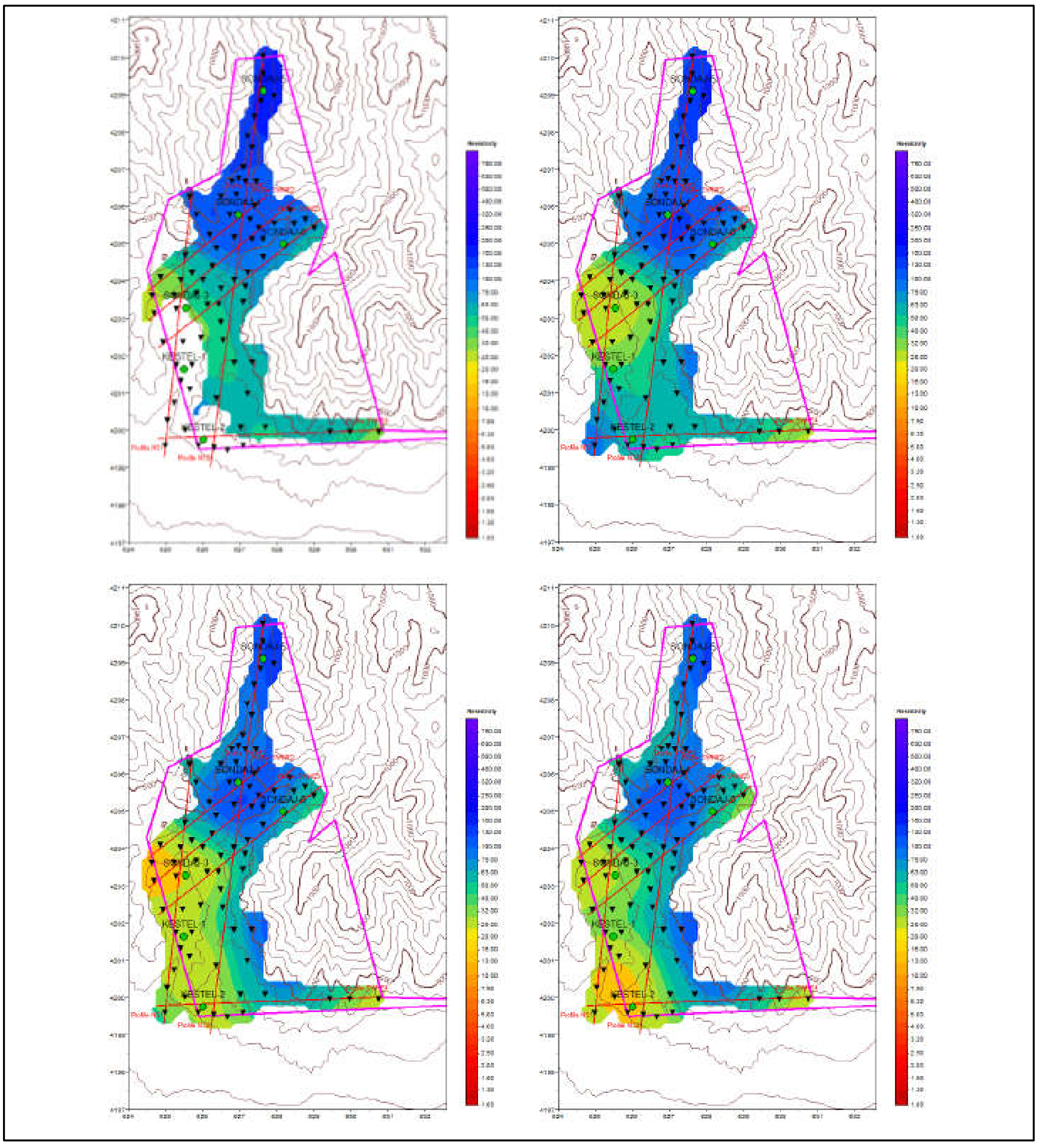

Figure 3.2. Resistivity maps at constant elevation through 3D MT resistivity model from 250 m a.s.l. to -500 m a.s.l., 250 m step, co-rendered with topography contour lines.

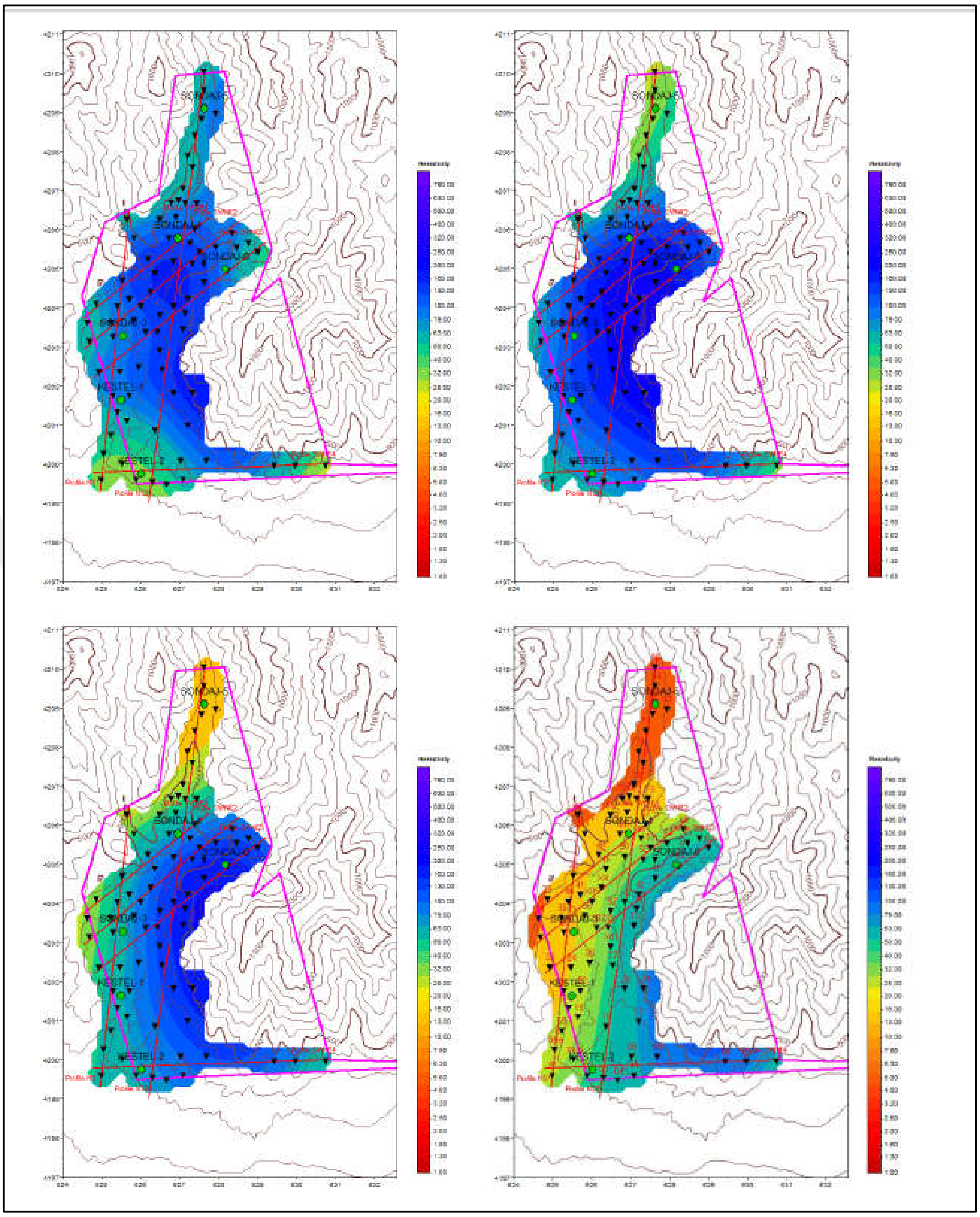

Figure 3.3. Resistivity maps at constant elevation through 3D MT resistivity model from -1000 m a.s.l. to -2500 m a.s.l., 500 m step, co-rendered with topography contour lines.

3.1.3 Inversion Workflow

Multiple 3D inversions were conducted, adjusting model parameters to achieve stability and minimize RMS misfit. The inversion process involved varying model smoothness and regularization parameters to balance local data fitting and overall RMS misfit, though this occasionally introduced roughness and extreme resistivity values.

The inversion began with a uniform half-space model and processed the entire frequency range from 120 Hz to 0.003 Hz in one step, testing different regularization weights and smoothing parameters. The final model used frequencies from 0.003-120 Hz with 7 frequencies per decade over 30 iterations.

3.1.4 Data Fitting

The RMS metric measures the fit of the 3D inversion, which is calculated from the observed and predicted data. The final RMS value was 1.55 after 30 iterations. The RMS map indicated some stations had higher RMS (>2), likely due to noisy data. Overall, the RMS was uniformly low (~1 or below), reflecting good data quality.

3.1.5 3D Inversion Results – Resistivity Structures

The resistivity cross sections are illustrated in Figure 3.4 to Figure 3.9. Finally, the 3D MT model can be seen in Figure 3.10. Notably, the resistivity maps were gridded for interpolated representations of a discrete resistivity model with a grid cell size of 125 m x 125 m.

The primary resistivity feature observed in the 3D unconstrained modeling reveals a sequence of alternating resistive and conductive layers. The inversion identifies a conductive layer bounded by two more resistive zones above and below. This feature is observed at elevations ranging from 250 m a.s.l. to -750 m a.s.l. A thick conductive zone is also prominently visible in all sections, centered around -3000 m a.s.l.

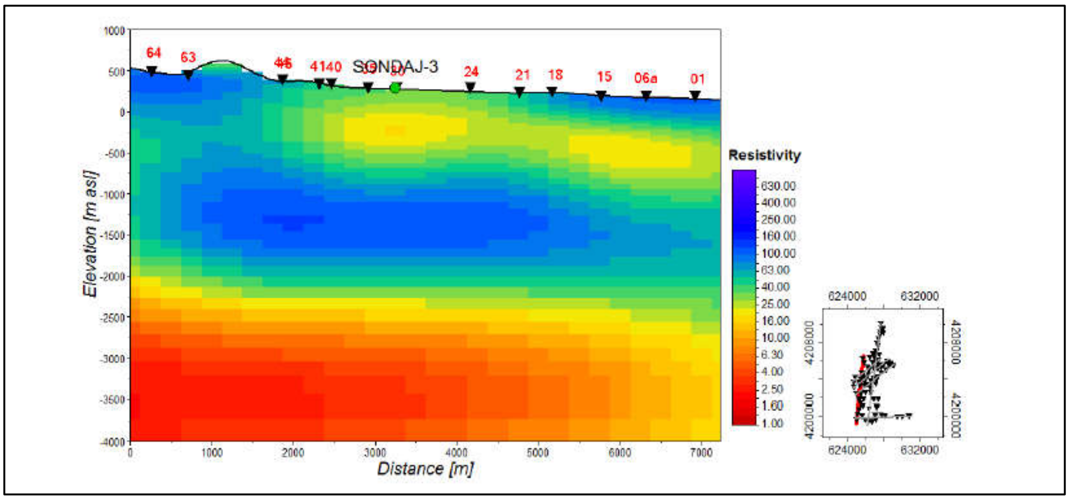

Figure 3.4. Cross-sections through the 3D MT resistivity model along profile NS1. North is to the left.

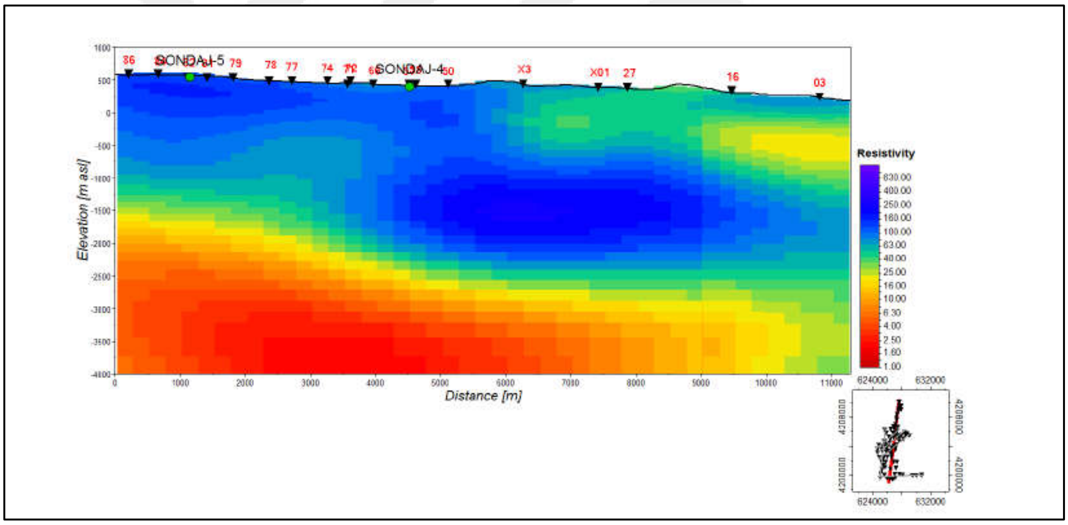

Figure 3.5. Cross-sections through the 3D MT resistivity model along profile NS2. North is to the left.

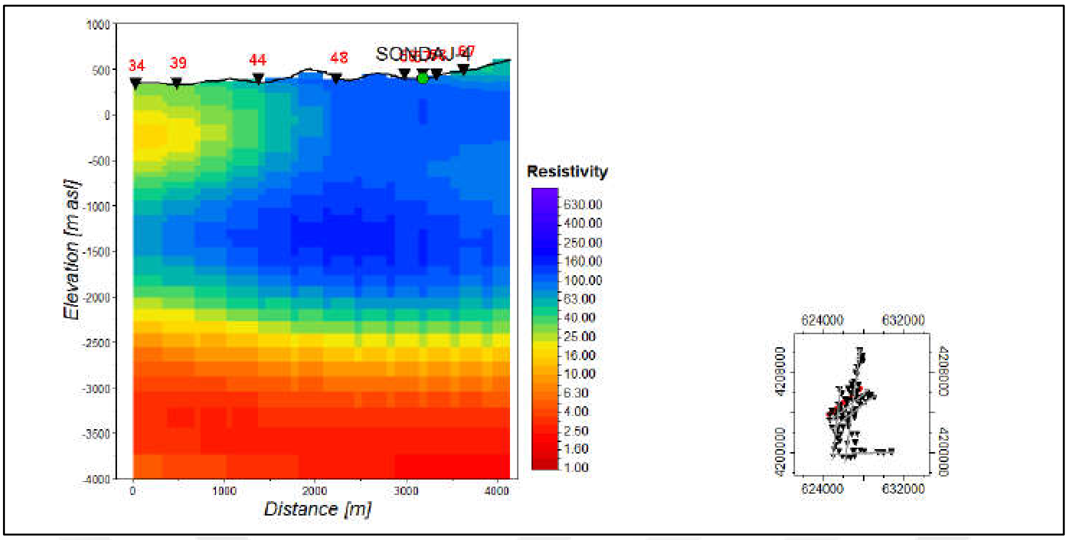

Figure 3.6. Cross-sections through the 3D MT resistivity model along profile SWNE1. SW is to the left.

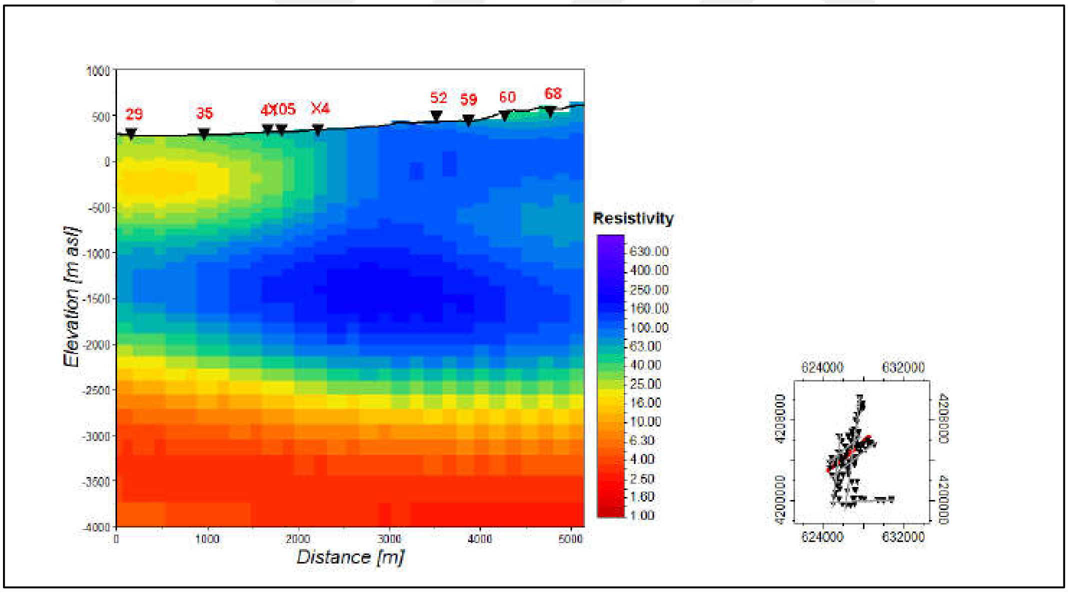

Figure 3.7. Cross-sections through the 3D MT resistivity model along profile SWNE2. SW is to the left.

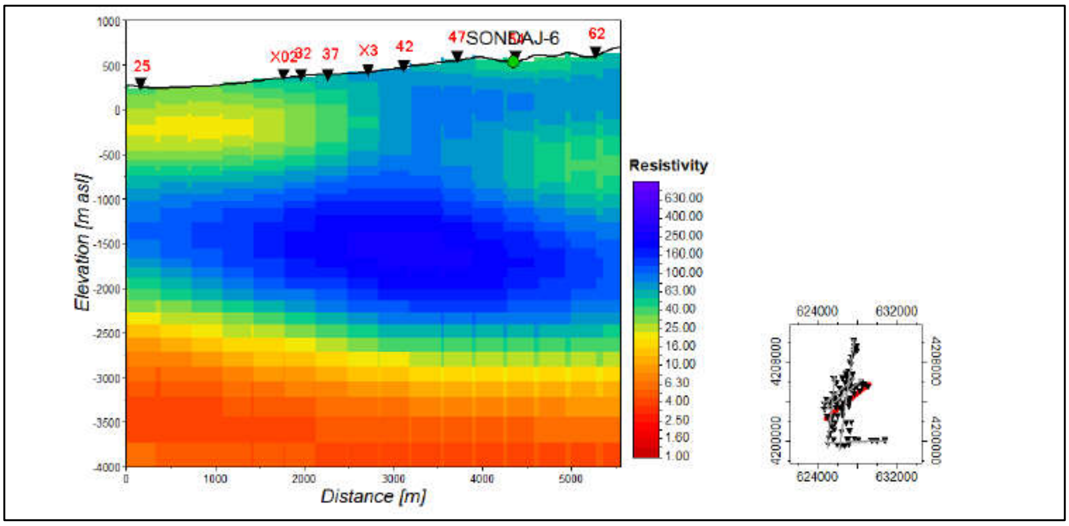

Figure 3.8. Cross-sections through the 3D MT resistivity model along profile SWNE3. SW is to the left.

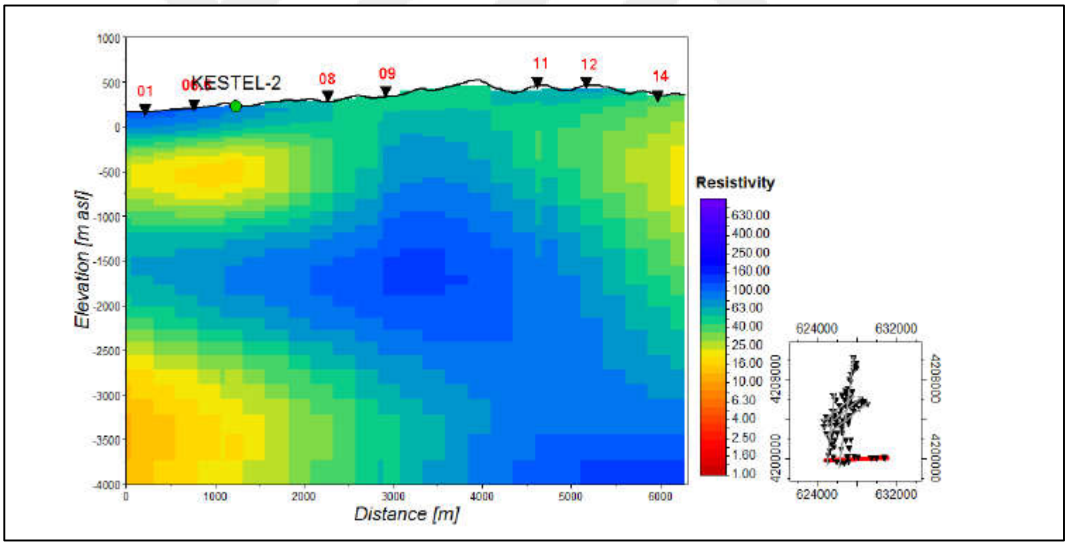

Figure 3.9. Cross-sections through the 3D MT resistivity model along profile SWNE4. SW is to the left.

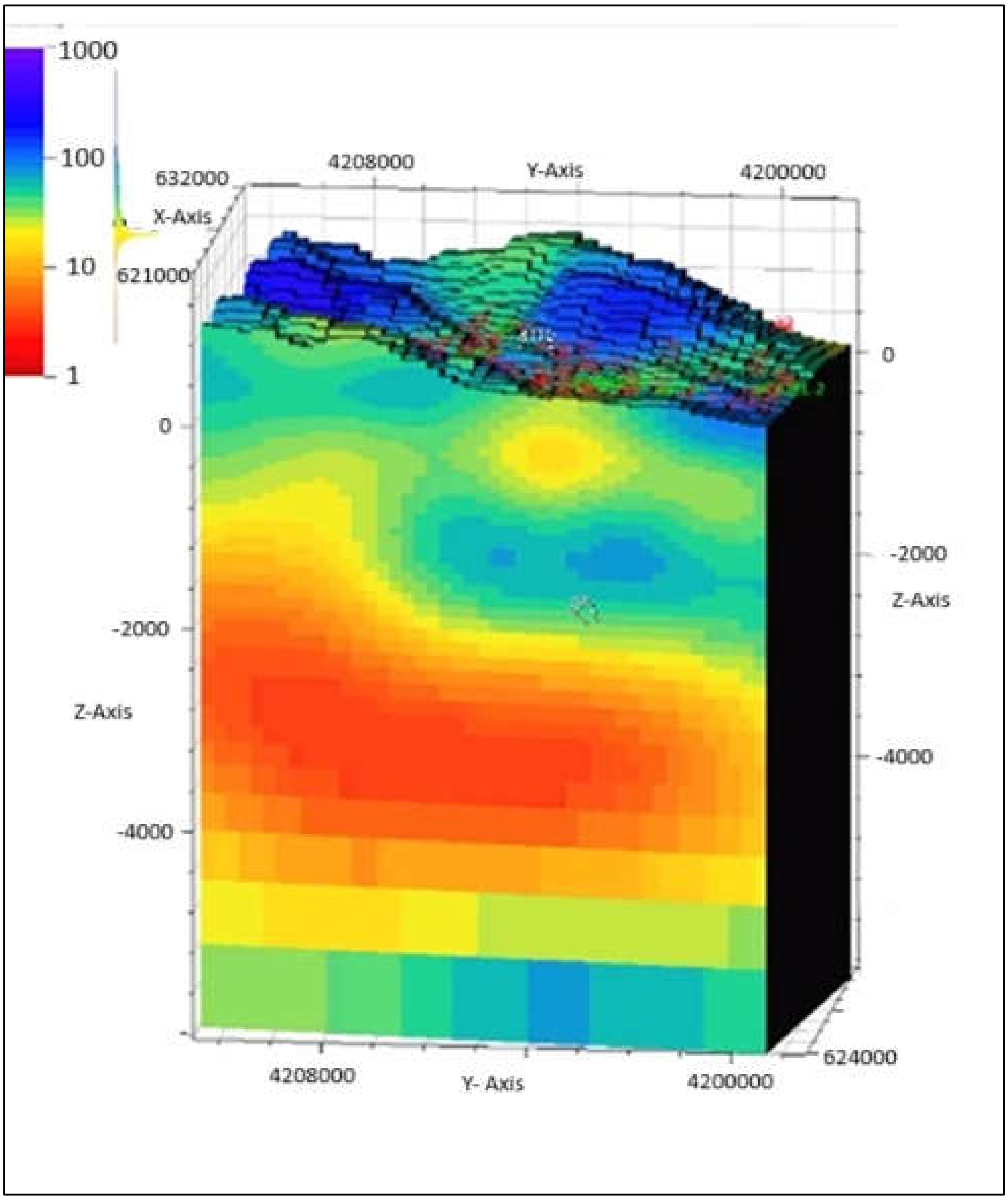

Figure 3.10. 3D MT Model

3.2 Deep Geothermal Drillings

The following sections provide general information on the deep geothermal wells, including the well design and the encountered geology.

3.2.1 KS-1 Well Drilling Operations

The KS-1 well was drilled within the Kuyucak license area (2013/22) in Aydın, Türkiye, by SDS Enerji A.Ş., following extensive scientific and geophysical surveys that indicated geothermal potential (Figure 3.11). The drilling operation commenced on September 18, 2014, and was successfully completed on November 18, 2014, after 62 days, reaching a total depth of 3,232 meters. Located at an elevation of 261 meters, the well's coordinates were 625481.9 Easting and 4201623.3 Northing, based on the UTM projection system (Zone 35) with the ED50 datum. The drilling was conducted by using a Drillmec MR-8000 rig, with the rig floor positioned at a height of 5.2 meters. The target formation for the well was marble.

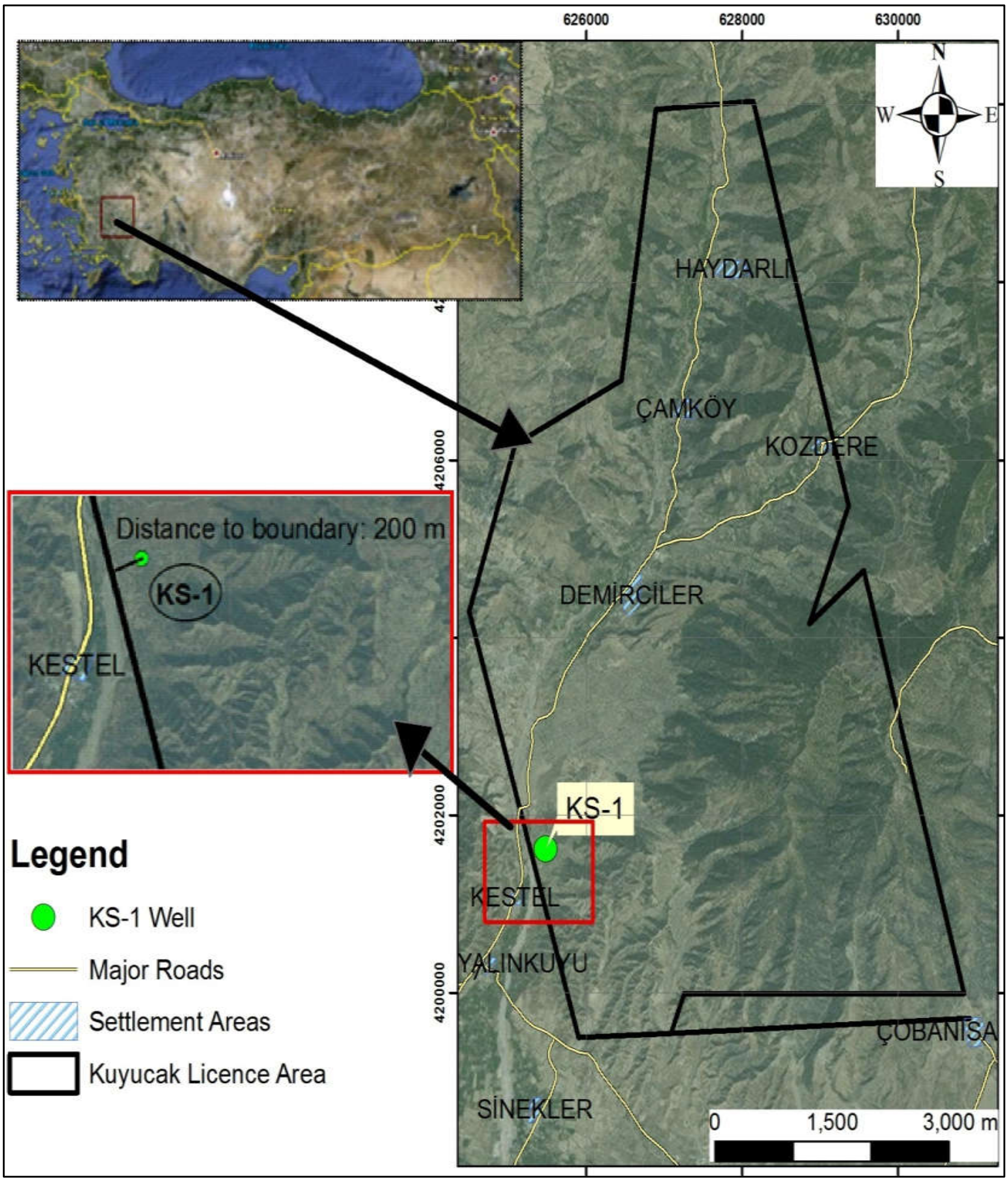

Figure 3.11. Location of the KS-1 Well

This section provides a comprehensive overview of the drilling operations, including a chronological account of the drilling activities, details of the equipment used, descriptions of the geological formations encountered, the final well geometry, and the results of down-hole measurements and tests.

Figure 3.12 shows a view of the borehole location and the drill rig.

Figure 3.12. View from KS-1 borehole location and drill rig

3.2.1.1 Chronological Drilling Summary

The KS-1 well was drilled in four sections, using different drill bits for each section: 26", 17 1/2", 12 1/4", and 8 1/2". The casing diameters, depths, and specifications of casings used in the KS-1 well are tabulated in Table 3.1.

Table 3.1. Casing diameters, depths, and specifications of casings used in the KS-1 well

Well Dia. (in.)	Casing Dia. (in.)	Class	Connection (Thread) Type	Weight (lb/ft)	Lowered depth (top, m.)	Lowered depth (bottom, m.)
26"	20"	J-55	BTC	94	0	103
$17^{1/2}$"	$13^{3/8}$"	K-55	BTC	61	0	614
$12^{1/4}$"	$9^{5/8}$"	K-55	BTC	40	0	451
$12^{1/4}$"	$9^{5/8}$"	K-55	BTC	43.5	451	1648
$12^{1/4}$"	$9^{5/8}$"	N-80	BTC	43.5	1648	1854
$8^{1/2}$"	7"*	K-55	BTC	29	1807	2048
$8^{1/2}$"	7"	L-80 (F)	BTC	29	2048	2216
$8^{1/2}$"	7"**	K-55 (F)	BTC	26	2216	3231

* Total of 1424 m. 7" liner casing was hanged (set) at 1807 m.
** After 2216 m. 7" slotted casing with total of 1015 m. length was used.

The drilling of the KS-1 well commenced with a 26" drill bit, reaching 103 meters, after which a 20" casing was installed, cemented, and the wellhead prepared for the next section. Drilling continued with a 17 1/2" bit down to 614 meters, incorporating TOTCO surveys and a two-stage cementing process to ensure well integrity. The 12 1/4" section extended to 1,854 meters, during which challenges such as pressure drops and high torque required multiple bit replacements and string inspections; the casing was installed and secured with two-stage cementing. The final 8 1/2" section reached a total depth of 3,232 meters, despite significant mud loss between 2,540 and 2,710 meters. A 7" liner was installed from 1,807 to 3,231 meters, transitioning from a solid liner to 2,216 meters, a slotted liner from 2,216 to 3,219 meters, and ending with an 11-meter solid liner.

3.2.1.2 Geological Formations Encountered

The geological units encountered during the drilling of the KS-1 well are described below, and the well log is presented in Figure 3.13.

The stratigraphy of the KS-1 well comprised three main units. The Alluvium Unit, extending from 0 to 60 meters, consisted of poorly graded pebbles, pebbly sand, sandy clay, gravel, and sand in gray tones. Below this, the Neogene Unit spanned depths of 60 to 700 meters and was characterized by moderately to coarsely grained gravel, sandstone, and intercalations of high-plasticity claystone, serving as the cover for the geothermal system. The Paleozoic Basement Unit, encountered from 700 to 3,232 meters, began with quartz-schist and graded into a mica-schist-dominated metamorphic sequence. Various schists, including chlorite-schist and graphite-schist, along with intercalated carbonate rock units, were identified within this unit. The primary reservoir zone was located within the marble units at depths of 2,558 to 2,942 meters, with another potential reservoir encountered between 3,029 and 3,232 meters.

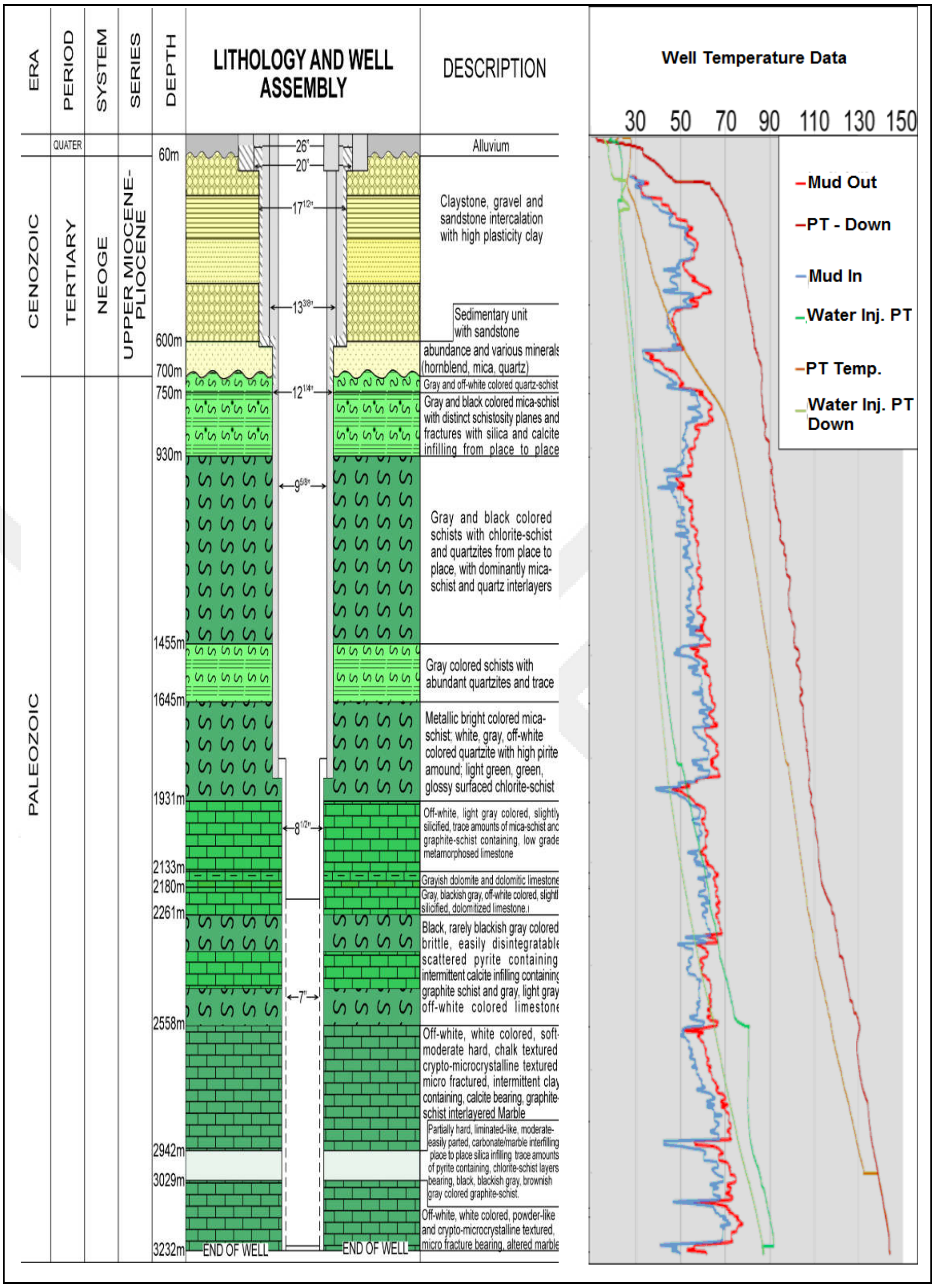

Figure 3.13. The well geometry, drilled lithological units, mud inlet-outlet temperatures, and the results of static PT log and water injection tests.

3.2.1.3 Reservoir Zone and Well Geometry

The reservoir zone showed significant geothermal potential, with total mud losses of approximately 6220 barrels, indicating high permeability (Figure 3.14). The well's final geometry, as determined by Gyro and MWD measurements, showed a deviation of 78.25 meters to the west and 11.17 meters to the south, with a lateral distance of approximately 79 meters between the bottom hole and the wellhead.

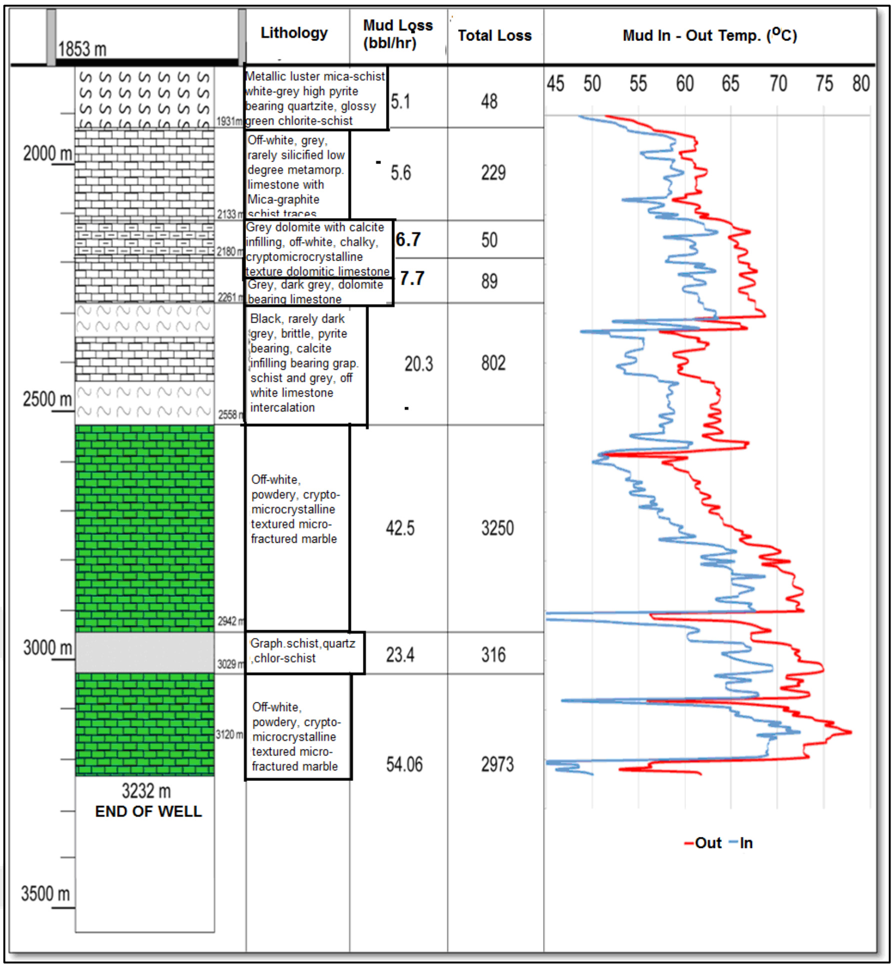

Figure 3.14. Total and hourly mud loss, mud inlet, and outlet temperatures at geological units drilled at 8 1/2" section.

3.2.2 KS-2 Well Drilling Operations

The drilling began on December 6, 2014, at coordinates 41 99 734 North and 626 025 East (Figure 6.22 and Figure 6.23). The drilling operations were completed on January 31, 2015, and a 7" casing (liner) was installed. This section summarizes the 62-day drilling activities from December 6, 2014, to February 5, 2015, detailing the KS-2 well's geometry down to a depth of 3,614 m, the lithologies encountered, the hourly mud temperature variations, and the correlation of this data.

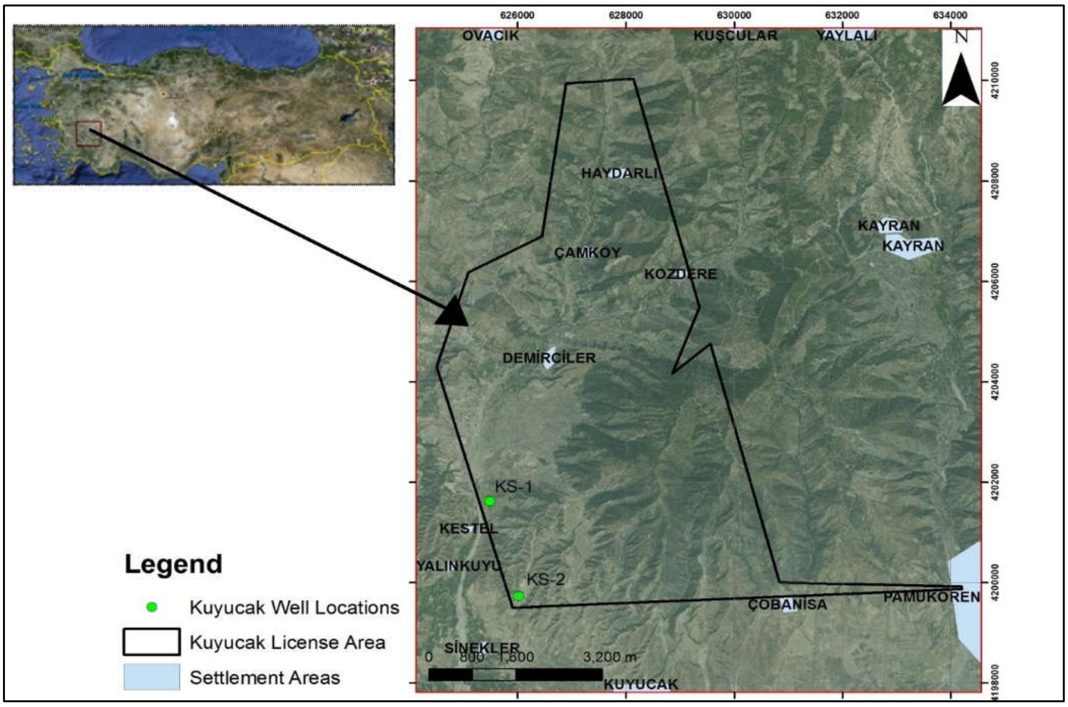

Figure 3.15. Location map of the study area

Figure 3.16. Views of the KS-2 location and drill rig.

3.2.2.1 Chronological Drilling Summary

The drilling of the KS-1 well was carried out in four main sections. The initial 26" section, drilled to a depth of 104 meters, involved installing a 20" casing followed by cementing and mounting a 21 1/4" wellhead. The 17 1/2" section extended from 104 meters to 679 meters, where a 13 3/8" casing was installed, cemented, and fitted with a 13 5/8" wellhead. Drilling from 679 meters to 1,903 meters used a 12 1/4" Mud Motor and PDC drill bit, with Cougar Company providing Mud Motor and MWD services, including well inclination and bottom-hole deviation surveys. A 9 5/8" casing was hung at 577 meters and cemented. The final 8 1/2" section utilized a PDC drill bit, extending from 1,903 meters to the total depth of 3,614 meters. A final survey at 3,369 meters recorded a bottom-hole deviation of 168 meters from the wellhead with an 8-degree inclination. A 7" casing was installed within the 9 5/8" casing at 1,815 meters, transitioning to a 7" solid liner down to 2,560 meters, a slotted liner from 2,560 to 3,585 meters, and a closed liner from 3,585 meters to the total depth (Figure 3.17).

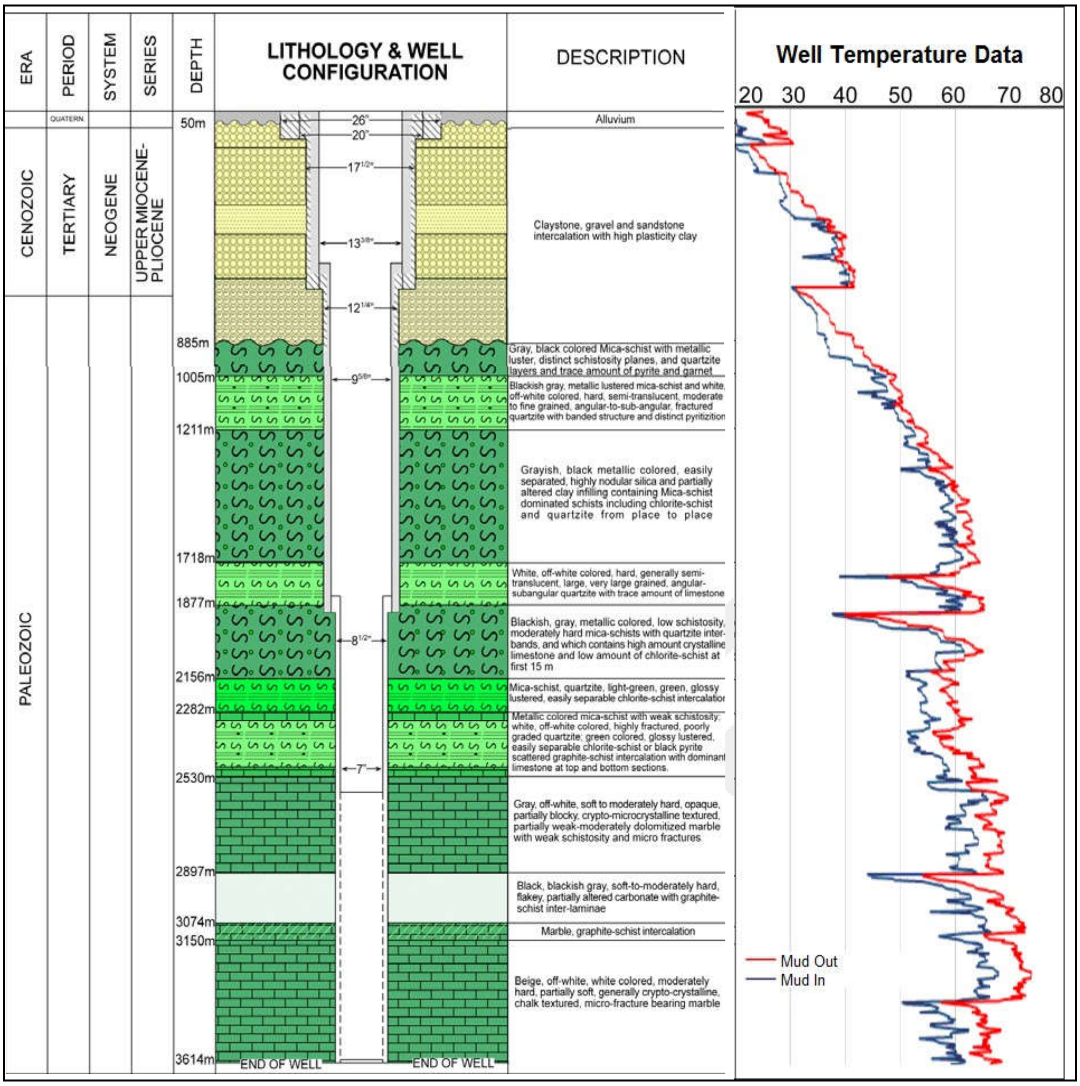

Figure 3.17. The well geometry, drilled geological units, and mud inlet/outlet temperatures.

3.2.2.2 Encountered Geological Units

The geological units encountered down to the total depth of 3,614 m are described herein.

From 0 to 50 meters, the Alluvium unit consisted of medium-grained, poorly graded pebbles, pebbly sand, sandy clay, gravel, and sand, all in gray tones. Beneath this, from 60 to 885 meters, lied the Neogene cover unit of the geothermal system, composed of gray to brown, medium-to-coarse-grained, poorly graded gravel, sandstone, and intercalated high-plasticity claystone (Figure 3.17). At 885 meters, the Paleozoic basement unit began, marked by gray to black, metallic, shiny mica-schist with prominent schistosity planes, quartzite, pyrite, and garnet, as well as interbedded white to off-white, hard, semi-translucent, fine-grained quartzite and black mica-schist. Between 1,211 and 1,718 meters, gray to black mica-schist with nodular silica, clay infillings, and chlorite-schist dominated.

From 1,718 to 2,530 meters, crystalline limestone, and various schist types were encountered, including mica-schist, quartzite, chlorite-schist, and graphite-schist (Figure 3.17). The well then intersected marble with geothermal reservoir characteristics, including microfracturing and partial dolomitization, between 2,530 and 2,897 meters. Below this, from 2,897 to 3,074 meters, a graphite-schist unit with intercalated carbonate rocks was observed. Finally, from 3,074 to 3,614 meters, beige to white marble with microfractures and a chalk-like texture was encountered in the well, indicating a second geothermal reservoir. Notably, gradual mud loss was observed starting at 3,325 meters within the marble unit, with a total loss of 4,216 barrels by the end of drilling.

3.2.2.3 Reservoir Zone and Well Geometry

Viking Mud-Lugging monitored the drill mud characteristics, including pH, viscosity, density, and plastic viscosity, as well as the load on the drill bit, standpipe pressure, assembly torque, RPM, ROP, mud flow rate, pump stroke count, electrical conductivity, and gas inlet and amount. The drilling company continuously recorded mud inlet and outlet temperatures, especially noting sections where mud temperatures exceeded 65ºC, necessitating cooling operations. The difference between inlet and outlet temperatures, typically ranging from 5 to 10ºC, suggests significant geothermal potential.

The geothermal potential was confirmed by the encountered lithologies, temperature data, and mud loss, similar to the KS-1 well located 2 km NNW of KS-2. Two geothermal reservoirs were identified, separated by a graphite-schist unit. The first reservoir had a thickness of 367 m between 2,530 m and 2,897 m, while the second reservoir, encountered at 3,150 m, could not be fully evaluated due to the cease of the operations because of mud loss.

The 3D Model, as seen in Figure 3.18, was constructed to depict the extent of the geothermal reservoir, where the red areas show the low resistive reservoir zones and the drilling locations. As can be seen from the figure, the reservoir depth encountered for both KS-1 and KS-2 wells were in agreement with the reservoir geometry extracted from MT data. This proved the existence of a geothermal reservoir with significant potential.

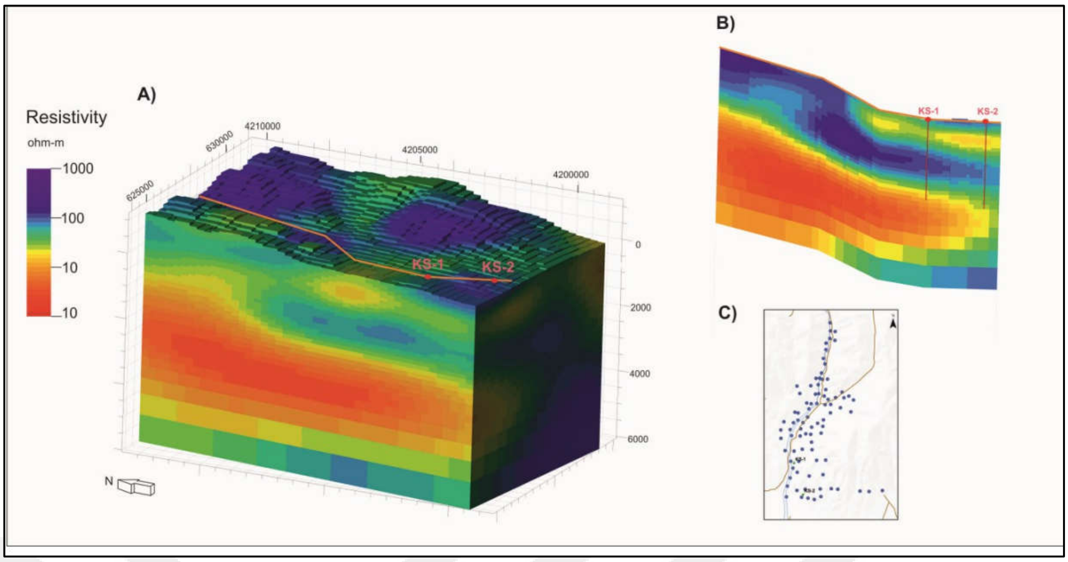

Figure 3.18. A) 3D-MT model of the study area B) Cross-section intersecting KS-1 and KS-2 wells C) MT measurement location.

CHAPTER 4

PRINCIPAL STRESS MAGNITUDE AND ORIENTATION

In this chapter, the methodology followed for the estimation of the principal stress magnitudes and orientations is provided. Fault kinematic measurements were conducted to determine the principal stress orientations, and the methods and results are presented in this chapter. All work for determining the principal stress orientations has been performed in the scope of the TUBITAK 1001 project under grant number 119Y535.

4.1 Principal Stress Magnitudes

The stress magnitudes were determined from the mudloss data. During the drilling operations, the mud density should be kept at a certain range which is referred to as the "mud window". If the mud density is below the mud window, well stability problems can be experienced, whereas if the mud density is above the mud window, the mud density surpasses the minimum principal stress and causes the formation of fractures that lead to mud loss to the formation. However, mud density may not be kept at the mud window due to the changing pore pressure and minimum principal stresses with depth, which give rise to well stability problems or the formation of hydraulic fractures. Complete loss in circulation at several depths has been observed at the wells drilled in the study area, which means that the well density exceeded the stress required to form fractures. Thus, the mud density at depths where complete loss in circulation was observed gives us information on the minimum principal stress magnitude.

Encountered marble units of Menderes Massive and the mud loss depths were used as the initial identifier of the reservoir units. The major total mud loss was observed between 2558-2942 meters (3250bbl) and 3029-3232 meters (2973 bbl), followed by less severe mud losses between 1931-2133 meters (229 bbl) and 2261-2558 meters (802bbl). The well was halted due to total mud loss at 3232 m. These levels were identified as potential reservoir units. The mudloss values at several depths in units of BBL/hr are given in Table 4.1. The average mud density corresponding to these depths was 8.6 g/cm^3.

Eaton's formula (Eaton, 1972) was used to calculate the least principal stress magnitude, which is as follows:

$$S_{hmin} = P_p + \frac{\vartheta}{1-\vartheta}(S_v - P_p) \quad \text{(Equation 4.1)}$$

where, S_{hmin} is the minimum horizontal stress, P_p is the pore pressure, and υ is the Poisson's ratio. In order to determine the pore pressure, mud density data was collected at depth where, the pore pressure gradient can be calculated as:

Mud density = pore pressure gradient (psi/feet) / 0.052 (Equation 4.2)

Overburden stress (vertical stress; S_v) or the maximum horizontal stress for a normal faulting environment is calculated as:

S_v= rock density x gravity constant x depth (Equation 4.3)

Table 4.1. Mud parameters at different depths

Depth (m)	Mud density (gr/cm^3)	Mud Loss (BBL/hr)
2577	8.8	100
2677	8.6	67
2686	8.6	68
2788	8.6	60
3023	8.7	50
3161	8.7	50
3213	8.6	300

Thus, the minimum stress gradient was calculated as 0.1 bar/m. The minimum stress values calculated accordingly can be seen in Figure 4.1. The theoretical vertical stress, or the maximum principal stress values for a normal faulting environment for a rock density of 2700 kg/m^3, are plotted in Figure 4.1.

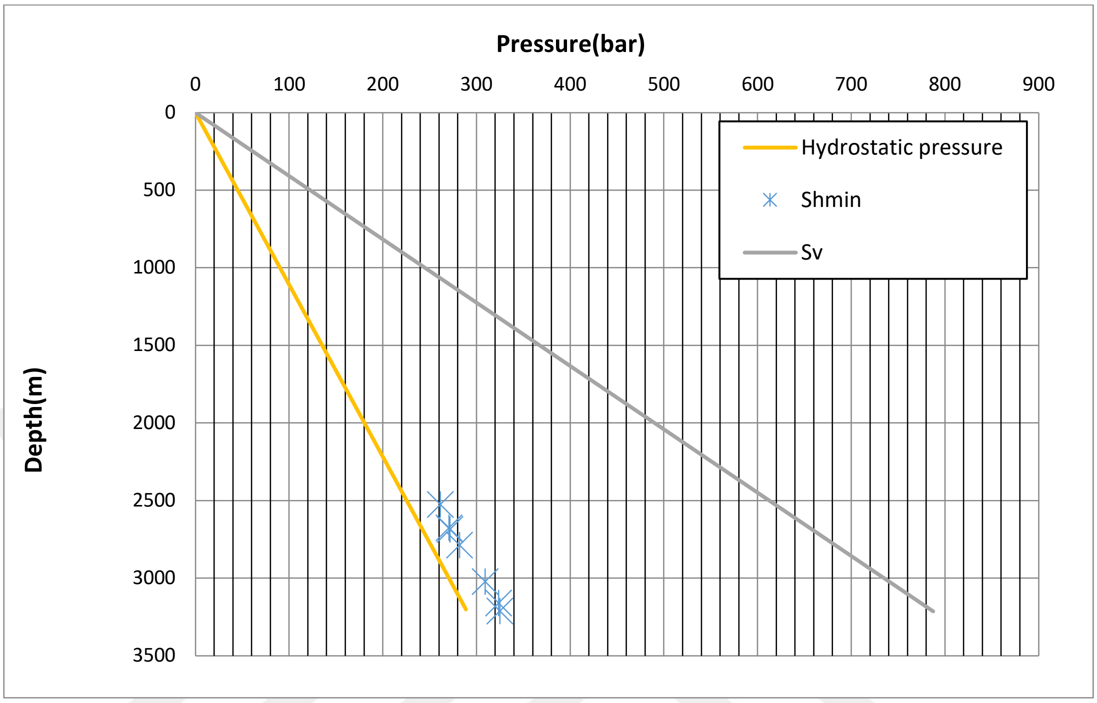

Figure 4.1. S_v, S_{hmin}, and hydrostatic pressure change with depth.

Figure 4.2 illustrates the S_{hmin}, S_v, pore pressure, and theoretical hydrostatic pressure values.

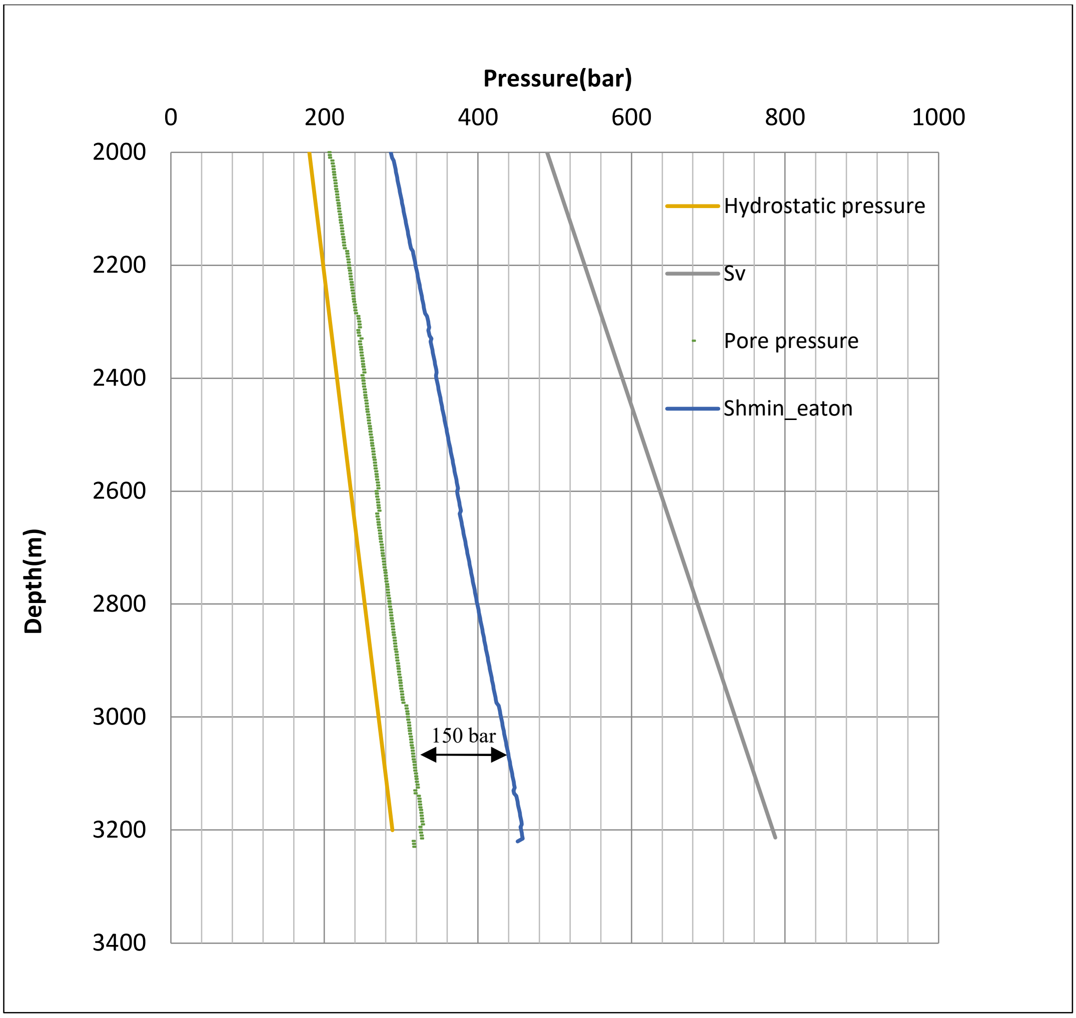

Figure 4.2. Pore pressure, S_{hmin}, and S_v magnitudes at depth

To initiate a hydraulic fracture, an injection pressure of approximately 150 bars is required in excess of the pore pressure to reach S_{hmin}, which could be achieved with flow rates around 400 l/min.

4.2 Principal Stress Orientation

4.2.1 Literature Review

The kinematic analysis methods using fault-slip data are essentially divided into graphical and numerical groups. The foundation of both methods is based on the principle that the slip direction (fault striations) coincides with the direction of maximum stress on the fault plane that caused the faulting. In other words, the fault striations represent the maximum stress on the plane. This idea was first theorized by Wallace (1951), and later, the mathematics behind this process was formulated by Bott (1959).

Following these pioneering works, Carey and Brunier (1974) reversed this process, developing a method to determine the principal stress directions that caused faulting through paleo stress inversion, using fault striations as a starting point. In the subsequent period, many other paleo stress inversion methods were developed, that considered different boundary conditions and variables (e.g., Etchecopar et al., 1981, Angelier et al., 1982, Armijo et al., 1982, Angelier, 1990, Yin and Ranalli, 1993). The fundamental logic of these methods relied on using at least four or more fault-slip data points from the same fault zone and deformation phase. In other words, the best-fit solution was found by minimizing the angle between the re-calculated eigenvectors from the data or the measured direction of each fault striation and the maximum shear stress calculated for each fault plane based on these striations (direct inversion). Many of the methods mentioned above represent variations of these two methods. On the other hand, other methods are more graphical, considering the tectonic setting (e.g., Alexandrowski, 1986, Krantz, 1988). These methods focus more on the nature of the deformation and relate slip direction with fault geometries and distributions by considering the 3D geometry of regional deformation (uniaxial or triaxial deformation).

This study used the rotational optimization (RO) method, as presented in the Win-Tensor program developed by Delvaux and Sperner (2003).

The paleo stress inversion techniques developed by Angelier (1989), which form the main mathematical framework for many paleo stress inversion software, operate on the principle of the reduced tensor. According to this principle, there are nine variables: three related to fault geometry, three related to the orientation of the principal stresses, and three related to the magnitudes of the stresses. Since the orientations of the faults can be measured in the field, the number of variables can be reduced to six. It is possible to establish a geometric relationship between the stress magnitudes depending on the type of deformation. This process can be performed by defining the stress magnitudes relative to each other or by subtracting the minimum stress magnitude (σ_3) from the other two stress magnitudes (σ_1 and σ_2) and using the geometry of the stress ellipsoid to reveal the magnitude relationship between the stresses. This ratio is called the shape factor and is defined by the following equation:

$R = (\sigma_2 - \sigma_3) / (\sigma_1 - \sigma_3)$ (stress ratio) (Equation 4)

Contrary to popular belief, the R-value is independent of the deformation regime (extension, strike-slip, or compression) and gives insight into whether the deformation is uniaxial (values approaching 0 or 1) or triaxial ($\sigma_1 > \sigma_2 > \sigma_3$).

As can be understood from the mathematical expression, if the minimum (σ_3) and intermediate principal stress (σ_2) values are close to each other, as deformation progresses, these two stresses can easily interchange, causing stress permutation and resulting in almost incompatible fault patterns (strain partitioning). For example, when the intermediate principal stress (σ_2) is vertical, strike-slip faults occur, while when the minimum principal stress (σ_3) is vertical, reverse faults form. According to the Coulomb-Mohr criteria, these two fault sets presents incompatible geometries

(Yin and Taylor, 2011). The same situation applies when the intermediate and maximum principal stress magnitudes are close to each other. If both stresses are horizontal and close in magnitude, almost perpendicular thrust/reverse faults form simultaneously (in both cases, σ_3 is vertical) on a geological time scale, while in cases where one is vertical, and the other is horizontal, strike-slip faults (σ_2 vertical) and normal faults (σ_1 vertical) will form simultaneously due to vertical axis changes.

On the other hand, there is a direct relationship between stress ratios, stress geometries, and transpression (compressional strike-slip system) or transtension (extensional strike-slip system). As can be inferred from the evaluations above, vertical σ_2 and σ_3 and a low R-value indicate transpression, while vertical σ_1 and σ_2 and a high R-value indicate transtension.

4.2.2 Collection of Fault Kinematic Data

Paleostress measurements are carried out by reading the strike, dip, and angles formed between the fault-slip striations and the strike from the fault plane. Additionally, it is necessary to determine the movement direction of the fault by evaluating kinematic indicators on the fault plane (such as mineral steps, tension cracks, stylolites, and Riedel fractures, etc.). Within the scope of the project (Akgün et al., 2024), paleostress data were collected from 37 different stations during field studies (Figure 4.3). In general, the fault-slip data were collected from Quaternary units, which define the recent basin fill, Miocene units that describe the older basin fill, and the schist-marble alternating units that make up the Menderes Massif.

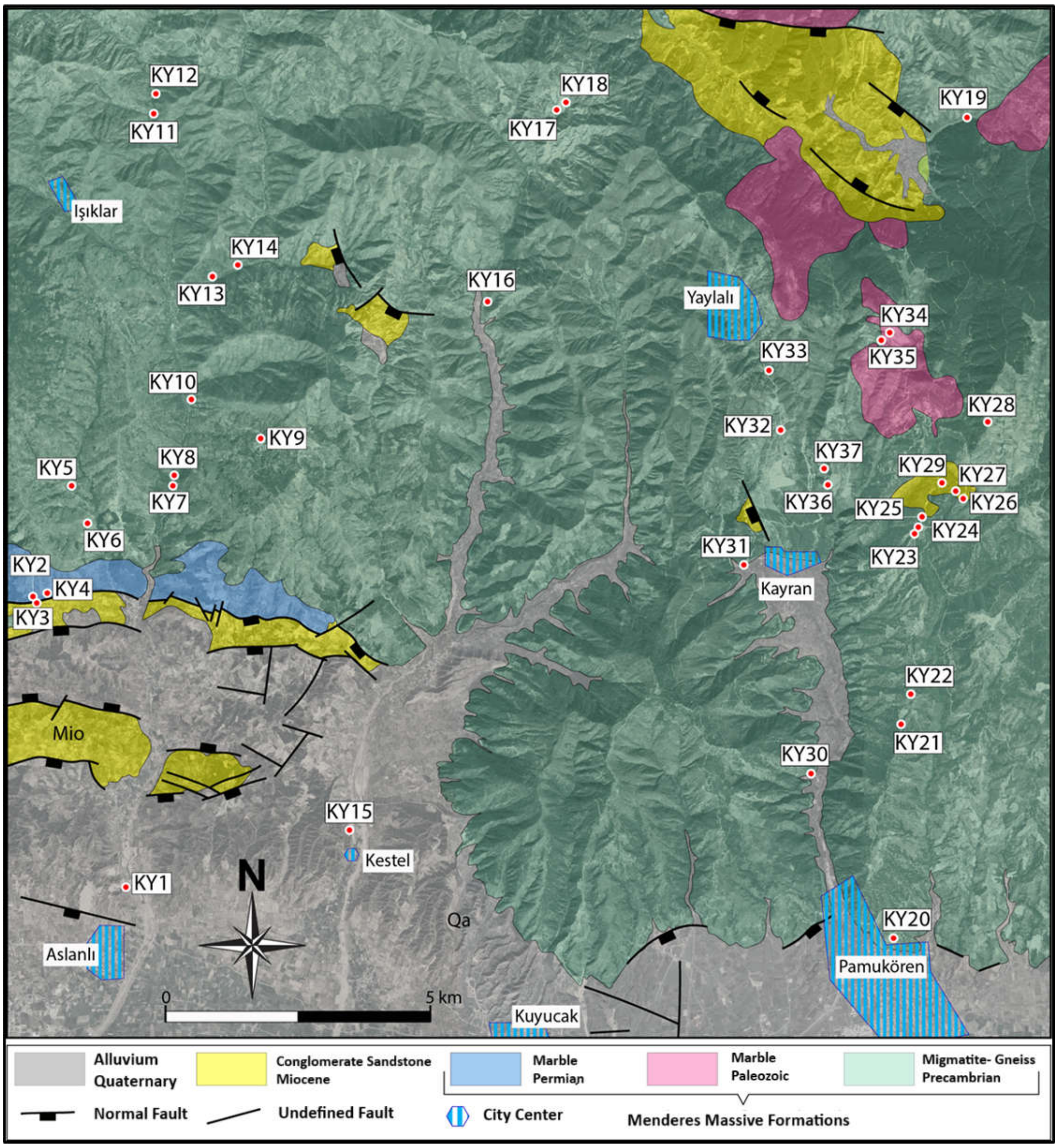

Figure 4.3. A map showing the locations of the stations where paleostress data were collected from the study area.

Due to the high displacement and rate of the fault planes required to define the large-scale faults that outline the graben boundary, it is often impossible to observe them in the field. In addition, the fault planes and, consequently, the fault striations formed on them are often not preserved in the field due to the lack of erosion resistance of the materials in the units cut by the main fault lines. The presence and type of the fault can be inferred from morphological changes and changes in layer orientations (Figure 4.4).

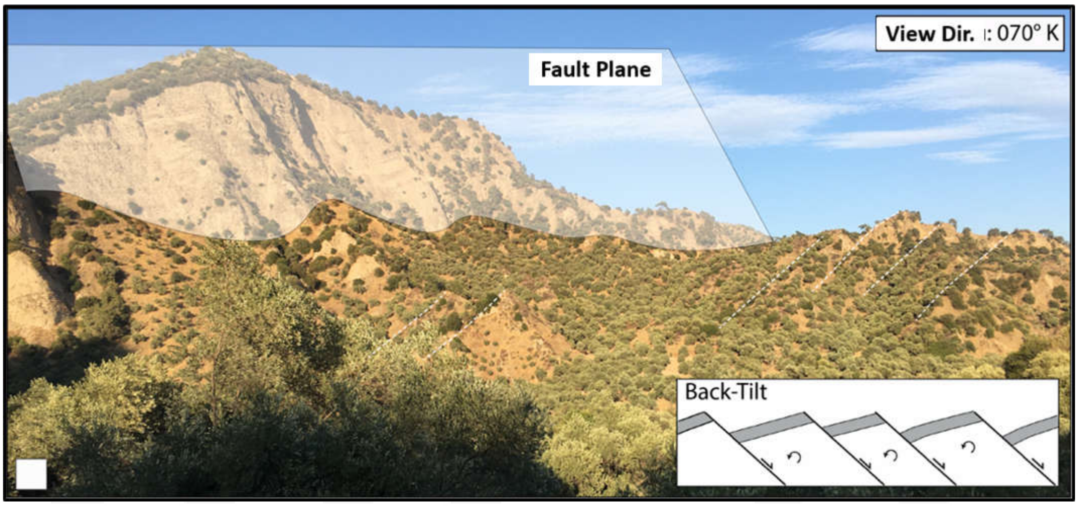

Figure 4.4. A map showing the locations of the stations where paleostress data were collected from the study area.

Fortunately for the project team, some well-preserved fault planes among the mesoscopic-scale normal faults developed within the younger Quaternary units (Figure 4.5a). These fault planes also captured well-developed fault striations (Figure 4.5b) noting that obtaining fault-slip data from Quaternary units is crucial in determining the active-present tectonic regime.

The inversion of fault-slip data shown in Figure 4.5c demonstrates the directions of the principal stress axes (σ_1: maximum, σ_2: intermediate, and σ_3: minimum principal stress axes). The fault plane, which has an average dip value of 50-60°, reflects the typical dip value of a normal fault, as theoretically accepted. In the stereographic projection (Schmidt equal-area, lower hemisphere), the obtained principal stress axes were found as σ1 = 88/262°, σ2 = 02/094°, and σ3 = 00/004°. Additionally, the shape factor was found to be Φ(R) = 0.03, while the slip deviation angle was kept below 30° (the histogram is shown under the title "slip deviation alpha" in Figure 4.5). This ratio reflected radial extensional (0 < R < 0.25) stress conditions when evaluating the shape factor value. However, the dominant extension direction was found to be roughly N-S. The strike of the fault plane aligned with the boundaries of the graben.

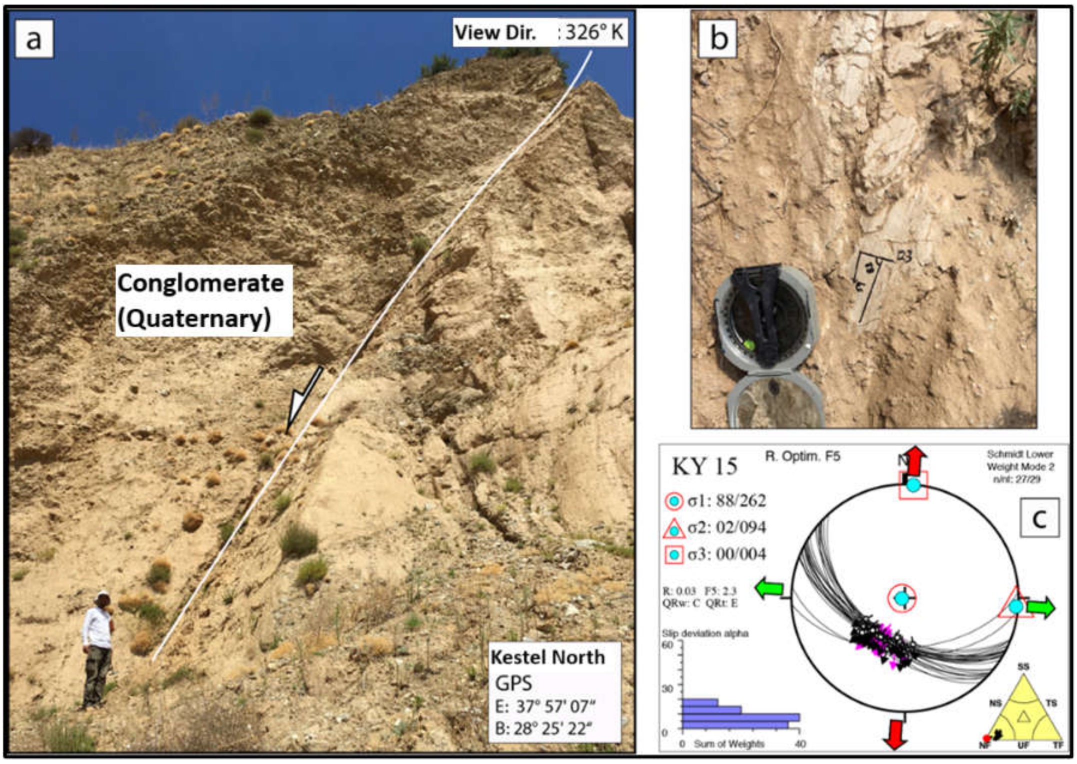

Figure 4.5. a) A normal fault observed within the Quaternary-aged conglomeratic unit north of Kestel, b) fault striations on the fault plane, and c) the inversion of the collected paleostress data.

During the field studies, although no direct fault data were observed within the Miocene units in the study area (Figure 4.6), normal faults that developed between the Miocene units and the marble units belonging to the basement were encountered (Figure 4.6a). It was observed that some levels of the marble unit were significantly altered (Figure 4.6a). Due to this alteration, deformations in the fault-slip striations on the fault plane became apparent (Figure 4.6b). Figure 4.6c shows the orientations of the principal stress axes obtained from the inversion of the fault-slip data collected from locations KY2 and KY4. The principal stress axes for KY2 were determined to be σ_1 = 67/274°, σ_2 = 18/055°, and σ_3 = 14/149°, while for KY4, the principal stress axes were σ_1 = 70/058°, σ_2 = 17/274°, and σ_3 = 11/181°. The shape factors were also determined to be Φ(R) = 0.49 and Φ(R) = 0.27, respectively. When evaluating the shape factor values, these ratios reflect pure extensional stress conditions ($0.25 < R < 0.75$). The extension direction was again found to be roughly N-S. While the strike of the fault plane at KY2 is well aligned with the graben boundaries, the data collected from KY4 indicate that the strike of the fault plane is approximately NW-SE. This is related to undulations in the fault's orientation during its evolution. The important point is that the maximum principal stress axis (σ_1) is vertical, while the minimum principal stress axis (σ_3) is horizontal. The small variations in the orientation of σ_3 are associated with local changes in the fault strike.

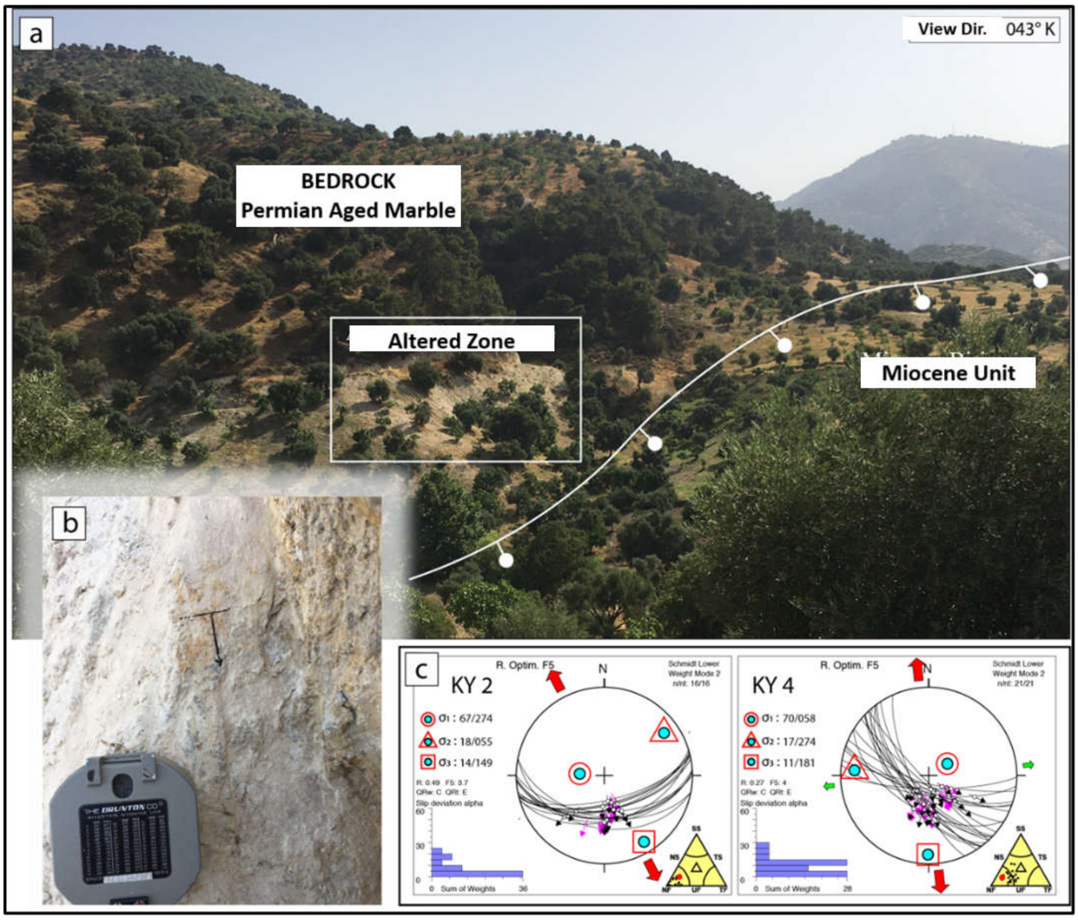

Figure 4.6. a) Normal faulting developed between altered Permian-aged marble units of the basement and Miocene-aged conglomeratic units, b) The fault-slip striations observed on the poorly preserved fault plane along this fault line, c) The orientations of the principal stress axes obtained from the inversion of the fault-slip data collected from the fault plane.

Paleostress data were also collected from the schist-marble interlayered unit constituting the Menderes Massif. The geometric relationship between the fault plane and the schistosity (foliation) plane was considered while collecting these data. At the same time, attention was paid to the presence of reference structures (such as different metamorphic units or vein formations, etc.) that could be used to test the displacements caused by the fault plane to ensure the reliability of the data (Figure 4.7).

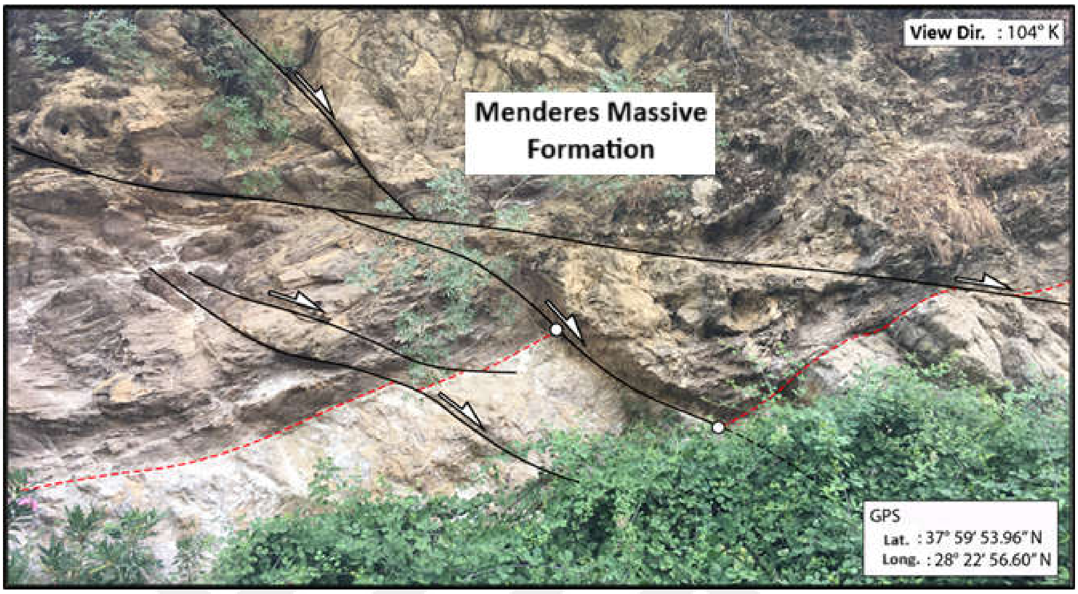

Figure 4.7. a) A field view provided as an example of the reference structures used for displacements caused by faulting in the schist units forming the Menderes Massif.

A field view of the fault-slip data collected from the units constituting the Menderes Massif and an example of a paleostress inversion for station KY17 are given in Figure 4.8. The orientations of the principal stress axes obtained from the inversion of the fault-slip data yielded σ_1 = 83/251°K, σ_2 = 01/155°K, and σ_3 = 07/065, while the shape parameter was determined as Φ(R) = 0.51. This ratio falls within $0.25 < R < 0.75$ when evaluating the shape parameter value, reflecting well-developed pure triaxial extensional stress conditions. The extension direction from this station was found to be approximately E-W.

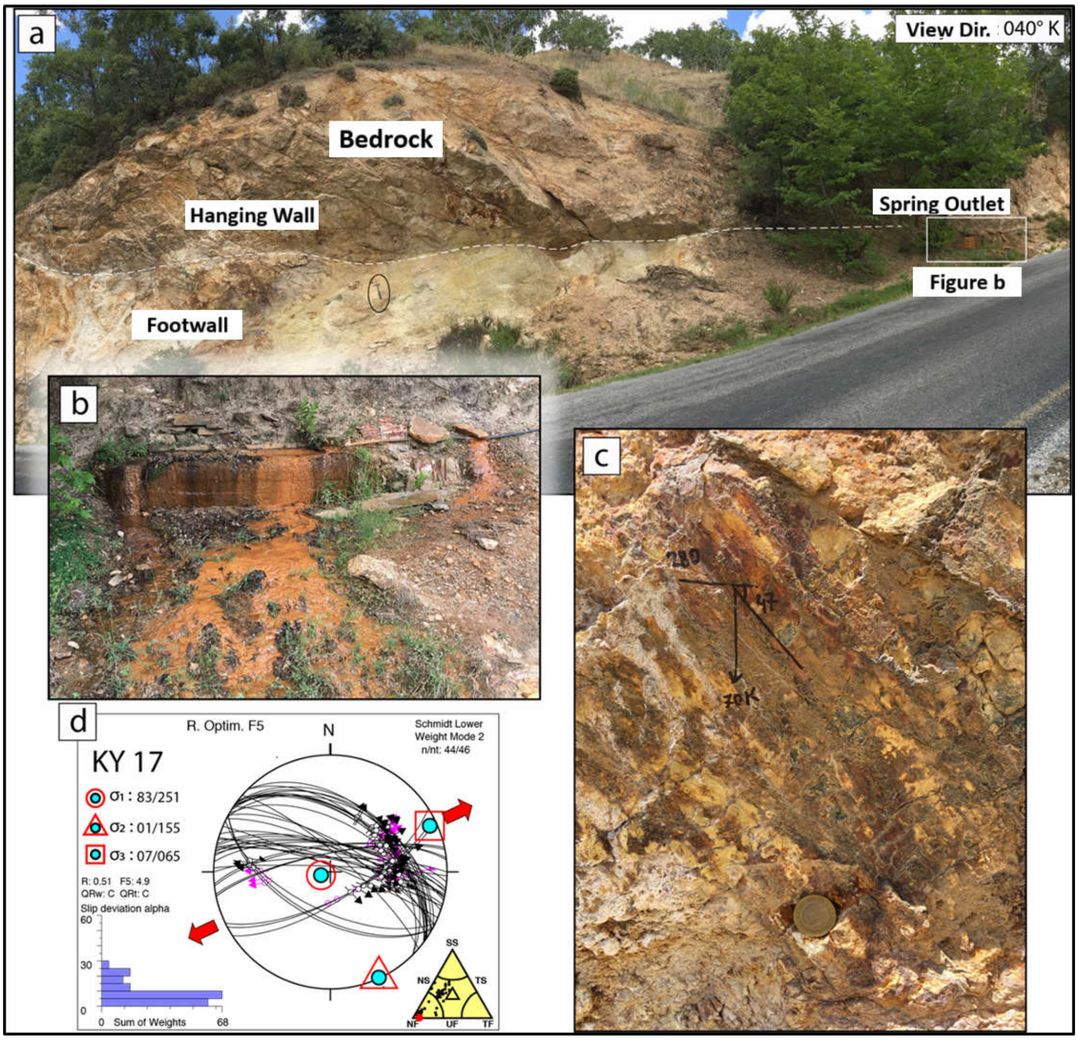

Figure 4.8. a) Field view of a normal fault developed within the units of the Menderes Massif, b) Spring development along the normal fault, c) Well-preserved fault-slip striations on the fault plane, d) Paleostress inversion of the data collected from the (KY17) plane.

Paleostress data were collected from 37 different stations in the study area as part of the project. For this scope, more than 1,000 fault-slip data containing information on strike, dip, rake, and direction of movement were collected from the field (Figure 4.9a). The dip-slip values measured on the fault plane are shown with arrows in Figure 4.9a. Although the slip direction indicated by these arrows appeared to be in all directions, the dominant direction could be evaluated as NE-SW. The Frohlich diagram presented in Figure 4.9b is significant in showing which types of faults the collected fault-slip data were obtained from, indicating that the collected fault-slip data were predominantly of normal (NF) fault character. However, the presence of a few strike-slip (SS) faults was also possible. Additionally, there were only five fault plane (UF) cases for which identification was problematic.

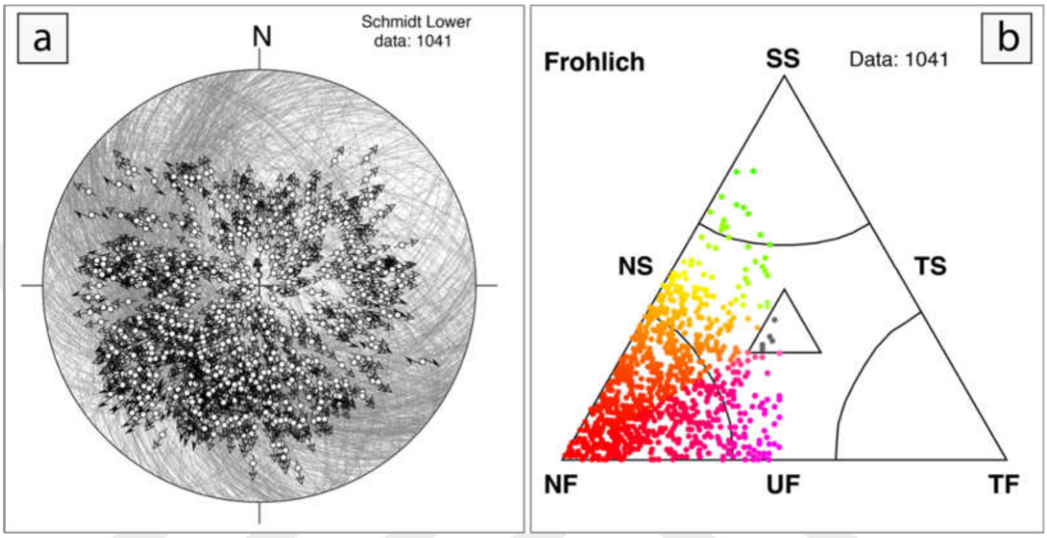

Figure 4.9. a) The stereographic projection of the collected fault-slip data (N > 1000) in the Schmidt lower hemisphere, and b) the Frohlich diagram of the collected fault-slip data.

When the poles of the fault planes were placed on the stereonet (Figure 4.10a), it was observed that the points representing the poles of the planes clustered in the NE-SW regions of the stereonet. The rose diagram showing the strike values of the collected data is presented in Figure 4.10b. The dominant strike direction in the rose diagram is approximately NW-SE, with a secondary group drawing attention to an N-S orientation. The presence of the secondary group is also evident in Figure 4.10b, which shows the poles of the fault planes.

To better analyze the data, a histogram of dip values was created (Figure 4.10c). According to the histogram, the maximum dip value has a frequency of about 60°, while the distribution range of dip values varies between 20° and 89° (Figure 4.10c).

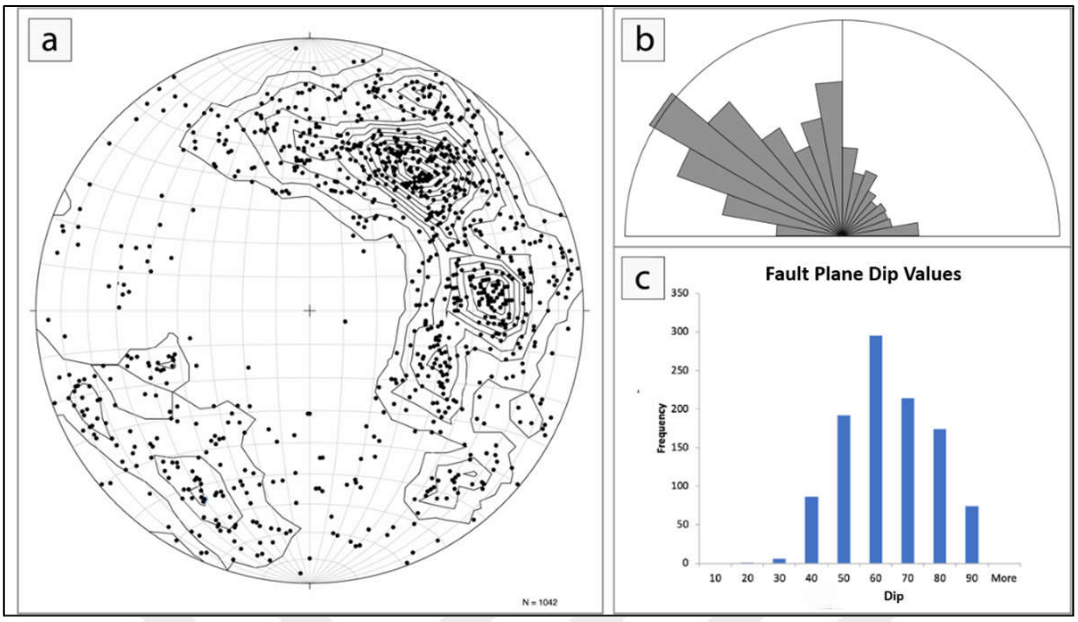

Figure 4.10. a) Stereographic projection of the poles of the collected fault-slip data (N = 1042) in the Schmidt lower hemisphere, b) Rose diagram of the strikes, and, c) Histogram of the dip values.

The fault-slip measurements collected from different regions of the study area were analyzed using the inversion method, and 38 stress configurations were obtained (Table 4.2 and Figure 4.11). The rotational optimization method (Delvaux and Sperner, 2003) was used to obtain the solutions presented in Figure 4.11. In this method, the Alpha (α) value, which defines the angular deviation between the calculated and measured slip vectors, was kept below 30°. As a result, the software automatically excluded 31 measurements, and 1,008 data points were used in the solution. The excluded data represent 3% of the total data. Two paleostress solutions were obtained from station KY32 by applying incompatibility criteria and separation procedures. These first and second solutions are labeled "A" and "B" in Figure 4.11.

Table 4.2. Coordinates of the fault-slip data collected from the study area and the paleostress principal axis orientation results. σ_1, σ_2 and σ_3 represent the plunge and azimuth of the maximum, intermediate, and minimum principal stress axes, respectively. Avg. α: The average amount of deviation in the slip vector, R(Φ): stress ratio (shape factor), R': Corrected shape factor based on the stress regime (Delvaux

et al., 1997), Nt: Number of measurements collected for each station, Nu: Number of measurements used in the analysis, Ns: Number of measurements excluded during the analysis (Akgün et al., 2024).

Station #	**Latitude (D°D′S″)**	**Longitude (D°D′S″)**	**σ_1 (P/D)**	**σ_2 (P/D)**	**σ_3 (P/D)**	**Ave. α**	**R(ϕ)**	**R'**	**Nu**	**Nt**	**Ns**	**Stress Type**
KY1	37 56 30	28 22 30	70/079	19/249	03/340	5.2	0.46	0.46	28	28	0	Pure Extension
KY2	37 59 24	28 21 21	67/274	18/055	14/149	7.0	0.49	0.49	16	16	0	Pure Extension
KY3	37 59 25	28 21 21	79/237	00/328	11/058	16.2	0.14	0.14	41	41	0	Radial Extension
KY4	37 59 27	28 21 28	70/058	17/274	11/181	9.1	0.27	0.27	21	21	0	Pure Extension
KY5	38 00 33	28 21 48	58/147	28/359	14/261	7.9	0.46	0.46	10	11	1	Pure Extension
KY6	38 00 10	28 22 00	79/253	11/067	01/157	8.4	0.02	0.02	13	13	0	Radial Extension
KY7	38 00 34	28 23 06	66/173	21/323	11/057	7.0	0.04	0.04	33	33	0	Radial Extension
KY8	38 00 39	28 23 07	65/176	20/316	15/052	3.8	0.40	0.40	44	44	0	Pure Extension
KY9	38 01 03	28 24 14	67/111	23/298	02/207	7.3	0.11	0.11	14	14	0	Radial Extension
KY10	38 01 25	28 23 20	57/313	33/127	03/219	5.2	0.23	0.23	5	5	0	Radial Extension
KY11	38 04 20	28 22 52	70/166	05/269	19/001	7.7	0.26	0.26	14	14	0	Pure Extension
KY12	38 04 31	28 22 53	73/250	15/041	08/133	13.3	0.05	0.05	9	9	0	Radial Extension
KY13	38 02 40	28 23 37	64/044	07/299	25/206	9.7	0.37	0.37	7	7	0	Pure Extension
KY14	38 02 48	28 23 56	86/085	03/299	02/209	8.8	0.69	0.69	22	22	0	Pure Extension
KY15	37 57 05	28 25 23	88/262	02/094	00/004	8.0	0.03	0.03	27	29	2	Radial Extension
KY16	38 02 25	28 27 08	71/102	09/345	17/252	9.1	0.42	0.42	16	16	0	Pure Extension
KY17	38 04 23	28 28 02	83/251	01/155	07/065	8.3	0.51	0.51	44	46	2	Pure Extension

Table 4.3. Continued.

.Station #	Latitude (D°D′S″)	Longitude (D°D′S″)	σ1 (P/D)	σ2 (P/D)	σ3 (P/D)	Ort. α	R(ϕ)	R'	Nu	Nt	Ns	Stress Type
KY18	38 04 25	28 28 08	87/139	03/319	00/229	10.8	0.36	0.36	19	19	0	Pure Extension
KY19	28 04 16	28 33 20	87/145	03/005	02/275	9.0	0.16	0.16	6	6	0	Radial Extension
KY20	37 55 59	28 32 22	85/076	03/307	04/217	14.4	0.43	0.43	28	30	2	Pure Extension
KY21	37 58 09	28 32 27	73/198	06/307	16/039	12.9	0.56	0.56	16	16	0	Pure Extension
KY22	37 58 27	28 32 34	74/309	16/123	02/213	13.9	0.52	0.52	23	26	3	Pure Extension
KY23	38 00 07	28 32 40	73/131	12/358	12/265	7.8	0.41	0.41	29	29	0	Pure Extension
KY24	38 00 08	28 32 42	85/097	04/315	03/225	12.4	0.30	0.30	41	41	0	Pure Extension
KY25	38 00 15	28 32 45	78/277	11/124	06/033	7.0	0.17	0.17	18	19	1	Radial Extension
KY26	38 00 30	28 33 10	79/139	11/310	02/041	7.2	0.25	0.25	20	23	3	Pure Extension
KY27	38 00 26	28 33 16	77/193	10/050	07/319	5.5	0.44	0.44	29	31	2	Pure Extension
KY28	38 01 12	28 33 35	80/119	08/337	06/246	12.7	0.22	0.22	32	32	0	Radial Extension
KY29	38 00 34	28 33 00	79/111	10/315	05/224	9.8	0.42	0.42	22	22	0	Pure Extension
KY30	37 57 38	28 31 18	70/217	04/115	20/024	11.5	0.50	0.50	38	42	4	Pure Extension
KY31	37 59 46	28 30 26	79/253	06/013	10/104	6.6	0.49	0.49	12	12	0	Pure Extension
KY32.A	38 01 07	28 30 55	74/293	08/172	13/080	9.6	0.47	0.47	64	65	1	Pure Extension
KY32.B			87/006	03/162	01/253	8.3	0.04	0.04	47	48	1	Radial Extension
KY33	38 01 43	28 30 46	61/112	27/268	10/003	6.1	0.27	0.27	9	9	0	Pure Extension
KY34	38 02 03	28 32 15	64/158	12/275	22/010	6.5	0.28	0.28	26	26	0	Pure Extension
KY35	38 02 05	28 32 18	87/153	00/055	03/325	15	0.36	0.36	22	29	7	Pure Extension
KY36	38 00 34	28 31 31	86/106	04/269	01/359	7.9	0.23	0.23	52	53	1	Radial Extension
KY37	38 00 43	28 31 29	68/212	02/306	22/037	11.2	0.28	0.28	91	92	1	Pure Extension

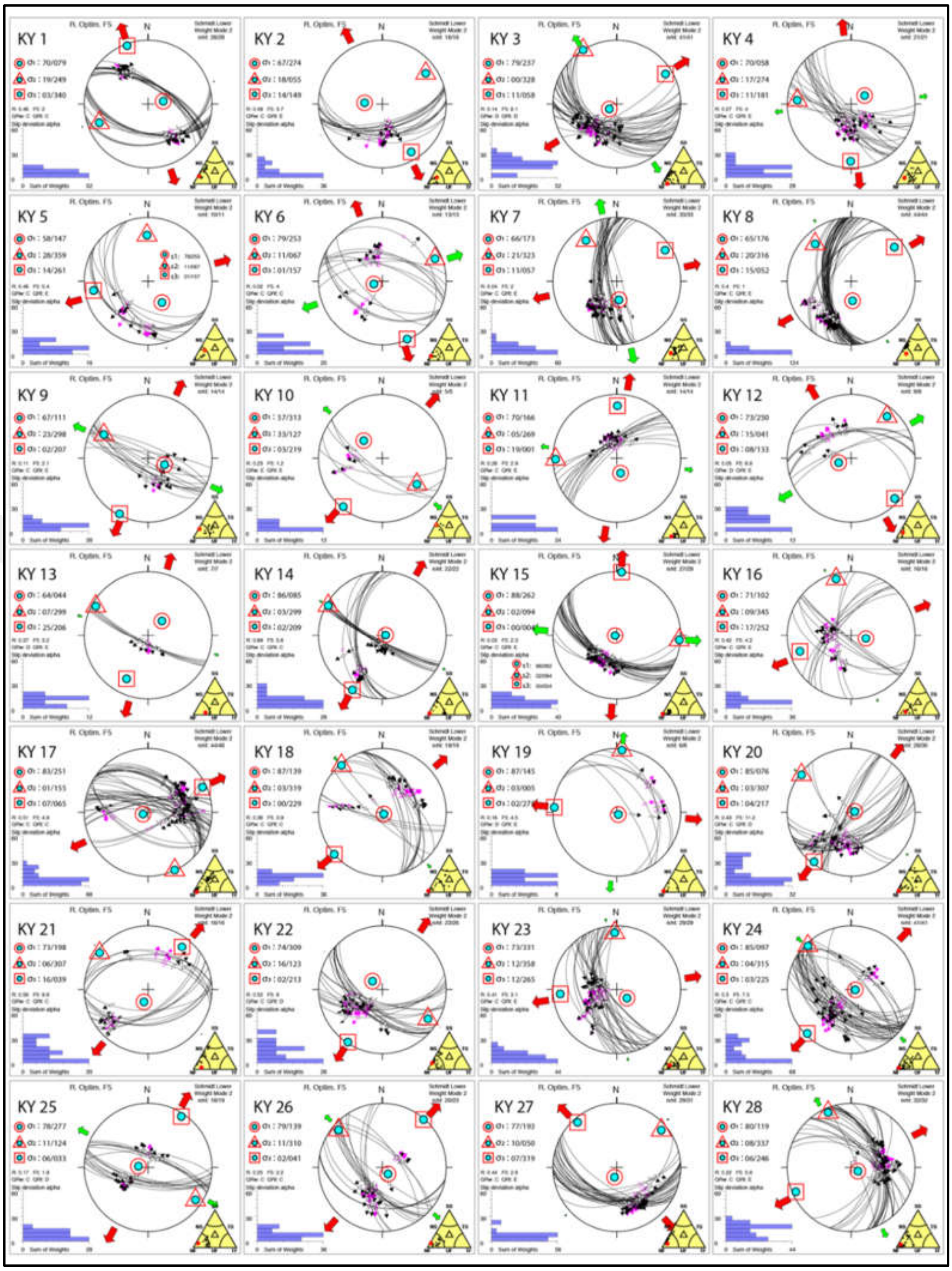

Figure 4.11. Stereographic projection (equal-area, lower hemisphere) showing the paleostress principal axes obtained from the inversion of fault-slip data collected from the study area (north of Kuyucak) (Akgün et al., 2024).

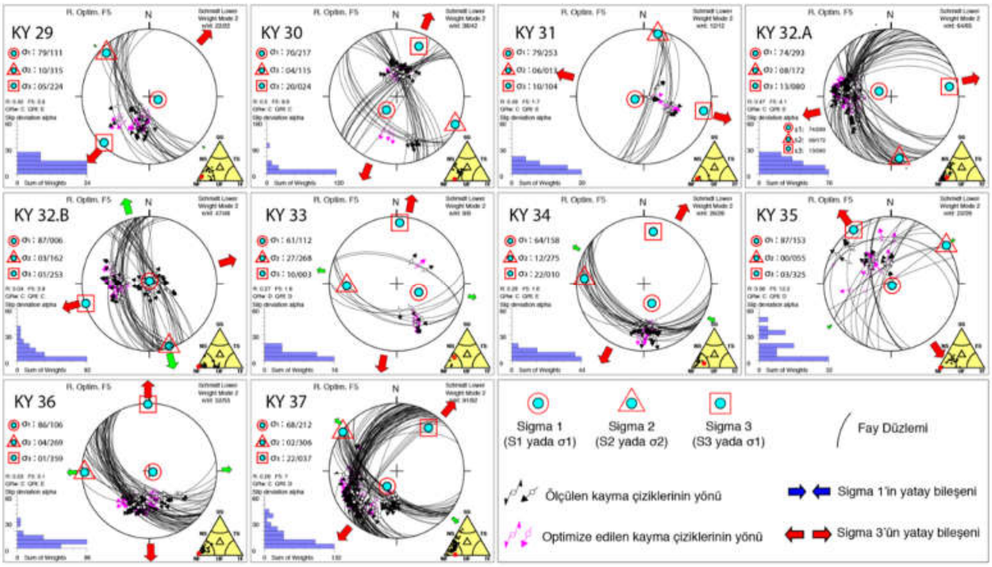

Figure 4.11. Continued.

CHAPTER 5

WELL TEST ANALYSIS

In this chapter, the well tests conducted in the KS-1 and KS-2 wells are described, as well as the well test analysis.

The data acquired from a deep geothermal production, namely KS-1, has been analysed. The well was drilled to a depth of 3,232 m, and a geothermal reservoir was encountered. The lithological logs, PTS logs, and well tests conducted at this well at different periods have been analyzed to understand the geometry, physical properties, and mechanical processes that control the fluid flow.

5.1 Description of the Data

Three sets of data were acquired from the KS-1 and KS-2 wells; one set was obtained right after the well was drilled in 2014, and the other two were acquired in 2017 and 2018. The data entailed lithological logs, Pressure-Temperature-Spinner (PTS) logs, water loss, injection, and build-up tests. The measurements were taken with Kuster K-10 PT and Pioneer PPS25XM PT tools.

5.1.1 Pressure-Temperature-Spinner

Two static temperature logs have been collected 2 years apart from each other (2014-2015 and 2017). It should be noted that the first measurement was collected after the drilling operations, which allowed the well to be produced for a short period. Therefore, divergence from the steady state conditions could be suspected. On the other hand, the measurement in 2017 could, in theory, represent the reservoir conditions. The temperature logs collected in 2014-2015 and 2017 are shown in

Figure 5.1. The recent logs show formation temperatures lower than the ones measured during the first production tests, which was the opposite of what was expected (increase in temperature) since the static conditions would have been expected to be reached after two years. In particular, the temperature distribution in the KS-1 well displayed a decrease in thermal gradient from a depth of about 1900 m, with a final maximum recorded value of about 130°C at the bottom hole. This last value was different from the maximum values measured at the bottom of the hole in December 2014, in static and dynamic conditions, respectively, which was about 145°C and 150°C. This decrease in temperature is suspected to be due to an interflow between two productive zones. Indeed, a recent log was carried out to suggest a possible "cold" water inlet at about a depth of 1900 m, flowing towards the well bottom, with a noticeable cooling effect. The cold water inlet was also observed in the spinner data (Figure 5.2) at a depth of approximately 1900 m. The other RPS changes were linked to the change in casing size. In addition, the water inlet was evidenced by the waterloss data, which will be discussed in the next section. When the well layout is to be considered, the end of the 9 5/8" casing was at a depth of 1,852 m. The cementing was performed up to this depth. The 7" casing was hung at 1,807 m where the 7" liner started from 2,216 m. Since the 7" liner was hung inside the 9 5/8" casing which ended at 1,854 m, the low-temperature interflow could occur at this depth which exactly corresponded to the start of the decrease in the temperature gradient. Thus, a fluid flow around the liner hanger's level from a cold reservoir through a sub-orthogonal fracture zone could allow fluid to flow into the well. Future drilling should be planned to perform a cement job down to the depth of 2,200 m, therefore avoiding this low-temperature productive zone.

When the temperature profile was correlated with the lithological log, a sudden increase in the temperature gradient after 2,300 m agreed well with the encountered geothermal fluid-bearing marble units of the Menderes Massif. The pressure-temperature-depth profile and the spinner data can be seen in Figure 5.1 and Figure 5.2.

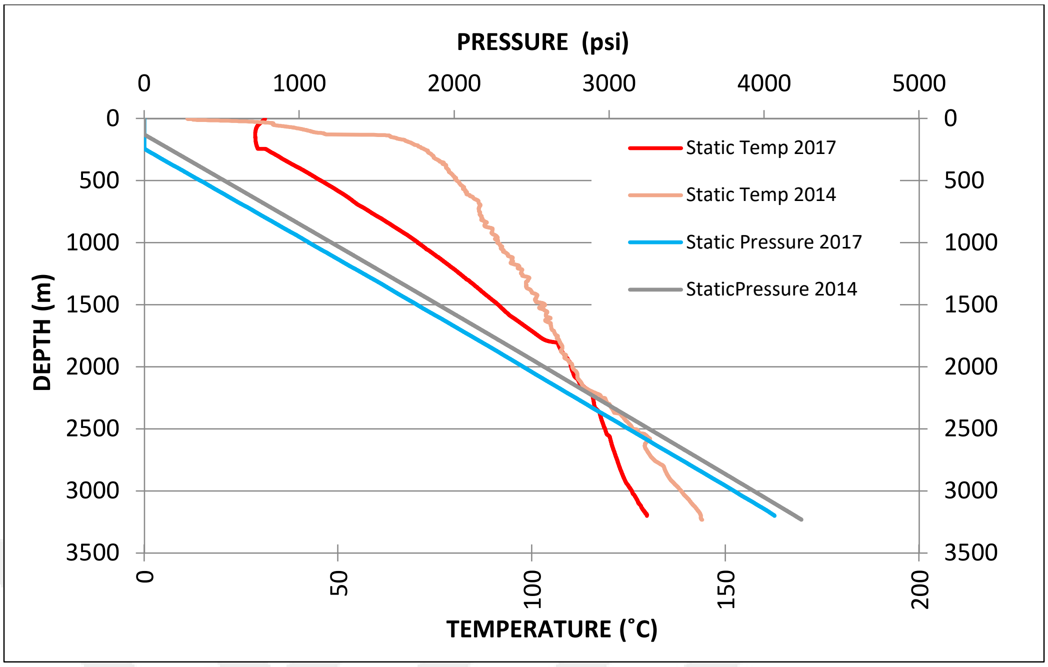

Figure 5.1. Pressure-Temperature profile

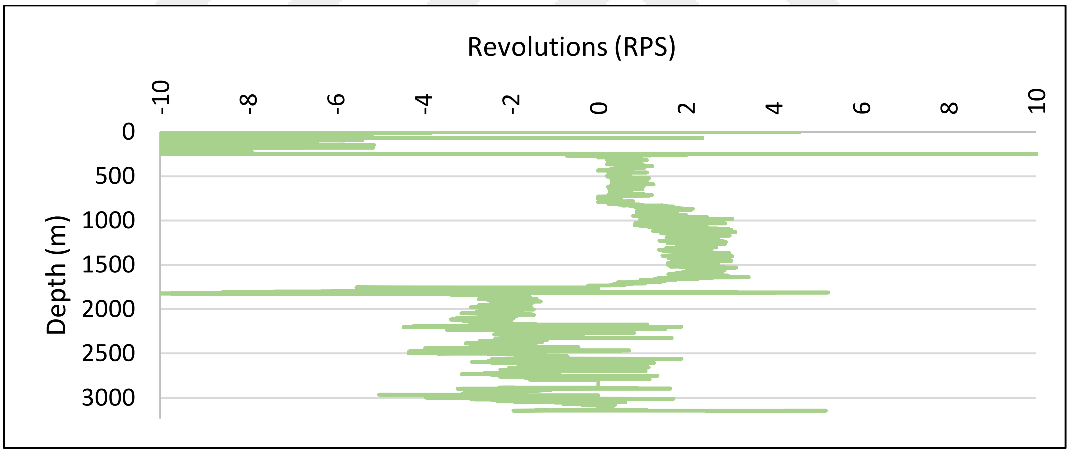

Figure 5.2. Spinner data depth versus revolutions

The pressure profiles taken in 2014 and 2017 are shown in Figure 5.1. A 3 bar pressure drop has been observed between the two measurements. The difference between these measurements could have been caused due to the cold reservoir layer at around 1900 m. During both tests, the KS-1 well needed nitrogen lifting operations to initiate the flow, suggesting possible clogging of flow pathways due to skin effects during dormant conditions. It is likely that the well could only have a limited connection with the hot deep reservoir, and the pressure distribution might be representative of the upper cold reservoir.

The analysis of this data revealed the presence of an upper reservoir with a cooling effect. This thesis proposes the optimal development strategy based on the available data. As part of this strategy, it is recommended to seal off this cold reservoir zone to mitigate the cooling effects, which could enhance the reservoir's capacity. In contrast, the following chapters will discuss mechanical enhancement strategies.

5.1.2 Productivity index

The productivity index (PI), defined as the flow rate per unit pressure drop, indicates the production potential of a well. PI is given as:

$$PI = \frac{Q}{P_R - P_{wf}} = \frac{Q}{\Delta P} \qquad \text{(Equation 5)}$$

where Q is the flow rate, P_R is the static pressure, and P_{wf} is the bottom hole flow pressure. In measuring the P_R the well needs to be shut in until static reservoir conditions are reached, whereas to measure P_{wf}, the well needs to be allowed to produce until pseudo-steady state conditions are reached, thus attaining a stabilized bottom hole pressure. Two static logs and the final pressure reading at the end of a build-up test could be used for P_R. For P_{wf}, since no drawdown test has been conducted at the site, the first pressure value measured at the beginning of the build-up tests could be used since prior to three build-up tests the well was allowed to produce for a sufficient amount of time which will be further elaborated in the Build-up Tests section.

As mentioned earlier, the well was allowed to be produced for a short period before taking the 2014 pressure log. Therefore, the steady-state pressure values should be higher than measured. For the second static pressure measurement in 2017, as discussed before, the pressure values may not have been completely representative of the deep reservoir but may have representative of the combined behavior of the upper cold reservoir and the deep geothermal reservoir; thus, PI values obtained from these measurements would be misleading. PI values were calculated from the existing data, assuming pressure values at these depths were above the bubble point, and fluid flow was Darcian. Average values for flow rates were used in the PI calculations. Both in the 2015 and 2018 tests, the flow rates were initially erratic, then settled to a constant rate for at least 2 days for both tests. It should also be noted that only the liquid flow rate has been used. The vapor phase corresponding to approximately 5% of the total flow rate has not been used.

Table 5.1. Productivity Index Values

Depth (m)	Source	P_R (psig)	Source	Pwf (psig)	Drawdown (psig)	Q (ton/hr)	PI (ton/h/psi)	PI (ton/h/bar)
3050	BU1-2015	3923	BU1-2015	3878	45	150	3.3	48.3
3050	STATIC-2014	4001	BU1-2015	3878	123	150	1.2	17.7
3200	BU2-2015	4050	BU2-2015	3824	226	150	0.7	9.6
3200	STATIC-2014	4201	BU2-2015	3824	377	150	0.4	5.8
3000	BU1-2018	3776	BU1-2018	3703	73	120	1.6	23.8
3000	STATIC-2014	3806	BU1-2018	3703	103	120	1.2	16.9

As can be observed from Table 5.1, a range of PI values were calculated. The BU1 and BU3 were conducted at around a depth of 3000, whereas the BU2 was conducted at 3200 m. As lithology also suggests, two fluid-bearing reservoir levels could be traversed by a possibly impermeable schistic level where the lower level was partially penetrated, which could cause the discrepancy between the PI values. Also, instead of using the pressure at the start time of the build-up test, the 2014 static pressure measurements were used, where more consistent PI values were obtained around 17 ton/h/bar. The average value of all calculated PI values was 21 tons/h/bar.

5.1.3 Waterloss

Two waterloss tests have been performed in 2014 and 2017, respectively. The water loss tests entail pumping cold water at a constant rate and stopping pumping water to the well for a period to allow mild heating. Moving the temperature instrument up and down the well tracked the advancing off the cold front of fluid. This test aims to identify permeable zones. When the advancement of cold water stops, a permeable zone is suspected; when it slows down, multiple permeable zones are suspected.

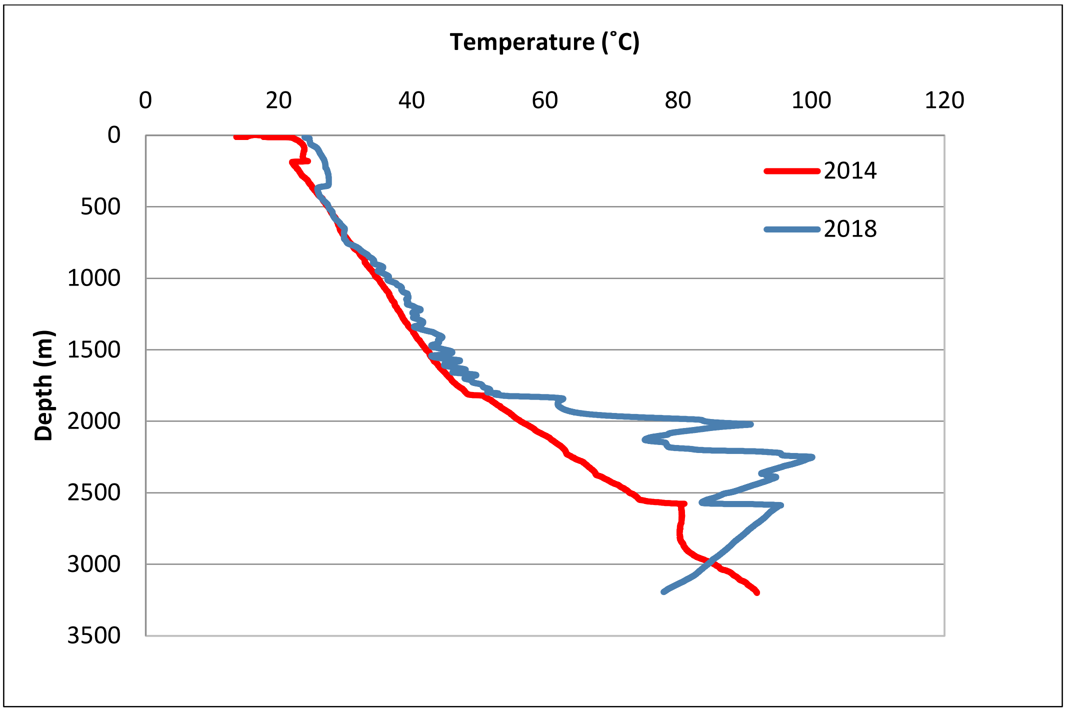

Figure 5.3: Temperature versus depth profile during waterloss test.

When cold water is pumped during waterloss testing, the impermeable zones can be cooled conductively, whereas the permeable zones could also be cooled conductively. Also, there is an interzonal flow possibility where the cold fluids could enter the formation at one permeable zone and leave the formation at another. Convection is a much more effective process of heat transfer in comparison to conduction. The temperature profile of an impermeable region will be smooth since the heating process will be very slow and will be governed only by conduction.

Interzonal flow can be identified when two sections of a well experience heating at varying rates. Two significantly different profiles were obtained from two tests conducted in 2014 (pumping rate: 15 lt/sec) and in 2018 (pumping rate: 20 lt/sec). In the 2014 profile, a convective zone below 2700 m was observed, whereas in the 2018 profile, several zones of convective heat transfer were suspected, with a possibility of an interzonal flow. The difference between these profiles arises mainly due to the enhancement operations performed to the well between two tests that caused the activation of a formally impermeable zone that indicates the fractured nature of the formations under investigation. The fastest warm-up of the cold front occurred at a depth of 2300 m with possibly the highest permeability followed by the zones at 2700 m and 2000 m in the 2018 test, with warm-up trends possibly indicating major interzonal and/or cross flow between these levels. Crossflow within a wellbore is characterized by a single isolated temperature peak in the heating profiles (Hole, 2003). Observed temperature peaks and rapid heating of one section of the well more than the others characterize a combination of both interzonal and cross flow in between permeable levels. Also, water loss test results depicting the complete movement of the instrument with the spinner data are also shown in Figure 5.4.

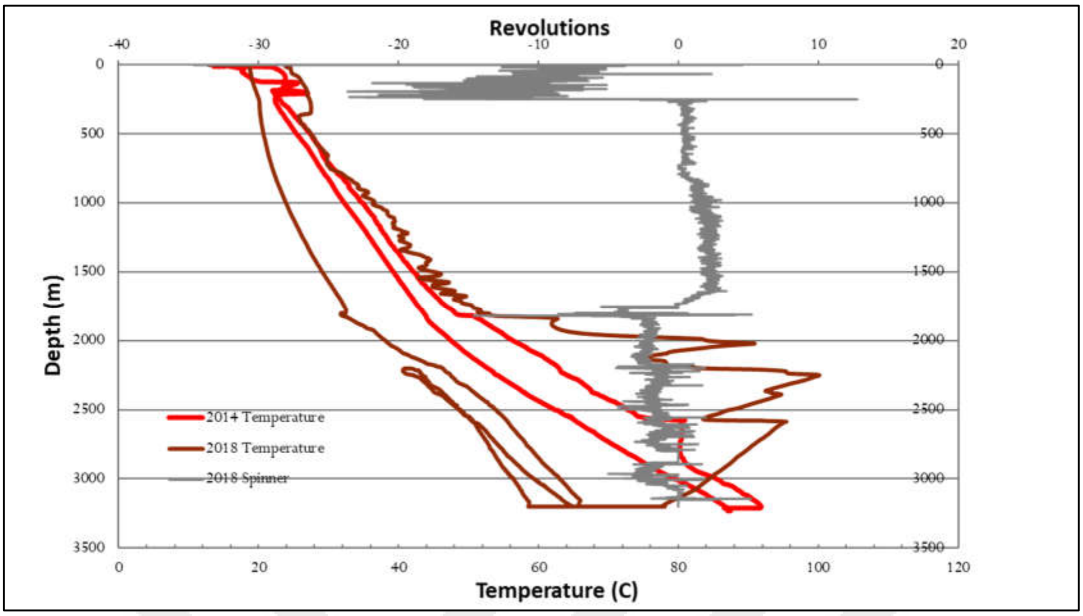

Figure 5.4. Waterloss test results and the spinner data.

This information indicates that the proper application of an enhancement operation at the right depths could significantly enhance the reservoir and increase well productivity, while an improper application could create pathways to a cold reservoir or cause interzonal/cross flow and decrease the well productivity and predictability.

5.1.4 Injection Tests

In the injection test conducted in 2018, the well was initially shut in to stabilize the bottomhole pressure (BHP) at the static reservoir pressure, providing a baseline for the test. Once the pressure stabilized, fluid was injected into the well at a constant rate with 4 injection steps: 5, 10, 15, and 20 l/s, and the steps lasted for 6 hours each. After the injection, a buildup period of 2.5 days was allowed. During this process, both the injection rate and the BHP were continuously monitored over time. The injection test was conducted twice, one before and one after the acid operations. The injection data is presented in Figure 5.5 throughFigure 5.8.

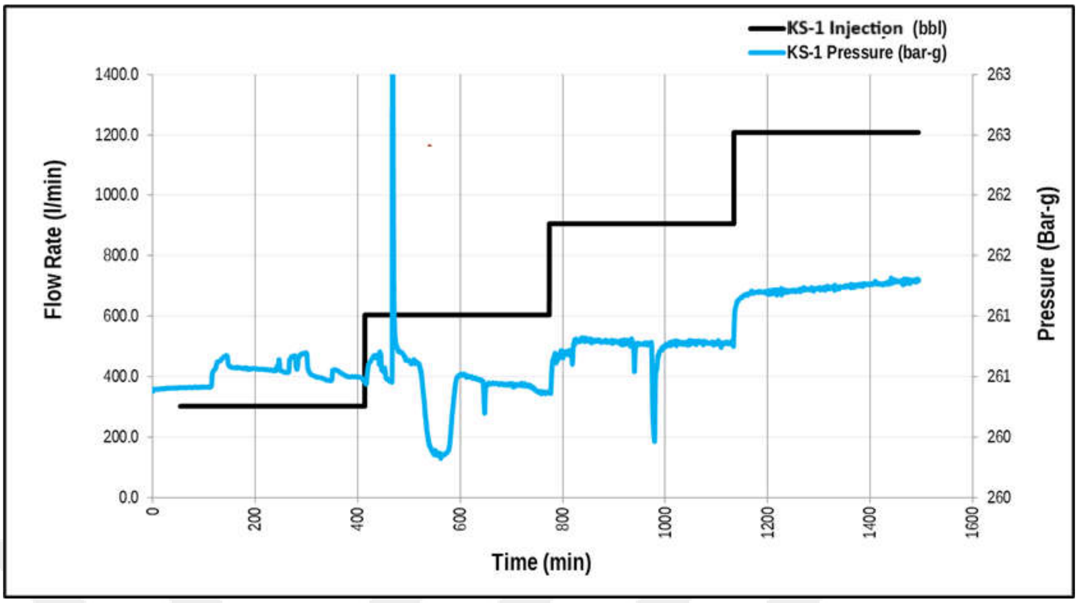

Figure 5.5.Injection test results before acid operations. Pressure - Flow Rate versus Time graph.

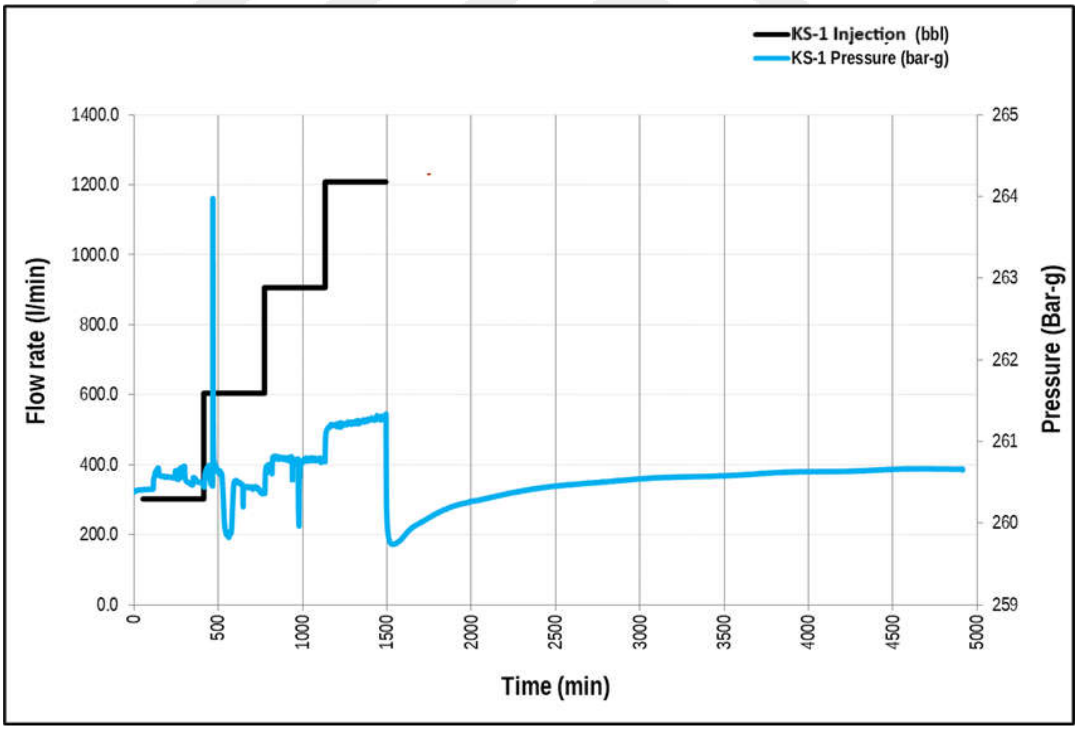

Figure 5.6. Injection test results with fall-off before acid operations. Pressure - Flow Rate versus Time graph.

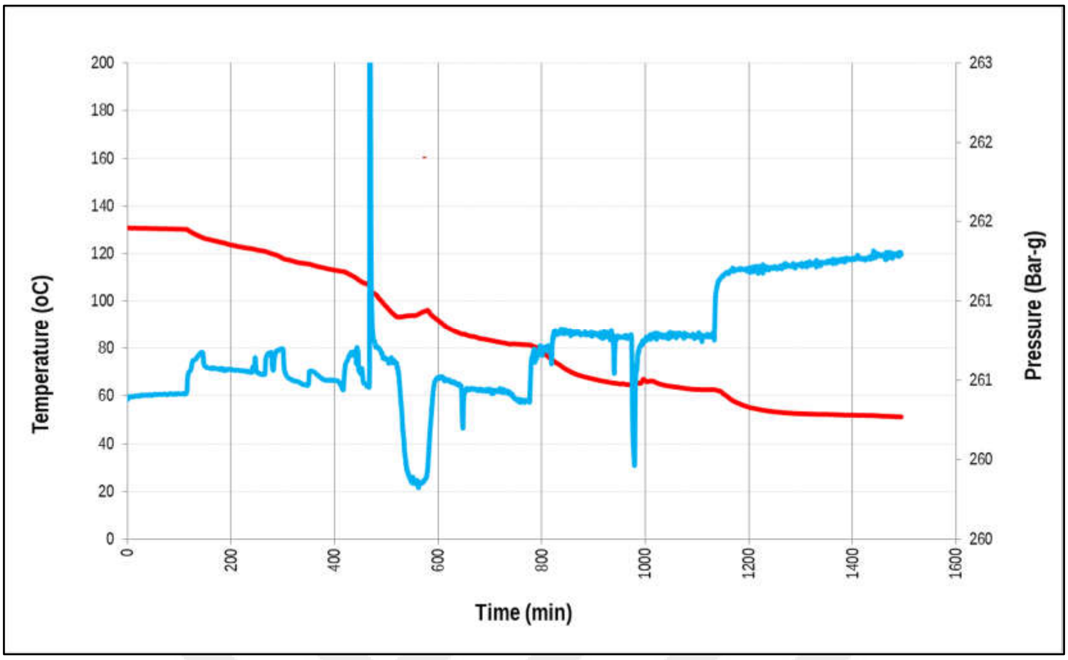

Figure 5.7. Injection test results before acid operations. Temperature - Flow Rate versus Time graph.

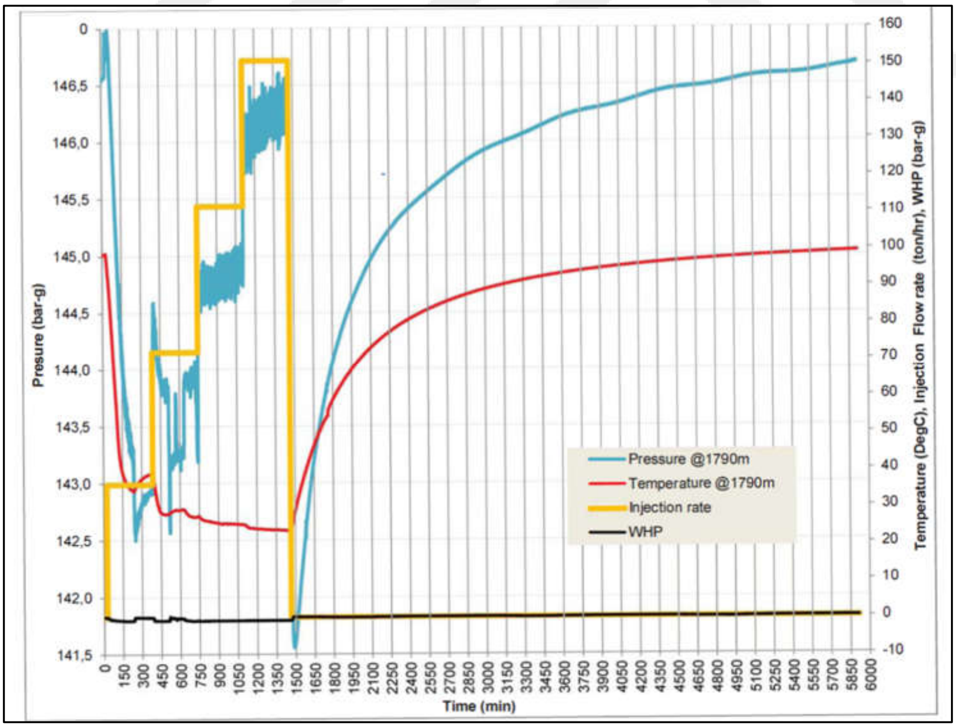

Figure 5.8. Injection test results after acid operations. Pressure - Flow Rate versus Time graph.

Both before and after injection, the pressure profiling showed unusual behavior. During the 3 first steps (5, 10, and 15 l/s), an erratic behavior with pressure drops and pikes were observed, which indicated the involvement of geomechanical processes. Moreover, during those 3 steps, the slope of the pressure curve was not the same and decreased at different rates. The pressure drop between the beginning and the end of a step could have signified a fractured opening. On the contrary, the last step showed a more traditional behavior with increasing pressure over time, which could suggest that above 20 l/s, the geomechanical behavior was stabilized.

At the beginning of the buildup, the pressure droped until it was lower than the initial reservoir pressure which suggested that the fractures were widely opened and that the inertia of the injection was pushing the water deeper into the formation. After this suction phase, the pressure rised to a reference higher than the original reservoir pressure. This could be assimilated as a “closed reservoir” behavior. Indeed, if the reservoir was closed, the injected water would have pressurized the reservoir so that the final reservoir pressure was higher than the original one. However, the interpretations of the build-up test results did not suggest the presence of a closed reservoir but an infinite-acting reservoir, which is further discussed in the next section. Thus, the geomechanical processes that took place during the injection test were regarded to be caused by the pressure rise. A spike might represent a fractured opening, which may provide a pathway to a more permeable zone that resulted in a sudden volume increase of the reservoir followed by a dissimilar pressure profile. The negative slope could be related to growth into a higher permeability zone, such as rapid out-of-zone growth. Much more complex behavior could occur if out-of-zone growth occured. If the fracture growed out-of-zone dramatically, the excess pressure might have decreased because of the growth more than the change in pressure due to friction in the fracture. A negative slope may appear in the post-fracturing regime.

However, it was impossible to interpret the pressure profile of the injection test quantitatively. Yet, it was concluded that it contained invaluable information for assessing the pressure limits of the formation for fracture activation. This theory was further elaborated in Chapter 10 in the mechanical reservoir modeling section.

5.1.5 Build-up Tests

Build-up tests were conducted at the KS-1 and KS-2 wells. The tests were conducted after allowing the well to produce for some time, then the well was shut in, and the pressure buildup at the well was recorded. The geometrical and physical properties of the reservoir could be determined by analyzing the pressure response. Information on the build-up tests is given in Table 5.2.

Table 5.2. Build-up Test Data

	Build-up No	**Production Time (days)**	**Elapsed Time (hours)**
KS-1	1	2.5	8.4
KS-2	1	1.0	13.1

The log-log pressure and pressure derivative time graphs can be observed in Figure 5.10 to Figure 5.11. For the well test analysis, Ecrin software was used, and the best fit for the pressure and the pressure derivative curve was found to be representative of a dual- porosity reservoir.

The double porosity model for a vertical well in an infinite reservoir describes fluid flow behavior in formations characterized by two distinct pore systems: matrix blocks and natural fissures. The wellbore storage effect, which accounts for the fluid compressibility and the wellbore volume, initially dominates the pressure response during fluid injection or withdrawal. Additionally, the skin effect, which represents the pressure drop near the wellbore due to formation damage or stimulation, influences fluid flow efficiency.

In this model, the reservoir is assumed to be infinite, with no external boundaries affecting fluid movement towards the well. The vertical well penetrates through the reservoir layers, interacting with the matrix blocks and the fissures. The matrix blocks are characterized by high storativity, meaning they can store a significant volume of fluid but have low permeability, leading to slow fluid flow. Conversely, the natural fissures have low storativity but high permeability, allowing them to act as primary conduits for rapid fluid movement.

Two key parameters define the interaction between the matrix and fissures: the storativity ratio (ω) and the inter-porosity flow coefficient (λ). The storativity ratio (ω) quantifies the proportion of fluid stored in the fissure system relative to the matrix, with a higher value indicating a more significant contribution of fissures to overall fluid storage. The inter-porosity flow coefficient (λ) measures the ability of fluid to flow from the matrix blocks into the fissure system, with a higher value suggesting more effective fluid transfer from the matrix to the fissures.

The initial flow regime in this model is dominated by fissure radial flow, where the high permeability of the fissures allows for rapid fluid movement towards or away from the well. This flow regime is crucial in determining the early-time pressure response and the overall productivity or injectivity of the Pseudo Steady State model as described by Chen (1989).

As a general note, the double porosity model for a vertical well in an infinite reservoir describes fluid flow behavior in formations characterized by two distinct pore systems: matrix blocks and natural fissures. The wellbore storage effect, which accounts for the fluid compressibility and the wellbore volume, initially dominates the pressure response during fluid injection or withdrawal. Additionally, the skin effect, which represents the pressure drop near the wellbore due to formation damage or stimulation, influences fluid flow efficiency.

Two key parameters define the interaction between the matrix and fissures: the storativity ratio (ω) and the interporosity flow coefficient (λ). The storativity ratio (ω) quantifies the proportion of fluid stored in the fissure system relative to the matrix, with a higher value indicating a greater contribution of fissures to overall fluid storage. The interporosity flow coefficient (λ) measures the ability of fluid to flow from the matrix blocks into the fissure system, with a higher value suggesting more effective fluid transfer from the matrix to the fissures. The initial flow regime in this model is dominated by fissure radial flow, where the high permeability of the fissures allows for rapid fluid movement towards or away from the well.

Figure 5.10 and Figure 5.11 present the log-log pressure and pressure derivative graphs for the build-up tests conducted in the KS-1 and KS-2 wells. The model parameters that best fit the data are shown below the figures. The permeability of the dual-porosity reservoir around the KS-1 well is estimated to be 1.49E-10 m^2, whereas the permeability around the KS-2 well is an order of magnitude lower, measured to be 1.63E-11 m^2. These permeability values are representative of both the matrix and the fracture network of the reservoir. Meanwhile, the permeability of fractures is considered to be higher than that of the matrix. Although fracture-controlled flow is undoubtedly present, the matrix is believed to play a significant role in fluid transfer due to its larger volume. Also, at these depths, not all fractures are expected to be open or can be stimulated by mechanical or chemical enhancement methods and further remain open.

Mi et al. (2016) demonstrated that the pore radius and fracture aperture influence the matrix and fracture permeability relationship. For this study, an average value is considered sufficient, so the ratio between fracture and matrix permeability is assumed to be one order of magnitude. Consequently, the matrix permeability in the fluid model shall be adjusted accordingly.

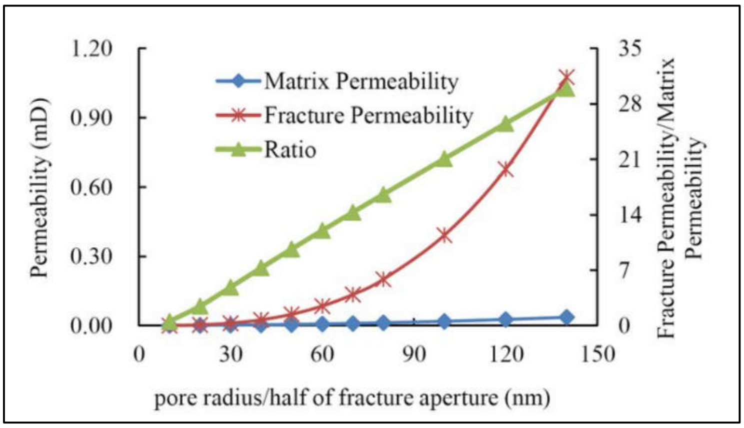

Figure 5.9. Relation between the matrix permeability fracture permeability ratio and the pore radius/half of fracture aperture.

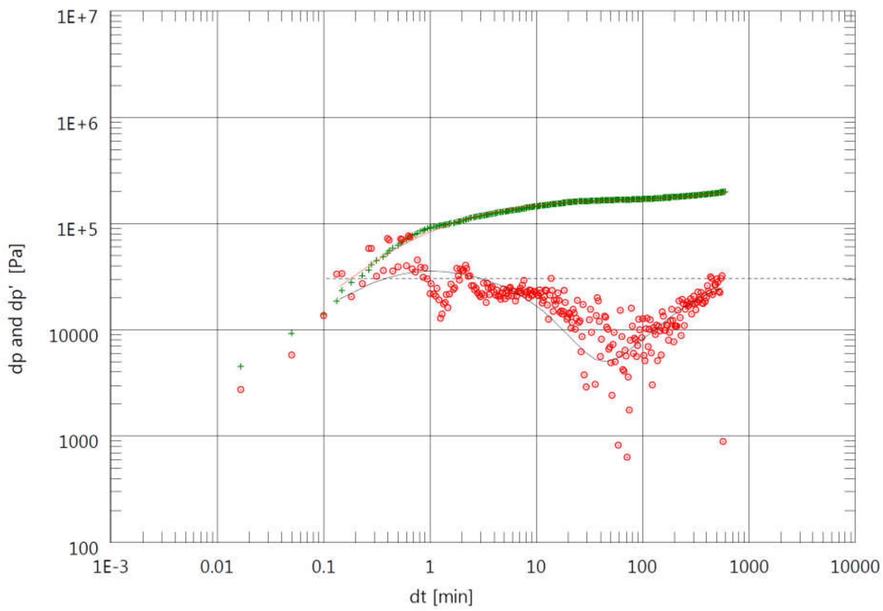

Pressure build-up #1
Rate 0 m3/sec
Rate change 168 m3/sec
P@dt=0 2.64156E+7 Pa
Pi 2.67069E+7 Pa
Smoothing 0.01

Selected Model
Model Option Standard Model
Well Vertical
Reservoir Two porosity PSS
Boundary Infinite

Main Model Parameters
TMatch 4.73 [min]-1
PMatch 1.64E-5 [Pa]-1
C 35 m3/kPa
Total Skin -9.21
k.h, total 8.77E-8 m3
k, average 1.49E-10 m2
Pi 2.67069E+7 Pa

Model Parameters
Well & Wellbore parameters (Tested well)
C 35 m3/kPa
Skin -9.21
Reservoir & Boundary parameters
Pi 2.67069E+7 Pa
k.h 8.77E-8 m3
k 1.49E-10 m2
Omega 0.0409
Lambda 6.81E-11

Derived & Secondary Parameters
Delta P (Total Skin) -5.61731E+5 Pa
Delta P Ratio (Total Skin) -2.84732 Fraction

Figure 5.10. KS-1 Well Build-up Test-1

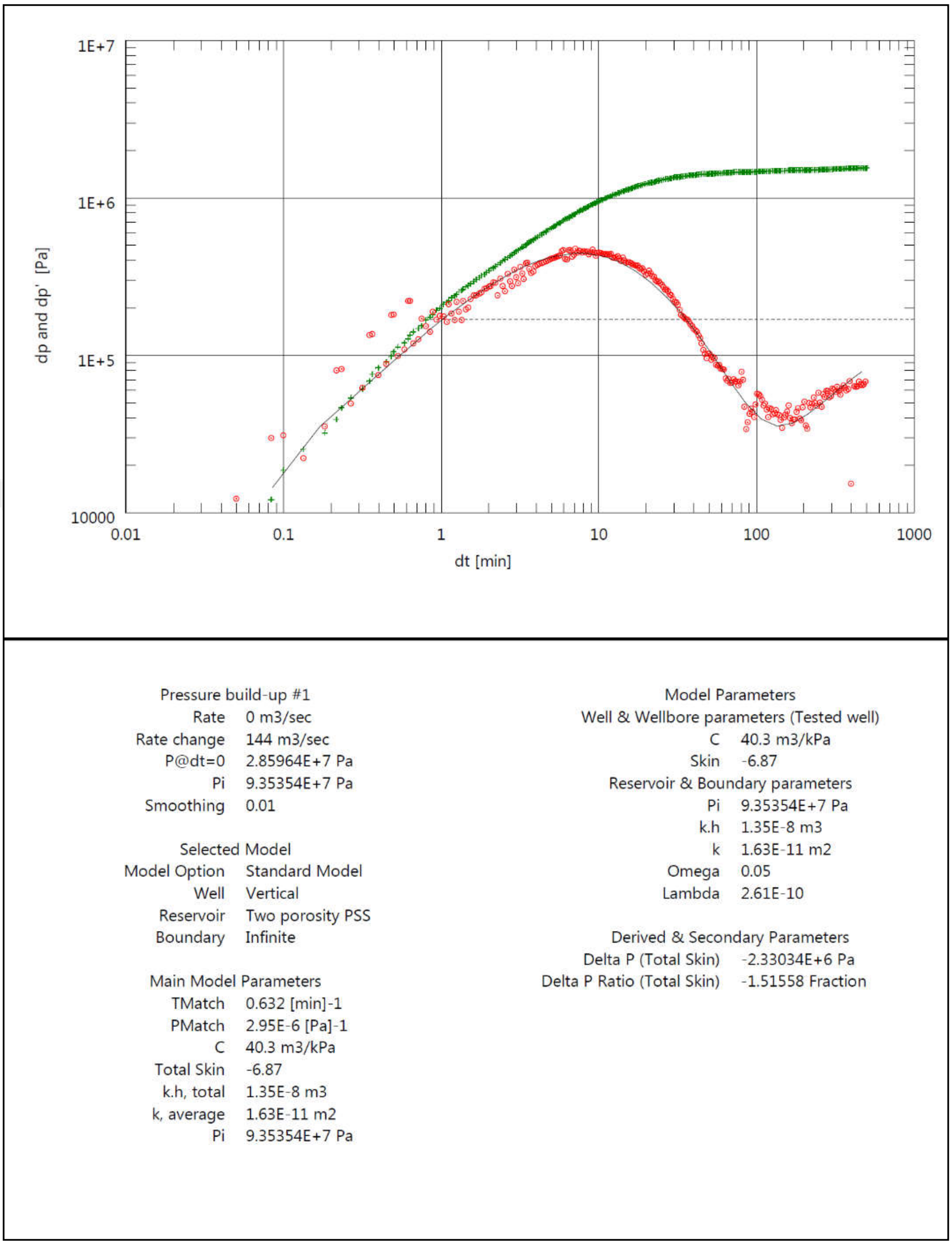

Figure 5.11. KS-2 Well Build-up Test-1

CHAPTER 6

FRACTURE NETWORK

This chapter explains the methods used to extract a representative fracture network for the mechanical model, including scan-line surveys for fracture sampling and photogrammetric techniques for fracture delineation. Further, the fractures are categorized based on their orientations concerning the paleo and neo-stress orientations discussed in Chapter 5. All works performed for the scan-line surveying, have been conducted within the scope of the TUBITAK 1001 project under grant number 119Y535 (Akgün et al., 2024).

6.1 Scan-line Survey

Fractures and other mechanical discontinuities are crucial in controlling fluid flow in fractured geothermal reservoirs. In this thesis, the terms “discontinuity” and “fracture” have been used inter-changably. An essential aspect of reservoir characterization involves acquiring fracture network data and upscaling their statistical properties (Long et al., 1982; Jackson et al., 2000; Blum et al., 2009).

Fracture networks are commonly characterized using outcrop analogs, well cores, or image logs (Dershowitz and Einstein, 1988; Priest, 1993; National Research Council, 1996; Mauldon et al., 2001; Bour et al., 2002; Laubach, 2003; Blum et al., 2007; Jing and Stephansson, 2007; Guerriero et al., 2011).

Watkins et al., 2015 compared the four primary methods for sampling fractures: linear scan-line sampling (Priest and Hudson, 1981; Priest, 1993), areal sampling (Wu and Pollard, 1995), rectangular window sampling (Pahl, 1981; Priest, 1993), and circular scan-line sampling (Mauldon et al., 2001; Rohrbaugh et al., 2002). These methods are briefly described in the following sections.

6.1.1.1 Linear Scan-line Sampling

The linear scan-line method is favored for its efficiency in capturing a broad range of fracture attributes, such as orientation, length, aperture, intensity, filling, and spacing. This technique involves placing a tape across an outcrop and measuring each fracture that intersects the tape (Priest and Hudson, 1981; Priest, 1993). However, this method is prone to orientation and length biases, and it can be sensitive to censoring, where larger fractures may be under-represented due to truncation by the outcrop's limits.

6.1.1.2 Areal Sampling

Areal sampling involves collecting fracture data in a two-dimensional plane, particularly useful for large-scale fractures or discontinuities. This method can be conducted remotely using aerial photographs (Wu and Pollard, 1995) or on bedding surfaces. Areal sampling is commonly used for assessing fracture variability across extensive structures or outcrops, with data often derived from photographs or satellite imagery to create 2D fracture trace maps (McQuillan, 1974; Mobasher and Babaie, 2008; Ghosh and Mitra, 2009). Although this method allows for rapid data collection, results can be limited by the resolution of source images and may require substantial quality control efforts.

6.1.1.3 Rectangular Window Sampling

Rectangular window sampling uses a defined rectangle placed on an outcrop to measure selected fracture attributes within that area (Pahl, 1981; Priest, 1993). This method reduces orientation bias by including all fractures within the rectangle, allowing for straightforward estimation of mean trace length. However, it can be time-consuming if many attributes need to be recorded, and it is still subject to censoring due to outcrop size or poor exposure.

6.1.1.4 Circular Scan-line Sampling

The circular scan-line method, as described by Mauldon et al. (2001) and Rohrbaugh et al. (2002), involves counting fracture intersections with the edge of a circular line placed on an outcrop and the terminations within the circle. These counts are used to calculate fracture density, intensity, and mean trace length. This method avoids length censoring and orientation bias associated with linear scan-lines but does not provide direct measurements of other fracture attributes such as orientation, aperture, or spacing. It is most effective for estimating average fracture characteristics in areas with evenly distributed fractures, though it does not capture spatial distribution details as thoroughly as other methods.

6.1.2 Sampling Methodology

Zeeb (2013) compared the fracture sampling methodologies and decided that window sampling was the most reliable method, requiring the least number of measurements and providing results with the lowest uncertainty, except for the estimates of fracture intensity. Thus, window sampling was selected in the scope of the field studies.

6.1.3 Scan-line Survey Results

During the field studies conducted between July 1-5, 2021, scan-line surveys were performed at locations where the Menderes Massif marbles, which serve as geothermal reservoir rocks were exposed. Rock mass characterization was carried out at these locations to determine the geomechanical properties of the marble units.

In this context, scan-line surveys were conducted to determine the discontinuity characteristics of the rock mass and the associated fracture system. The orientations and displacements of the discontinuities were determined at the identified locations. These data have later been compared with the principal stress orientations inferred from the fault kinematic measurements. The discontinuity analyses conducted in the field were based on characterizing faults, joints, cracks, and other discontinuities within the rock mass. The process involved determining the orientation (strike and dip), aperture, spacing, continuity, roughness, and infilling material of the discontinuities on the planes identified in the field (Figure 6.1) and recording these characteristics in the field, followed by a stereographic evaluation of the strike and dip data. It is recommended that the scan-line surveys conducted during field studies have a length of at least 10 times the aperture of the discontinuities (Priest and Hudson, 1976; ISRM, 1978; USBR, 1991).

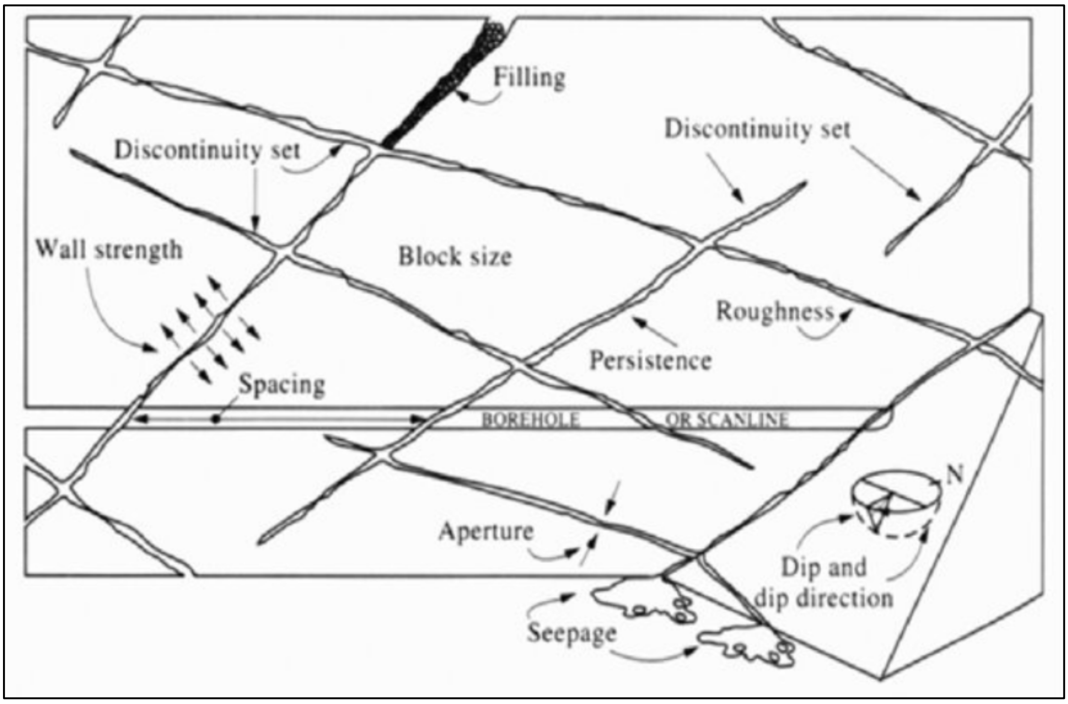

Figure 6.1. Discontinuity characteristics (Hudson, 1989).

All measurements taken during the scan-line surveys are provided in Appendix A. As discussed, the scan-line survey studies were conducted using the window mapping method. The basis of this method, proposed by Pahl (1981) as a different perspective on the scan-line survey method, is to define and/or measure the characteristics of the discontinuities within a selected area on the outcrop (Figure 6.2. The only difference between this method and traditional scan-line surveys, which are essentially very similar, is that it considers all discontinuities within the defined area, not just those intersecting a specific survey line. The errors related to orientation and size parameters in measurements taken along a linear line are reduced in this method.

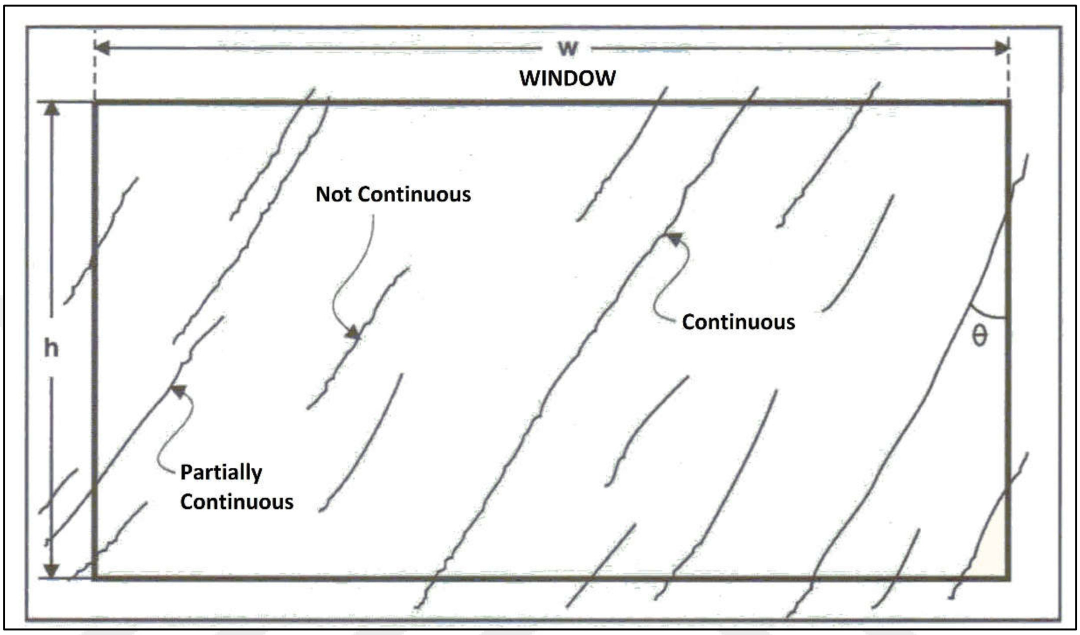

Figure 6.2. Window map technique and discontinuities observed within the boundaries of the window (Pahl, 1981).

The locations where scan-line surveys were conducted during the field studies are listed below and shown in Figure 6.3 to Figure 6.6.

Locations where line surveys were conducted during the field studies are listed below:

- Kuyucak – Belenova – Paleozoic Marble
- Gökkiriş Tepe – Jurassic Marble
- Almacık Tepe Alt – Paleozoic Marble
- Almacık Tepe Üst – Paleozoic Marble
- Yukarıkayacık Road – Permian Marble
- İmambaba Summit – Permian Marble

- İmambaba Summit Return – Permian Marble
- Halilbeyli – Paleozoic Marble

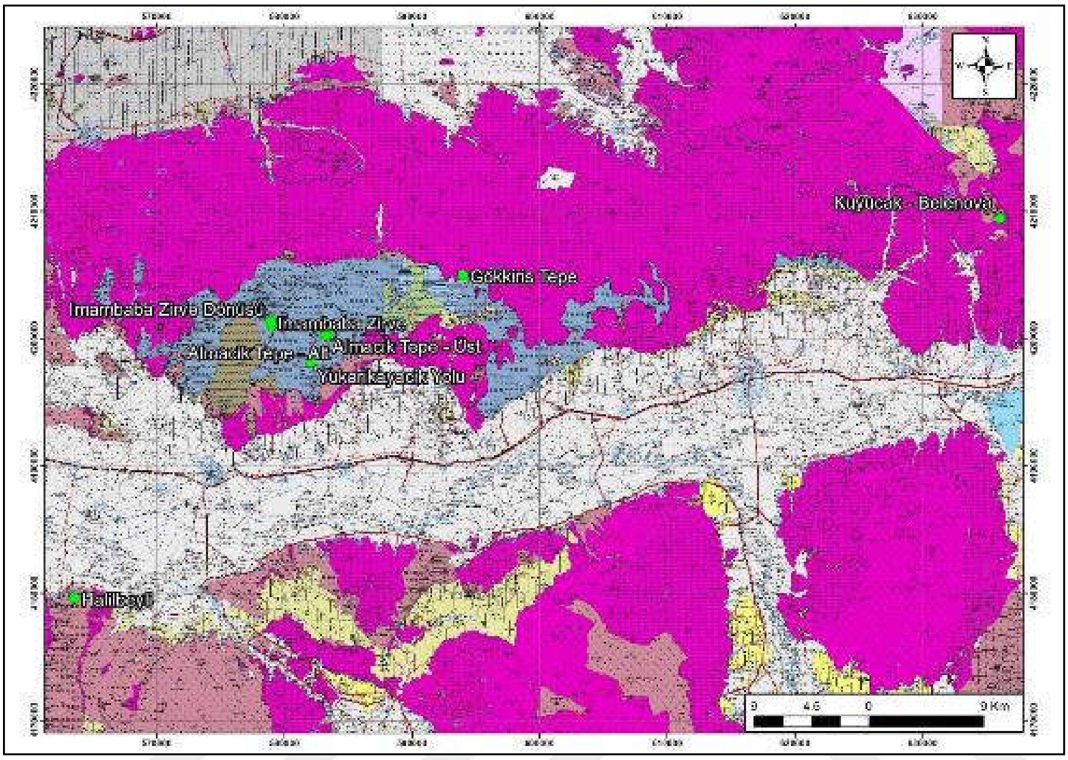

Figure 6.3. Scan-line survey locations (Akgün et al., 2024).

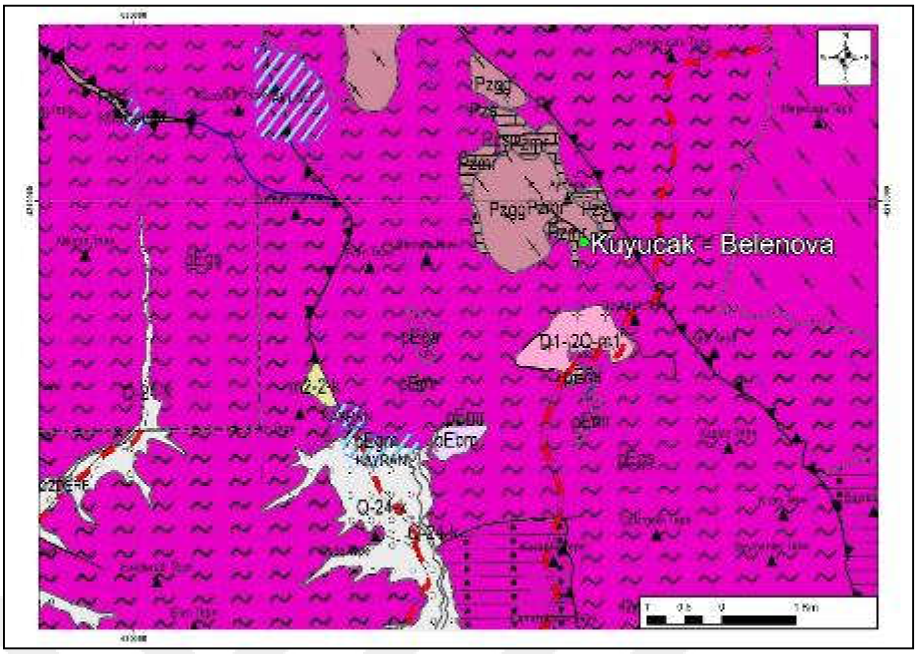

Figure 6.4. Scan-line survey locations, Kuyucak-Belenova location (Akgün et al., 2024).

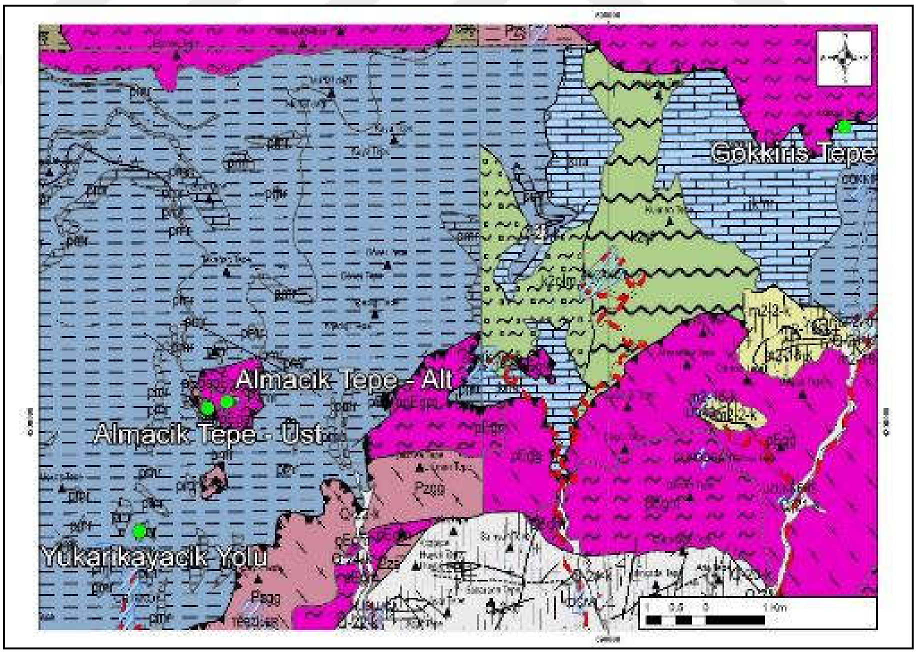

Figure 6.5. Scan-line survey locations, Yukarıkayacık, Gökkiriş Tepe, and İmambaba Summit locations (Akgün et al., 2024).

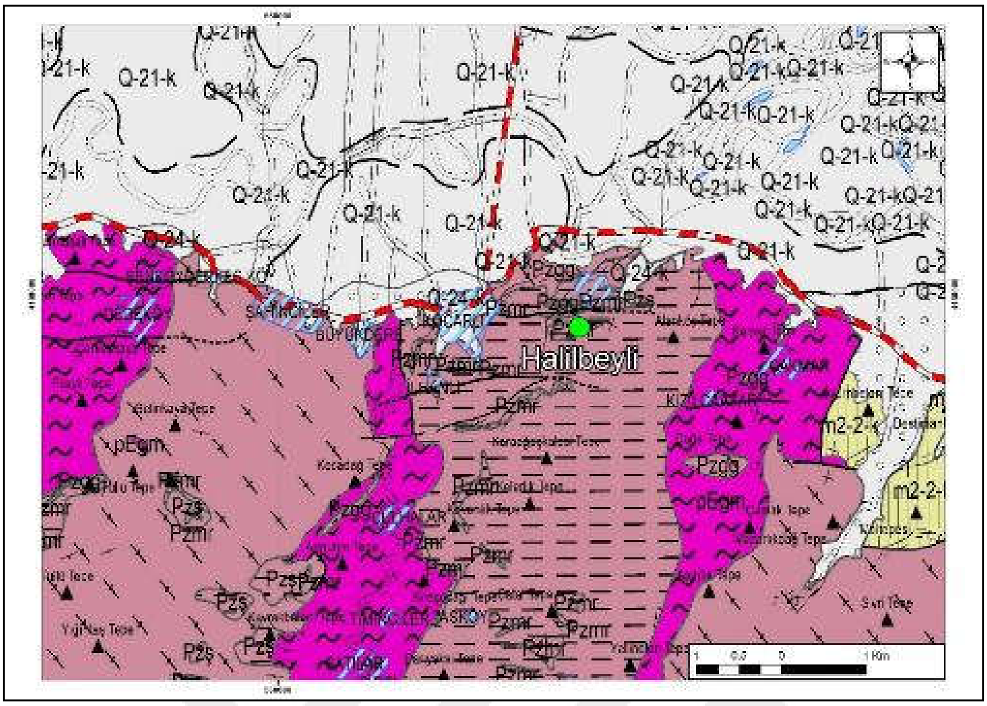

Figure 6.6. Scan-line survey locations, Halilbeyli location (Akgün et al., 2024).

The discontinuity orientations, measured with the aid of a compass during the scanline surveys, were analyzed by plotting them on a stereonet using the DIPS software (Rocscience, 2021). The number of sets of discontinuities and their orientations were determined based on the measurement density. The distributions of the discontinuities are shown in Figure 6.14, and the orientations of the discontinuity sets are provided in Table 6.1.

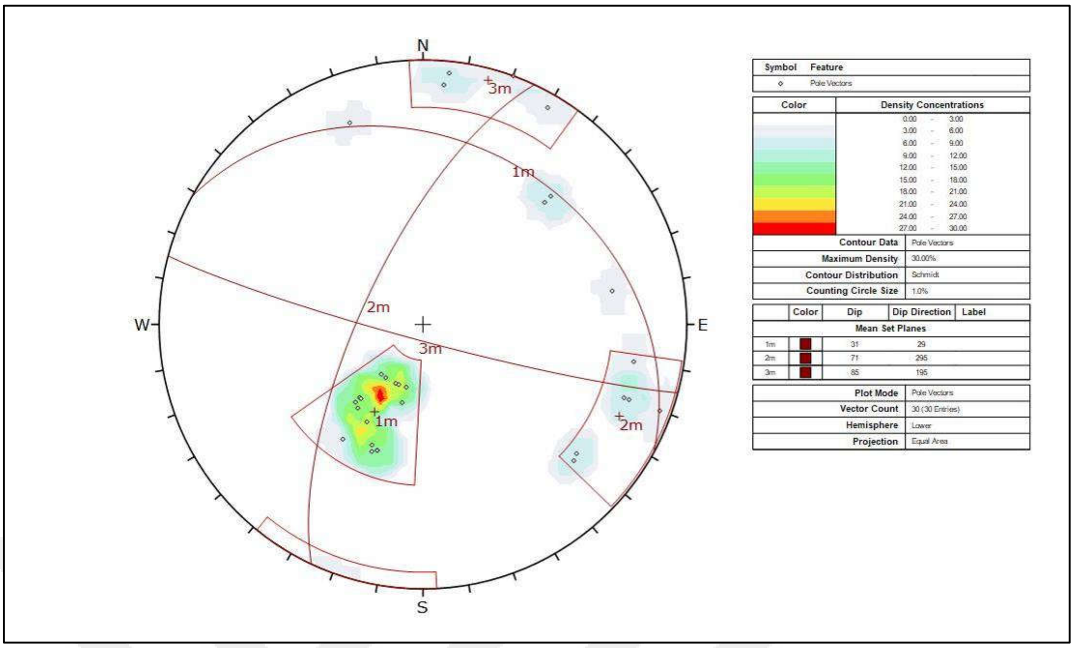

Figure 6.7. Scan-line survey measurement values and analysis results: Kuyucak-Belenova (Akgün et al., 2024).

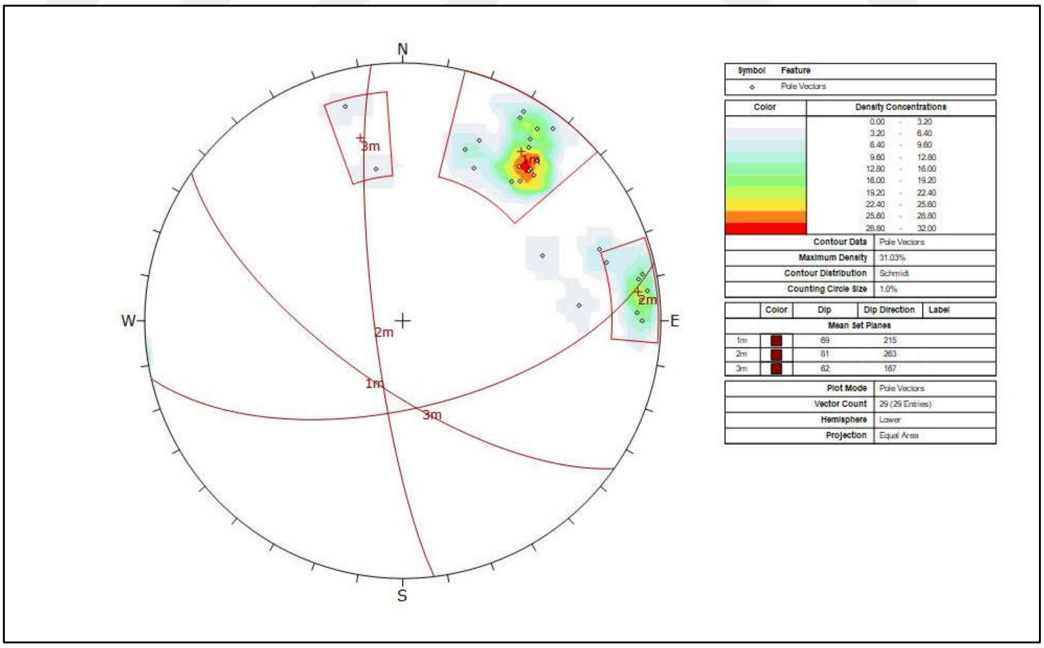

Figure 6.8. Scan-line survey measurement values and analysis results: Gökkiriş Tepe (Akgün et al., 2024).

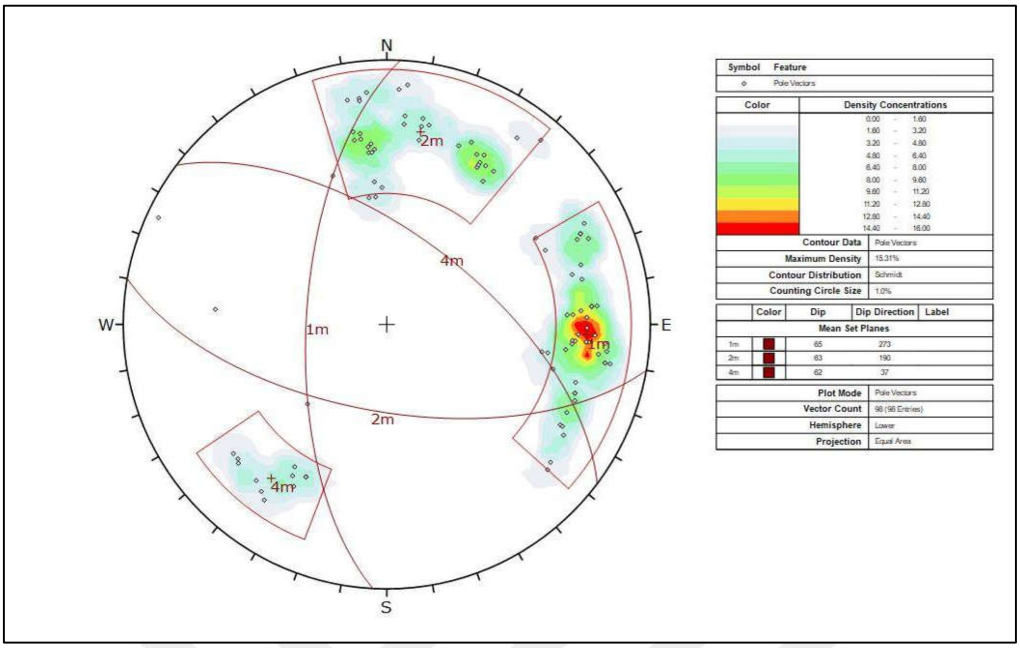

Figure 6.9. Scan-line survey measurement values and analysis results: Almacık Tepe-Alt (Akgün et al., 2024).

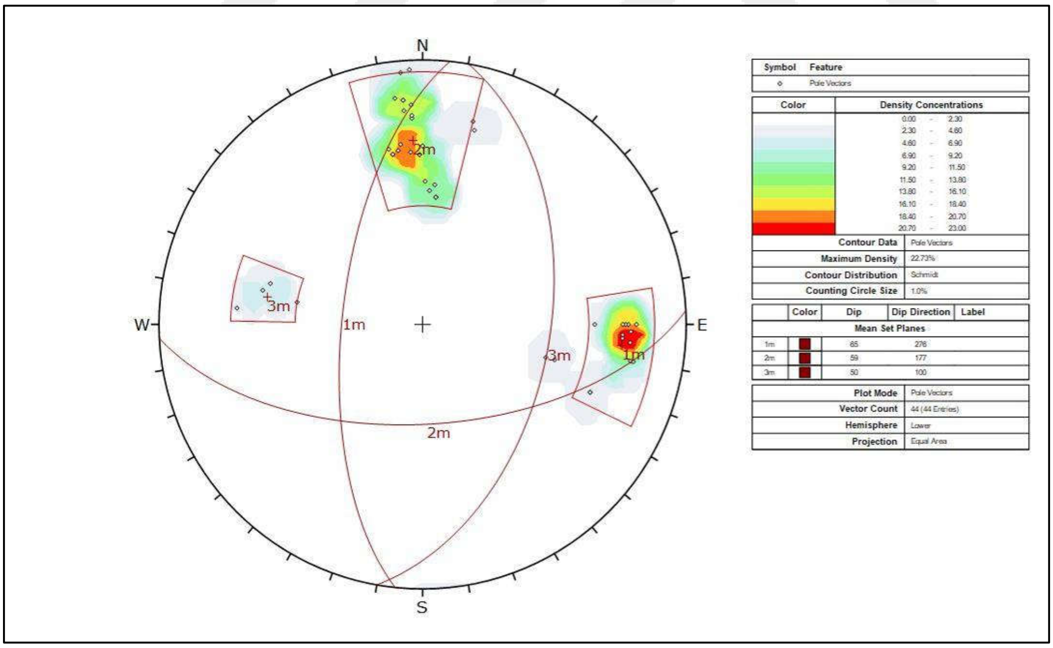

Figure 6.10. Scan-line survey measurement values and analysis results: Almacık Tepe-Üst (Akgün et al., 2024).

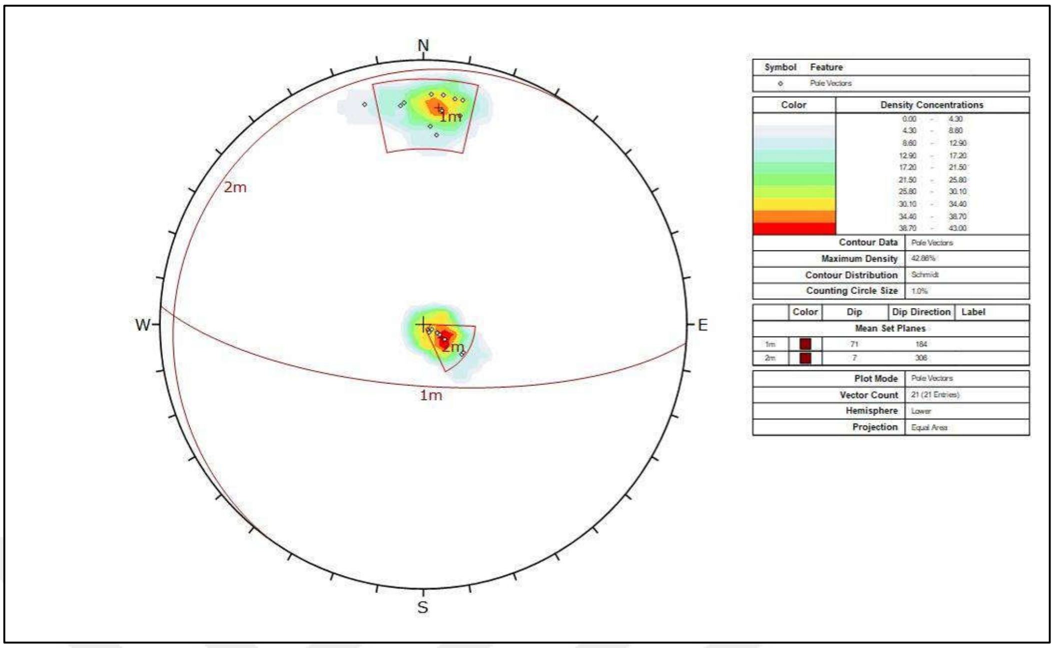

Figure 6.11. Scan-line survey measurement values and analysis results: Yukarıkayacık Road (Akgün et al., 2024).

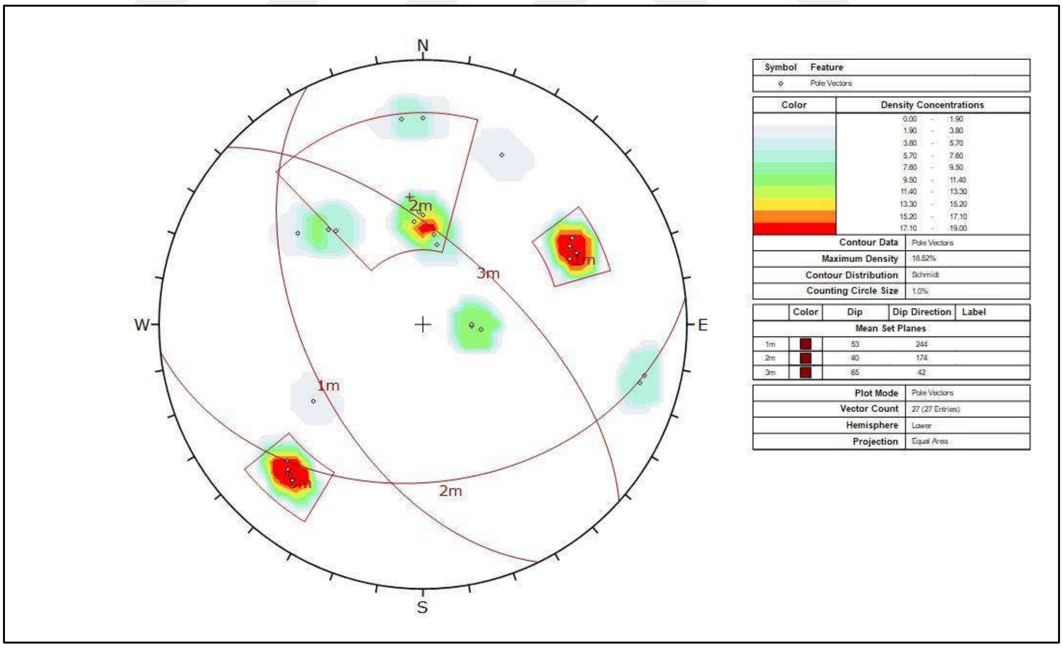

Figure 6.12. Scan-line survey measurement values and analysis results: İmambaba Summit (Akgün et al., 2024).

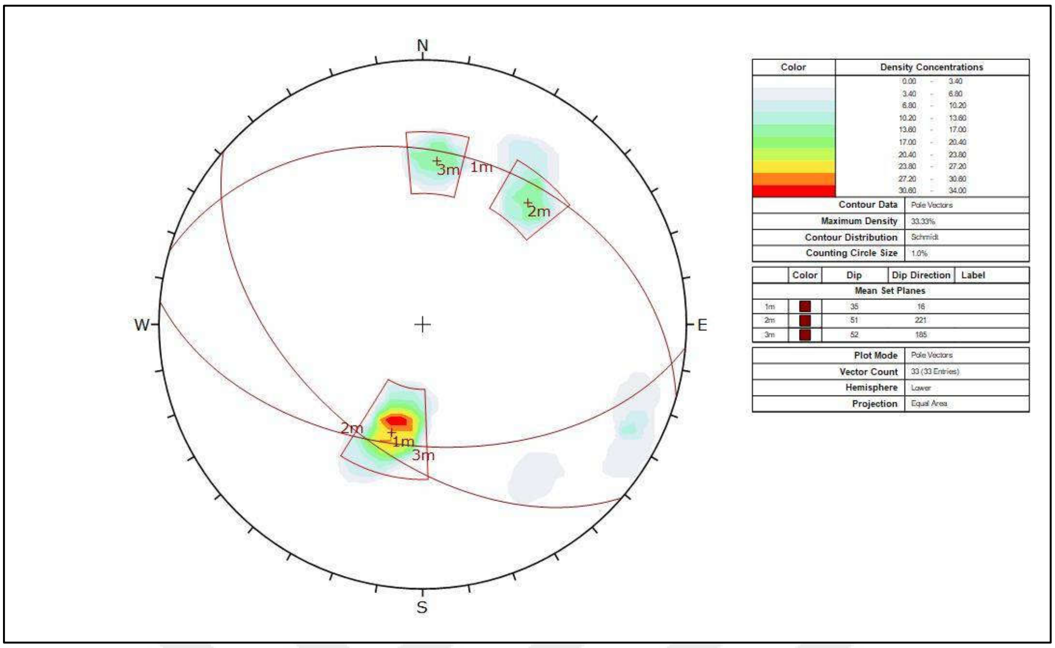

Figure 6.13. Scan-line survey measurement values and analysis results: İmambaba Summit return path (Akgün et al., 2024).

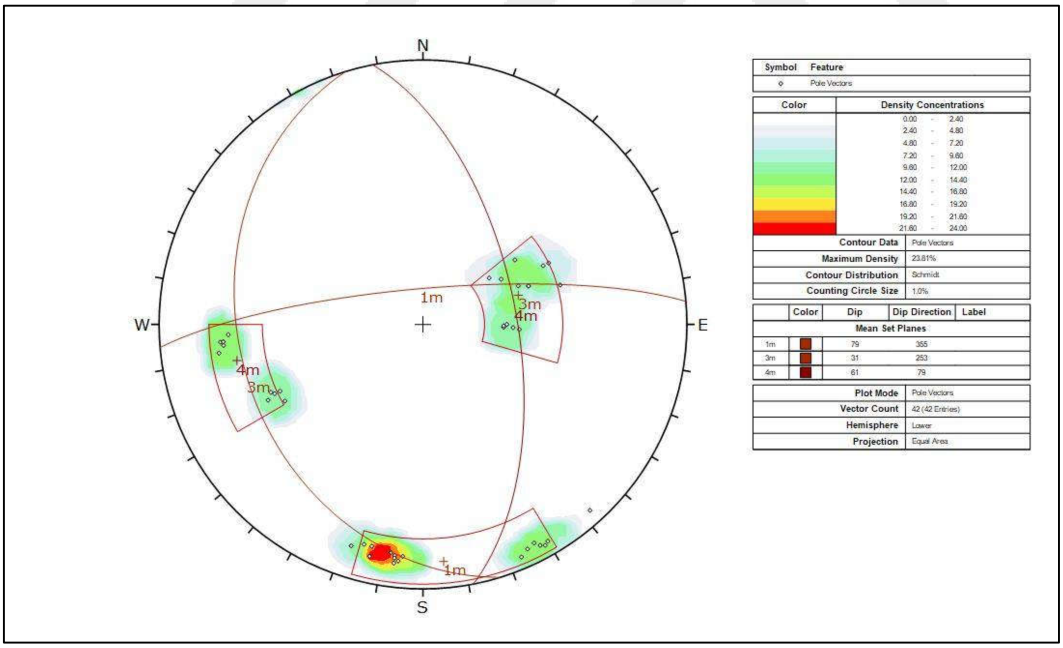

Figure 6.14. Scan-line survey measurement values and analysis results: Halilbeyli (Akgün et al., 2024).

Table 6.1. Discontinuity orientations obtained from scan-line survey measurements (Akgün et al., 2024).

Location Description	**Location Code**	**Set**	**Orientation**	
			Dip	**Dip Direction**
Kuyucak Belenova	Kuy-4 (1.3)	Bedding Plane (BP)	31	29
		Joint Set-1 (J1)	71	295
		Joint Set-2 (J2)	85	195
Gökkiriş Tepe	Gkrş (6)	Bedding Plane (BP)	69	215
		Joint Set-1 (J1)	81	263
		Joint Set-2 (J2)	62	167
Almacık Tepe Alt	S8-Alt (8)	Bedding Plane (BP)	63	190
		Joint Set-1 (J1)	65	273
		Joint Set-- (J2)	62	37
Almacık Tepe Üst	S8-Üst (9)	Bedding Plane (BP)	59	177
		Joint Set-1 (J1)	65	276
		Joint Set-2 (J2)	50	100
Yukarıkayacık Dönüşü	12	Bedding Plane (BP)	71	184
		Joint Set-1 (J1)	7	306
İmambaba Zirve	16	Bedding Plane (BP)	40	174
		Joint Set-1 (J1)	53	244
		Joint Set-2 (J2)	65	42
İmambaba Zirve Dönüşü	17	Bedding Plane (BP)	35	16
		Joint Set-1 (J1)	51	221
		Joint Set-2 (J2)	520	185
Halilbeyli	14	Bedding Plane (BP)	79	355
		Joint Set-1 (J1)	31	253
		Joint Set-2 (J2)	61	79

The discontinuity characteristics measured during the scan-line surveys (Akgün et al., 2024) were classified according to ISRM (2014). The rock mass characterizations conducted at the locations where scanline surveys were performed are described in the following paragraphs.

The outcrops at the Kuyucak-Belenova location consisted of gray-dark gray schist-bearing marbles. Three discontinuity sets were measured (one bedding plane and two joint sets). The surfaces were slightly weathered. Discontinuity spacings, ranging from 50 to 510 mm, were classified as closely spaced to moderately spaced, according to ISRM (2014). The discontinuities were highly continuous, with apertures observed to range from 10 to 350 mm, generally classified as very wide. Calcite filling was observed in the apertures. The surfaces of the discontinuities ranged from wavy rough to wavy smooth.

The marbles at the Gökkiriş Tepe location were cream-colored. Three discontinuity sets were measured (one bedding plane and two joint sets). Discontinuity spacings, ranging from 15 to 65 mm, were classified as closely spaced according to ISRM (2014). The discontinuities were highly continuous. Apertures were observed to range from 0.2 to 10 mm and classified as slightly open according to ISRM (2014), but there were also numerous discontinuities with wide to moderately wide apertures. The surfaces of the discontinuities ranged from wavy rough to wavy smooth. Karstic voids of varying sizes, ranging from 10 cm to 1.5-2 m in width, were also observed at this location.

The marbles at the Almacık Tepe Alt location were dirty white-light gray. Three discontinuity sets were measured (one bedding plane and two joint sets). The surfaces were slightly weathered. Discontinuity spacings, ranging from 30 to 500 mm, were classified as moderately spaced, according to ISRM (2014). The discontinuities had moderate to low continuity. Apertures were observed to range from 1 to 50 mm and were classified as moderately open according to ISRM (2014), but very wide, wide, and open apertures were also present. Calcite filling was observed in some apertures. The surfaces of the discontinuities ranged from wavy rough to wavy smooth.

The marbles at the Almacık Tepe Üst location were dirty white-light gray. Three discontinuity sets were measured (one bedding plane and two joint sets). Discontinuity spacings, ranging from 50 to 1000 mm, were classified as moderately spaced, according to ISRM (2014). The discontinuities generally had moderate continuity. Apertures were observed to range from 1 to 100 mm and were classified as very wide according to ISRM (2014), but wide, moderately wide, and open apertures were also present. Calcite filling was observed in some apertures. The surfaces of the discontinuities were undulating smooth. Karst formations were observed at this location.

The outcrops at the Yukarıkayacık location were dark gray marble. Two discontinuity sets were measured (one bedding plane and one joint set). The surfaces were slightly weathered. Discontinuity spacings, ranging from 50 to 500 mm, were classified as moderately spaced, according to ISRM (2014). The discontinuities had moderate to low continuity. Apertures were observed to range from 1 to 15 mm and were classified as open according to ISRM (2014), but very wide, wide, and moderately wide apertures were also present. Calcite filling was observed in some apertures. The surfaces of the discontinuities were undulating smooth.

The outcrops at the İmambaba Summit location were dark gray-black colored marble. Three discontinuity sets were measured (one bedding plane and two joint sets). The surfaces were slightly weathered. Discontinuity spacings, ranging from 30 to 500 mm, were classified as moderately spaced, according to ISRM (2014). The discontinuities had low continuity. Apertures were observed to range from 1 to 50 mm and were classified as moderately open according to ISRM (2014), but very wide, wide, and open apertures were also present. Calcite filling was observed in some apertures. The surfaces of the discontinuities were undulating rough.

The outcrops at the Halilbeyli location were dark gray-light brown marble. Three discontinuity sets were measured (one bedding plane and two joint sets). The surfaces were slightly weathered. Discontinuity spacings, ranging from 30 to 500 mm, were classified as moderately spaced, according to ISRM (2014). The discontinuities had low continuity. Apertures were observed to range from 1 to 50 mm and classified as moderately open according to ISRM (2014), but very wide, wide, and open apertures were also present. Calcite filling was observed in some apertures. The surfaces of the discontinuities ranged from undulating smooth to stepped rough.

As a summary, all bedding planes had an approximately east-west orientation. When the joint sets were to be considered, it was observed that the first joint sets, except for the Imambaba Zirve location, generally had a north-south orientation. At the İmambaba Zirve location, both identified joint sets were east-west oriented, with dip directions approximately towards the south. In light of these observations, it has been concluded that the bedding planes were aligned approximately east-west, consistent with the region's current tectonic regime.

Within the scope of this study, a crack orientation and distribution image representing the reservoir's fracture distribution was created using photogrammetric field images obtained at the line-survey location Figure 6.15. The following process was followed to obtain the fracture network distribution that will be included in the model based on this sample image.

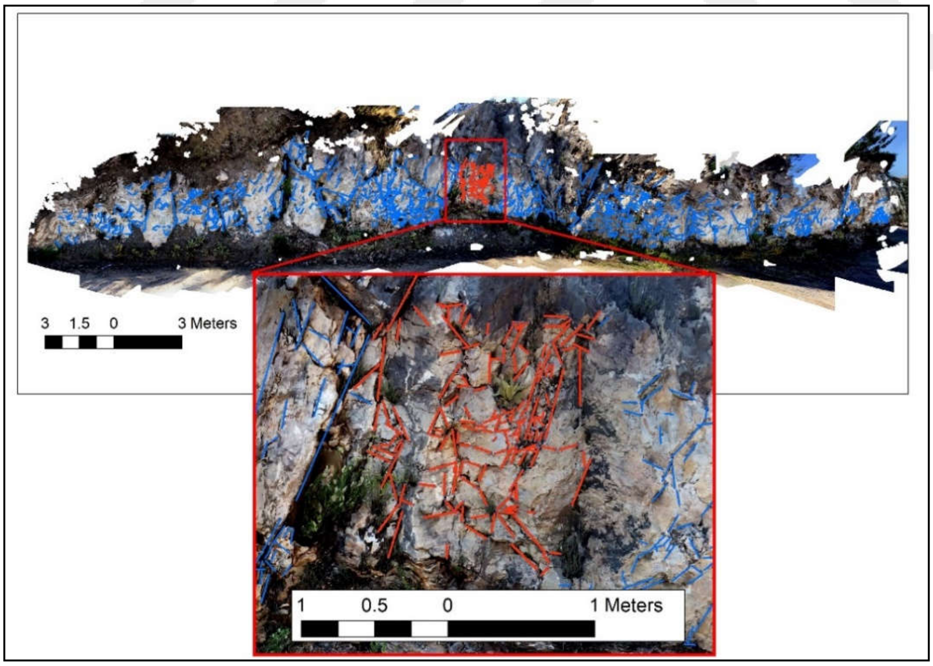

Figure 6.15. Discontinuity lineament analysis results performed on the image obtained from the scan-line survey location and the sector used for the sample fracture network.

6.1.4 Photogrammetry

In addition to direct field measurements, scaled photographs were taken with an 8-megapixel camera at suitable scan-line survey locations to form the basis for creating the fracture network. Initially, the images from the location identified as the Yukarı Kayacık, with an approximately 35-meter surface oriented at 060°, were analyzed (Figure 6.16). For this purpose, 69 photographs were first positioned according to camera positions and angles (Figure 6.17), and then a 3D model was obtained using these images (Figure 6.18). This model was converted into an orthophoto with a pixel size of 1.25 mm in the X-Z plane, and analyses were conducted. The observed discontinuities were linearly transferred to a GIS database (Figure 6.19).

Figure 6.16. Orthophoto view of the Yukarı Kayacık Bend scan-line survey location.

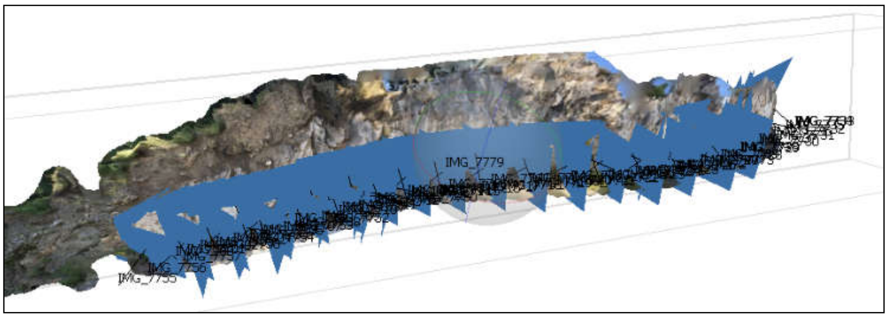

Figure 6.17. Locations of the photographs taken at the scan-line survey location.

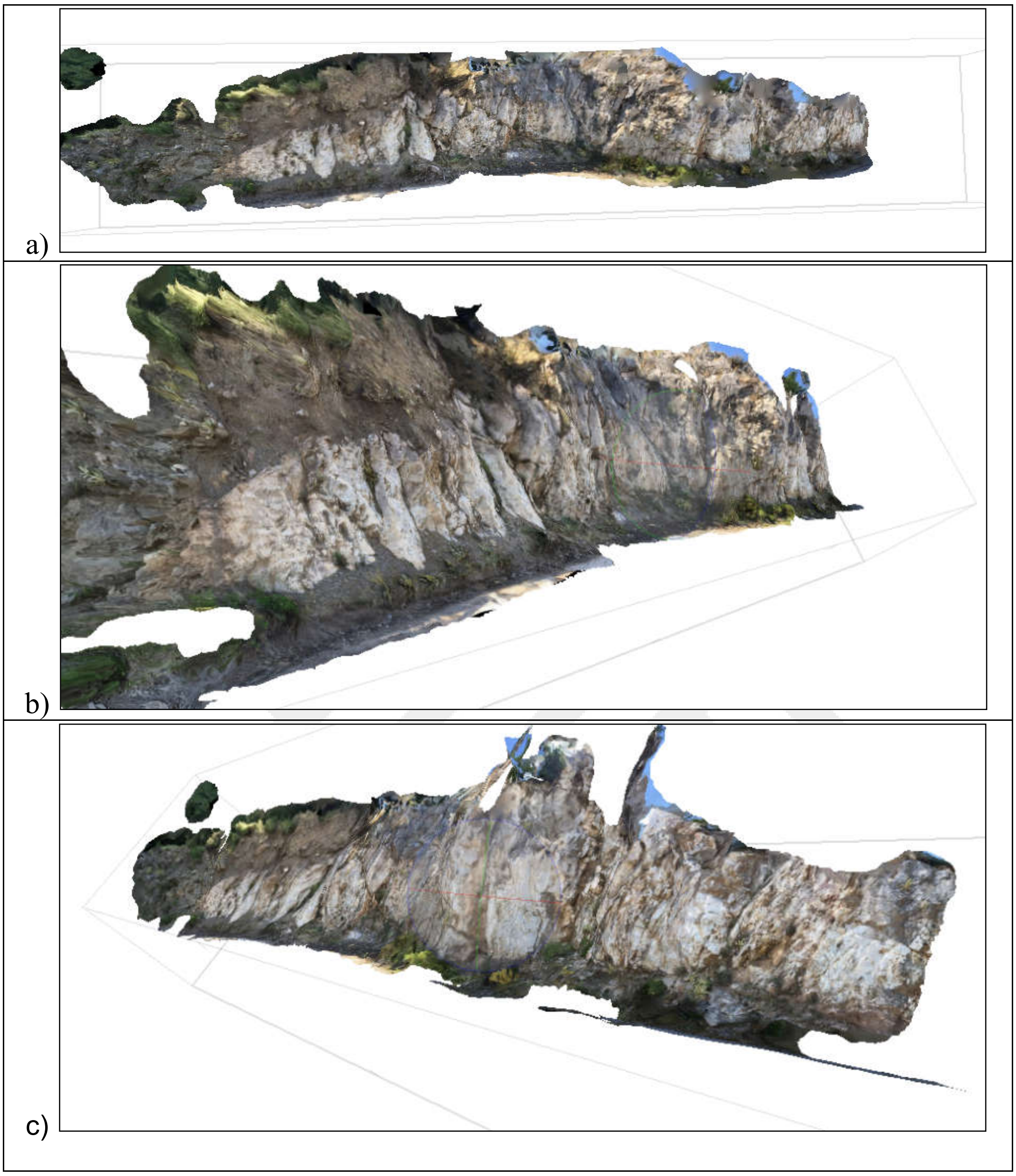

Figure 6.18. The views of the 3D model obtained from the scan-line survey location from a) 330° direction, b) northeast direction, and c) west direction.

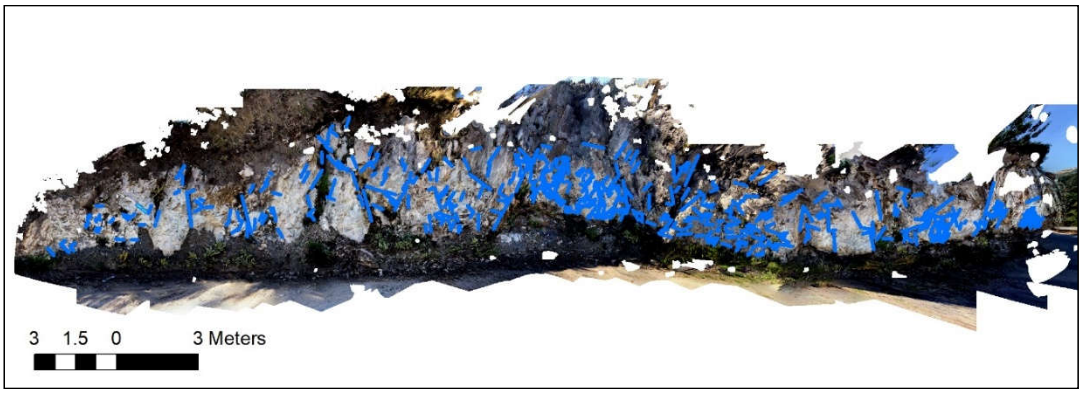

Figure 6.19. Discontinuities extracted from the image of the scan-line survey location.

Table 6-2 and Figure 6-20 provide information on the main discontinuity planes.

Table 6.2. Summary table of the scan-line survey studies.

Location	**Set**	**Orientation**	
		Dip	Dip Direction
Yukarıkayacık Turn	Bedding Plane (BP)	71	184
	Joint Set -1 (J1)	7	306

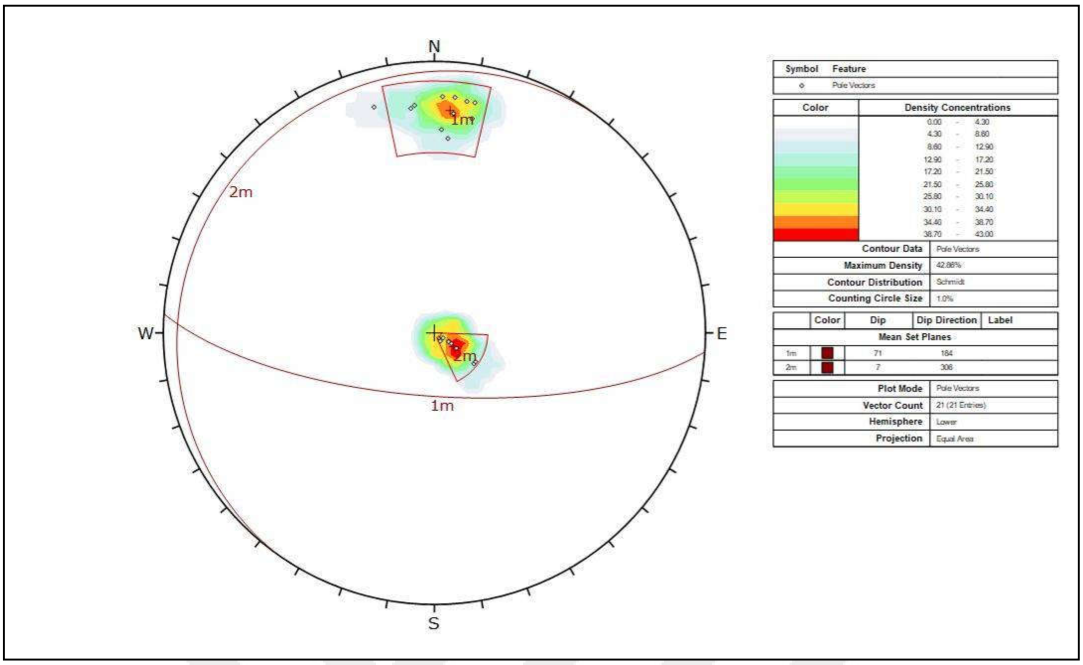

Figure 6.20. Scan-line survey values and analysis results of the Yukarı Kayacık-Maden Bend location.

Analyses were conducted on the 3D point cloud image obtained from the Yukarı Kayacık scan-line survey location using CloudCompare software and the Compass plugin. The results of these analyses are presented in Table 6.3, and the analysis results obtained using RocScience DIPS software are also presented in Figure 6.21. The discontinuity sets obtained with DIPS software are listed in Table 6.4. Although the results do not exactly match due to the point cloud distribution, they are consistent with the field results when compared. A third discontinuity set was also identified using CloudCompare software (Figure 6.21).

Table 6.3. Analysis results obtained from the point cloud using CloudCompare software's Compass plugin.

Meas.	Dip	Dip Dir.	Meas.	Dip	Dip Dir.	Meas.	Dip	Dip Dir.
1	73.2	139.2	41	84.6	191.8	81	85.4	197.9
2	79.3	159.0	42	78.2	178.3	82	66.2	18.1
3	61.2	199.5	43	82.9	200.8	83	81.6	288.3
4	69.9	358.8	44	42.4	356.9	84	16.7	288.5
5	52.2	190.6	45	57.7	175.1	85	52.4	312.3
6	60.0	203.2	46	77.5	72.4	86	73.3	22.0
7	74.4	157.9	47	79.0	81.5	87	21.6	359.0
8	71.2	150.4	48	66.4	287.2	88	26.0	344.5
9	88.2	158.7	49	62.1	289.8	89	80.7	143.7
10	72.0	162.1	50	56.2	265.2	90	68.2	141.1
11	89.4	133.7	51	34.1	329.2	91	74.7	194.7
12	72.3	153.3	52	42.7	350.2	92	62.0	194.8
13	64.8	291.0	53	26.0	341.4	93	53.7	142.7
14	68.9	94.9	54	20.2	343.3	94	26.2	7.5
15	66.5	172.2	55	31.4	14.5	95	39.7	21.1
16	52.4	111.0	56	19.0	331.6	96	17.6	357.2
17	15.5	356.9	57	51.2	322.3	97	71.9	7.9
18	73.2	148.5	58	75.7	277.8	98	59.1	17.7
19	30.0	39.6	59	61.3	198.8	99	38.5	329.9
20	75.9	127.5	60	53.7	211.7	100	21.0	8.0
21	70.6	177.9	61	50.0	210.6	101	15.8	1.8
22	70.6	177.9	62	61.8	194.5	102	40.9	354.9
23	52.7	125.9	63	81.5	281.6	103	70.0	142.8
24	57.6	171.4	64	52.4	354.8	104	83.5	335.3
25	78.0	98.2	65	54.8	337.6	105	73.9	332.4
26	76.3	151.7	66	65.1	267.1	106	63.7	322.9
27	84.8	170.9	67	74.7	156.0	107	77.2	332.6
28	75.2	186.7	68	64.8	186.2	108	62.8	318.7
29	88.6	312.7	69	57.6	275.8	109	88.3	118.0
30	74.8	289.0	70	90.0	304.5	110	39.0	334.7
31	60.4	298.4	71	59.1	161.3	111	67.9	195.3
32	70.9	137.7	72	70.2	176.1	112	71.9	9.2
33	84.5	143.6	73	88.3	193.5	113	66.2	199.4
34	87.2	283.6	74	43.9	179.2	114	44.2	178.0
35	74.9	338.4	75	79.9	300.9	115	83.5	141.7
36	85.0	155.8	76	89.9	115.7	116	58.7	197.4
37	86.6	63.3	77	52.9	348.0	117	67.4	356.4
38	83.4	322.8	78	77.4	266.6			
39	84.0	184.6	79	83.8	286.6			
40	78.0	172.4	80	71.1	28.8			

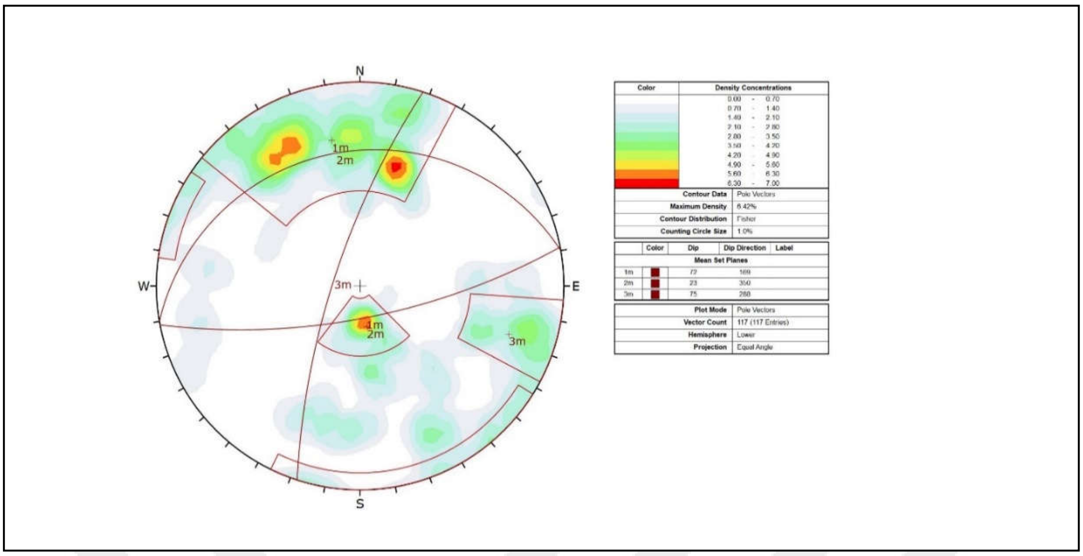

Figure 6.21. Analysis results of the point cloud conducted with DIPS

Table 6.44. Discontinuity sets extracted from the analysis results obtained with DIPS software.

Discontinuity	Dip	Dip Direction
1	72	169
2	23	350
3	75	288

Additionally, automatic analyses were conducted on the same point cloud using the Discontinuity Set Extractor (DSE) Matlab code, dividing it into four regions of approximately 10 meters each (Figure 6.22). The main reason for dividing the point cloud into sectors is that field measurements were concentrated mainly in Sector 2 and Sector 3. In these analyses, 10-point proximity was considered. The results are presented in Table 6.5. The analyses were also repeated for the entire point cloud, and the results are presented in Table 6.6 and Figure 6.23 along with Figure 6.24.

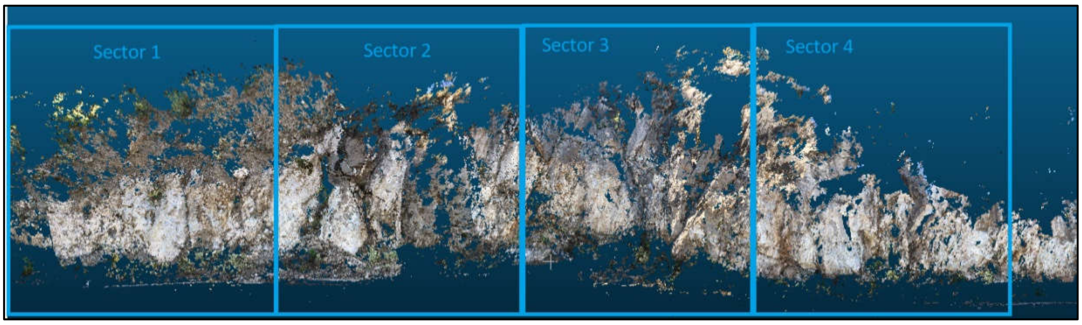

Figure 6.22. Sector division of the point cloud at the Yukarı Kayacık line survey location.

Table 6.5. Distribution of discontinuity planes obtained on the point cloud by sector using DSE software.

Dip Direction	**Dip Angle**	**Density**	**Dip Direction**	**Dip Angle**	**Density**
Sector 1			**Sector 3**		
135.00	45.98	1.20	191.31	54.03	1.13
315.00	16.10	0.78	315.00	16.10	0.78
278.13	70.53	0.28	353.66	84.32	0.30
6.34	84.32	0.16			
Sector 2			**Sector 4**		
315.00	16.10	1.05	191.31	54.03	0.78
168.69	54.03	0.86	120.96	60.49	0.76
108.43	35.10	0.83	315.00	16.10	0.40
353.66	84.32	0.20	293.20	74.58	0.37

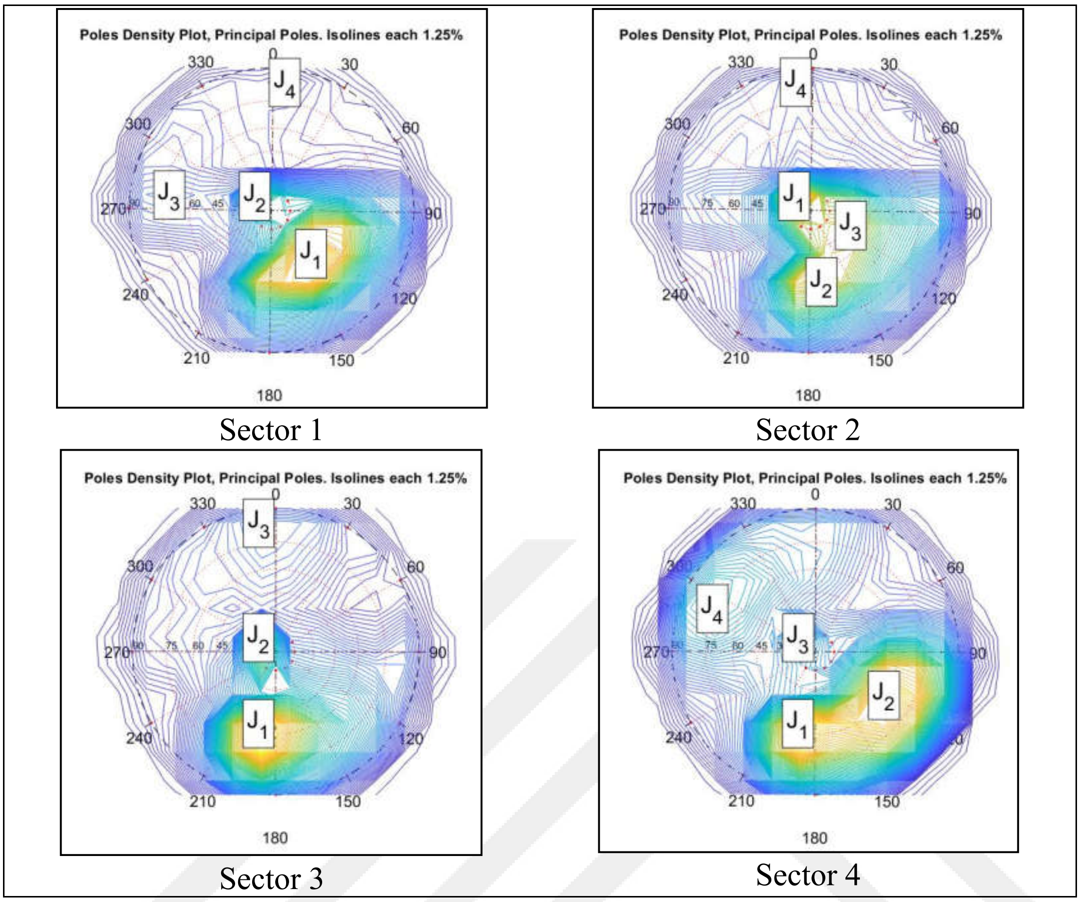

Figure 6.23. DSE analysis results by sector.

Table 6.6. Analysis results obtained on the entire point cloud.

Dip Direction	Dip Angle	Density
191.31	54.03	0.92
315	16.10	0.74
278.13	70.53	0.26
353.66	84.32	0.23

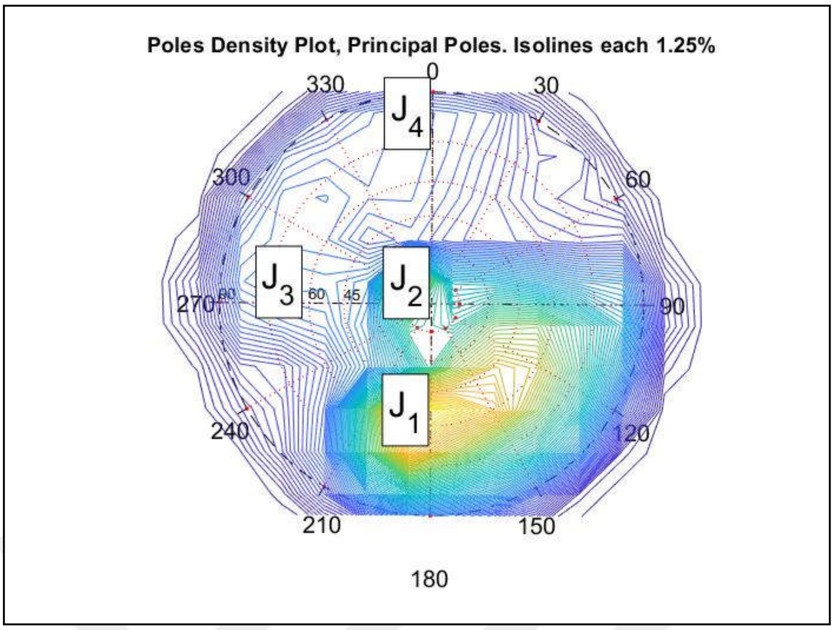

Figure 6.24. Analysis results on the entire point cloud conducted with DSE software.

Three analyses—manual analysis using CloudCompare software, automatic analysis with DSE software, and field measurements—were observed to be consistent with each other. Moreover, more discontinuity sets were identified in the point cloud analyses since they allowed the evaluation of points that are inaccessible in the field. However, in the automatic extraction, a fourth discontinuity plane was identified, with a dip direction of 6.34° in Sector 1, 353° in Sectors 2 and 3, and 120° in Sector 4, and this plane was inconsistent with the discontinuity planes obtained manually in the field or with the assistance of CloudCompare software. Therefore, the need for controlled execution of automatic analyses has also been demonstrated. In this context, this study has tested the suitability of supporting field results with analyses conducted on 3D point clouds obtained from photogrammetric images taken at the pilot locations.

Finally, considering the dip and dip-direction values of each point, the planes were assessed to belong to either the neotectonic or paleotectonic period.

6.2 Categorization of the fractures

The reservoir rock that hosts the geothermal fluids is the marble formations of the Büyük Menderes Massive, which is represented by a fracture network that serves as the main conduit for the fluid flow. Thus, a representative fracture network was extracted through scan-line surveys and photogrammetric methods. Several locations of the marble outcrops have been identified, and the fracture network at these locations was extracted.

Considering the paleostress solutions, fault study results, and focal mechanisms obtained from the literature and solutions, it was determined that the principal stress direction σ_3 is approximately in the K-G direction. Accordingly, plane points with inclination orientations (in the same direction as σ_3) ranging between 350-30 and 170-210 degrees (or strike directions between 260-300 and 80-120 degrees) were assigned to the neotectonic period, considering the current stress distribution of the Büyük Menderes Graben.

Data obtained from field observations and three-dimensional point cloud-based plane analyses were evaluated in this regard. Lineaments identified on the orthophoto image were categorized into 3 groups: 1) discontinuities representing the neotectonic period (NEO1), 2) discontinuities representing the paleotectonic period (PALEO), and 3) discontinuities representing the probable neotectonic period (NEO-3) (Figure 6.25).

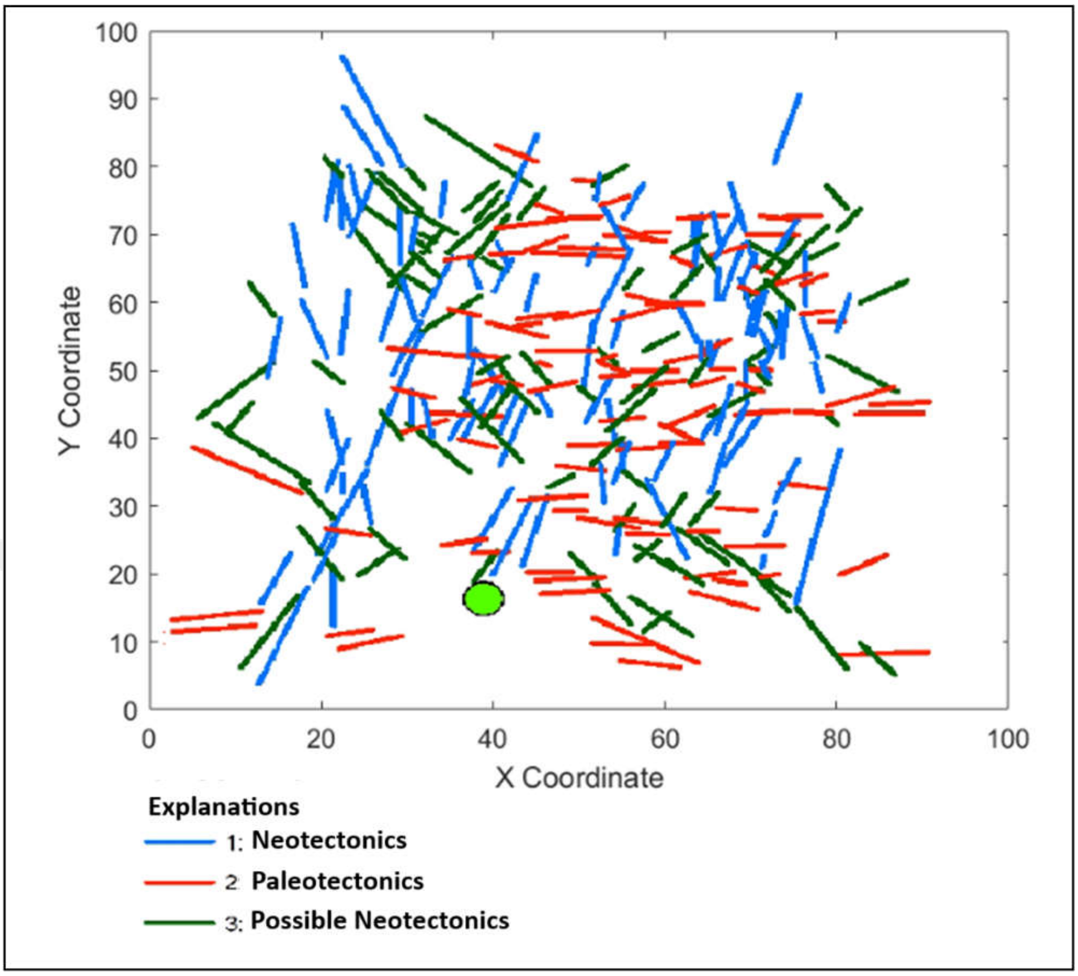

Figure 6.25. Fracture Classification.

CHAPTER 7

GEOTECHNICAL LABORATORY TESTS

In order to determine the geomechanical properties of the Menderes Massif, rock mechanics tests, including uniaxial compression, triaxial compression, static deformability, and point load tests, have been conducted (Akgün et al., 2024). The collection of the samples, summary of the test procedures, and test results are provided in this chapter.

7.1 Sample Collection

Rock mechanics tests were conducted on block samples taken from marble units of the Menderes Metamorphics, which exhibit reservoir rock characteristics, to determine the geomechanical properties of the rocks. For this purpose, block rock samples obtained during the field study were first prepared as core samples at the METU Department of Mining Engineering - Rock Mechanics Laboratory, and then rock mechanics tests were carried out. Static Deformability, Uniaxial Compressive Strength (UCS), and Triaxial Compressive Strength (TCS) tests were performed within this work package. Rock mechanics tests were conducted according to the standards recommended by the International Society for Rock Mechanics (ISRM, 2007).

Two field trips 2 months apart were conducted, and block samples were collected from several locations, as indicated below (Akgün et al., 2024);

During the first field study:

1. Gökkiriş Tepe (Köşk) (1 sample)
2. Yukarı Kayacık – Almacık Tepe (Efeler) (1 sample)

3. Yukarıkayacık Kuzeyi – Maden (Efeler) (2 samples)
4. İmambaba Zirve (Efeler) (1 sample)
5. Halilbeyli (Koçarlı) (1 sample)

A total of 6 block samples were collected from these locations. The location map of these samples is provided in Figure 7.1 through Figure 7.4, and general information about the samples is summarized in Table 3.1 Table 7.1. Additionally, samples of sufficient number and size were collected from each location for Point Load tests.

Among the collected samples, it was determined that the block sample from the Efeler – Yukarı Kayacık – Almacık Tepe location was not sufficient for core sampling due to its physical condition and size. As a result, it was decided to collect two additional block samples from this and two new locations, and a new field study was conducted.

During this second field study:

1. Kuyucak – Belenova (1 block sample)
2. Almacık Tepe (Efeler) (2 block samples)
3. Yukarıkayacık Kuzeyi – Maden (Efeler) (3 block samples)
4. Terziler (Efeler) (2 block samples)

A total of 8 block samples were collected from these locations. Additionally, samples of sufficient number and size were collected from each location for Point Load tests. Below are general views of the locations where the block samples were collected and sample images provided (Figure 7.5 - Figure 7.11).

Table 7.1. Locations of samples collected for rock mechanics tests

Sample Location	Code	Age	Collection Date
Gökkiriş Tepe	GK – Block 1	Jurassic	02/07/2021
Yukarıkayacık Kuzeyi – Maden	S11 – Block 3	Permian	03/07/2021
			18/09/2021
İmambaba Zirve	İM – Block 4	Permian	04/07/2021
Halilbeyli	HB – Block 5	Paleozoic	04/07/2021
Kuyucak – Belenova	Kuy-4	Paleozoic	17/09/2021
Almacık Tepe	S8	Paleozoic	18/09/2021
Terziler	TY2	Permian	18/09/2021

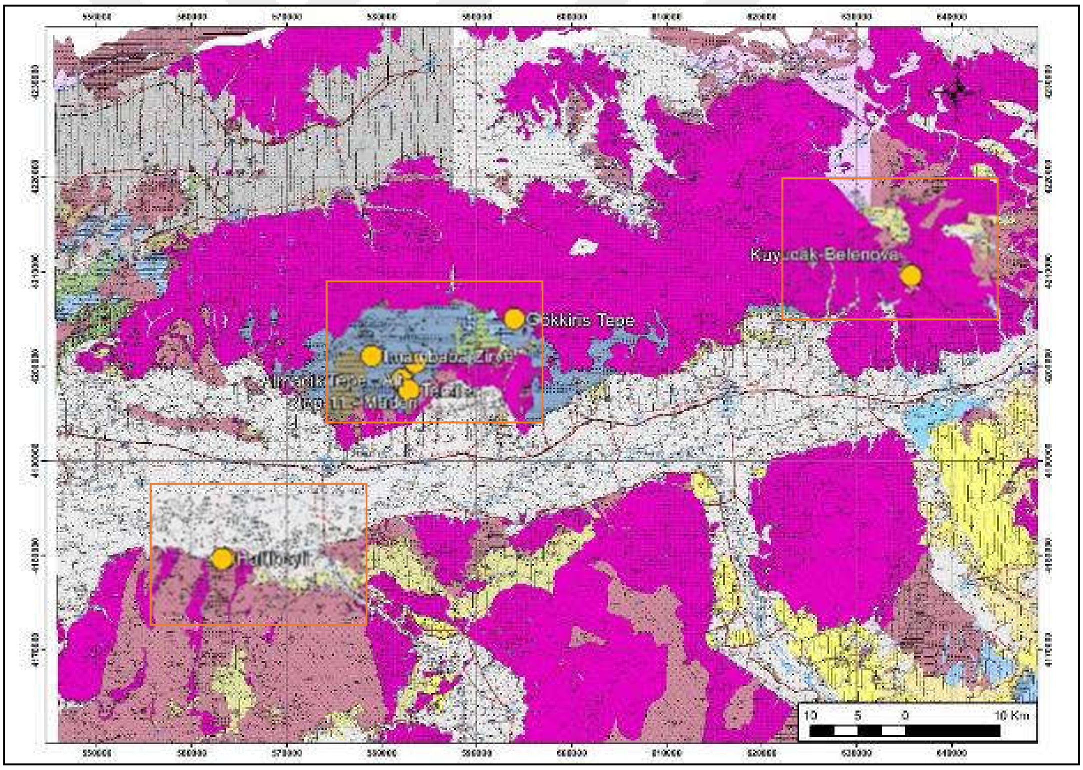

Figure 7.1. Locations where samples were collected for rock mechanics tests.

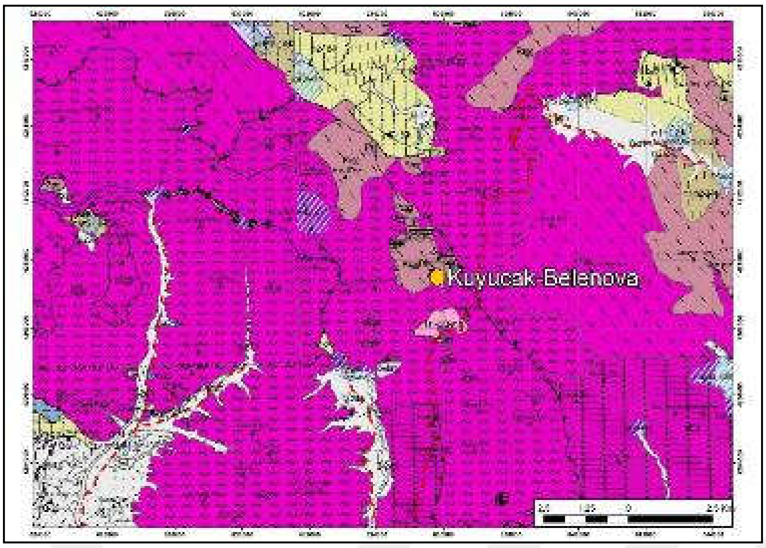

Figure 7.2. Sample locations for rock mechanics tests, Kuyucak-Belenova point.

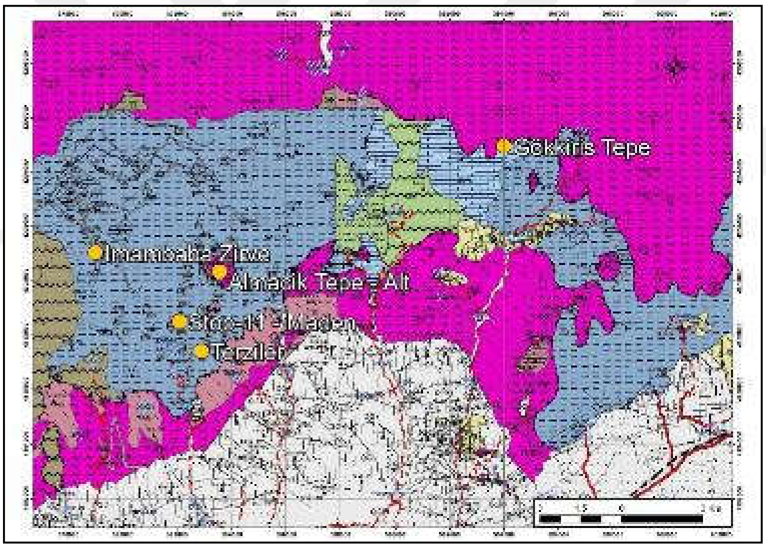

Figure 7.3. Sample locations for rock mechanics tests, Yukarıkayacık, Gökkiriş, and İmambaba Zirve points.

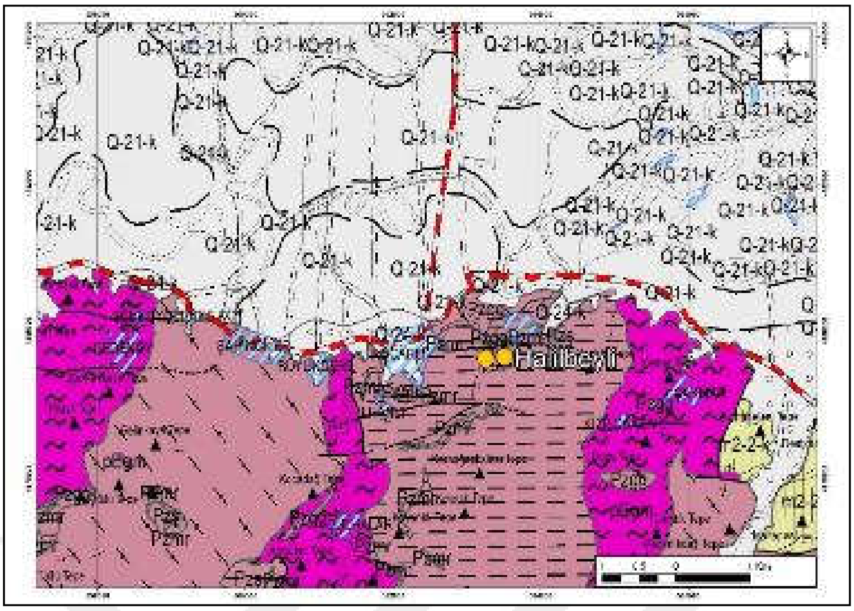

Figure 7.4. Sample locations for rock mechanics tests, Halilbeyli point.

Figure 7.5. Gökkiriş Tepe.

Figure 7.6. İmambaba Zirve, Permian marbles.

Figure 7.7. Southern wing, Halilbeyli, Paleozoic marbles.

Figure 7.8. Kuyucak-Belenova location, heavily fractured Paleozoic marbles.

Figure 7.9. Yukarıkayacık-Maden location, Permian marble material.

Figure 7.10. Almacık Tepe lower location, Paleozoic marbles.

Figure 7.11. Terziler Road, TY2 location, Permian marbles.

7.2 Uniaxial Compressive Strength Tests

The uniaxial compressive strength tests were conducted to determine the failure load prior to the triaxial compressive strength tests and to determine the uniaxial compressive strengths of different marble units. The uniaxial compressive strength tests were carried out in the METU Department of Mining Engineering, Rock Mechanics Laboratory, following ISRM standards (ISRM, 2007). These tests were performed to determine the uniaxial compressive strength of the cylindrical intact rock samples. Samples were prepared with a length/diameter (L/D) ratio of 2.25-2.45. The dimensions of the tested samples and detailed photographs are provided in Appendix B and in Akgün et al., 2024.

The sample was placed between the hydraulic press platens in this test set-up. To ensure a homogeneous distribution of the load on the sample, steel discs of the same diameter as the sample (preferably half the length of the diameter) were placed on the top and bottom of the sample. The press was operated until no gap between the hydraulic press platens existed and then, the lower platen was raised. An axial load was applied to the sample during 5-10 minutes or at a rate of 5-10 kgf/cm² per second. The failure load was read from the load gauge or computer at the moment of failure. When the sample failed, the applied load value decreased suddenly or gradually. This value represented the maximum load that could be applied to the sample and thus, that defines the strength limit of the sample. The uniaxial compressive strength value (σ_b) (σ_{ci}=UCS) was calculated by dividing the failure load (F) by the surface area (A) of the sample where the load was applied.

7.3 Triaxial Compressive Strength Tests

The triaxial tests were conducted as per ISRM (2019). The test involved applying constant lateral pressure while increasing vertical load until failure. Samples with a length-to-diameter ratio of 2.0–3.0 were used. A Hoek cell and membrane suitable for the sample diameter facilitated the set-up. The Hoek cell was filled with oil to apply lateral pressure via a hydraulic jack, ensuring no air gaps remained.

During the test, lateral pressure was applied until a fixed value (σ_3) was reached, after which vertical loading continued until failure. The failure mechanism, typically a shear crack along the σ_1 direction, was analyzed using Mohr circles. Stress components acting on the failure plane are shown in Figure 7.12.

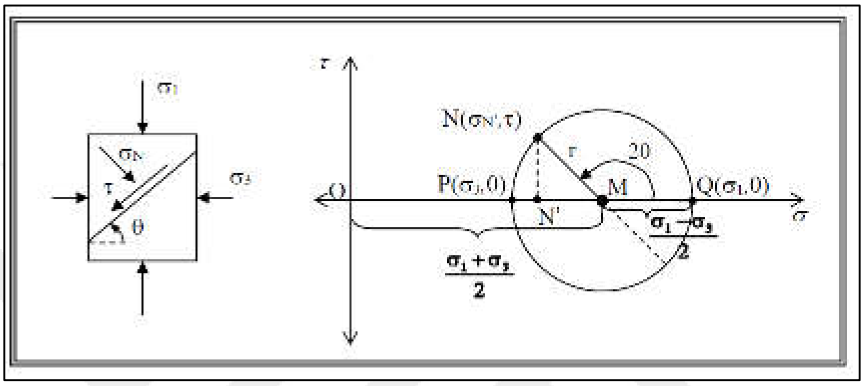

Figure 7.12. Determination of stress components acting on the failure plane using Mohr circles.

Principal stresses (σ_1 and σ_3) were used to plot Mohr circles, and the failure envelope (linear or curved) was derived to determine the internal friction angle (ϕ) and cohesion (c). If the failure envelope was linear, ϕ was determined from the angle of the envelope with the horizontal, and c was derived from the τ-axis intercept. For curved envelopes, tangents were drawn at contact points with Mohr circles, yielding varying ϕ and c values. The method for determining stress components is illustrated inFigure 7.13, and the principles of the p-q graph are depicted inFigure 7.14.

The summary of test results is presented in Table 7.2, with additional details and photographs provided in Appendix B and in Akgün et al., 2024.

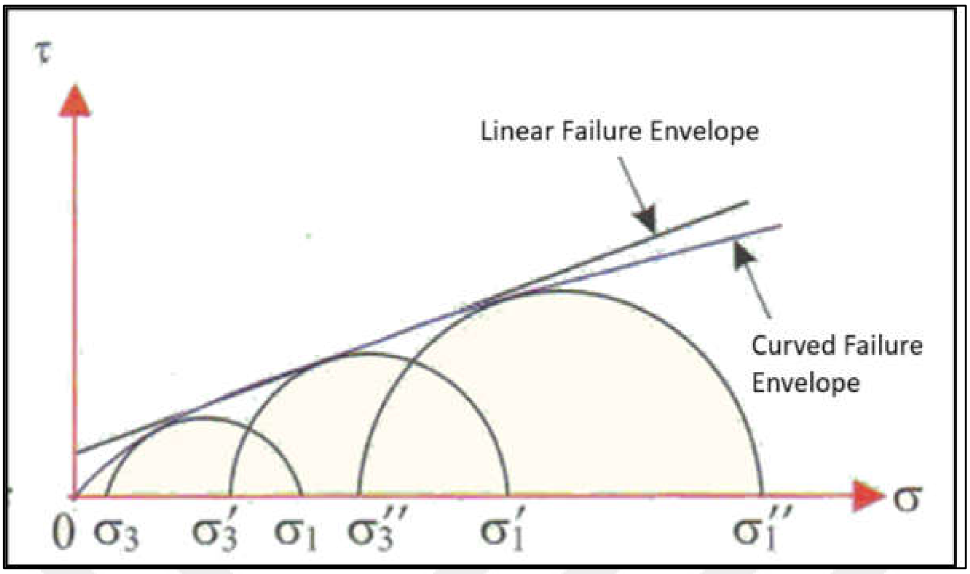

Figure 7.13. Linear and curved failure envelopes.

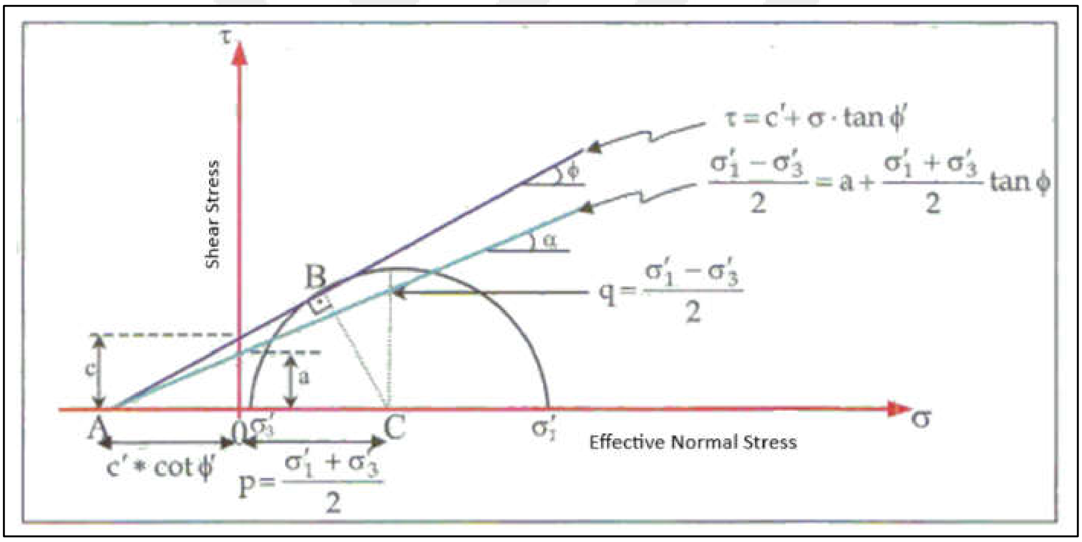

Figure 7.14. Principles of p-q graph. (Fell and Jeffery, 1987)

7.4 Static Deformability Test

Static deformability tests were conducted on 18 samples from marble units with reservoir rock properties to determine the Elasticity Modulus (E) and Poisson's Ratio (ν) as per ISRM (2007). These tests were performed in three sets, similar to triaxial compression tests. Detailed results, including pre-and post-test photographs, Mohr circles, and static deformability graphs, are presented in Appendix B.

The tests involved plotting "stress-strain" curves for cylindrical samples under uniaxial loading conditions. Samples with a length-to-diameter ratio of 2.5–3.0, free from defects, and with smooth surfaces were prepared. A deformation jacket measured axial (ε_a) and circumferential (ε_d) strains. The tests employed a loading rate to cause failure within 5–10 minutes, recording axial loads and corresponding strains.

Circumferential and axial stress-strain graphs, illustrating the deformation behavior, are shown inFigure 7.15. Young's Modulus (E) was calculated from axial stress and strain using tangent, average, or secant methods, as demonstrated in Figure 7.16.

The summarized results are available in Appendix B and in Akgün et al., 2024.

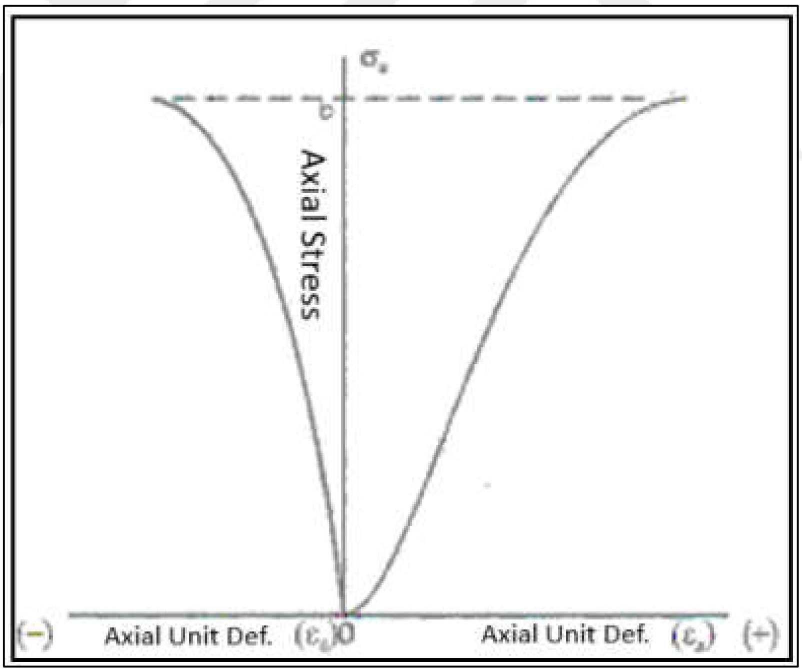

Figure 7.15. Circumferential and axial stress-strain graphs. (ISRM, 2007)

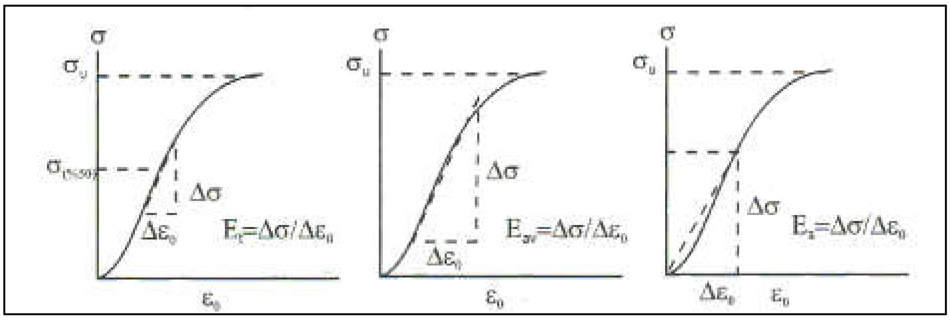

Figure 7.16. Calculation of different Elasticity Modulus values from the axial strain-vertical stress curve: (a) tangent, (b) average, and (c) secant moduli. (ISRM, 2007)

7.5 Point Load Test

Finally, in addition to tests conducted at the METU Mining Engineering Department, point load tests were carried out at the METU Geological Engineering Department on samples obtained from marble blocks collected from the field (Akgün et al., 2024). The IS (50) parameters and associated uniaxial compressive strengths (UCS) were determined. The tests were performed according to the standards recommended by the International Society for Rock Mechanics (ISRM, 2016). Block samples were cut from the collected samples, and the dimensions and failure pressures of each sample were recorded. Summary results of these tests are presented in Table 7.5, and complete data and details are provided in Akgün et al., 2024.

This test determines the point load strength index used to classify rock strengths. The point load strength index is indirectly used to determine other strength parameters such as uniaxial compressive and tensile strength, and to assess crack toughness.

For this test, cylindrical core samples and block and irregularly shaped samples can be used. In this study, block samples of suitable size were tested (Figure 7.17). Block samples with a W/D ratio between 0.3 and 1.0 were prepared for this test according to ISRM standards. The block sample was placed between conical loading heads either perpendicular or parallel to the block axis, loaded to failure within 10-60 seconds, and the failure load (P) was read from the load gauge.

Block and irregularly shaped samples with dimensions around 50 ± 35 mm, as shown in Figure 7.17, are suitable for this type of test. The thickness (D) and width (W) ratio should be between 0.3 and 1.0, preferably close to 1, and the distance M, which is the distance between the contact points of the conical tips and the nearest free end, should be at least 0.5D.

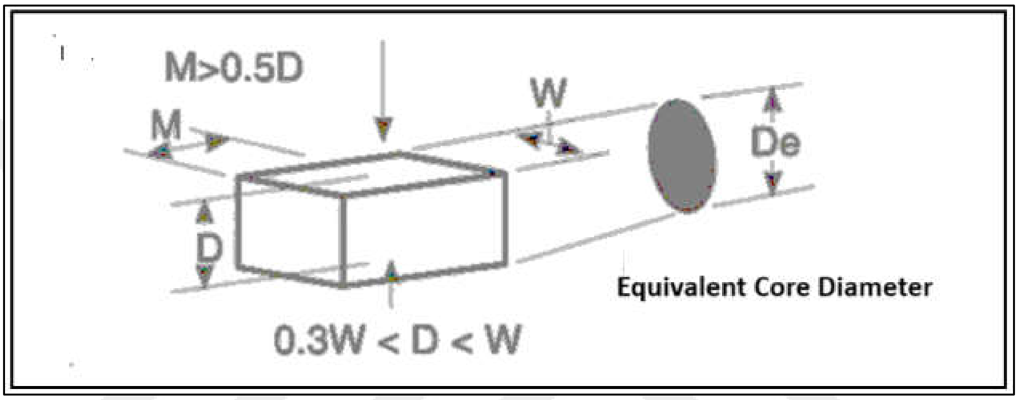

Figure 7.17. Sample shape for block specimens.

The uncorrected point load strength index (kPa) is calculated using $I_s = P / D_e^{2,}$ where P is the failure load, and D_e is the equivalent core diameter. For axial tests, in block and irregular samples: $D_e^2 = 4A / n$ (A=WD; the smallest cross-sectional area of the sample passing through the contact points of the conical tips).

The I_s value varies as a function of D in circumferential tests and D_e in other test types. Therefore, the I_s value must be corrected to a standard core diameter (D=50 mm). This is achieved using a nomogram prepared to determine the corrected point load strength index, I_s (50). If no nomogram is available, the corrected point load strength index is calculated using: $I_s (50) = F \times I_{s,}$ where the size correction factor (F) is determined using $F = (D_e /50)^{0.45}$.

Photos taken during the conduction of the Point Load Test can be seen in Figure 7.18.

Figure 7.18. Photos taken during point load testing

7.6 Test Results

The test results are shown in Table 7.2 through Table 7.5.

Table 7.2. Uniaxial Compressive Strength Test Results

Sample Name	Length (mm)	Diameter (mm)	UCS (MPa)
Gökkiriş (Block 1)-D	126.46	52.6	44.89
Halilbeyli (Block 5)-A	126.66	52.86	46.51
Kuy4-1	126.46	51.73	82.36
S8-3	119.93	52.87	89.88
S11-3	120.14	52.94	90.33
TY2-2	119.61	52.94	93.79

Table 7.3. Triaxial Compressive Strength (TCS) Test Results

Sample Name	Length (mm)	Diameter (mm)	Lateral Pressure (MPa)	Failure Load (kg)	kg/cm²	Sig 1 (MPa)	Cohesion (MPa)	Internal Friction Angle (degrees)
Gökkiriş-1	117.51	52.83	2.5	21751	992.27	97.34	26.86	27.87
Gökkiriş-2	116.2	52.88	5	22476	1023.4	100.4		
Gökkiriş-3	119.18	52.89	7.5	24888	1132.8	111.13		
Stop11-1	121.8	52.87	2.5	27113	1235.01	121.15	29.01	31.31
Stop11-2	121.21	52.83	5	22107	1008.51	98.93	2.93	61.24
Stop11-3	121.39	52.82	7.5	30596	1396.3	136.98		
İmamb. -1	121.75	52.7	4.5	16793	769.87	75.52	6.16	55.64
İmamb. -2	122.33	52.77	9	34933	1597.25	156.69		
İmamb. -3	121.68	52.6	13.5	37584	1729.58	169.67		
Halilb. -1	121.58	52.56	2.5	19481	897.86	88.08	8.82	57.08
Halilb. -2	121.56	52.5	5	25947	1198.61	117.58		
Halilb. -3	121.44	52.31	7.5	31848	1481.91	145.38		
S8-A	120.21	52.9	4	25100	1142.02	112.03	25.35	35.18
S8-B	119.54	52.93	8	28885	1312.74	128.78		
S8-C	119.9	52.86	12	31717	1445.27	141.78		
S11-A	120.02	52.94	5	25073	1139.07	111.74	21.06	40.99
S11-B	120.1	52.85	10	33555	1529.6	150.05		
S11-D	118.78	52.9	15	35818	1629.67	159.87		
S11-C	120.46	52.95	15	33061	1501.39	147.29	Not included*	Not included*
TY2-2	119.61	52.94	0			93.79	27.22	29.47
TY2-B	119.65	52.98	8	25909	1175.27	115.29		
TY2-C	120.86	52.93	12	29053	1320.38	129.53		
TY2-A	119.6	52.97	4	16567	751.79	73.75	Not included**	Not included**

* Sample S11-D was used in the Triaxial Compressive Strength test due to the lower fracture load of sample S11-C, despite having a higher lateral pressure than the S11-B core sample.

** The UCS values of TY2-2 were used to calculate of Cohesion and Internal Friction Angle because the fracture load of the TY2-A core sample was lower than its uniaxial compressive strength.

Table 7.4. Static Deformability Test Results

Sample Name	Length (mm)	Diameter (mm)	UCS (MPa)	Average UCS (MPa)	Elastic Modulus (GPa)	Average Elastic Modulus (GPa)	Poisson Ratio	Average Poisson Ratio
Gökkiriş (Block-1) .A	126.58	52.77	25.94	48.31	84.36	80.2	0.32	0.24
Gökkiriş (Block-1) .B	126.22	52.87	53.48		79.06		0.13	
Gökkiriş (Block-1) .C	126.25	52.82	65.51		77.18		0.27	
İmam. (Block-4) .A	127.88	52.88	91.91	84.99	61.72	73.78	0.17	0.15
İmam. (Block-4) .B	125.15	53.02	48.93		87.7		0.18	
İmam. (Block-4) .C	126.3	52.9	114.13		71.93		0.11	
Kuy4-1 (Not Included)	126.46	51.73	82.36	72.78	66.64	70.73	0.55	0.11
Kuy4-3	119.76	52.75	78.31		70.44		0.11	
Kuy4-4	120.32	52.55	67.25		71.02		0.12	
S8-1 (Not Included)	120.23	52.94	66.01	90.35	65.58	57.16		

Table 7.5. Point Load Test Results

Location	# of Valid Test	Height-D (mm)	Depth-W (mm)	Width-L (mm)	Average Failure Load (kgf)	Failure Load Standard Deviation (kgf)	$I_s(50)$ (MPa) Average	$I_s(50)$ (MPa) Standard Deviation
Kuyucak-Belenova	36	30.49	38.73	53.08	674.24	383.12	3.86	2.39
S8 – Almacık Tep	36	30.12	41.77	53.48	614.79	281.96	3.47	1.67
İmambaba	24	29.89	40.98	62.85	896.21	232.80	5.08	1.34
Gökkiriş	43	31.99	41.49	79.57	665.83	239.95	3.55	1.27
Terziler	47	31.74	41.26	70.91	822.16	287.92	4.41	1.90
Halilbeyli	13	30.12	38.98	41.46	945.27	240.50	5.53	1.39
S11 – Yukarıkayacık - Maden	11	31.04	42.29	48.15	813.90	101.09	4.33	0.64

CHAPTER 8

MECHANICAL MODEL

In this chapter, the studies conducted in order to simulate the mechanical response of the reservoir to fluid injection are presented. The fracture network acquired by scan-line survey and photogrammetric methods has been used in the model.

8.1 Failure model and governing equations - Shear

The fluid flow-induced fracture failure (Deb and Jenny, 2017; Kresse et al., 2013; McClure and Horne, 2014; Sesetty and Ghassemi, 2015) that has been investigated by many researchers over the years, commonly focused on the induced seismicity introduced by the formation and/or activation of fractures. However, in this study, fracture failure was investigated, considering the injection of fluids to enhance a conventional reservoir by causing shear failure.

Ye and Ghassemi (2018) investigated shear stimulation, which reactivates critical or near-critical preexisting fractures through pressurized fluid injection under laboratory conditions, inducing slip and dilation to enhance production in geothermal and unconventional petroleum reservoirs. Molaghab et al. (2019) investigated the fault reactivation potential by considering the current in-situ stress field. This study implemented a Matlab code that simulates fluid injection into a fractured reservoir, focusing on the shear failure of fractures due to changing stress conditions. The simulation uses the Mohr-Coulomb failure criterion to determine whether fractures fail under shear stress as injection pressure increases. The model incorporates principal stresses, fracture geometry, and pore pressure, adjusting the stress state on each fracture throughout the simulation steps.

The principal influences on the stress state on fracture stresses are σ_1, σ_2, and σ_3 acting on the reservoir, representing the maximum, intermediate, and minimum principal stresses, respectively. For each fracture, the orientation of the fracture for these stresses is essential, and the stress tensor for each fracture is calculated as follows:

The normal and shear stresses on a fracture are computed from the rotated principal stresses based on the fracture orientation θ. The stress tensor components are computed as:

$$\sigma_{normal} = \frac{\sigma_1+\sigma_3}{2} + \frac{\sigma_1-\sigma_3}{2}\cos(2\theta) \quad \text{(Equation 8.1)}$$

$$\sigma_{shear} = \frac{\sigma_1-\sigma_3}{2}\sin(2\theta) \quad \text{(Equation 8.2)}$$

where σ_1 and σ_3 are the principal stresses, and θ is the angle of the fracture concerning the principal stress direction. The orientation of the principal stresses themselves (e.g., σ_1 along 0° and σ_3 along 90°) has also been taken into account.

Pore pressure reduces the effective normal stress on a fracture. The effective stress is given by:

$$\sigma_{effective} = \sigma_{normal} - p_{pore} \quad \text{(Equation 8.3)}$$

where σ_{normal} is the normal stress on the fracture and p_{pore} is the current pore pressure. The code increments the pore pressure during fluid injection and updates the normal stress accordingly.

The Mohr-Coulomb failure criterion determines whether a shear failure occurs on a fracture. The criterion states that shear failure occurs if the shear stress on the fracture exceeds the shear strength, which is defined as:

$$\tau_{failure} = c - \sigma_{effective}\tan(\phi) \quad \text{(Equation 8.4)}$$

where $\tau_{failure}$ is the shear stress required for failure, c is the cohesion on the fracture, $\sigma_{effective}$ is the effective normal stress, and ϕ is the friction angle on the fracture. In the code, the shear stress is compared to failure stress to determine whether a fracture fails:

$$Shear\ Failure\ if\ \tau \geq \tau_{failure} \qquad \text{(Equation 8.5)}$$

The code reads fracture data from an Excel file, including the start and end coordinates, cohesion, and friction angle of each fracture. It initializes the grid and defines the principal stresses, initial pressure, and other reservoir properties.

The code simulates fluid injection by incrementing the pore pressure in the injection well cell. For each fracture, it computes the normal and shear stresses using the rotated principal stresses and subtracts the pore pressure from the normal stress to get the effective stress.

The code applies the Mohr-Coulomb criterion to each fracture by comparing the shear stress on the fracture with the required shear stress for failure. If the shear stress exceeds the failure threshold, the fracture fails. The Matlab code is provided in Appendix C.

8.1.1 Results of Failure Model

The initial model simulation used fluid pressures similar to the injection pressure recorded during field testing, set at 10 l/s. However, it is essential to note that the injection flow rate and the pressure exerted in a well are complexly interdependent, and accurately predicting the pressure caused by a given flow rate is not always straightforward. Several factors contribute to this uncertainty. First, the heterogeneity of the reservoir can cause significant variations in permeability, porosity, and fluid characteristics throughout the formation, making it challenging to model the pressure response precisely. Permeability, for instance, is often not uniform and can vary on a local scale, meaning that injection flow rates will result in different pressure responses depending on the specific characteristics of the surrounding rock. Additionally, the behavior of fractures and faults within the reservoir can complicate pressure predictions, as they can create pathways of lower resistance, altering the flow dynamics. The effects of skin damage near the wellbore, changes in reservoir properties over time (such as compaction or clogging), and the influence of temperature and fluid viscosity further complicate the relationship between flow rate and pressure. Furthermore, while models based on Darcy's law and similar principles can provide estimates, they often rely on constant permeability or ideal fluid behaviour assumptions. In this model, the pressure exerted is increased step by step, and the failure is observed.

Geomechanical properties obtained from laboratory testing were incorporated into the model, and all identified fractures were allowed to fail due to the initial injection pressure. The failed fractures are given in Figure 8.1.

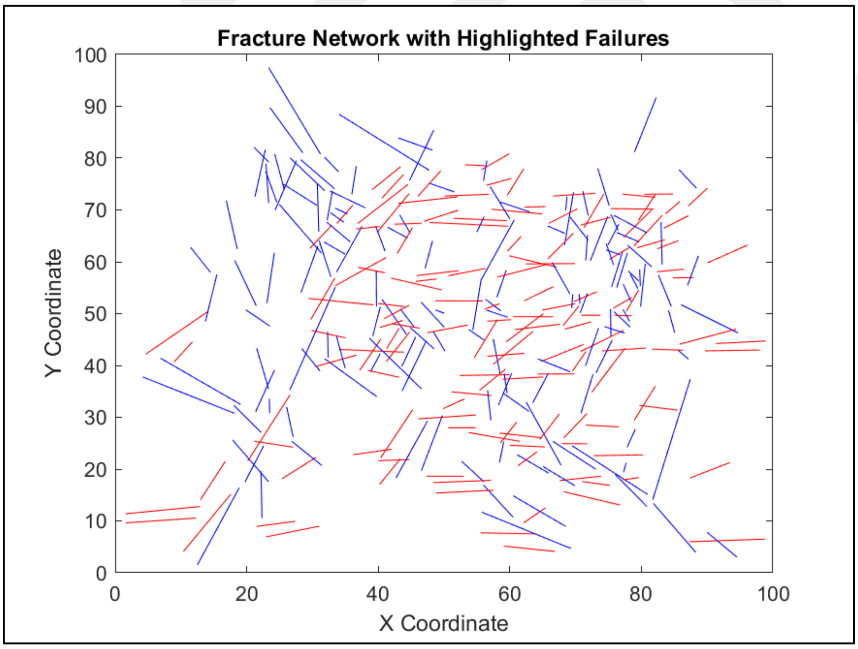

Figure 8.1. Failure at the initial injection rate.

A second model was run with progressively higher injection pressures. In this case, fracture failure was observed only when the water injection rate was increased five-folds, resulting in pressures that possibly exceeded the pore pressure. At these pressures, the fractures classified as paleo fractures that are unfavorably oriented compared to current principle stress directions also failed. The failed fractures with the increased injection pressure are given in Figure 8.2, noting that at these pressures, tensile failure is also expected to occur.

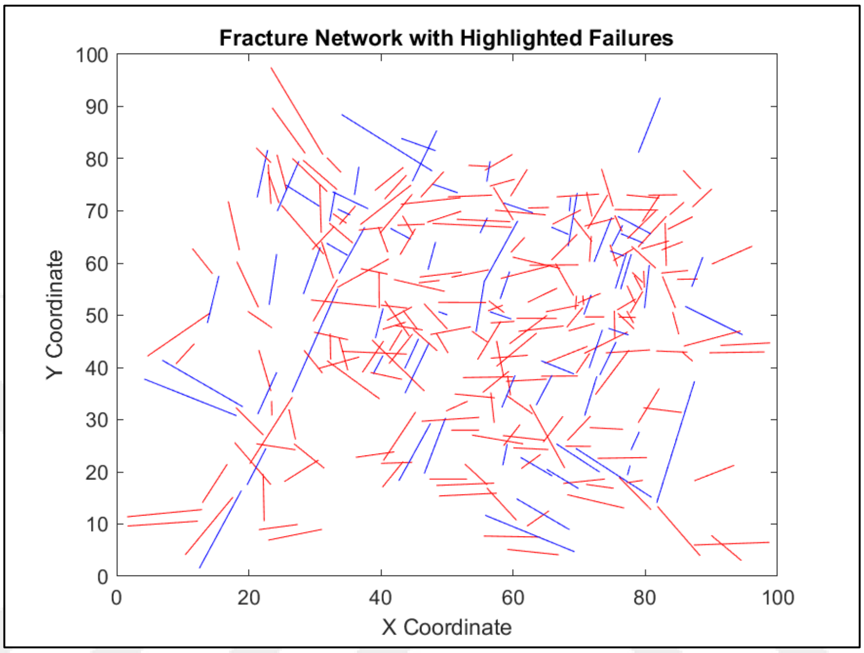

Figure 8.2. Failure at the fivefold increase in injection rate.

These results indicate that it is likely that the erratic behaviour observed in the pressure response of the well to the injection test can be caused by mechanical failure of the favorably oriented fractures. However, the degree to which an increase in permeability through mechanical failure can be achieved is limited to a degree. In order to achieve a greater increase in the permeability, much higher injection pressures should be applied. However, such high pressures can only be achieved by special equipment where it may not be possible to justify the economic feasibility of the application, and it also carries the risk of induced seismicity, particularly close to active fault zones. Different failure scenarios are assessed using the fluid model in Chapter 10. The model is run by increasing the pressure ten-folds, and several more fractures are failed; however, this output will not be used in the fluid model given that the exerted pressures cannot realistically be created at the field.

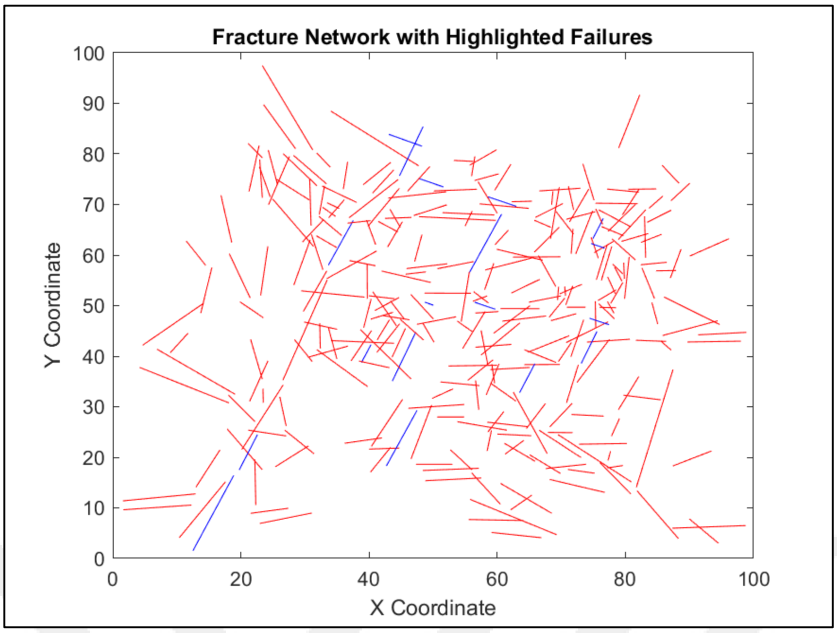

Figure 8.3. Failure at the ten-fold increase in injection rate.

8.2 Failure model and governing equations – Tensile

8.2.1 Hydraulic Fracturing

Hydraulic fracturing involves injecting water, sand, and chemicals under high pressure into a bedrock formation through a well. The intention is to create new fractures in the rock as well as increase the size, extent, and connectivity of existing fractures. Hydraulic fracturing is a well-stimulation technique to create improved permeability in underground geothermal reservoirs where increasing the connectivity of the reservoir would lead to increased production or injectivity in geothermal reservoirs.

In hydraulic fracturing, fluids are injected into the formation to cause failure. Two major failure modes can be experienced during fracture propagation (Figure 8.4).

- A tensile or opening mode (mode I) in which the displacements are perpendicular to the fracture plane

- Sliding shear mode where the displacements are parallel to the fracture plane (mode II)

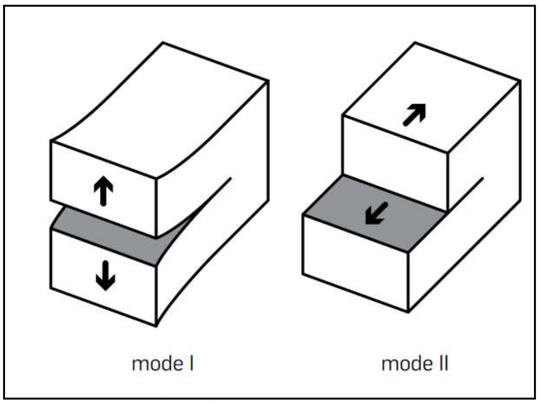

Figure 8.4. Opening mode I and shearing mode II failure

The combinations of these modes are also possible and usually referred to as mixed mode. Large-scale geological features analogous to mode I fracture propagation are joints. In contrast, faults, which exhibit some degree of displacement parallel to the fault plane, are classified as mode II or mixed-mode features. (Engelder, 1987).

In enhanced geothermal systems studies, induced slip on pre-existing fractures (Pure Shear Stimulation- Mode II) is assumed, whereas in the shale gas industry, stimulation is typically considered to be opening and propagation of new fractures (Pure Opening Mode - Mode I). However, many researchers have also studied combining these failures in EGS and Shale gas applications. Due to the frequent presence of natural joints, fractures and/or faults in Menderes Massif Marbles, both failure modes are expected to be possible for conventional reservoir applications.

The fracturing process requires an advanced understanding of formation in-situ stress conditions and stress behavior around the fracture as it generates and propagates to the formation of the excess pressure, causing a natural fracture to slip or open. The parameters that control the process can be expressed in two groups: parameters that can be controlled and site-specific parameters that cannot be controlled. Parameters that can be controlled are injection rate and fluid properties.

In contrast, the site-specific parameters are in-situ stresses, natural fracture/joint orientations and properties, and the geomechanical properties of the reservoir rock.

8.2.2 Modeling Approach

XFEM is a numerical method based on the generalized finite element method (GFEM) and the partition of unity method (PUM). PUM, in general, allows the incorporation of known features of the solution in the numerical approximation in the form of enrichment functions; for problems involving localized phenomena, such as fracture, enrichment functions are used locally to a subset of nodes to increase the efficiency of the method. XFEM is a powerful method for discontinuous problems in mechanics, such as crack growth. Due to its independence on the internal geometry and physical interfaces, meshing and re-meshing difficulties in discontinuous problems can be overcome. XFEM allows the simulation of the initiation and propagation of a crack along an arbitrary path without the requirement of remeshing. XFEM achieves this by locally enriching the FE approximation with local partitions of unity enrichment functions. The most common enrichment functions are jump enrichment and tip enrichment.

8.2.2.1 Enrichment

Jump enrichment functions represent the displacement jump along the crack surface, whereas tip enrichment functions represent the discontinuity at the crack tip. The standard finite element approximation is thus explicitly enriched by adding enrichment functions as follows.

However, an alternative approach appropriate for problems in which brittle crack propagation occurs, as in the case of this study, which is the near-tip asymptotic singularity (tip enrichment part) is not considered, and only the displacement jump across a cracked element is considered. Therefore, the crack has to propagate across an entire element simultaneously to avoid the need to model the stress singularity.

Phantom nodes are introduced into the model to represent the discontinuity of the cracked element when the fracture criterion is satisfied. The real node and the corresponding phantom node will separate when the equivalent strain energy release rate exceeds the critical strain energy release rate at the crack tip in an enriched element. The traction is initially carried as equal and opposite forces on the two surfaces of the cracked element. The traction is ramped down linearly over the separation between the two surfaces, with the dissipated strain energy equal to either the critical strain energy required to initiate the separation or the critical strain energy required to propagate the crack, depending on the specified Virtual Crack Closure Technique criterion. VCCT uses the principles of linear elastic fracture mechanics (LEFM) and, it uses the assumption that the strain energy released when a certain amount extends a crack is the same as the energy required to close the crack by the same amount.

8.2.2.2 Geometrical representation of crack surfaces

To allow the evaluation of the enrichment functions as well as the definition of the nodal sets involved in the enrichment approximation, some kind of geometrical representation of the cracks is necessary. Instead of explicitly representing the crack surfaces with linear or triangular segments that cause computational burden, an implicit representation of the crack surfaces with a level set method will be implemented.

Two level set functions must be defined, including the normal level set (signed distance to the crack surface) and tangent level set (signed distance from a surface normal to the crack surface and intersecting the crack surface at the crack tip). No explicit representation of the crack surface is needed because the nodal data entirely represent them. Two signed distance functions per node are generally required to describe a crack geometry. This method and an extended finite element method make it possible to model arbitrary crack growth without remeshing.

8.2.2.3 XFEM advantages, assumptions and application

The advantages of XFEM are as follows;

- Ease difficulties in solving problems with localized features that mesh refinement does not resolve efficiently.
- Allows simulation of initiation and propagation of a crack along an arbitrary path without the requirement of remeshing.
- Save computational costs significantly.
- Convenient to implement in commercial software and with parallel computing.
- The description for the discontinuous field is entirely independent of the mesh.
- Not only simulates cracks but also heterogeneous materials with voids and inclusions.

XFEM could only be applied to Linear Elastic Fracture Mechanics where the damage zone associated with the rock failure near the advancing fracture front is lumped into a single point under the assumption that the extent of the damage zone is small compared to structural dimensions.

ABAQUS software will be used for hydro-mechanical modeling because it can effectively apply the Extended Finite Elements method (XFEM).

XFEM is a great tool because it can effectively model strong discontinuities (HF, NF) and interfacial boundaries (the existence of discontinuous fields being the reservoir zone and the bonding formation layers).

As for the final model, where a hypothetical fracturing operation will be simulated, the fracture pattern determined from the field data will be introduced to the model. Introducing a complex fracture pattern would not cause a significant computational burden since XFEM allows the simulation of the initiation and propagation of a crack along an arbitrary path without the requirement of re-meshing.

Fracture propagation modeling in a complex, naturally fractured network is beyond the scope of this study. However, the development and initiation of a single fracture illustrates the orientation of tensile fractures and depicts the pressure response to fracture opening. This example provides insight into the behaviour of fractures under pressure and highlights the mechanics of fracture opening in response to stress conditions (Abaqus Documentation, 2023). The results of the model that serve are shown in Figures 8.5 through 8.7, including the generated stress field and the pore pressure distribution. As expected, fractures propagate in the direction of σ_1 and open in the direction of σ_3, and the resultant pressure curve can be seen in Figure 8.8. The pressure exhibits an initial peak followed by a dip, similar to the behaviour observed during the injection tests conducted at the site (Figure 5.8Figure 8.8). It is assumed that the initiation of fracture propagation causes the momentary pressure peak, while the subsequent dip is attributed to the fracture opening. After this, the pressure gradually stabilizes over time.

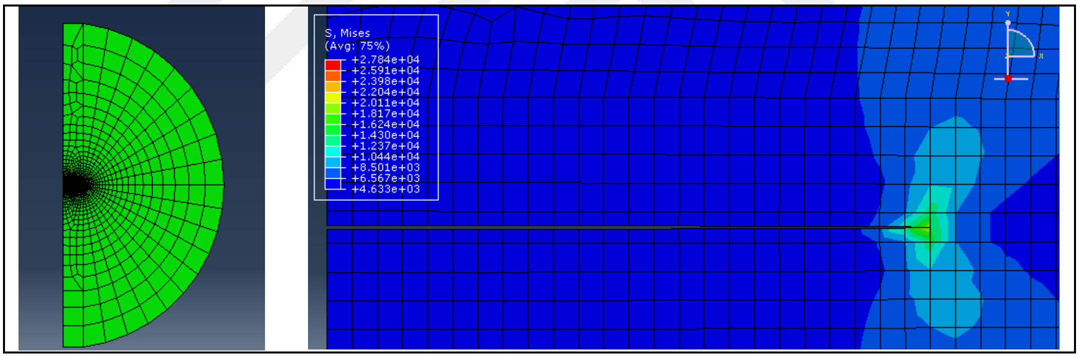

Figure 8.5. Model domain and the stress field at the end of the analysis

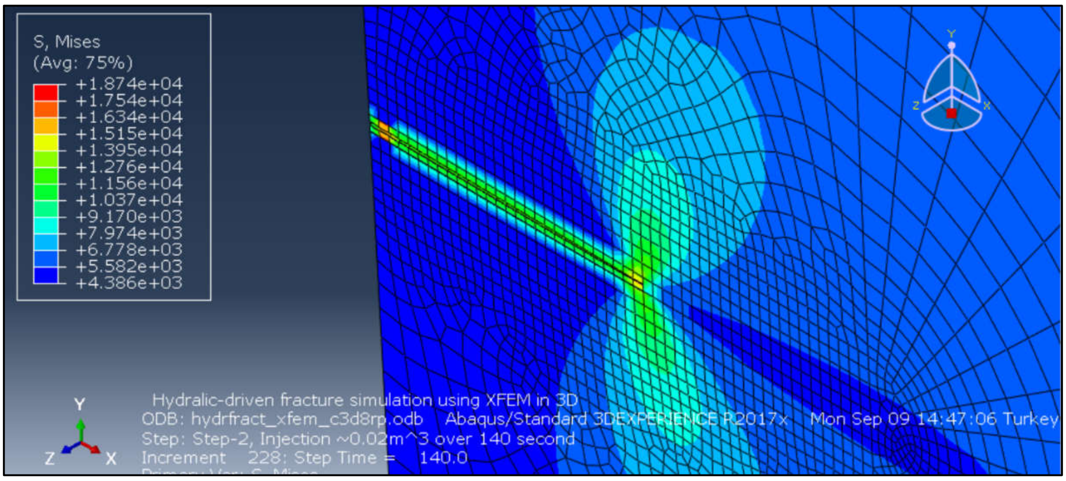

Figure 8.6. Stress field at the end of the analysis

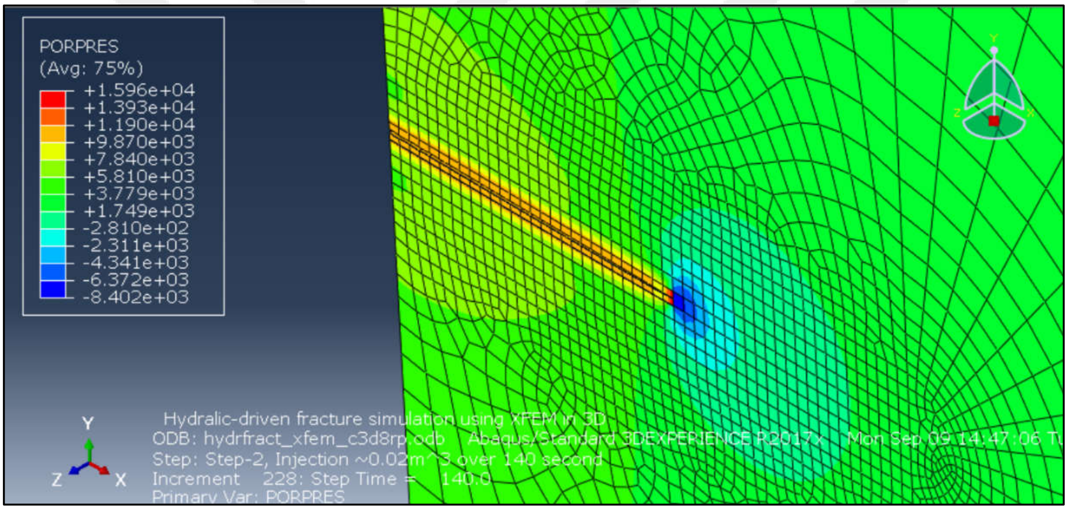

Figure 8.7. Pressure distribution at the end of the analysis

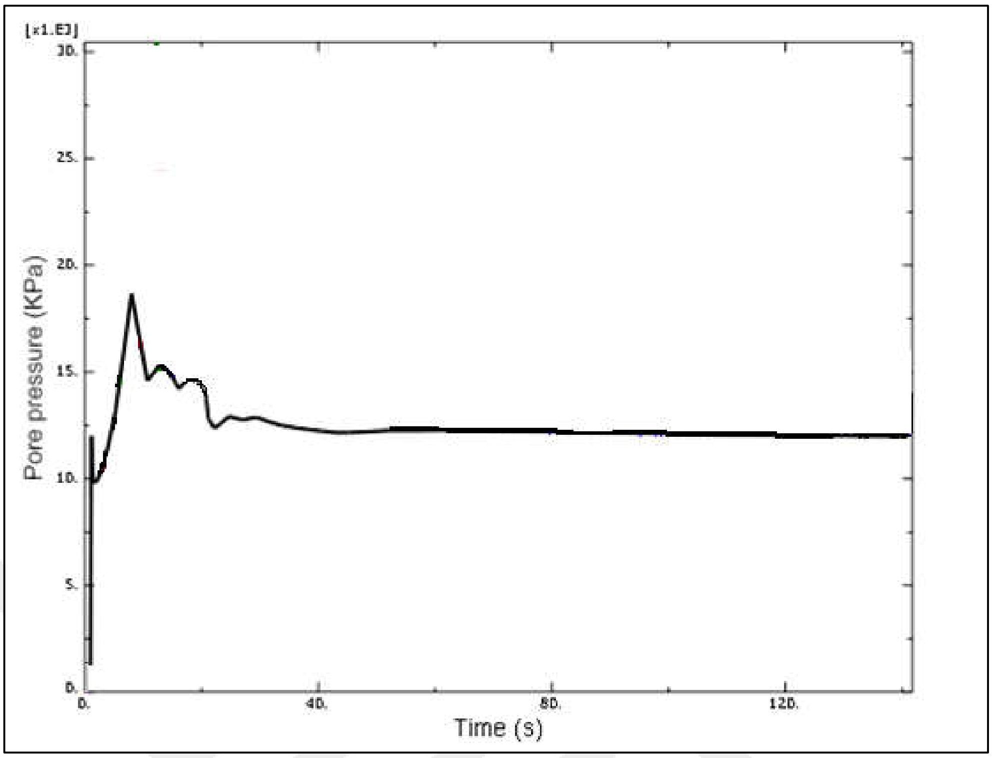

Figure 8.8. Pressure versus time curve

CHAPTER 9

FLUID MODEL

The modeling studies to simulate the fluid flow are presented in this chapter. The mathematical and modeling approaches are discussed.

9.1 Discrete Fracture Network Approach

Barenblatt and Zheltov (1960) and Barenblatt et al. (1960) first proposed the ‘double continuum’, or 'double-porosity' model. In this model, the fractured porous medium is represented by two interacting subsystems: a fracture network and porous blocks. The fluid exchange between these two continua is allowed. While Barenblatt and Zheltov (1960) proposed two interacting continua, the fracture network is separated into multiple continua. These subsystems, such as microfractures or larger fractures, may vary in orientation, hydraulic conductivity, and inter-connectedness.

Bear (1993) classified the problem into several categories: 'very near field', 'near field', and 'far-field’, which are related to the scale of the problem domain. The 'very near field' represents the area close to a source/sink and may involve a single fracture intersecting a well. If the domain of interest is slightly larger but still unsuitable for the continuum approach, a 'near field' model is used, which requires detailed information about each fracture. When fracture data is only available statistically, statistical models can be constructed to study the domain and its behaviour. Such large-scale domains are referred to as the 'far-field' and 'very far field' zones. In the scope of this thesis, since the fracture data is collected using scan-line and photogrammetric methods, a near-field approach is adopted.

Dual-continuum models, first introduced by Barenblatt et al. (1960) and later expanded by Warren and Root (1963), describe a flow medium with two types of porosity: matrix porosity and secondary porosity from processes like fracturing. In these models, unfractured rock contributes significantly to storage but minimally to permeability, while fractures offer high permeability but negligible storage. The porous medium and fractures are treated as two overlapping continua, with fluid mass transfer occurring at their interface. Review of different modeling approaches has been introduced by Berkowitz (2002), Dietrich et al. (2005), Hoteit and Firoozabadi (2008), Sahimi (2011), and Singhal and Gupta (2010). The fractured porous media systems can be classified into two general categories: discrete fracture-matrix (DFM) models and continuum fracture models. Many mathematical methods have been developed to simulate the flow in naturally fractured reservoirs. In these models, fractures can be represented implicitly or explicitly (Berre et al., 2019). In implicit methods, fractures are converted into equivalent porous media, following a continuum modeling approach. The dual-porosity model is an example of this modeling approach, which represents fractures as a secondary porous medium that interacts with the matrix via transfer functions (Tecklenburg et al., 2016). The fracture networks are often multiscale; representing them as a continuum that unfavorably affects their reliability.

Discrete fracture models are based on mathematical models representing the fractures explicitly. The fractures are represented closest to their natural geometric complexity in these models. Vo et al. (2023) compared DFM and dual-permeability models, highlighting several shortcomings of the dual-permeability method in accurately capturing viscous displacement.

The modeling in this thesis is based on the DFN approach, explicitly utilizing the Embedded Discrete Fracture Model (Wong, 2021). In EDFM, the fracture and matrix grids are generated independently. In EDFM, the need for grid conformity is relaxed by modeling fractures as line sources or sinks, allowing fractures to be represented separately from of the grid structure. By employing finite-volume discretization, EDFM remains compatible with conventional reservoir simulators. EDFM was first introduced by Lee et al. (2018) was further extended by Li and Lee (2008) to account for a network of connected fractures. Improvements were then made by Moinfar et al.

who made improvements to the use of inclined fractures. The EDFM approach has been used by many researchers over the years (i.e., Karvounis and Jenny, 2016; Shakiba et al., 2015).

EDFM offers two main advantages over other DFM methods: it allows the use of structured grids by eliminating the need for conforming grids, simplifying meshing and preprocessing, and it is compatible with conventional reservoir simulators due to its use of finite-volume discretization and two-point flux approximation (TPFA). However, EDFM is limited to conductive fractures, and continuity of pressure and saturation across fractures may cause errors when dealing with sealed fractures.

9.2 Fracture Permeability

To model the flow in fractures rather than using the more complex Navier–Stokes equation for conductive fractures, the cubic law can determine permeability:

$$k_f = \frac{a^3}{12 f_c}, \quad \text{(Equation 9.1)}$$

where k_f is the fracture permeability, a fracture aperture f_c' is the correction factor, which equals one (1.0) for laminar flow. The cubic law, validated by Witherspoon et al., 1980 shows that the volumetric flow rate is proportional to a^3, and while f_c' accounts for surface roughness, it is often assumed to be one (1.0) due to practical uncertainties.

9.3 Mathematical Formulation

In this section, the mathematical formulation of EDFM is presented as described by (Wong, 2021) based on the work of Lee et al. (2018), Li and Lee (2008), and Moinfar et al. (2013). EDFM treats fractures as sub-dimensional objects rather than as a continuum. Moreover, the transfer functions in EDFM do not assume a uniform geometry for matrix blocks, allowing for a more realistic representation of fracture flow.

In a fracture system, flow in the fractures is described by mass-conservation equations, with each fracture indexed by i. For fractures, the governing equation;

$$\frac{\partial(\emptyset^i \rho_\alpha S_\alpha^i)}{\partial t} + \nabla.\left(\vec{u}_\alpha^i\right) = \frac{\rho_\alpha}{a_i}\left[q_\alpha^i - q_\alpha^{i,0} - \sum_{j-1,j\neq i}^{N_f} q_\alpha^{i,j}\right], \Omega_i \subset \mathbb{R}^2 \qquad \text{(Equation 9.2)}$$

Similarly, flow in the matrix is modeled with a mass conservation equation.

$$\frac{\partial(\emptyset^0 \rho_\alpha S_\alpha^0)}{\partial t} + \nabla.\left(\rho_\alpha\, \vec{u}_\alpha^0\right) = \rho_\alpha\left[q_\alpha^0 - \sum_{i=1}^{N_f} q_\alpha^{0,i}\right], \Omega_0 \subset \mathbb{R}^3 \qquad \text{(Equation 9.3)}$$

For the fractures ϕ_i account for effects such as mineralization, the matrix (i = 0), the pore spaces that are open to flow is φ_0. The density of fluid phase α is ρ_α. The aperture of fracture i is a_i. The saturation of fluid phase α in medium i is S_α^{Si}. The transfer function $q_\alpha^{i,0}$ determines fluid flow from fracture i to the matrix, whereas $q_\alpha^{0,i}$ flows in the opposite direction. Similarly, $q_\alpha^{i,j}$, is the transfer function for flow from fracture i to fracture j. The source/sink terms in the matrix and fractures are q_α^0 and q_α^i respectively.

Darcy's law is applied to model fluid velocity in both the fractures and matrix;

$$\vec{u}_\alpha^i = -\frac{k_{r\alpha}^i}{\mu_\alpha}\mathbf{K}^i\nabla\left(p_\alpha^i - p_\alpha^i\, \vec{g}\right), \qquad \text{(Equation 9.4)}$$

Where $k_{r\alpha}^i$ and p_α^i refer to the relative permeability and pressure of fluid phase α in medium i, $\vec{u}_\alpha^i$, is the viscosity of fluid, $\mathbf{K}^i$ is the permeability, $\vec{g}$ is the gravitational acceleration.

EDFM, transfer functions are not defined continuously but within a finite-volume discretization framework. Fractures are discretized along with the matrix grid, with each fracture cell corresponding to a matrix cell. The flow between matrix and fracture cells is modeled using volumetric flow rates.

$$Q_\alpha^{m,f} = \int_{V_m} q_\alpha^{m,f}\, dV = T^{mf}\frac{k_{r\alpha}}{u_\alpha}\left(p_\alpha^m - p_\alpha^f\right), \qquad \text{(Equation 9.5)}$$

$$Q_\alpha^{f,m} = \int_{A_f} q_\alpha^{f,m}\, dA = T^{mf}\frac{k_{r\alpha}}{u_\alpha}\left(p_\alpha^f - p_\alpha^m\right), \qquad \text{(Equation 9.6)}$$

$Q_\alpha^{m,f}$ is the volumetric flow rate from the matrix to the fracture cell, whereas $Q_\alpha^{f,m}$ is the volumetric flow rate from the fracture cell to the matrix cell. $\frac{k_{r\alpha}}{u_\alpha}$ is the mobility term. The transmissibility unique to each matrix-fracture cell pair and is defined as

$$T^{mf} = \frac{k^{mf} A^{mf}}{\langle d \rangle^{mf}}, \qquad \text{(Equation 9.7)}$$

k^{mf} is the pore volume weighted harmonic average of fracture and matrix permeabilities, A^{mf} is matrix-fracture fluid exchange area and $\langle d \rangle^{mf}$ is the average normal distance between the points.

$$\langle d \rangle^{mf} = \frac{\int_{V_m} |(\vec{x} - \vec{x}_{ref}).\vec{n}_f| dV}{\int_{V_m} dV}, \qquad \text{(Equation 9.8)}$$

$\vec{x}_{ref}$ is any reference point on the fracture plane, $\vec{n}_f$ is the unit normal vector of the fracture plane.

Similarly, the exchange between intersecting fracture cells is modeled by volumetric flow rates,

$$Q_\alpha^{f1,f2} = \int_{A_{f1}} q_\alpha^{f1,f2} dA = T^{ff} \frac{k_{r\alpha}}{u_\alpha} (p_\alpha^{f1} - p_\alpha^{f2}), \qquad \text{(Equation 9.9)}$$

$$Q_\alpha^{f2,f1} = \int_{A_{f2}} q_\alpha^{f2,f1} dA = T^{ff} \frac{k_{r\alpha}}{u_\alpha} (p_\alpha^{f2} - p_\alpha^{f1}), \qquad \text{(Equation 9.10)}$$

T^{ff} is transmissibility which is 0 for nonintersecting fractures or else positive. The transmissibility between intersecting fractures calculated through half-transmissibilities

$$T_{1/2}^{fi} = \frac{k^{fi} \alpha^{fi} L_\cap^{f1,f2}}{d_\cap^{fi}}, \forall i \in \{1,2\} \qquad \text{(Equation 9.11)}$$

k is the permeability and α is the aperture of fracture cell, $L_\cap^{f1,f2}$ is the length of the intersection line between two cells $d_\cap^{fi}$ is the average normal distance from the centers of the subsegments to the intersection line.

In summary, the EDFM approach simplifies the modeling process by avoiding the need for grid conformity but assumes that fractures intersect in pairs. When multiple fractures intersect, transmissibility values can still be assigned, though the literature has not thoroughly explored this scenario. This thesis focuses on the case of two-fracture intersections.

In summary, the EDFM method involves three main steps:

1. Constructing a fractured grid based on the pre-existing matrix grid,
2. Establishing matrix–fracture connectivity using transmissibility values,
3. Connecting intersecting fracture cells using transmissibility between them.

For the application of EDFM, the Matlab Reservoir Simulation Tool (MRST) has been utilized (Lie and Moyner, 2021). The source code was slightly modified, considering the requirements of this study, and provided in Appendix D.

9.4 Results of the Fluid Flow Model

The fluid model was run for three different scenarios, the first being that all identified fractures can transfer fluids. This was representative of a best-case scenario where all fractures are activated, thus increasing the overall permeability of the reservoir. In the second scenario, only fractures that fail under low injection pressures close to the pressures that are usually exerted during field injection tests were allowed to transfer fluids. The final scenario was run where the injection rates were increased five-folds. The results of the simulations can be seen in Figure 9.1, Figure 9.2, and Figure 9.3, where the pressure values at a location near the well for each scenario are compared. It can be seen from the graph that, as expected, the decrease in pressure in response to water extraction was higher with scenario one, assuming all mapped fractures were active.

The fluid model was simulated under three distinct scenarios. The first scenario assumed that all identified fractures were fully activated and could transfer fluids. This represented a best-case scenario where every mapped fracture was assumed to contribute to increased reservoir permeability. In the second scenario, it was assumed that only fractures that failed under relatively low injection pressures, similar to those observed during field injection tests, were active. The third scenario modeled an increased injection rate of five times the base rate.

The results of the simulations are presented in Figure 9.1, Figure 9.2, and Figure 9.3, while Figure 9.4 compares the pressure response at a location near the well for each scenario. As shown, Scenario 1, where all fractures were assumed to be active, resulted in a greater decrease in pressure in response to water extraction. This outcome aligned with expectations, as the full activation of fractures maximized permeability enhancement within the model.

It should be noted that this model did not quantify the permeability increase from mechanical enhancement in absolute terms, as the fracture connectivity increase was not fully considered, and the model represented a 2D representation. A 3D model with fracture connectivity would likely have generated fluid conduits showing a more pronounced permeability enhancement. Further investigation with a 3D model could have provided better insights into the effects of fracture activation and connectivity on permeability dynamics, which is beyond the scope of this study.

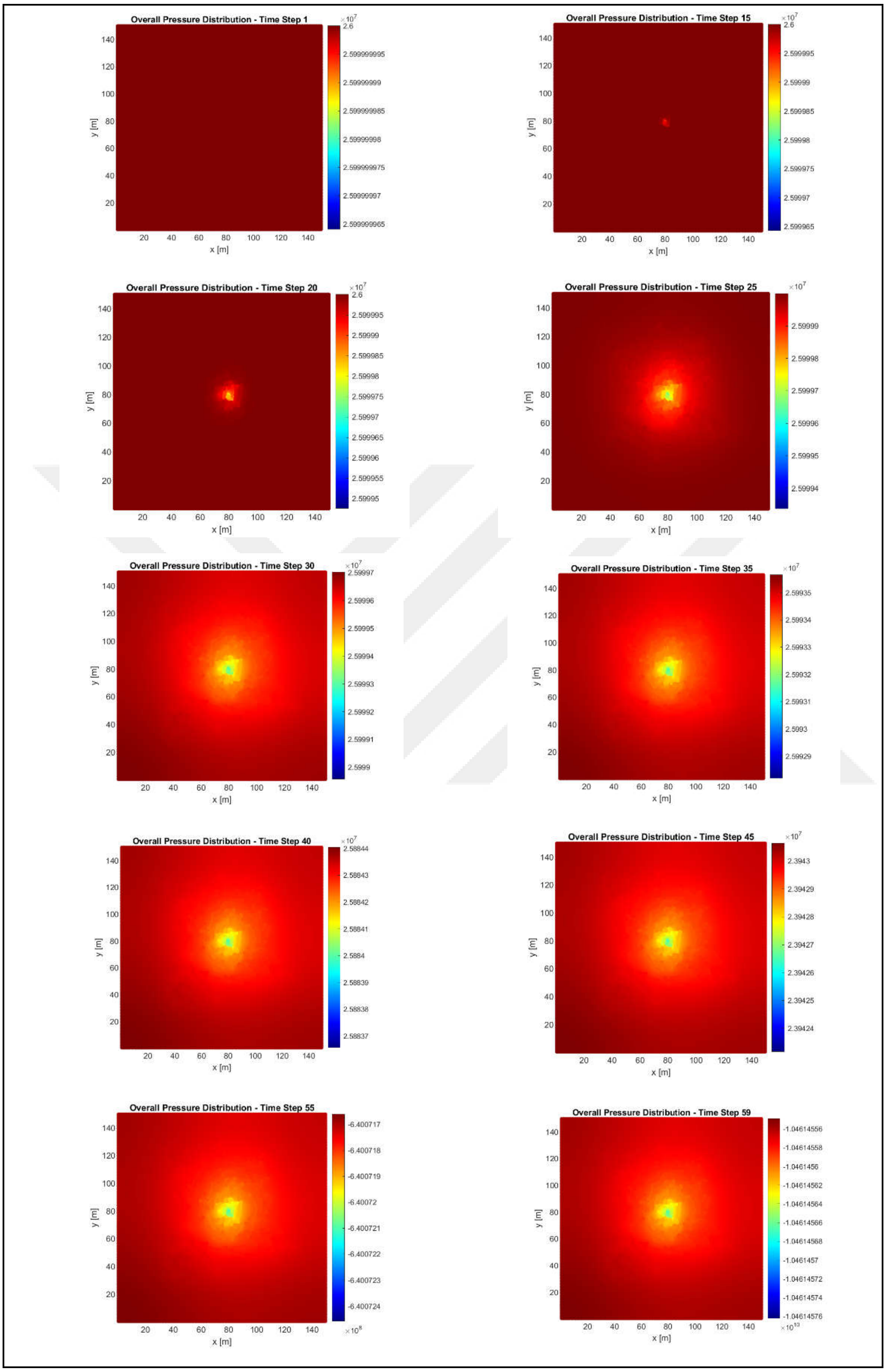

Figure 9.1. Scenario-1: Model in different time steps as per Matlab code.

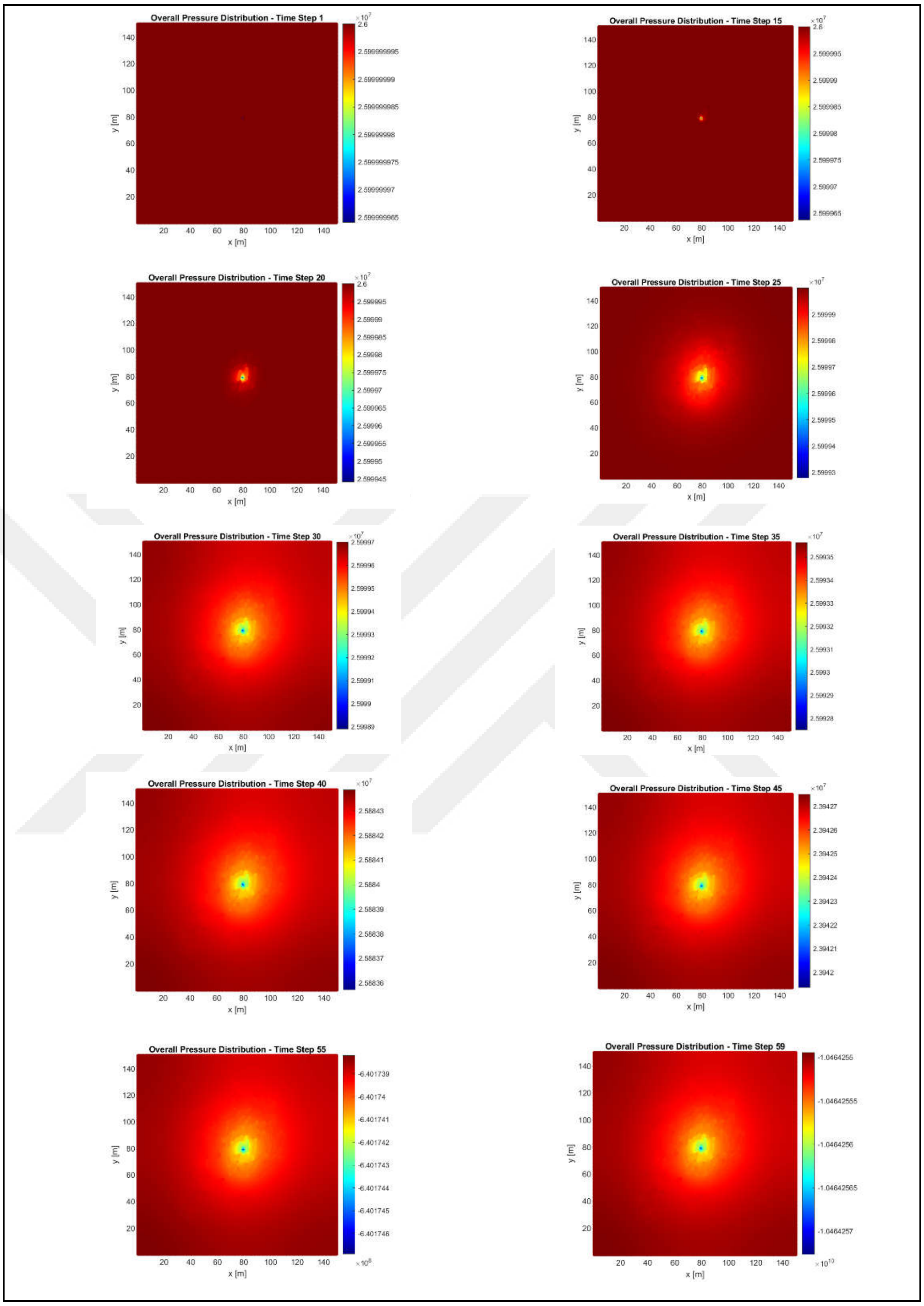

Figure 9.2. Scenario-2: Model in different time steps as per Matlab code.

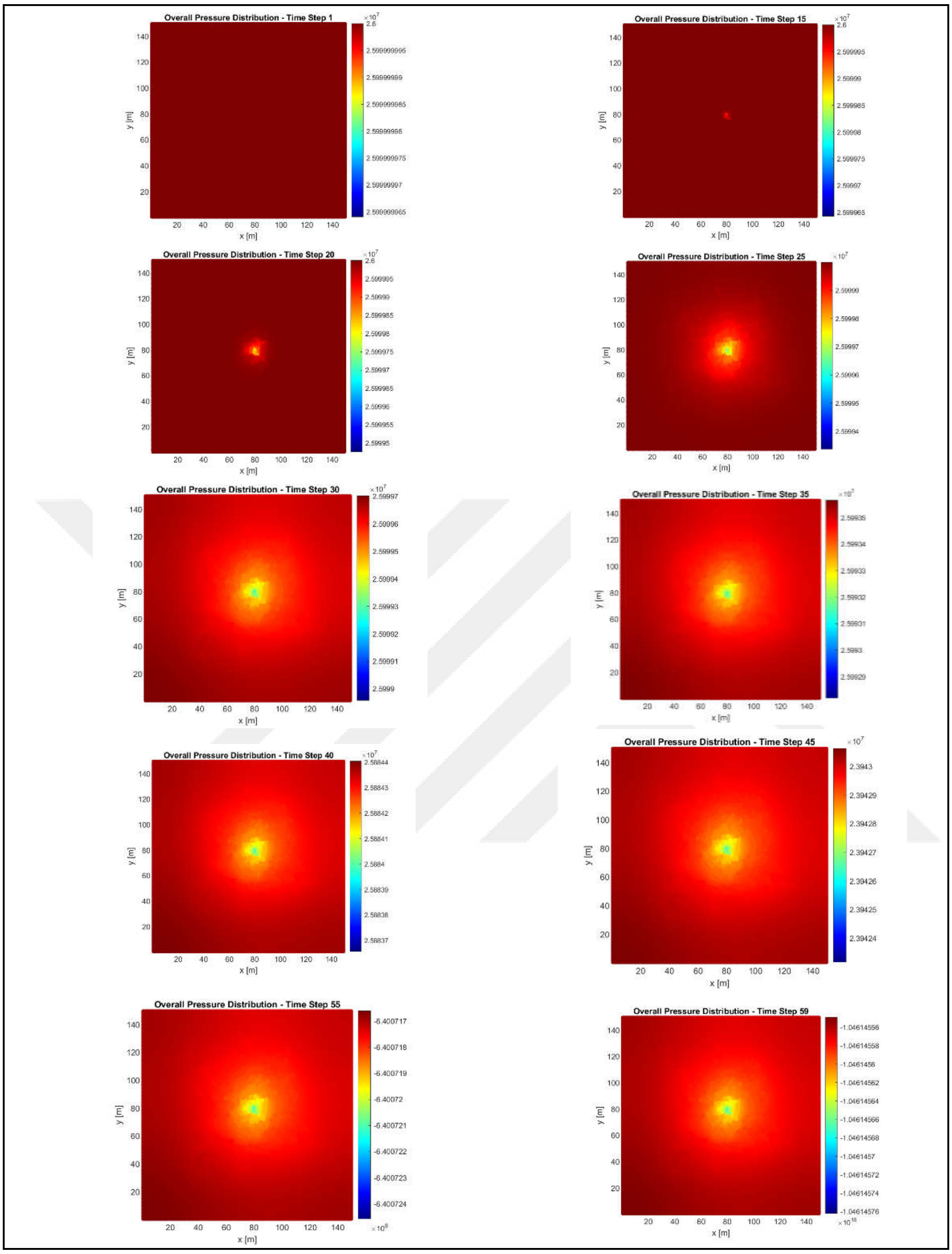

Figure 9.3. Scenario-3: Model in different time steps as per Matlab code.

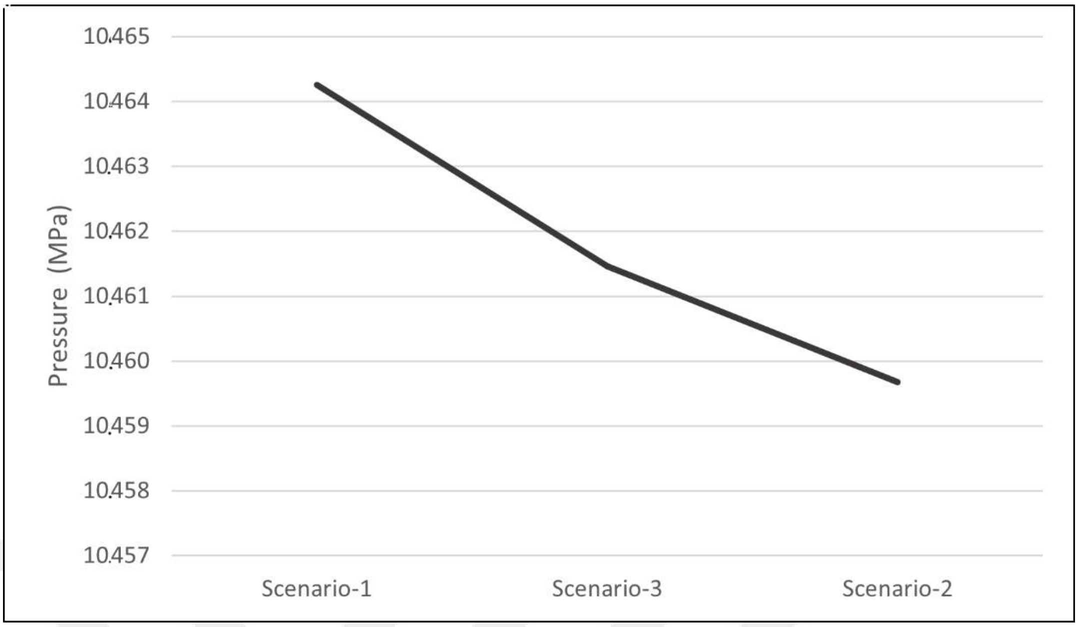

Figure 9.4. The pressure difference between different scenarios near the well.

CHAPTER 10

RESULTS AND DISCUSSION

The study area is located in the Kuyucak Geothermal Field within the Büyük Menderes Graben, which has an installed power capacity exceeding 1000 MW. This thesis focuses on optimizing development strategies for the Kuyucak Geothermal Field by integrating data collected during field studies with legacy and literature data. These efforts aim to improve the understanding of flow behaviour and the mechanical controls on fluid movement within fracture-controlled geothermal reservoirs.

The regional and structural geology reveals a well-defined geothermal system. The Neogene and alluvial units serve as the cap rock, while the highly fractured marble units of the Menderes Massif function as the reservoir rock. In the northern sections of the study area, where the Neogene cover is absent, fine-grained schists, such as mica and chlorite schists, act as the cap rock, effectively retaining heat within the system. The basement rocks, comprising Paleozoic units like chlorite-schist and graphite-schist, form the foundation of the system. This geological framework, supported by field observations, establishes the presence of a robust geothermal system.

Geophysical investigations, including MT measurements, were conducted to delineate the reservoir. Low-resistivity zones identified in the MT data were validated by drilling results, indicating that the reservoir lies around 3,000 meters in the southern sections of the study area and becomes shallower, at approximately 2,000 meters, towards the north. The KS-1 and KS-2 wells, drilled in the southern region, confirm the reservoir depth predicted by the 3D MT model. This geophysical and drilling data provided a key input for subsequent mechanical modeling, where stress magnitudes corresponding to these depths were applied.

To determine the principal stress magnitudes, mud loss data from drilling operations was analyzed. Complete circulation losses provided critical information on the least principal stress gradient, which was then incorporated into the mechanical model. Principal stress orientations were derived from fault kinematic measurements and focal mechanism solutions from the literature. These analyses revealed that the minimum principal stress (σ_3) was oriented in the NE-SW direction. The study also categorized fractures based on their inclination and strike orientations. Fractures inclined in the same direction as σ_3, with orientations ranging from 350°–30° and 170°–210° (or strike directions between 260°–300° and 80°–120°), were attributed to neotectonic activity, highlighting their role in controlling fluid flow.

Fracture characterization was carried out using scan-line surveys and photogrammetric measurements, enabling the construction of a DFN for the modelling studies. The fractures were classified as Neo and Paleo fractures based on their orientation relative to the current stress orientations. Thus, fracture network was a crucial input for understanding fluid flow mechanisms and mechanical responses within the reservoir.

Well test analyses further highlighted the dual-porosity nature of the reservoir, where both matrix and fracture permeability contributed to overall fluid flow. Injection tests revealed pressure anomalies, such as transient spikes that stabilized over time, indicating a mechanical response of the reservoir to injection. The behavior observed in the pressure-time curves of the injection tests revealed initial pressure spikes followed by a drop, which was expected due to the opening of fractures. A zone of low pressure was created as the fluid flows toward this zone, causing the pressure to drop. The initial pressure increase, prior to the drop, could not be fully explained in the scope of this thesis. This phenomenon was likely related to the complex interaction between fluid, fractures, and the reservoir matrix. It could have involved localized sealing of fractures (Zhu et al., 2022), far-field reactivation of natural fractures (Zhang et al., 2024) or other mechanical responses within the reservoir that require further investigation.

Localized sealing in fractured reservoirs can lead to pressure increases due to several mechanisms. When fractures are sealed or partially sealed, the permeability of the rock matrix decreases, restricting fluid flow and creating a bottleneck that causes pressure to rise in the surrounding areas. Fracture closure, caused by mineral deposition, compaction, or other processes, can reduce fracture connectivity, preventing fluid from moving freely and leading to pressure build-up. Additionally, sealing fractures could alter the stress distribution within the rock, causing higher effective stress around the sealed fractures and increased pressure. Lastly, the accumulation of pore pressure within sealed fractures could contribute to localized pressure spikes, especially if the surrounding rock remains permeable and is able to transmit fluid. These mechanisms could result in unexpected pressure fluctuations, as observed in injection tests, where localized sealing inhibits the anticipated fluid flow behavior.

In addition, far-field reactivation of natural fractures could contribute to pressure increases in certain reservoir conditions. This phenomenon could occur when changes in the stress field, typically caused by fluid injection or other external forces, trigger the reactivation of pre-existing fractures. The re-activation of these fractures could alter the permeability of the reservoir, leading to localized flow paths that could either enhance or restrict fluid movement. If the re-activated fractures are sealed or partially sealed, they can lead to increased pressure in the surrounding areas as fluid accumulates. Additionally, the re-activation of fractures could re-distribute the stress within the reservoir, causing a localized increase in pore pressure. In some cases, re-activation could also lead to the creation of new fractures or the enlargement of existing ones, further disrupting fluid flow and causing pressure fluctuations. Therefore, far-field re-activation of natural fractures could be a significant factor influencing pressure dynamics in the reservoir, potentially leading to unexpected pressure increases during fluid injection or extraction.

A more detailed model incorporating additional physical phenomena, such as fracture sealing, far-field fracture re-activation processes or complex pore pressure dynamics, would be needed to fully understand this unexplained behaviour.

The permeability near KS-1 was measured to be 1.49E-10 m², while KS-2 exhibited a lower permeability of 1.63E-11 m². Permeability values estimated around the KS-1 and KS-2 wells showed significant spatial variation which is believed to be representative of the heterogeneous structure of the geothermal system in Büyük Menderes Graben. Thus, the modelling studies while believed to be representative of the entire geothermal system in Büyük Menderes graben, also highlight the importance of site-specific studies to determine the exact production parameters and development strategies.

Laboratory testing on rock samples collected from the field provided key geomechanical parameters, including uniaxial and triaxial compressive strength, Poisson's ratio, cohesion, internal friction angle, and fracture toughness. However, it should be noted that since the samples were collected from the outcrops, they cannot be considered as fully representative of the reservoir formation at depth due to the significantly different pressure and thermal conditions. In order to attain more representative values samples from core logs should be used, when available. Also, the laboratory tests conducted utilizing thermally controlled test assemblies would improve the reliability of the test results (Zhang et al., 2010).

The geomechanical parameters obtained from the lab tests were essential for mechanical modelling, which simulated failure using the Mohr-Coulomb failure criterion under increasing fluid injection rates. The results demonstrated that favourably oriented fractures could fail under injection rates as low as 10 l/s while unfavourably oriented fractures may require pressures exceeding the least principal stress, where these pressures will also potentially lead to tensile failure.

To evaluate the impact of fracture activation on reservoir permeability, a fluid flow model was developed using the EDFM implemented in MRST. The model was run under three scenarios: (1) all fractures active, representing a best-case scenario with maximum permeability; (2) fractures active only under field-scale injection pressures; and (3) a scenario with increased injection rates. The simulations revealed that full fracture activation significantly enhances permeability, leading to the greatest pressure decrease near the well during production. These findings underscore the critical role of fracture activation in optimizing reservoir performance.

This integrated approach, combining geological, geophysical, and mechanical insights with fluid modelling, highlights the importance of incorporating field and legacy data to enhance the understanding of flow mechanisms in fracture-controlled reservoirs. The results provide a foundation for developing optimized strategies for geothermal reservoir management and for improving the productivity of fractured systems. In addition, the methodology followed in the scope of this thesis, is believed to be invaluable in providing input for Enhanced Geothermal Systems studies.

CHAPTER 11

CONCLUSIONS AND RECOMMENDATIONS FOR FUTURE STUDIES

In this thesis, extensive research has been conducted to understand the mechanical processes governing the behavior of the fracture-controlled geothermal reservoir in the Kuyucak Geothermal Field, located within the Büyük Menderes Graben. The study integrated various geological, geophysical, and geomechanical data to comprehensively understand the reservoir's characteristics and it’s response to stress conditions. The methodology employed in this thesis enabled the quantification of both intrinsic and extrinsic parameters of the reservoir, facilitating the prediction and understanding of the reservoir's behavior in the Kuyucak Geothermal Field, with potential for extension to other areas of the Büyük Menderes Graben.

Key tasks completed during the research included a detailed analysis of the fracture network and its implications on fluid flow dynamics, highlighting the importance of incorporating fractures into reservoir models for improved accuracy. The distinction between fluid movement in fracture-controlled systems and traditional porous media flow was a focal point, emphasizing how fractures create preferential pathways, thus contributing to more complex, heterogeneous flow behavior. The research further demonstrated how these processes can enhance permeability and ultimately impact reservoir performance through shear failure mechanism simulations.

The study successfully explained the heterogeneous flow behaviour in a fracture-controlled reservoir but could not fully address the physical phenomena driving the failure response during fracture activation. To explain this phenomenon, additional processes, such as localized fracture sealing, far-field activation of natural fractures, or other mechanical and thermal effects, need to be considered. Models incorporating these phenomena can provide insights into the process controlling the failure behaviour.

Additionally, a comprehensive assessment of the current stress regime, fault kinematics, and reservoir properties was conducted using a combination of geophysical investigations, well drilling, well test analyses, and scan-line surveys. These datasets provided critical inputs for the mechanical and fluid flow models developed in this study, allowing for a more accurate prediction of the reservoir's behavior under varying conditions. However, the rock samples collected from the outcrops in the field were not fully representative of the reservoir conditions at depth. Testing rock samples obtained from cored drillings could have better provided a more accurate representation of the reservoir's subsurface conditions.

The geologically constrained fracture network was delineated from the scan-line surveys and photogrammetry using a near-field approach. However, for future studies, a far-field or a nearly far-field approach could be considered by generating a statistical fracture network that incorporates geological constraints. This could enhance computational efficiency, particularly for larger or more complex three-dimensional models, and could accommodate additional heterogeneity, such as varying permeability or structural features.

Geomechanical tests on rock samples, coupled with well test analysis, provided insights into the mechanical properties and stress conditions influencing fluid flow. The results from injection tests, which showed irregular flow patterns, further suggested that mechanical factors were effective in controlling the fluid movement within the reservoir. The mechanical model results implied that injection rates that create pressures below the minimum principal stress could cause the activation of favorably oriented natural fractures. However, the activation of unfavorably oriented fractures occured at pressures that exceeded the pore pressure, thus exceeding the minimum principal stress corresponding to injection rates around 400 l/min. Hydraulic fracturing was expected to occur at this stage, causing tensile failure. The fluid model used an EDFM approach implemented with MRST. Three scenarios were simulated: (1) full fracture activation, representing optimal permeability conditions; (2) activation limited to fractures failing at low pressures; and (3) increased injection rates five times the base rate. Results show that full fracture activation yielded the greatest pressure reduction. Though the model's 2D framework limited precise quantification of permeability gains, it showed that the fractures could be activated through fluid injection in the reservoir through shear failure at manageable fluid pressures. While this study required further development to produce actual parameters for field application, it demonstrated the potential for reservoir permeability enhancement through mechanical fracture activation. The simulation results suggest that activating fractures under favourable pressure conditions could increase fluid flow, with the best-case scenario showing the greatest pressure reduction near the injection site. Although limitations arose from the 2D model and the absence of fracture connectivity effects, this approach illustrateed how mechanical failure could enhance reservoir permeability. Future work incorporating a 3D model with comprehensive fracture network connectivity could yield more accurate insights into fluid transport dynamics and reservoir behaviour under varied injection pressures.

REFERENCES

Abaqus Documentation. (n.d.). Abaqus documentation. Massachusetts Institute of Technology. Retrieved January 1, 2023, from https://abaqus-docs.mit.edu/

Akgün, H., Koçkar, M. K., Koç, A., Gök, E., Yal, G. P., & Cambazoğlu, S. (2023). Fracture network enhancement mechanism and parameter estimation via hydro-mechanical modelling through identification of geomechanical properties and principal stresses of marble units of Menderes Massif: Final report (TÜBİTAK-1001-119Y535 scientific research project, p. 166). Middle East Technical University, Turkey.

Alexandrowski, P. (1986). Graphical determination of principal directions for slickenside lineation populations: An attempt to modify Arthaud's method. Journal of Structural Geology, 7(1), 73–82.

Angelier, J. (1990). Inversion of field data in fault tectonics to obtain the regional stress—III. A new rapid direct inversion method by analytical means. Geophysical Journal International, 103(2), 363-376.

Angelier, J., Tarantola, A., Valette, B., & Manoussis, S. (1982). Inversion of field data in fault tectonics to obtain the regional stress; I. Single phase fault populations: A new method of computing the stress tensor. Geophysical Journal of the Royal Astronomical Society, 69(2), 607-621.

Armijo, R., Carey, E., & Cisternas, A. (1982). The inverse problem in microtectonics and the separation of tectonic phases. Tectonophysics, 82(1–2), 145–160.

Aydın, İ., Karat, H. İ., & Koçak, A. (2005). Curie-point depth map of Turkey. Geophysical Journal International, 162(2), 633–640.

Barenblatt, G. I., Zheltov, I. P., & Kochina, I. N. (1960). Basic concepts in the theory of seepage of homogeneous liquids in fissured rocks. Journal of Applied Mathematics and Mechanics, 24(5), 1286-1303.

Bear, J. (1993). Modeling flow and contaminant transport in fractured rocks. In J. Bear, C.-F. Tsang, & G. de Marsily (Eds.), Flow and contaminant transport in fractured rock. Academic Press.

Berkowitz, B. (2002). Characterizing flow and transport in fractured geological media: A review. Advances in Water Resources, 25(8–12), 861–884.

Berre, I., Doster, F., & Keilegavlen, E. (2019). Flow in fractured porous media: A review of conceptual models and discretization approaches. Transport in Porous Media, 130(1), 215–236.

Bilim, F., Akay, T., Aydemir, A., & Koşaroğlu, S. (2016). Curie point depth, heat flow, and radiogenic heat production deduced from the spectral analysis of the aeromagnetic data for geothermal investigation on the Menderes Massif and the Aegean Region, Western Turkey. Geothermics, 60, 44–57.

Blum, P., Mackay, R., & Riley, M. S. (2009). Stochastic simulations of regional-scale advective transport in fractured rock masses using block upscaled hydro-mechanical rock property data. Journal of Hydrology, 369(3–4), 318–325.

Blum, P., Mackay, R., Riley, M. S., & Knight, J. L. (2007). Hydraulische Modellierung und die Ermittlung des repräsentativen Elementarvolumens (REV) im Kluftgestein. Grundwasser, 12(1), 48–65.

Bott, M. H. P. (1959). The mechanics of oblique slip faulting. Geological Magazine, 96(2), 109–117.

Bour, O., Davy, P., Darcel, C., & Odling, N. (2002). A statistical scaling model for fracture network geometry, with validation on a multiscale mapping of a joint network (Hornelen Basin, Norway). Journal of Geophysical Research: Solid Earth, 107(B6), 1–15.

Bozkurt, E. (2000). Timing of extension on the Büyük Menderes Graben, western Turkey, and its tectonic implications. Geological Society, London, Special Publications, 173(1), 385–403.

Bozkurt, E. (2002). Discussion on the extensional folding in the Alaşehir (Gediz) Graben, western Turkey. Journal of the Geological Society, 159(1), 105–109.

Bozkurt, E. (2004). Granitoid rocks of the southern Menderes Massif (southwestern Turkey): Field evidence for Tertiary magmatism in an extensional shear zone. International Journal of Earth Sciences, 93(1), 52–71.

Bozkurt, E., & Park, R. G. (1994). Southern Menderes Massif: An incipient metamorphic core complex in western Anatolia, Turkey. Journal of the Geological Society, 151(1), 213–216.

Bozkurt, E., & Park, R. G. (1997). Microstructures of deformed grains in the augen gneisses of Southern Menderes Massif and their tectonic significance, western Turkey. Geologische Rundschau, 86(1), 101–119.

Bozkurt, E., & Park, R. G. (1999). The structure of the Palaeozoic schists in the southern Menderes Massif, western Turkey: A new approach to the origin of the main Menderes metamorphism and its relation to the Lycian Nappes. Geodinamica Acta, 12(1), 25–42.

Bozkurt, E., & Rojay, B. (2005). Episodic, two-stage Neogene extension and short-term intervening compression in western Anatolia: Field evidence from the Kiraz Basin and Bozdağ Horst. Geodinamica Acta, 18(4), 295–312.

Bozkurt, E., & Satır, M. (2000). The southern Menderes Massif (western Turkey): Geochronology and exhumation history. Geological Journal, 35(3–4), 285–296.

Bozkurt, E. (1996). Metamorphism in the Palaeozoic schists of the Southern Menderes Massif: Field, petrographic, textural and fabric data from Selimiye (Milas-Muğla) area. Turkish Journal of Earth Sciences, 5, 105–121.

Bozkurt, E., Park, R. G., & Winchester, J. A. (1993). Evidence challenging the core/cover interpretation of the southern sector of the Menderes Massif, western Turkey. Terra Nova, 5(5), 445–451.

Bozkurt, E., & Sözbilir, H. (2004). Tectonic evolution of the Gediz Graben: Field evidence for an episodic, two-stage extension in western Turkey. Geological Magazine, 141, 63–79.

Bozkurt, E., Winchester, J. A., & Park, R. G. (1995). Geochemistry and tectonic significance of augen gneisses from the southern Menderes Massif (west Turkey). Geological Magazine, 132(3), 287–301.

Çağlayan, A., Öztürk, E., Öztürk, Z., Sav, H., & Akat, U. (1980). Menderes Masifi güneyine ait bulgular ve yapısal yorum. Jeoloji Mühendisliği Dergisi, 4(1), 9–18.

Candan, O. (1995). Menderes Masifi'ndeki kalıntı granulit fasiyesi metamorfizması. Turkish Journal of Earth Sciences, 4, 35–55.

Carey, E., & Brunier, B. (1974). Analyse théorique et numérique d'un modéle mécanique élémentaire appliqué à l'étude d'une population de failles. C. R. Acad. Sci., Paris, Ser. D, 279(8917894), 51–65.

Chen, Z. X. (1989). Transient flow of slightly compressible fluids through double-porosity, double-permeability systems—a state-of-the-art review. Transport in Porous Media, 4, 147–184.

Çiftçi, G., Pamukçu, O., Çoruh, C., Çopur, S., & Sözbilir, H. (2011). Shallow and deep structure of a supradetachment basin based on geological, conventional deep seismic reflection sections and gravity data in the Büyük Menderes Graben, western Anatolia. Surveys in Geophysics, 32(3), 271–290. https://doi.org/10.1007/s10712-010-9109-8

Deb, R., & Jenny, P. (2017). Finite volume–based modeling of flow-induced shear failure along fracture manifolds. International Journal for Numerical and Analytical Methods in Geomechanics, 41(10), 1205–1223.

Delvaux, D., & Sperner, B. (2003). New aspects of tectonic stress inversion with reference to the TENSOR program. Geological Society, London, Special Publications, 212(1), 75–100.

Dershowitz, W. S., & Einstein, H. H. (1988). Characterizing rock joint geometry with joint system models. Rock Mechanics and Rock Engineering, 21(1), 21–51.

Dewey, J. F. (1988). Extensional collapse of orogens. Tectonics, 7(6), 1123–1139.

Dewey, J. F., & Şengör, A. M. C. (1979). Aegean and surrounding regions: Complex multiplate and continuum tectonics in a convergent zone. GSA Bulletin, 90(1), 84–92.

Dewey, J. F., Pitman, W. C., Ryan, W. B., & Bonnin, J. (1973). Plate tectonics and the evolution of the Alpine system. Geological Society of America Bulletin, 84(10), 3137–3156.

Dietrich, P., Helmig, R., Sauter, M., Hötzl, H., Köngeter, J., & Teutsch, G. (2005). Flow and transport in fractured porous media. Springer.

Dolmaz, M. N., Ustaömer, T., Hisarli, Z. M., & Orbay, N. (2005). Curie point depth variations to infer thermal structure of the crust at the African-Eurasian convergence zone, SW Turkey. Earth, Planets and Space, 57(5), 373–383.

Eaton, B. A. (1972). Graphical method predicts geopressure worldwide. World Oil, 182, 51–56.

Engelder, T. (1987). Joints and shear fractures in rocks. In B. K. Atkinson (Ed.), Fracture mechanics of rock (pp. 27–69). Academic Press.

Etchecopar, A., Vasseur, G., & Daignières, M. (1981). An inverse problem in microtectonics for the determination of stress tensors from fault striation analysis. Journal of Structural Geology, 3(1), 51–65.

Faulds, J. E., Bouchot, V., Moeck, I., & Oğuz, K. (2009). Structural controls of geothermal systems in western Turkey: A preliminary report. Geothermal Resources Council Transactions, 33, 375–383.

Gessner, K., Piazolo, S., Güngör, T., Ring, U., Kröner, A., & Passchier, C. W. (2001). Tectonic significance of the deformation patterns in granitoid rocks of the Menderes nappes, Anatolide belt, southwest Turkey. International Journal of Earth Sciences, 89(4), 766–780.

Ghosh, K., & Mitra, S. (2009). Two-dimensional simulation of controls of fracture parameters on fracture connectivity. AAPG Bulletin, 93(11), 1517–1533.

Govers, R., & Fichtner, A. (2016). Signature of slab fragmentation beneath Anatolia from full-waveform tomography. Earth and Planetary Science Letters, 450, 10–19.

Guerriero, V., Vitale, S., Ciarcia, S., & Mazzoli, S. (2011). Improved statistical multi-scale analysis of fractured reservoir analogues. Tectonophysics, 504(1–4), 14–24.

Gürer, Ö. F., Sarıca-Filoreau, N., Özburan, M., Sangu, E., & Doğan, B. (2009). Progressive development of the Büyük Menderes Graben based on new data, western Turkey. Geological Magazine, 146(5), 652–673. https://doi.org/10.1017/S0016756809006359

Hetzel, R., & Reischmann, T. (1996). Intrusion age of Pan-African augen gneisses in the southern Menderes massif and the age of cooling after Alpine ductile extensional deformation. Geological Magazine, 133, 565–572.

Hoteit, H., & Firoozabadi, A. (2008). Numerical modeling of two-phase flow in heterogeneous permeable media with different capillary pressures. Advances in Water Resources, 31(1), 56–73.

ISRM. (1978). Suggested methods for quantitative description of discontinuities in rock masses. International Society for Rock Mechanics and Rock Engineering.

ISRM. (2016). The ISRM suggested methods for rock characterization, testing and monitoring: 2007–2014. Springer.

ISRM. (2017). Suggested method for laboratory acoustic emission monitoring. International Society for Rock Mechanics and Rock Engineering.

ISRM. (2019). Suggested method: Determining deformation and failure characteristics of rocks subjected to true triaxial compression. International Society for Rock Mechanics and Rock Engineering.

Jackson, J. A., & McKenzie, D. P. (1988). The relationship between plate motions and seismic moment tensors, and the rates of active deformation in the Mediterranean and Middle East. Geophysical Journal International, 93(1), 45–73.

Jackson, M. D., Hampson, G. J., & Sech, R. P. (2009). Three-dimensional modeling of a shoreface-shelf parasequence reservoir analog: Part 2. Geologic controls on fluid flow and hydrocarbon recovery. AAPG Bulletin, 93(9), 1183–1208.

Jing, L., & Stephansson, O. (2007). Fundamentals of discrete element methods for rock engineering: Theory and applications. Elsevier.

Jolivet, L., Faccenna, C., & Piromallo, C. (2003). From mantle to crust: Stretching the Mediterranean. Earth and Planetary Science Letters, 210(1–2), 1–17.

Jolivet, L., et al. (2013). Aegean tectonics: Strain localization, slab tearing and trench retreat. Tectonophysics, 597–598, 1–33.

Karamanderesi, İ. H. (2013). Characteristics of geothermal reservoirs in Turkey. IGA Academy Report, 102.

Karvounis, D., & Jenny, P. (2016). Adaptive hierarchical fracture model for enhanced geothermal systems. Multiscale Modeling & Simulation, 14(1), 207–231.

Kaya, A. (2015). The effects of extensional structures on the heat transport mechanism: An example from the Ortakçı geothermal field (Büyük Menderes Graben, SW Turkey). Journal of African Earth Sciences, 108, 1–12.

Koçyiğit, A. (2005). The Denizli graben-horst system and the eastern limit of western Anatolian continental extension: Basin fill, structure, deformational mode, throw amount, and episodic evolutionary history, SW Turkey. Geodinamica Acta, 18(3–4), 199–226.

Koçyiğit, A. (2015). An overview of the main stratigraphic and structural features of a geothermal area: The case of the Nazilli-Buharkent section of the Büyük Menderes Graben, SW Turkey. Geodinamica Acta, 27(2–3), 85–109.

Koçyiğit, A., & Özacar, A. A. (2003). Extensional neotectonic regime through the NE edge of the Outer Isparta Angle, SW Turkey: New field and seismic data. Turkish Journal of Earth Sciences, 12, 67–90.

Koçyiğit, A., Yusufoğlu, H., & Bozkurt, E. (1999). Evidence from the Gediz Graben for episodic two-stage extension in western Turkey. Journal of the Geological Society, London, 156(4), 605–616.

Konak, N., Akdeniz, N., & Öztürk, E. M. (1987). Geology of the south of Menderes Massif. In IGCP Project 5: Guidebook field excursion western Anatolia, Turkey (pp. 42–53). Mineral Research and Exploration Institute of Turkey.

Krantz, R. W. (1988). Multiple fault sets and three-dimensional strain: Theory and application. Journal of Structural Geology, 10, 225–237.

Kresse, O., Weng, X., Gu, H., & Wu, R. (2013). Numerical modeling of hydraulic fracture interaction in complex naturally fractured formations. Rock Mechanics and Rock Engineering, 46(3), 555–568. https://doi.org/10.1007/s00603-012-0270-y

Laubach, S. E. (2003). Practical approaches to identifying sealed and open fractures. AAPG Bulletin, 87(4), 561–579.

Le Pichon, X., & Angelier, J. (1979). The Hellenic Arc and trench system: A key to the neotectonic evolution of the Eastern Mediterranean area. Tectonophysics, 60(1–2), 1–42.

Le Pichon, X., & Angelier, J. (1981). The Aegean Sea. Philosophical Transactions of the Royal Society of London. Series A, Mathematical and Physical Sciences, 300(1454), 357–372.

Lee, H. P., Olson, J. E., & Schultz, R. A. (2018). Interaction analysis of propagating opening mode fractures with veins using the discrete element method. International Journal of Rock Mechanics and Mining Sciences, 103, 275–288.

Li, L., & Lee, S. H. (2008). Efficient field-scale simulation of black oil in a naturally fractured reservoir through discrete fracture networks and homogenized media. SPE Reservoir Evaluation & Engineering, 11(4), 750–758.

Lie, K.-A., & Møyner, O. (Eds.). (2021). Advanced modelling with the MATLAB Reservoir Simulation Toolbox. Cambridge University Press.

Long, J. C., Remer, J. S., Wilson, C. R., & Witherspoon, P. A. (1982). Porous media equivalents for networks of discontinuous fractures. Water Resources Research, 18(3), 645–658.

Loos, S., & Reischmann, T. (1999). The evolution of the southern Menderes Massif in SW Turkey as revealed by zircon dating. Journal of the Geological Society, 156(5), 1021–1030.

Mackie, R. L., & Madden, T. R. (1993). Three-dimensional magnetotelluric inversion using conjugate gradients. Geophysical Journal International, 115(1), 215–227.

Mauldon, M., Dunne, W. M., & Rohrbaugh, M. B. Jr. (2001). Circular scanlines and circular windows: New tools for characterizing the geometry of fracture traces. Journal of Structural Geology, 23(2–3), 247–258.

McClure, M., & Horne, R. (2013). Conditions required for shear stimulation in EGS. In Proceedings of the European Geothermal Conference, Pisa, Italy.

McKenzie, D. P. (1970). Plate tectonics of the Mediterranean region. Nature, 226(5242), 239–243.

McKenzie, D. P. (1972). Active tectonics of the Mediterranean region. Geophysical Journal International, 30(2), 109–185.

McKenzie, D. P. (1978). Active tectonics of the Alpine-Himalayan Belt: The Aegean Sea and surrounding regions. Geophysical Journal International, 55(1), 217–254.

McQuillan, H. (1974). Fracture patterns on Kuh-e Asmari anticline, Southwest Iran. AAPG Bulletin, 58(2), 236–246.

Meijer, P. T., & Wortel, M. J. R. (1997). Present-day dynamics of the Aegean region: A model analysis of the horizontal pattern of stress and deformation. Journal of Geophysical Research: Solid Earth, 102(B6), 11991–12000.

Mi, L., Jiang, H., Tang, L., Liu, C., Li, J., Wang, Y., Cao, Y., & Killough, J. (2016). A utility discrete fracture network model for field-scale simulation of naturally fractured shale reservoirs. In SPE Argentina Exploration and Production of Unconventional Resources Symposium, Buenos Aires, Argentina, June 2016.

Mobasher, K., & Babaie, H. A. (2008). Kinematic significance of fold- and fault-related fracture systems in the Zagros Mountains, southern Iran. Tectonophysics, 451, 156–169.

Moinfar, A., Varavei, A., Sepehrnoori, K., & Johns, R. T. (2013). Development of an efficient embedded discrete fracture model for 3D compositional reservoir simulation in fractured reservoirs. SPE Journal, 19(2), 289–303.

Moores, E. M., Robinson, P. T., Malpas, J., & Xenophonotos, C. (1984). Model for the origin of the Troodos massif, Cyprus, and other Mideast ophiolites. Geology, 12(8), 500–503.

National Research Council, Commission on Geosciences, Environment, and Resources, Board on Earth Sciences and Resources, U.S. National Committee for Rock Mechanics, & Panel on Conceptual Models of Flow and Transport in the Fractured Vadose Zone. (1996). Conceptual models of flow and transport in the fractured vadose zone. National Academies Press.

Pahl, P. J. (1981). Estimating the mean length of discontinuity traces. International Journal of Rock Mechanics and Mining Sciences & Geomechanics Abstracts, 18, 221–228.

Philippon, M., Brun, J.-P., Gueydan, F., & Sokoutis, D. (2014). The interaction between Aegean back-arc extension and Anatolia escape since Middle Miocene. Tectonophysics, 631, 176–188.

Priest, S. D. (1993). Discontinuity analysis for rock engineering. Chapman & Hall.

Priest, S. D., & Hudson, J. A. (1981). Estimation of discontinuity spacing and trace length using scanline surveys. International Journal of Rock Mechanics and Mining Sciences & Geomechanics Abstracts, 18(3), 183–197.

Priest, S. D., & Hudson, J. A. (1976). Discontinuity spacings in rock. International Journal of Rock Mechanics and Mining Sciences, 13, 135–148.

Purvis, M., & Robertson, A. (2005). Sedimentation of the Neogene–Recent Alaşehir (Gediz) continental graben system used to test alternative tectonic models for western (Aegean) Turkey. Sedimentary Geology, 173(1–4), 373–408.

Rimmelé, G., Oberhänsli, R., Goffé, B., Jolivet, L., Candan, O., & Çetinkaplan, M. (2003). First evidence of high-pressure metamorphism in the “Cover Series” of the southern Menderes Massif. Tectonic and metamorphic implications for the evolution of SW Turkey. Lithos, 71(1), 19–46.

Rohrbaugh Jr, M. B., Dunne, W. M., & Mauldon, M. (2002). Estimating fracture trace intensity, density, and mean length using circular scan lines and windows. AAPG Bulletin, 86(12), 2089–2104.

Royden, L. H. (1993). Evolution of retreating subduction boundaries formed during continental collision. Tectonics, 12(3), 629–638.

Sahimi, M. (2011). Flow and transport in porous media and fractured rock: From classical methods to modern approaches. John Wiley & Sons.

Satir, M., & Friedrichsen, H. (1986). The origin and evolution of the Menderes Massif, W-Turkey: A rubidium/strontium and oxygen isotope study. Geologische Rundschau, 75(3), 703–714. https://doi.org/10.1007/BF01820619

Şengör, A. C., & Yilmaz, Y. (1981). Tethyan evolution of Turkey: A plate tectonic approach. Tectonophysics, 75(3–4), 181–241. https://doi.org/10.1016/0040-1951(81)90275-8

Şengör, A. M. C. (1979). The North Anatolian transform fault: Its age, offset and tectonic significance. Journal of the Geological Society, 136(3), 269–282. https://doi.org/10.1144/gsjgs.136.3.0269

Şengör, A. M. C., & Kidd, W. S. F. (1979). Post-collisional tectonics of the Turkish-Iranian Plateau and a comparison with Tibet. Tectonophysics, 55(3–4), 361–376. https://doi.org/10.1016/0040-1951(79)90150-9

Şengör, A. M. C., Satir, M., & Akkök, R. (1984). Timing of tectonic events in the Menderes Massif, western Turkey: Implications for tectonic evolution and evidence for Pan-African basement in Turkey. Tectonics, 3(7), 693–707. https://doi.org/10.1029/TC003i007p00693

Şengör, A. M. C., Yılmaz, Y., & Sungurlu, O. (1984). Tectonics of the Mediterranean Cimmerides: Nature and evolution of the western termination of Palaeo-Tethys. Geological Society, London, Special Publications, 17(1), 77–112. https://doi.org/10.1144/GSL.SP.1984.017.01.05

Sesetty, V., & Ghassemi, A. (2015). Modeling and analysis of sequential and simultaneous hydraulic fracturing in single and multi-lateral horizontal wells. International Journal of Petroleum Science and Engineering, 132, 65–76. https://doi.org/10.1016/j.petrol.2015.01.009

Shakiba, M., & Sepehrnoori, K. (2015). Using embedded discrete fracture model (EDFM) and microseismic monitoring data to characterize the complex hydraulic fracture networks. SPE Annual Technical Conference and Exhibition. Houston, TX: Society of Petroleum Engineers. https://doi.org/10.2118/175148-MS

Singhal, B. B. S., & Gupta, R. P. (2010). Applied hydrogeology of fractured rocks. Springer Science & Business Media. https://doi.org/10.1007/978-90-481-8799-7

Taghipour, M., Ghafoori, M., Lashkaripour, G. R., & Molaghab, A. (2019). Estimation of the current stress field and fault reactivation analysis in the Asmari reservoir, SW Iran. Petroleum Science, 16(4), 811–825. https://doi.org/10.1007/s12182-019-0325-8

Tecklenburg, J., Neuweiler, I., Carrera, J., & Dentz, M. (2016). Multi-rate mass transfer modeling of two-phase flow in highly heterogeneous fractured and porous media. Advances in Water Resources, 91, 63–77. https://doi.org/10.1016/j.advwatres.2016.01.006

Ulusay, R. (Ed.). (2014). The ISRM Suggested Methods for Rock Characterization, Testing and Monitoring: 2007–2014. Springer. https://doi.org/10.1007/978-3-319-07713-0

U.S. Bureau of Reclamation (USBR). (1991). Engineering geology field manual. Washington, DC: U.S. Department of the Interior, Bureau of Reclamation Press.

Vo, H., Flodin, E., Hui, R., Earnest, E., & Trindade, M. (2023, May). Insights on gas and water coning/channeling processes in a fractured carbonate reservoir from embedded discrete fracture modeling. SPE Western Regional Meeting. Anchorage, AK: Society of Petroleum Engineers. https://doi.org/10.2118/209752-MS

Wallace, R. E. (1951). Geometry of shearing stress and relation to faulting. The Journal of Geology, 59(2), 118–130. https://doi.org/10.1086/625831

Warren, J. E., & Root, P. J. (1963). The behavior of naturally fractured reservoirs. Society of Petroleum Engineers Journal, 3(3), 245–255. https://doi.org/10.2118/426-PA

Witherspoon, P. A., Wang, J. S. Y., Iwai, K., & Gale, J. E. (1980). Validity of cubic law for fluid flow in a deformable rock fracture. Water Resources Research, 16(6), 1016–1024. https://doi.org/10.1029/WR016i006p01016

Wong, D. L. Y., Doster, F., & Geiger, S. (2021). Embedded discrete fracture models. In Advanced Modeling with the MATLAB Reservoir Simulation Toolbox (pp. 375–408). Springer. https://doi.org/10.1007/978-3-030-52186-2_14

Wu, H., & Pollard, D. D. (1995). An experimental study of the relationship between joint spacing and layer thickness. Journal of Structural Geology, 17(6), 887–905. https://doi.org/10.1016/0191-8141(94)00097-4

Ye, Z., & Ghassemi, A. (2018). Injection-induced shear slip and permeability enhancement in granite fractures. Journal of Geophysical Research: Solid Earth, 123(10), 9009–9032. https://doi.org/10.1029/2018JB015888

Yılmaz, A., Adamia, S., Chabukiani, A., Chkhotua, T., ErdoĞan, K., Tuzcu, S., & KarabiyikoĞlu, M. (2000). Structural correlation of the southern Transcaucasus (Georgia)-eastern Pontides (Turkey). Geological Society, London, Special Publications, 173(1), 171–182. https://doi.org/10.1144/GSL.SP.2000.173.01.11

Yılmaz, Y. (2017). Major problems of Western Anatolian geology: Neotectonics and earthquake potential of the Eastern Mediterranean region. In Active Global Seismology (pp. 141–187). Springer. https://doi.org/10.1007/978-3-319-55115-9_7

Yin, A., & Taylor, M. H. (2011). Mechanics of V-shaped conjugate strike-slip faults and the corresponding continuum mode of continental deformation. Bulletin, 123(9–10), 1798–1821. https://doi.org/10.1130/B30359.1

Yin, Z. M., & Ranalli, G. (1993). Determination of tectonic stress field from fault slip data: Toward a probabilistic model. Journal of Geophysical Research: Solid Earth, 98(B7), 12165–12176. https://doi.org/10.1029/93JB00670

Zeeb, C., Gomez-Rivas, E., Bons, P. D., & Blum, P. (2013). Evaluation of sampling methods for fracture network characterization using outcrops. American Association of Petroleum Geologists Bulletin, 97(10), 1545–1566. https://doi.org/10.1306/02121312025

Zhang, S., Nakano, H., Xiong, Y., Nishimura, T., & Zhang, F. (2010). Temperature-controlled triaxial compression/creep test device for thermodynamic properties of soft sedimentary rock and corresponding theoretical prediction. Journal of Rock Mechanics and Geotechnical Engineering, 2(3), 255–261. https://doi.org/10.3724/SP.J.1235.2010.00255

Zhang, Z., Yu, H., Xu, W., Wang, Q., Meng, S., Jin, X., Liu, H., & Wu, H. (2024). Far-field reactivation of natural fractures by stress shadow effect. Engineering Fracture Mechanics, 311, 110596. https://doi.org/10.1016/j.engfracmech.2023.110596.

Zhu, W., He, X., Khirevich, S., & Patzek, T. W. (2022). Fracture sealing and its impact on the percolation of subsurface fracture networks. Journal of Petroleum Science and Engineering, 218, 111023. https://doi.org/10.1016/j.petrol.2022.111023.

APPENDICES

A. Land Photographs and Detailed Information about Scan-line Survey Study

Figure 1. Kuyucak-Belenova location, highly fractured Paleozoic marbles.

Figure 2. Kuyucak-Belenova location, highly fractured Paleozoic marbles.

Figure 3. Gökkiriş location, highly fractured Jurassic marbles.

Figutre 4. S8 – Almacık Tepe sub location, Paleozoic marbles.

Figure 5. S8 – Almacık Tepe upper location, scan-line survey location Paleozoic marbles.

Figure 6. S8 – Almacık Tepe upper location, scan-line survey location Paleozoic marbles.

Figure 7. S11 –Yukarıkayacık-Maden turn scan-line survey location, Permian marbles.

Figure 8. İmambaba Peak, peak location, Permian marbles.

Figure 9. İmambaba Peak, peak location, Permian marbles.

Figure 10. İmambaba Peak road location, highly fractured Permian marbles.

Figure 11. İmambaba Peak road location, highly fractured Permian marbles.

Figure 12. Halilbeyli, scan-line survey location Paleozoic marbles.

Figure 13. Halilbeyli, Paleozoic marbles.

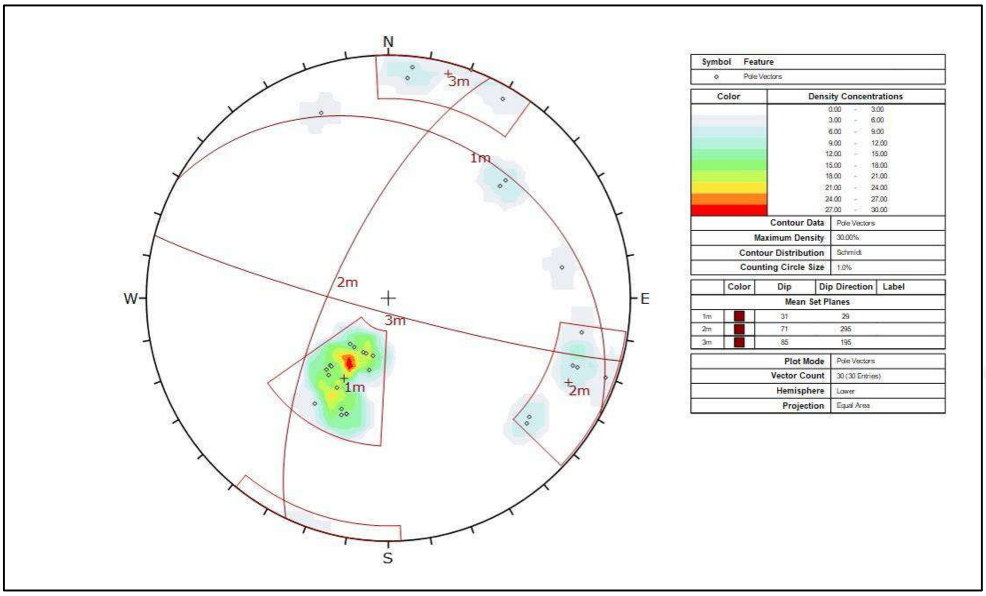

Figure 14. Kuyucak-Belenova location scan-line survey measurement values and analysis results.

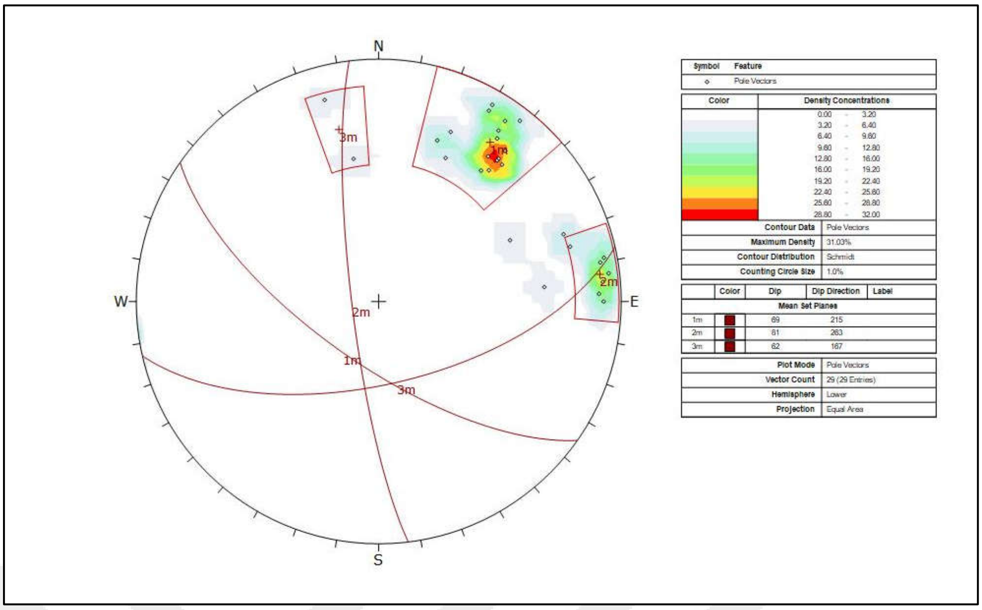

Figure 15. Gökkiriş location scan-line survey measurement values and analysis results.

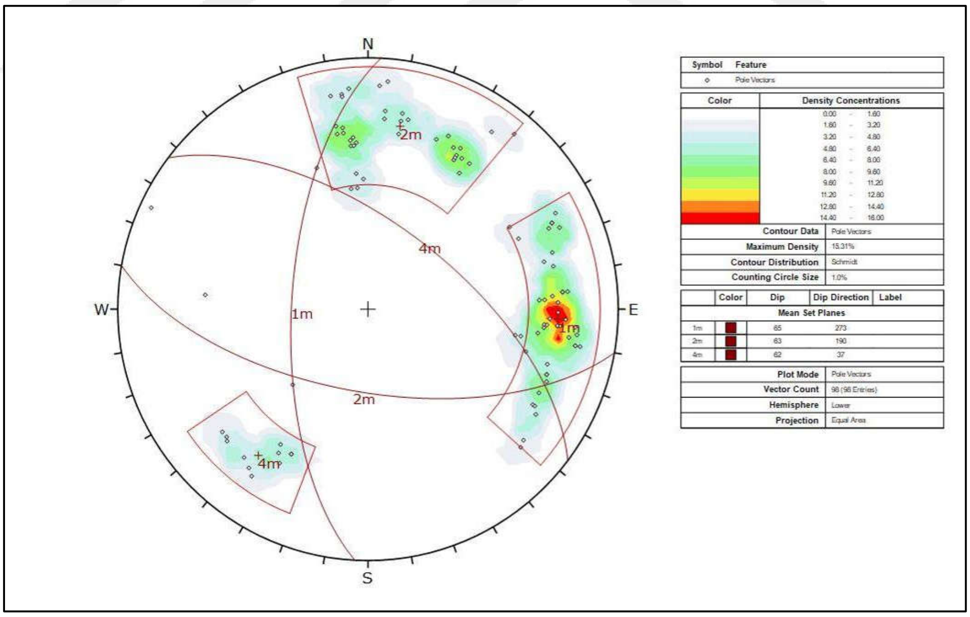

Figure 16. Almacık Hill Bottom location scan-line survey measurement values and analysis results.

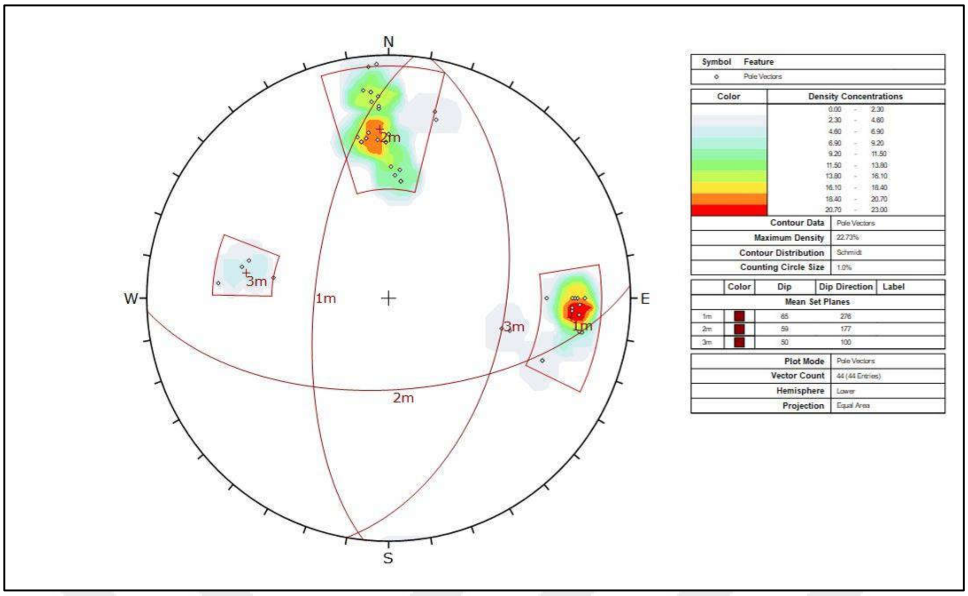

Figure 17. Almacık Hill Top location scan-line survey measurement values and analysis results.

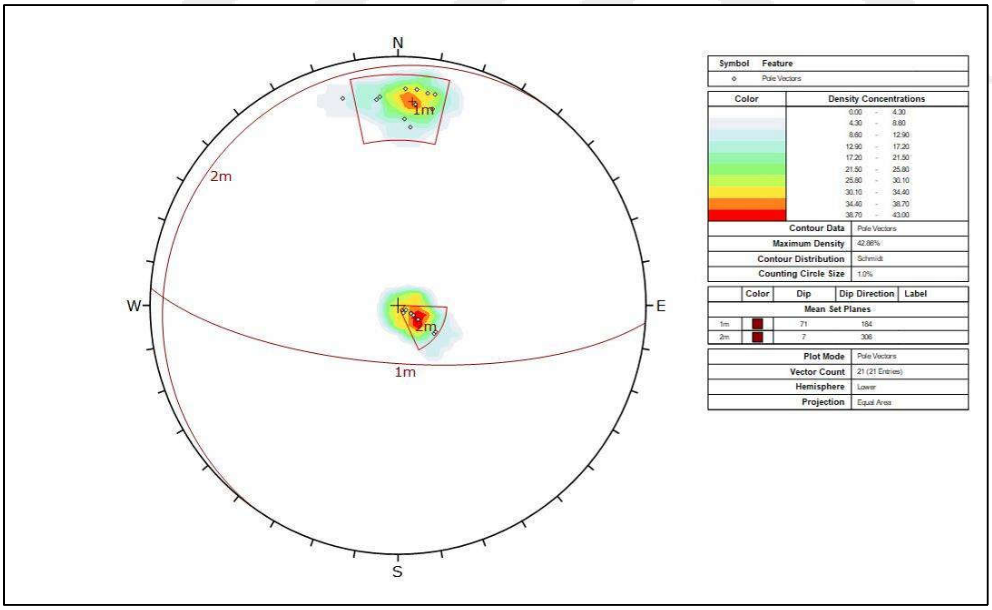

Figure 18. Yukarıkayacık-Maden turn location scan-line survey measurement values and analysis results.

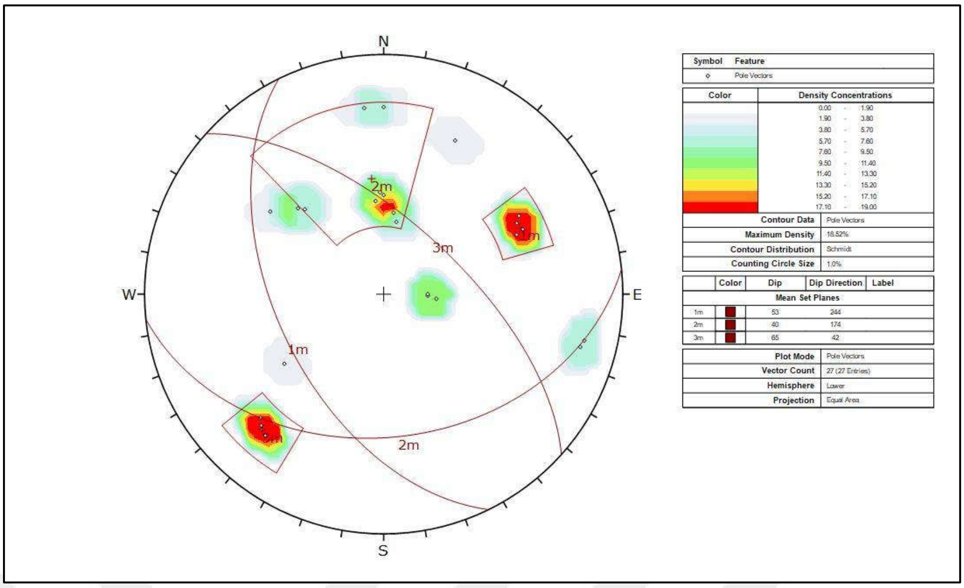

Figure 19. İmambaba Peak location scan-line survey measurement values and analysis results.

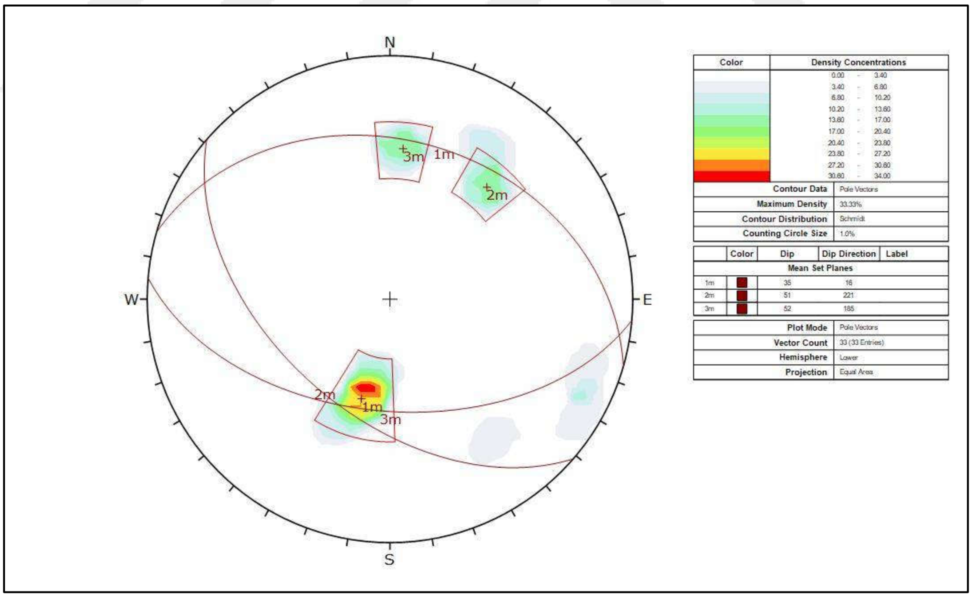

Figure 20. İmambaba Peak Turn location scan-line survey measurement values and analysis results.

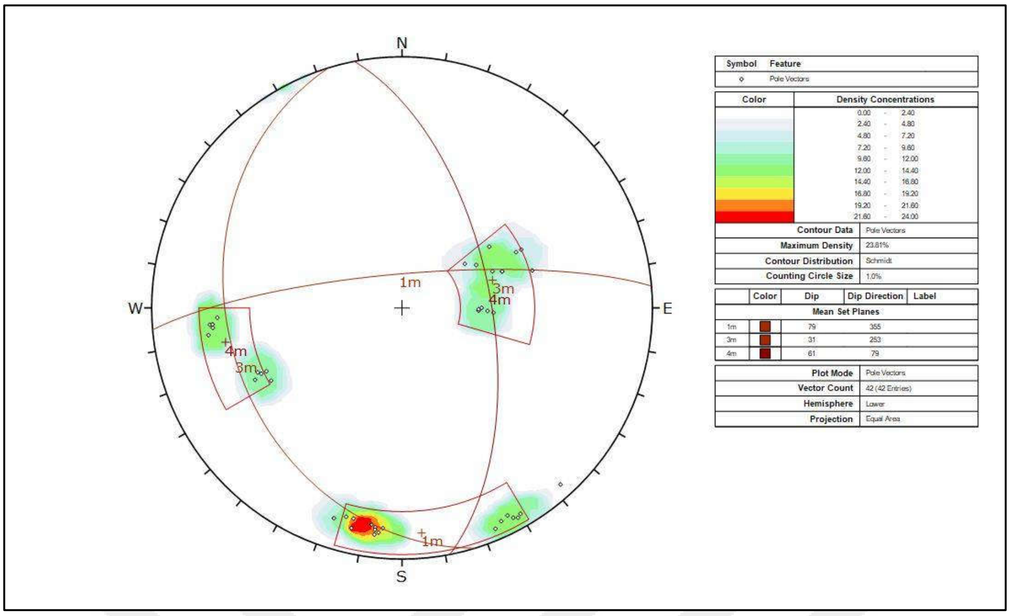

Figure 21. Halilbeyli location scan-line survey measurement values and analysis results.

B. Uniaxial Compressive Strength, Static Deformability and Triaxial Compressive Strength Rock Mechanics Experiments Sample Photos and Test Results

Table 1. Rock mechanics experiments: Uniaxial Compression test results

Sample Name	Length (mm)	Diameter(mm)	UCS (MPa)
Gökkiriş Hill (Block 1)-D	126.46	52.6	44.89
Halilbeyli (Block 5)-A	126.66	52.86	46.51
Kuyucak-Belenova (Kuy4-1)	126.46	51.73	82.36
Almacık Hill (S8-3)	119.93	52.87	89.88
Yukarıkayacık – Maden (S11-3)	120.14	52.94	90.33
Terziler (TY2-2)	119.61	52.94	93.79

Table 2. Rock mechanics experiments: Static Deformability test results

Sample Name	Length (mm)	Dia, (mm)	UCS (MPa)	Average UCS (MPa)	Elastic Modulus (GPa)	Average Elastic Modulus (GPa)	Poisson's Ratio	Average Poisson's Ratio
Gökkiriş (Block-1). A	126.58	52.77	25.94		84.36		0.32	
Gökkiriş (Block-1). B	126.22	52.87	53.48	48.31	79.06	80.2	0.13	0.24
Gökkiriş (Block-1). C	126.25	52.82	65.51		77.18		0.27	
İmambaba (Block-4). A	127.88	52.88	91.91		61.72		0.17	
İmambaba (Block-4). B	125.15	53.02	48.93	84.99	87.7	73.78	0.18	0.15
İmambaba (Block-4). C	126.3	52.9	114.13		71.93		0.11	
Kuyucak-Belenova (Kuy4-1) (Not included)	126.46	51.73	82.36		66.64		0.55	
Kuyucak-Belenova (Kuy4-3)	119.76	52.75	78.31	72.78	70.44	70.73	0.11	0.11
Kuyucak-Belenova (Kuy4-4)	120.32	52.55	67.25		71.02		0.12	
Almacık Hill (S8-1) (Not included)	120.23	52.94	66.01		65.58		0.45	
Almacık Hill (S8-2)	119.62	52.92	97.82	90.35	59.08	57.16	0.09	0.14
Almacık Hill (S8-5)	120.17	52.95	82.88		55.23		0.18	
Yukarıkayacık-Maden (S11-1)	120.38	52.88	96.95		88.49		0.22	
Yukarıkayacık-Maden (S11-2)	120.33	52.9	99.26	109.54	89.82	88.59	0.14	0.16
Yukarıkayacık-Maden (S11-5)	120.89	52.88	132.4		87.47		0.13	
Terziler (TY2-1)	118.86	52.81	87.47		76.95		0.13	
Terziler (TY2-3) (Not included)	120.76	52.88	47.99	90.05	59.36	73.79	0.13	0.15
Terziler (TY2-4)	119.43	52.98	92.64		70.64		0.17	

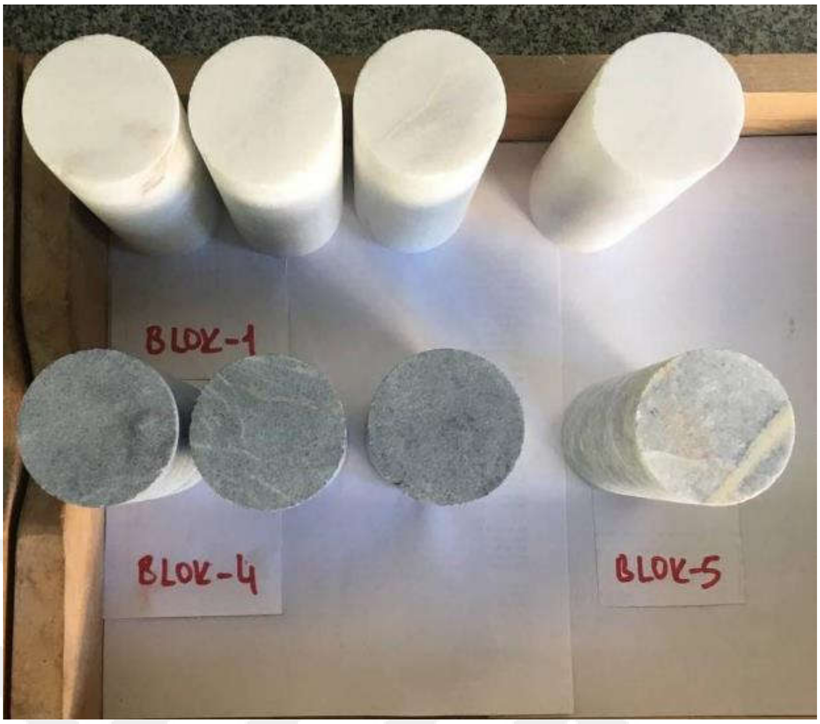

Figure 22. B-1: Gökkiriş, B-4: İmambaba, B-5: Halilbeyli samples photo collected before the UCS and Static Deformability Tests

Figure 23. Kuyucak-Belenova (Kuy4) Core Samples photo collected before the UCS and Static Deformability Tests

Figure 24. Almacık Hill (S8) Core samples photo collected before the UCS and Static Deformability Tests

Figure 25. Yukarıkayacık-Maden (S11) Core samples photo collected before the UCS and Static Deformability Tests

Figure 26. Terziler (TY-2) Core samples

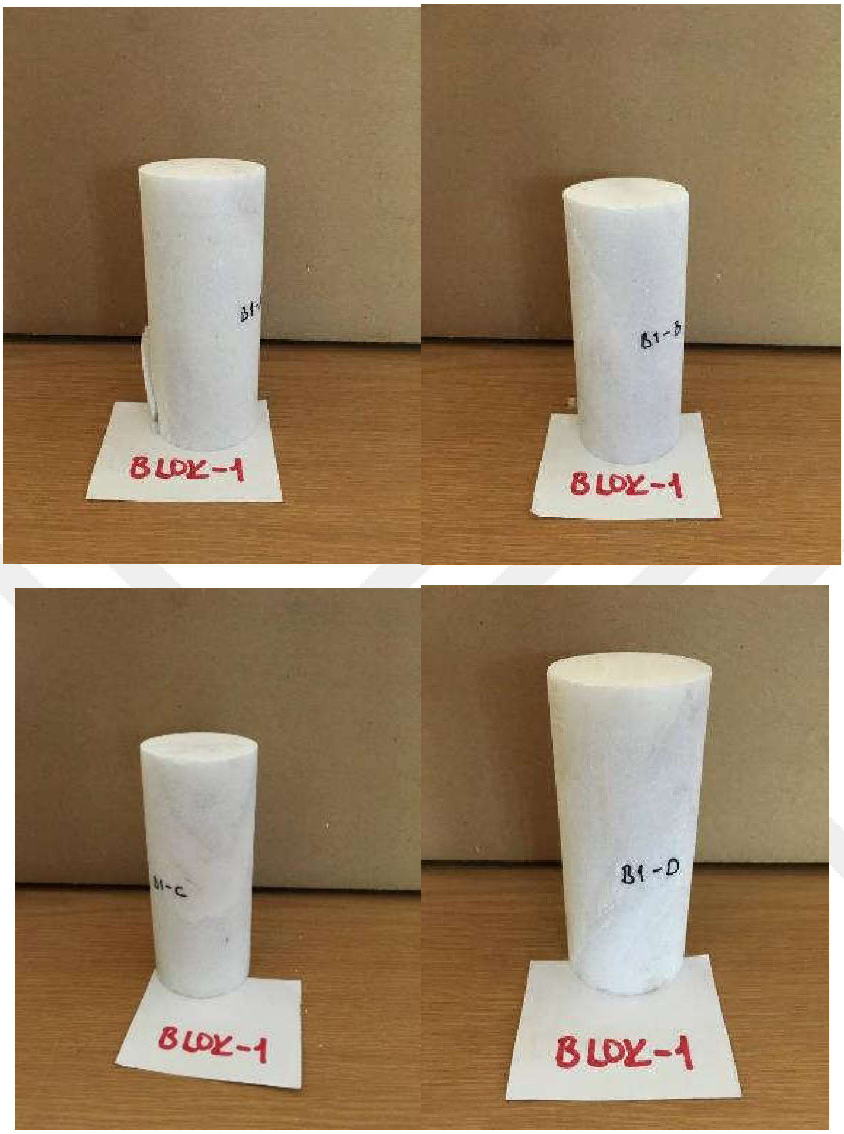

Figure 27. B - 1: Gökkiriş samples photo

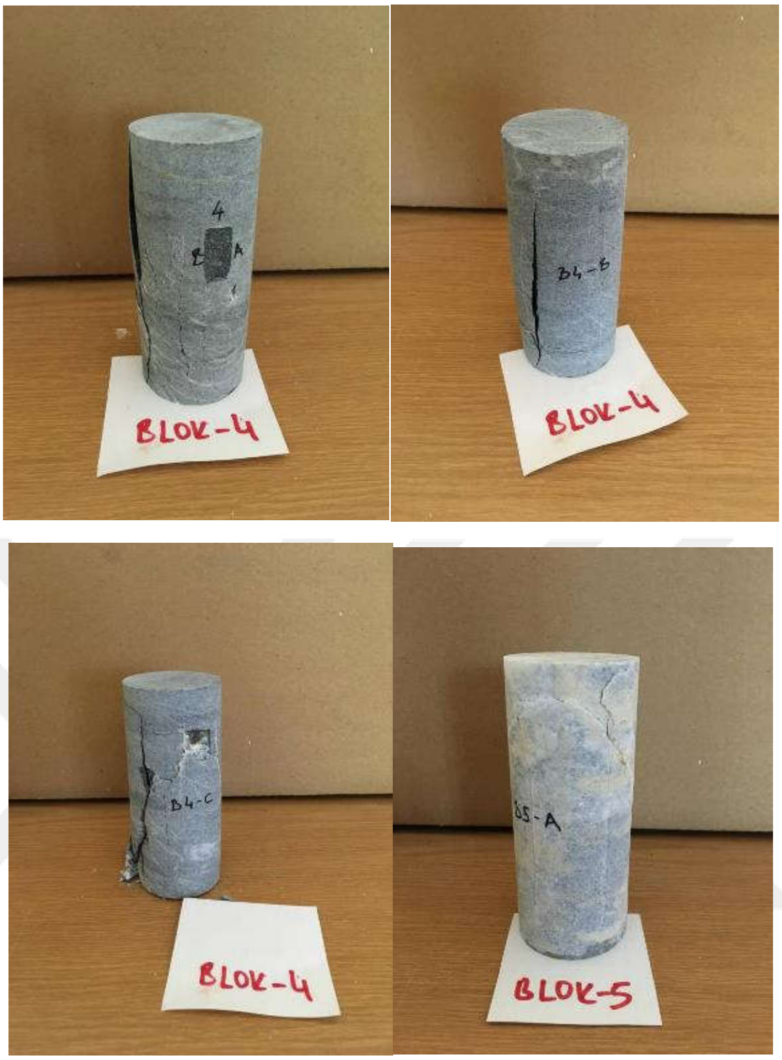

Figure 28. B - 4: İmambaba, B - 5: Halilbeyli samples

Figure 29. Kuy4 Core Samples UCS and Static Deformability Post-experiment view

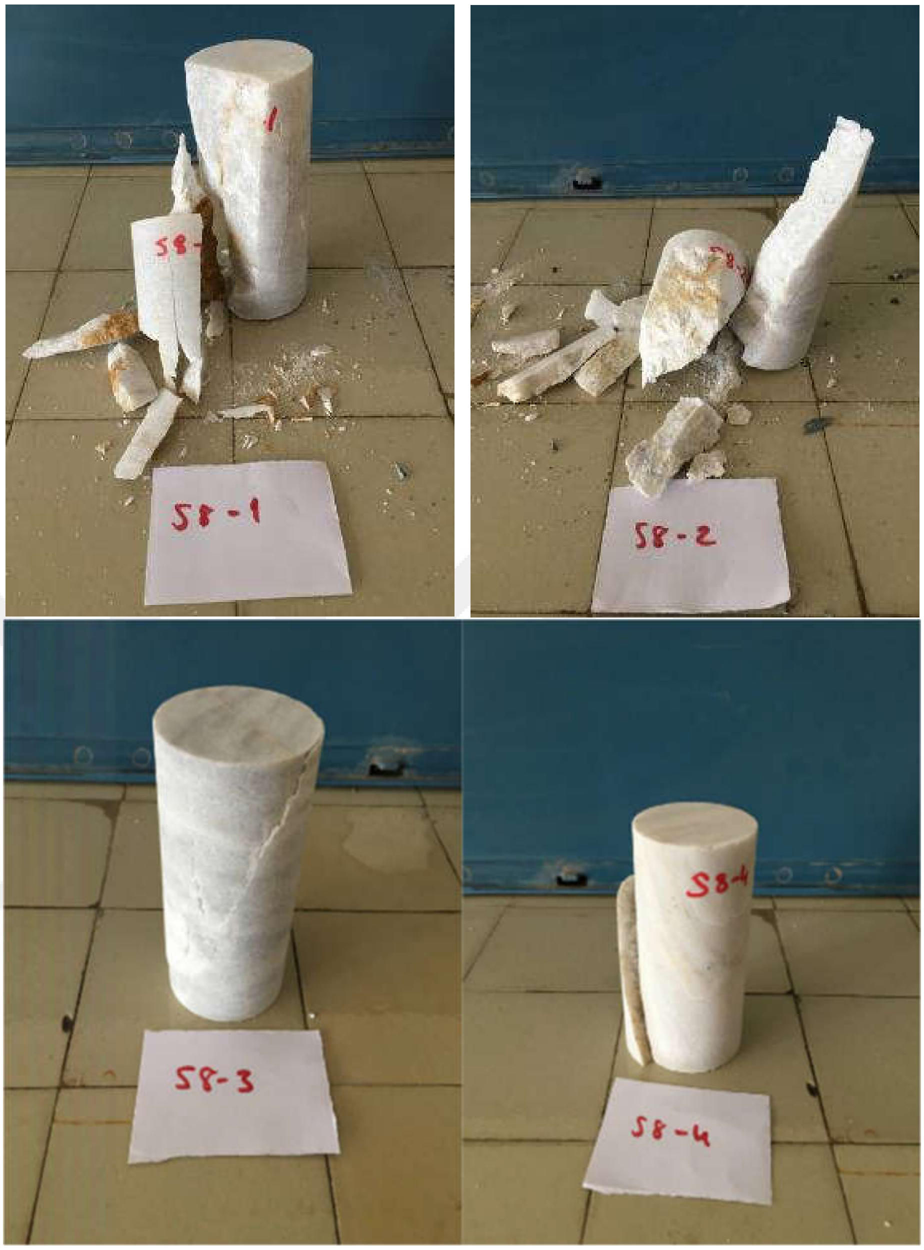

Figure 30. Almacık Hill (S8) Core Samples

Figure 31. Almacık Hill (S8) Core Samples

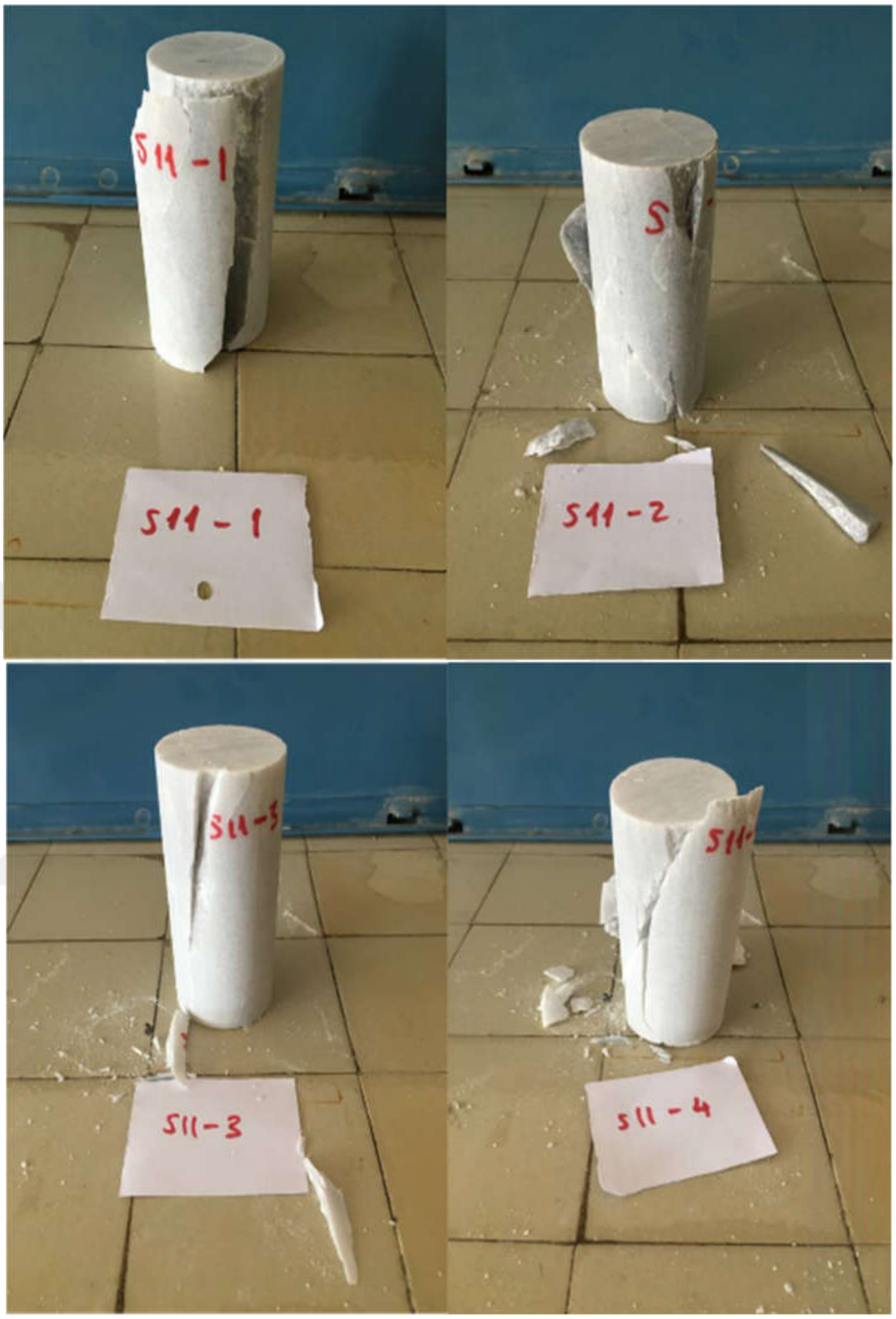

Figure 32. Yukarıkayacık-Maden (S11) Core Samples

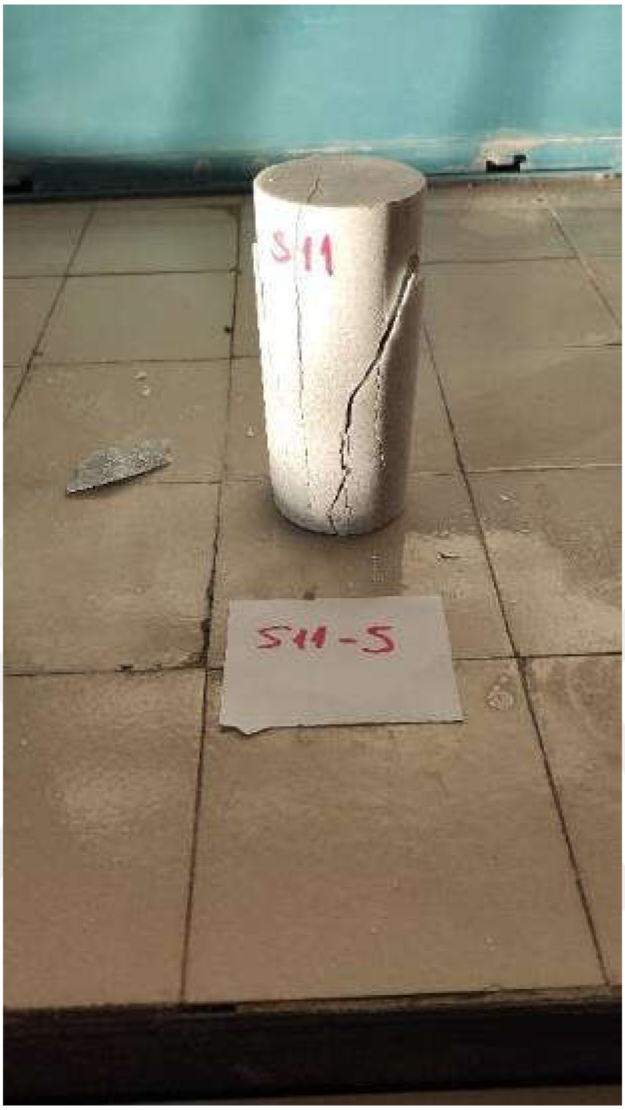

Figure 33. Yukarıkayacık-Maden (S11) Core Samples

Figure 34. Terziler (TY-2) Core Samples

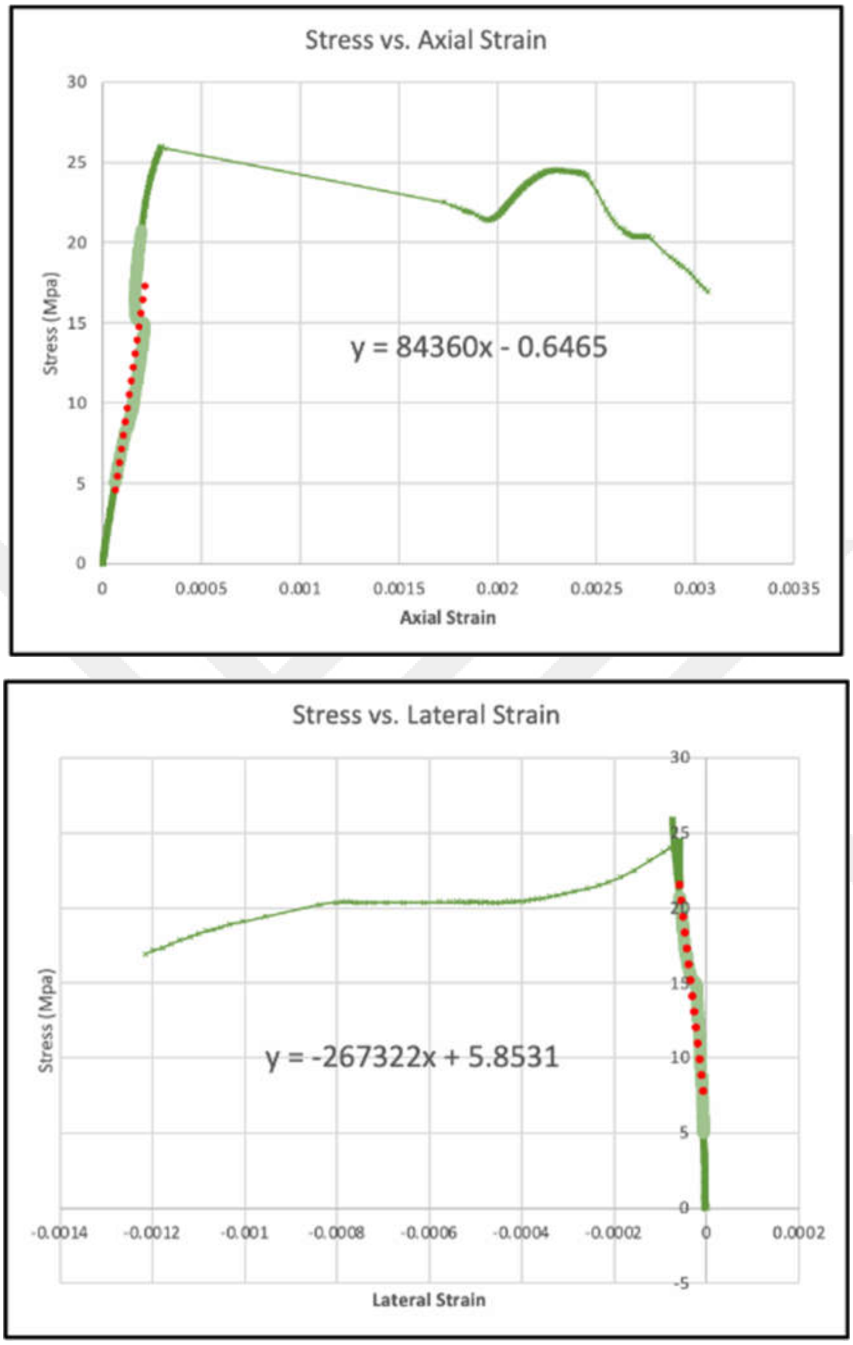

Figure 35. Block 1-A: Gökkiriş, Stress-related Axial and Lateral Strain

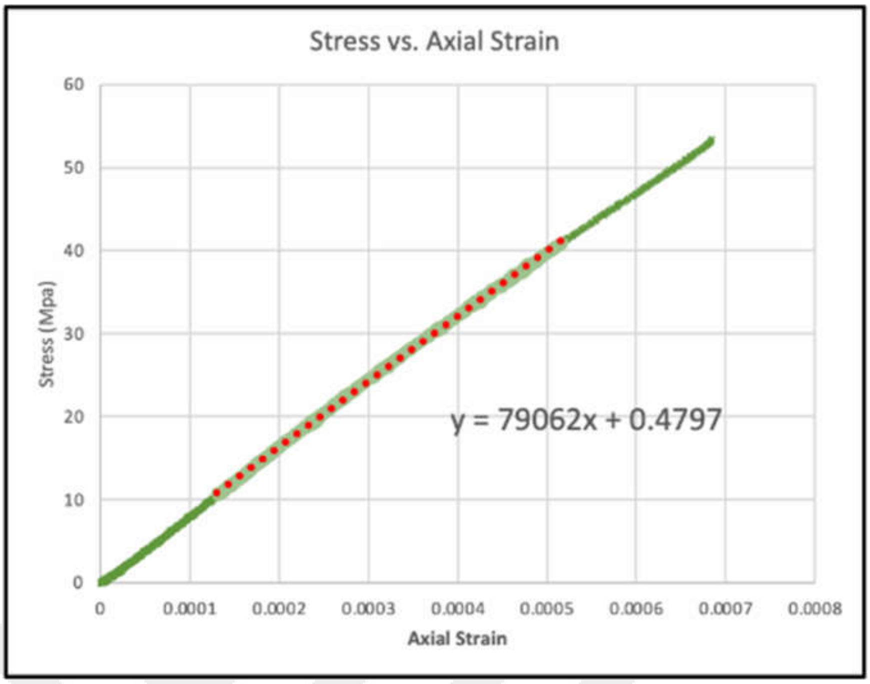

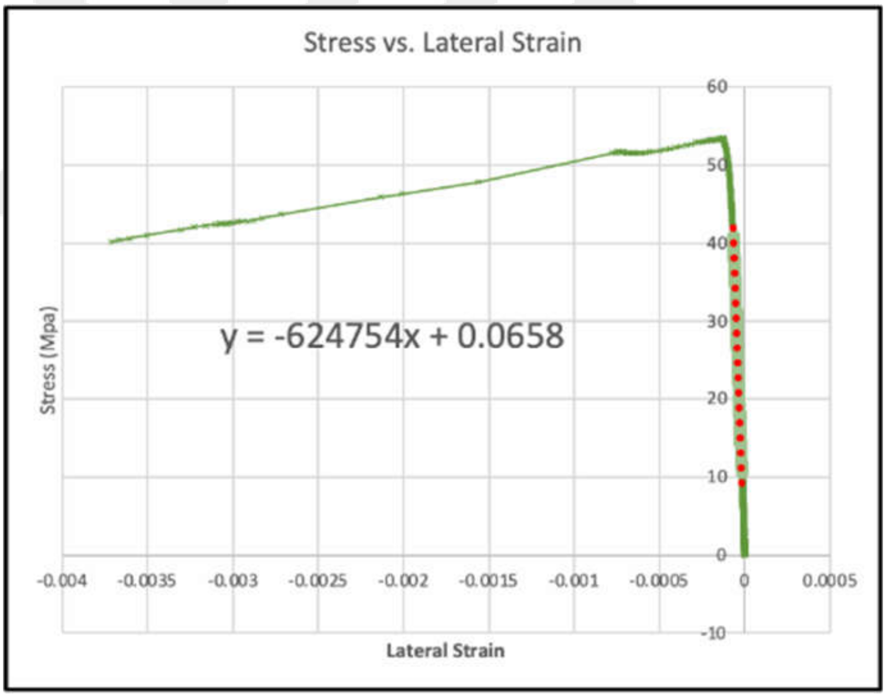

Figure 36. Block 1-B: Gökkiriş, Stress-related Axial and Lateral Strain

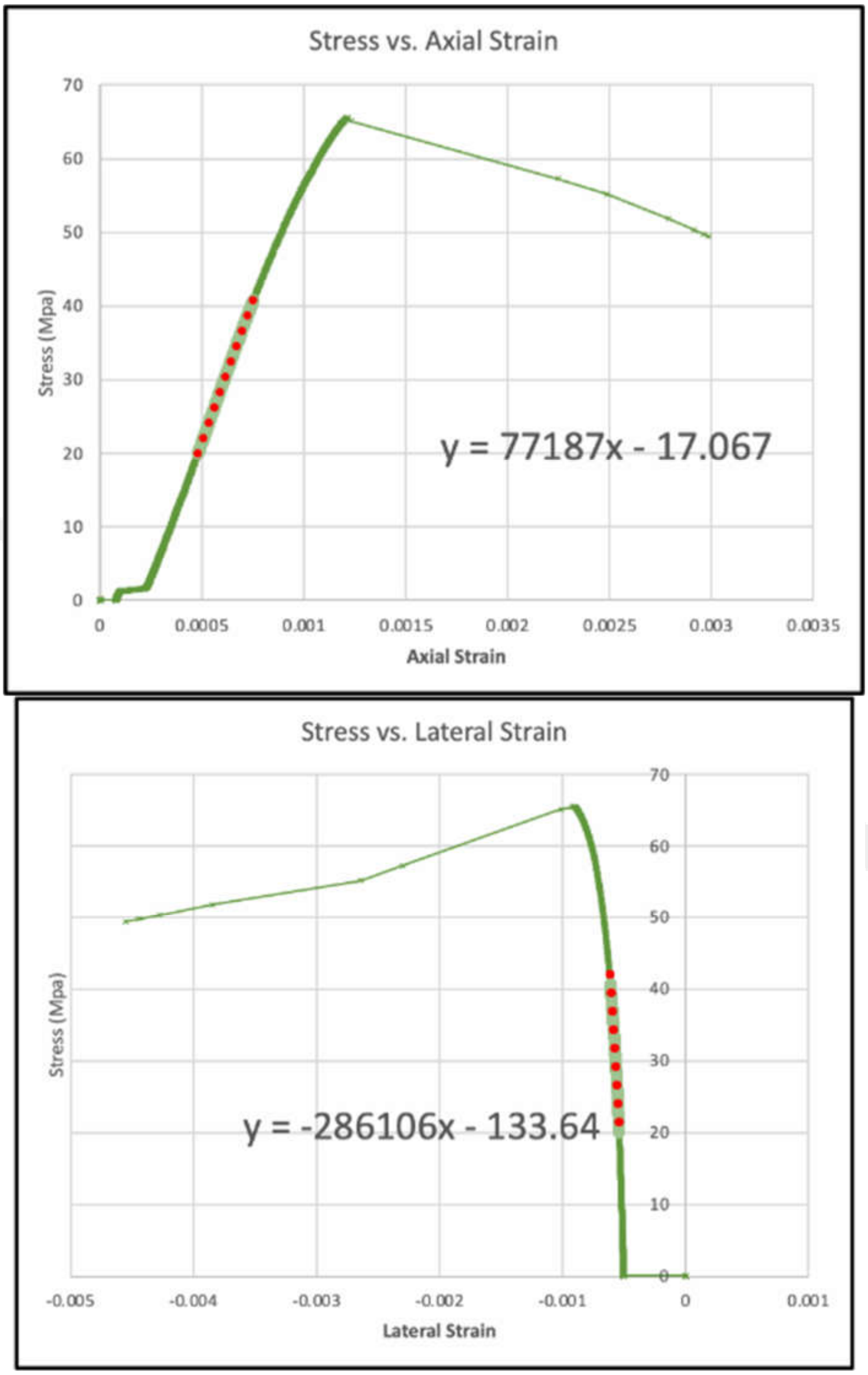

Figure 37. Block 1-C: Gökkiriş, Stress-related Axial and Lateral Strain Graphs

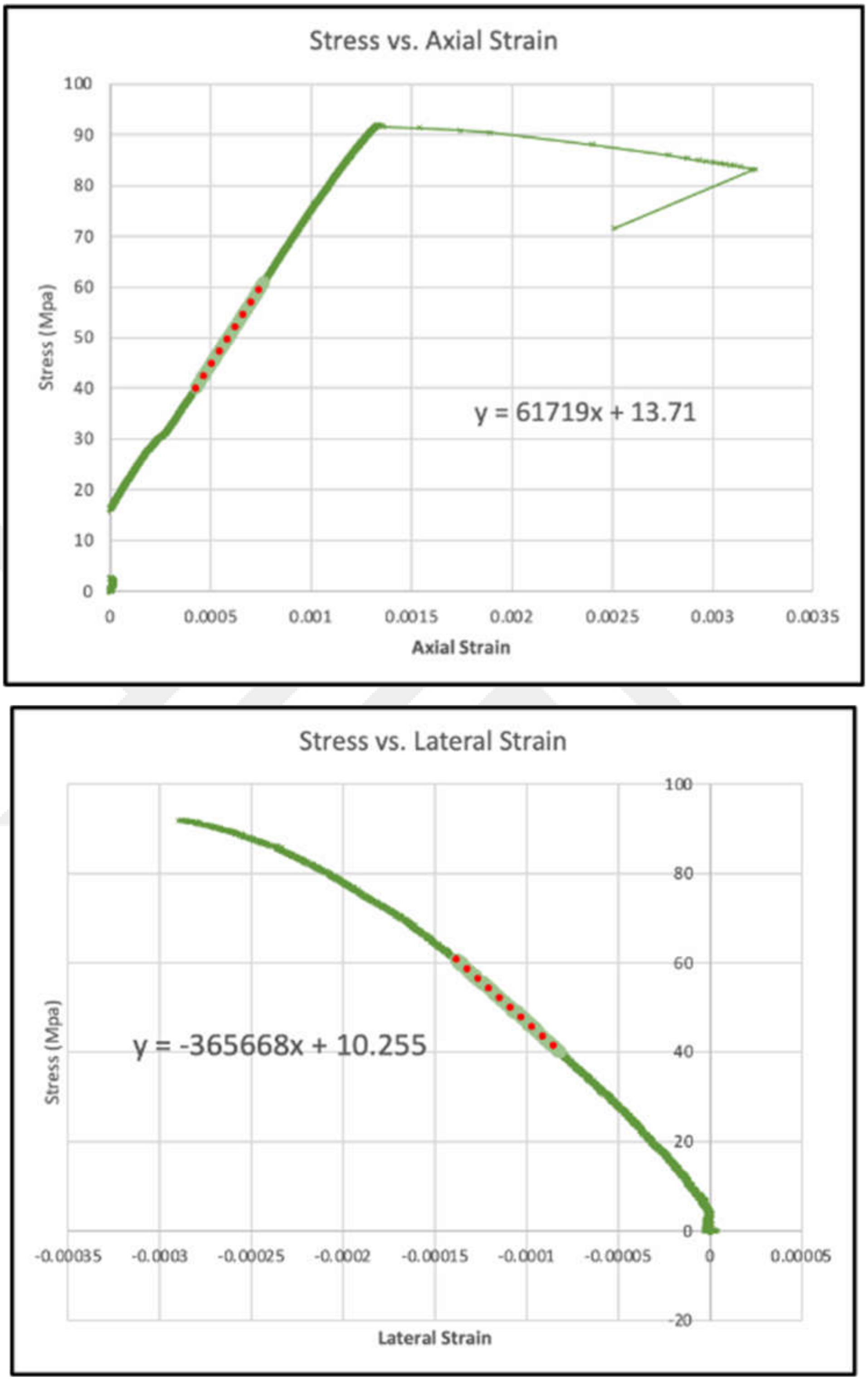

Figure 38. Block 4-A: İmambaba, Stress-related Axial and Lateral Strain

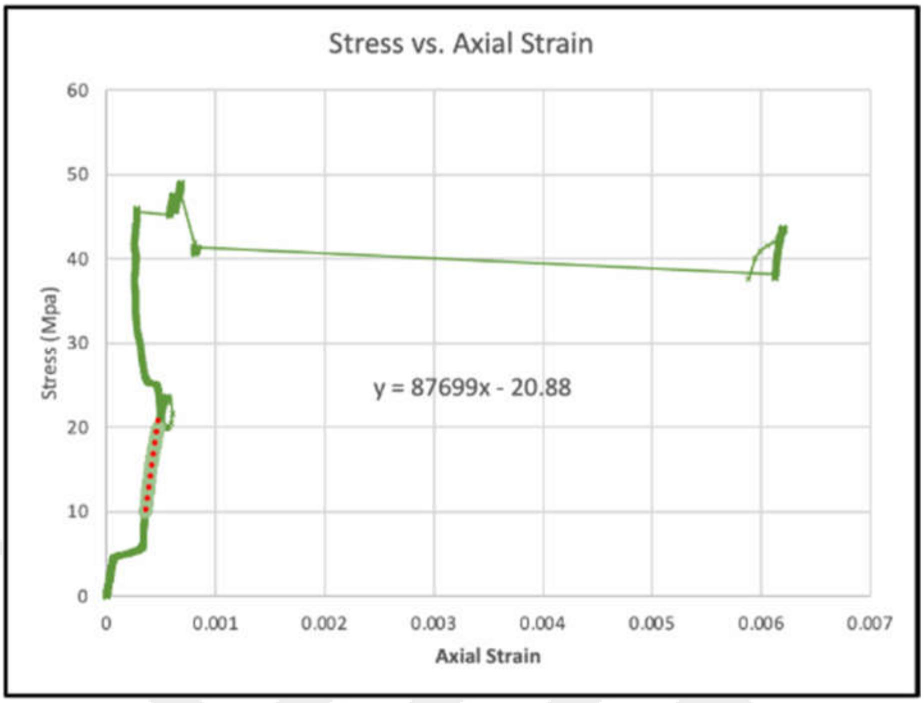

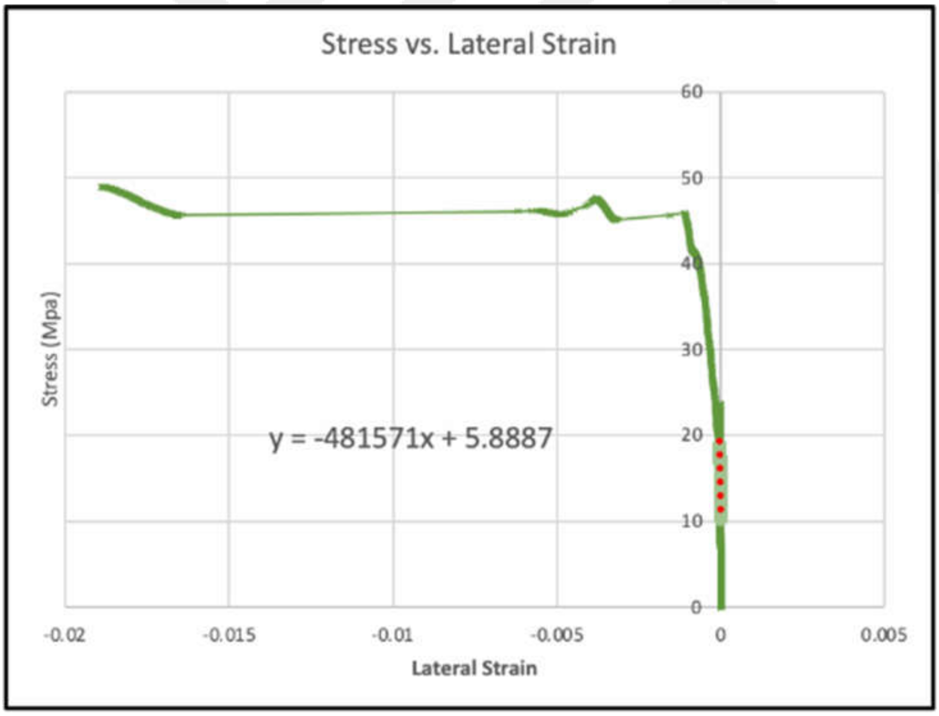

Figure 39. Block 4-B: İmambaba, Stress-related Axial and Lateral Strain

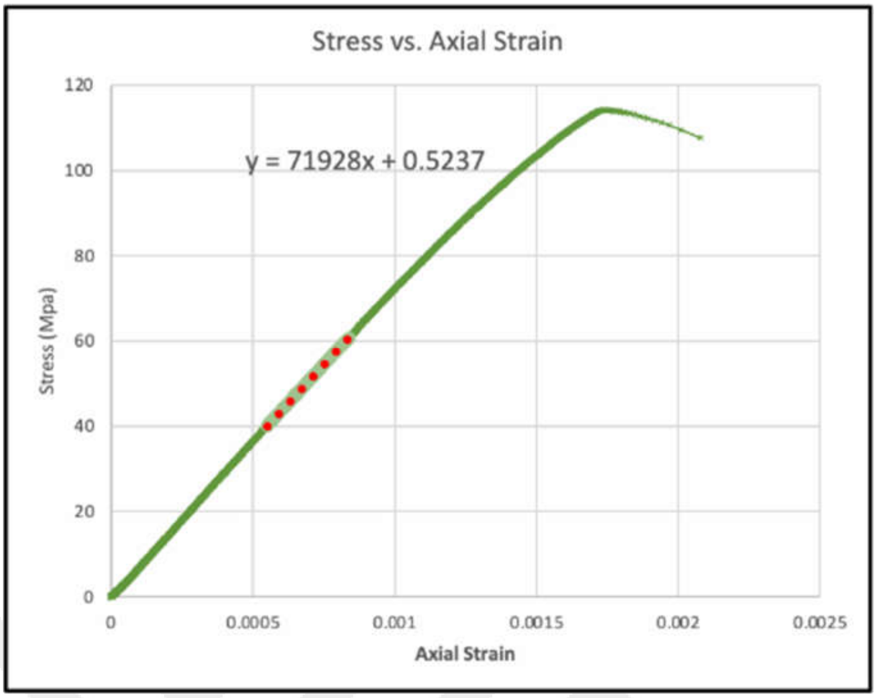

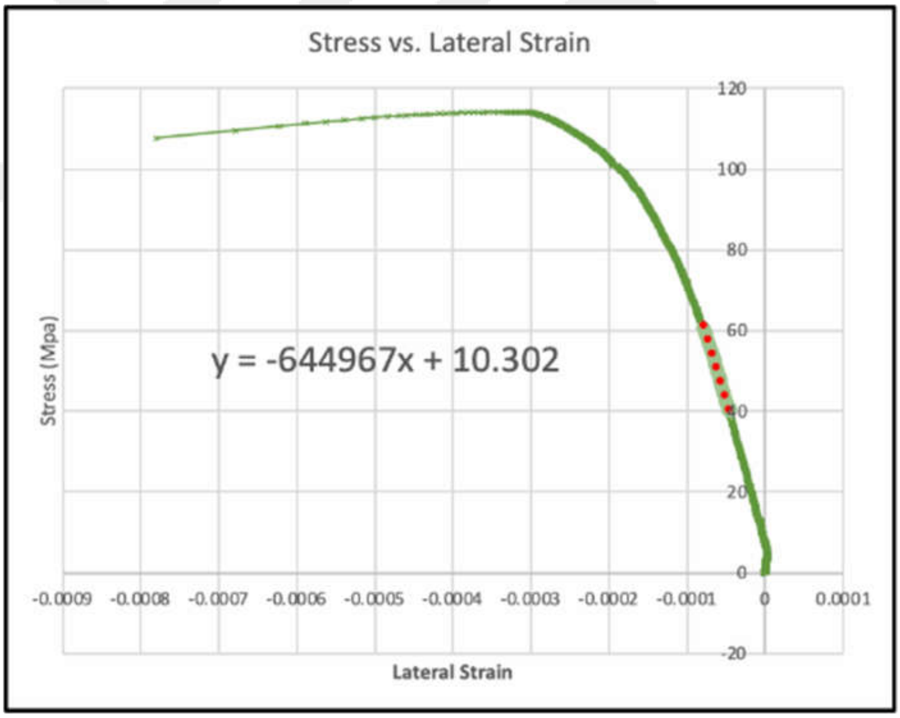

Figure 40. Block 4-C: İmambaba, Stress-related Axial and Lateral Strain

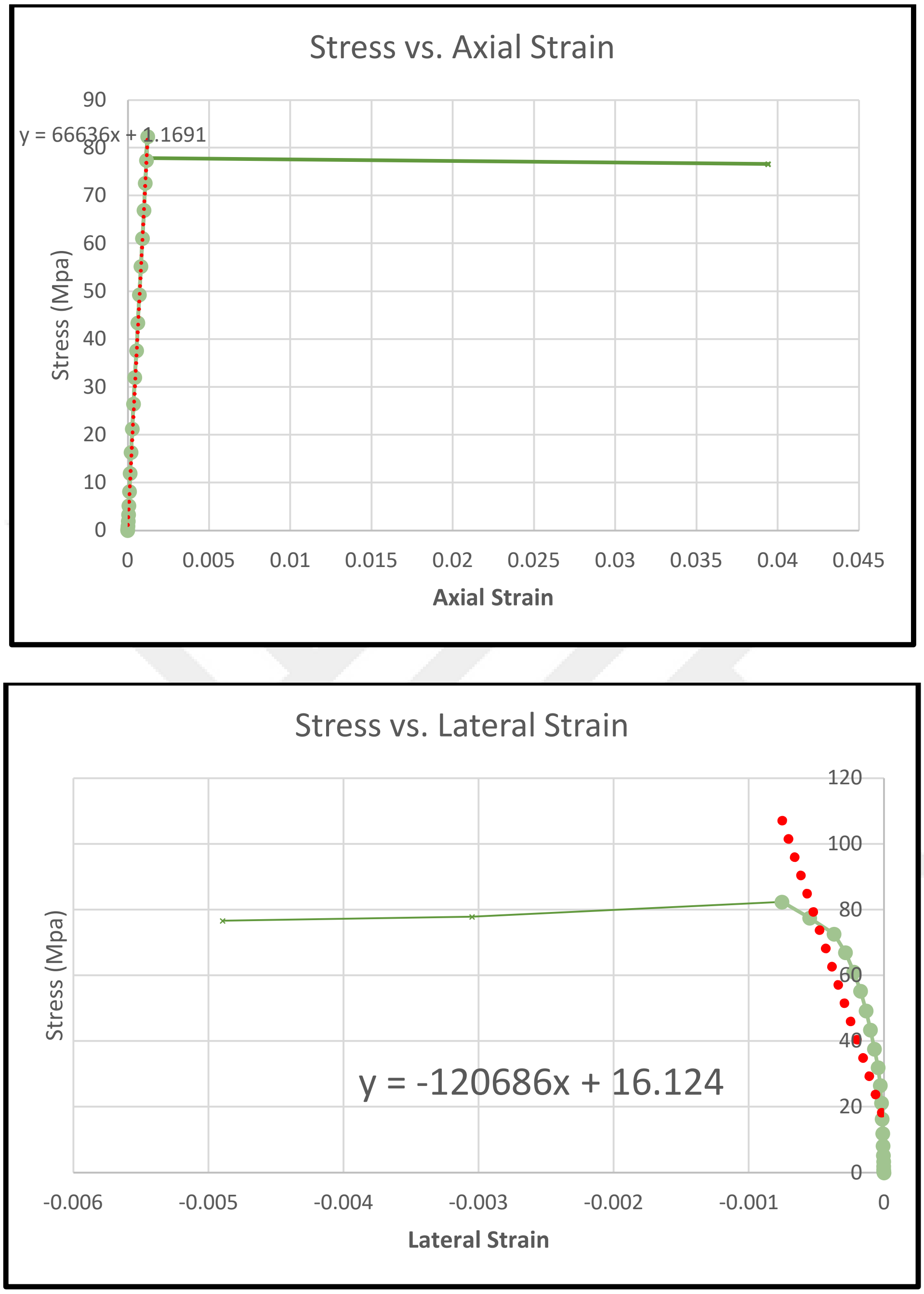

Figure 41. KUY4-1: Kuyucak-Belenova, Stress-related Axial and Lateral Strain

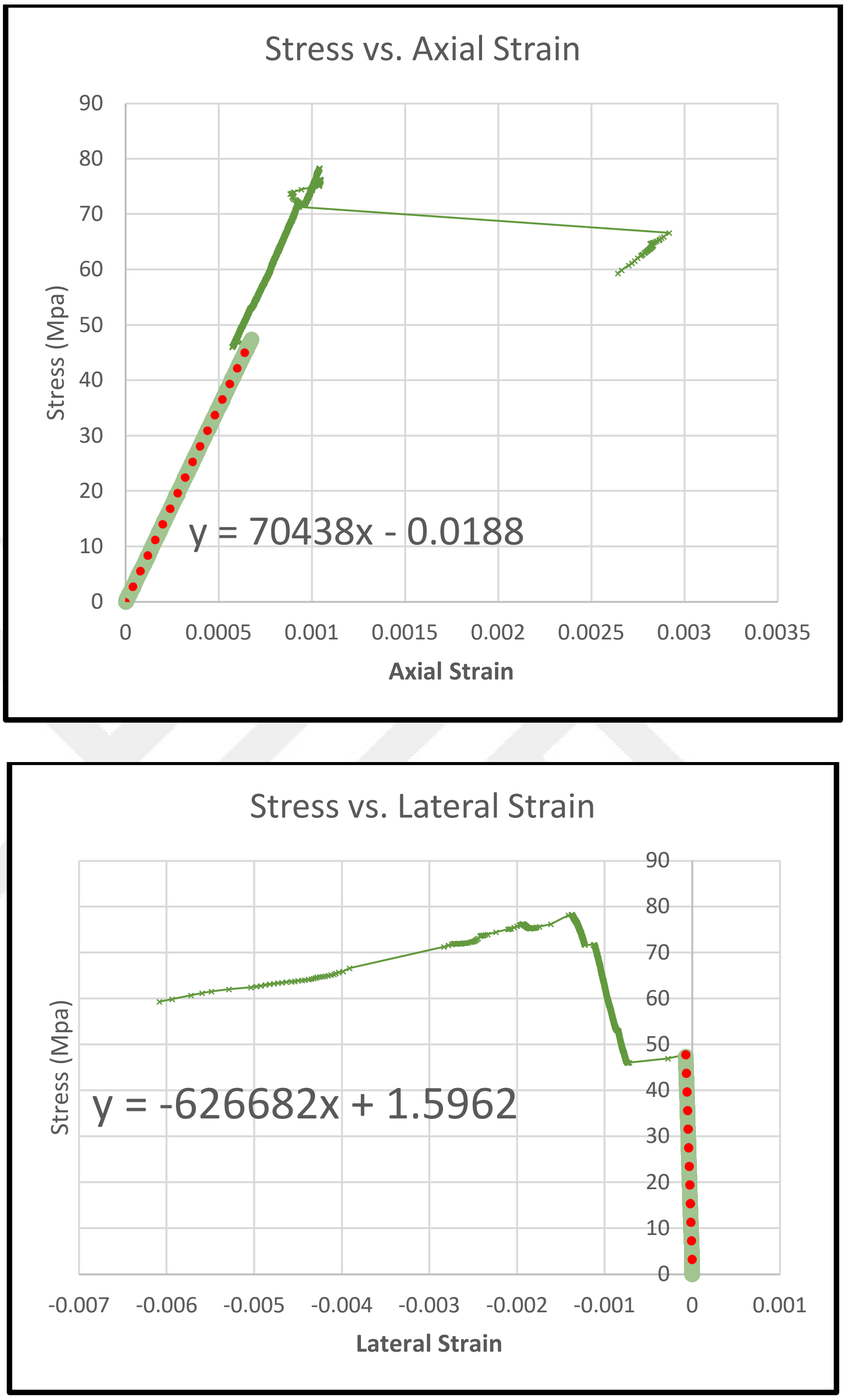

Figure 42. KUY4-3: Kuyucak-Belenova, Stress-related Axial and Lateral Strain

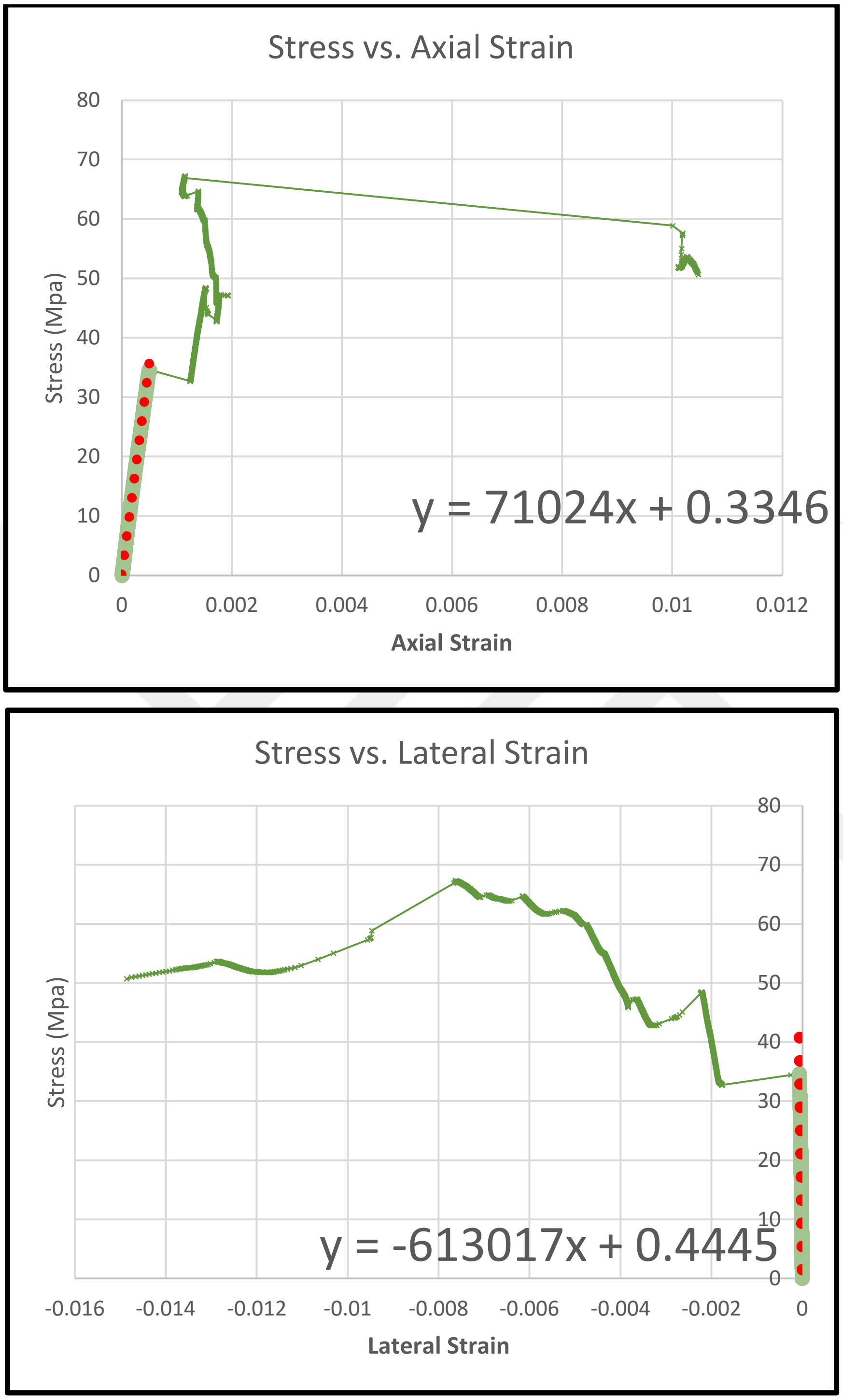

Figure 43. KUY4-4: Kuyucak-Belenova, Stress-related Axial and Lateral Strain

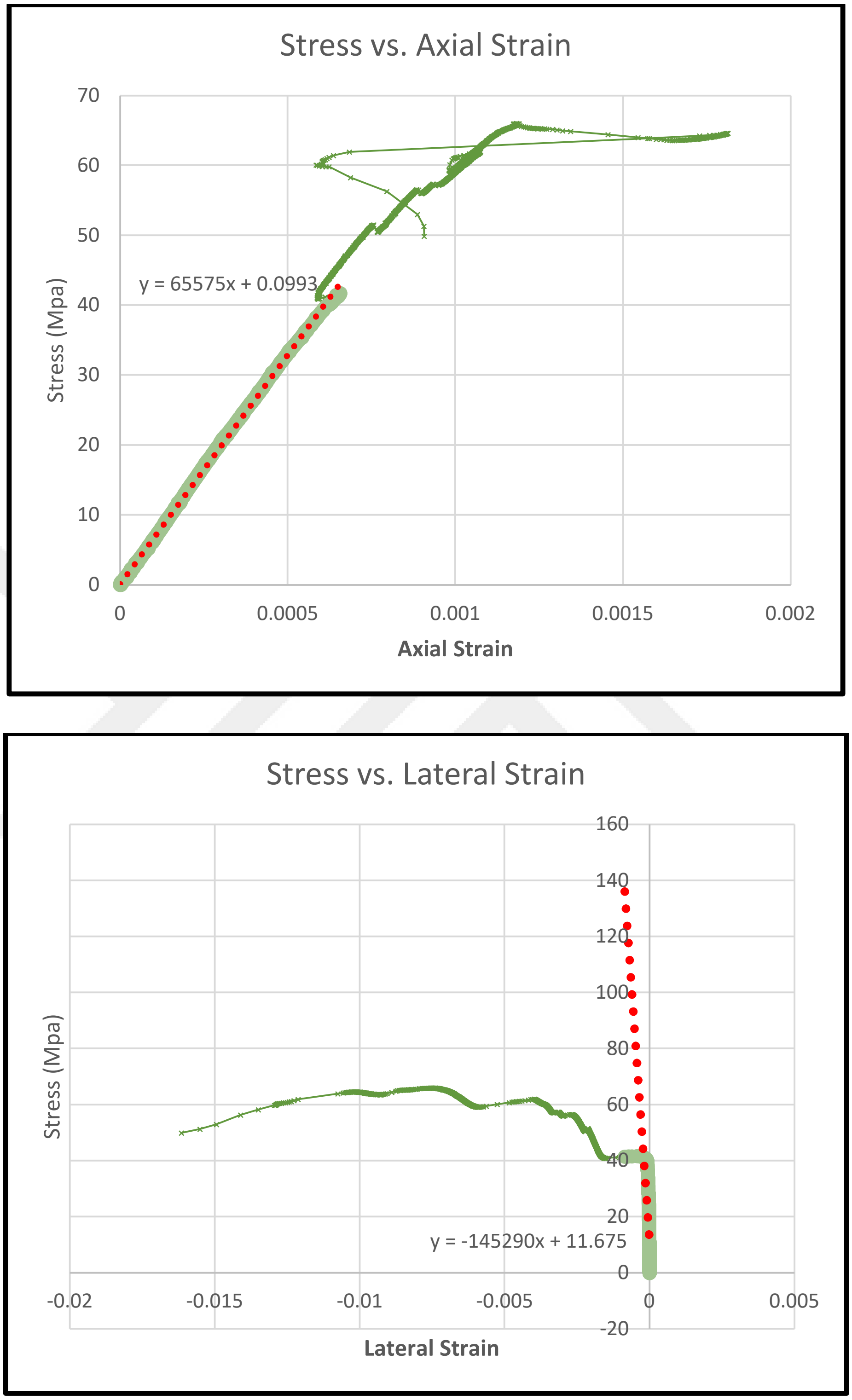

Figure 44. S8-1: Almacik Hill, Stress-related Axial and Lateral Strain

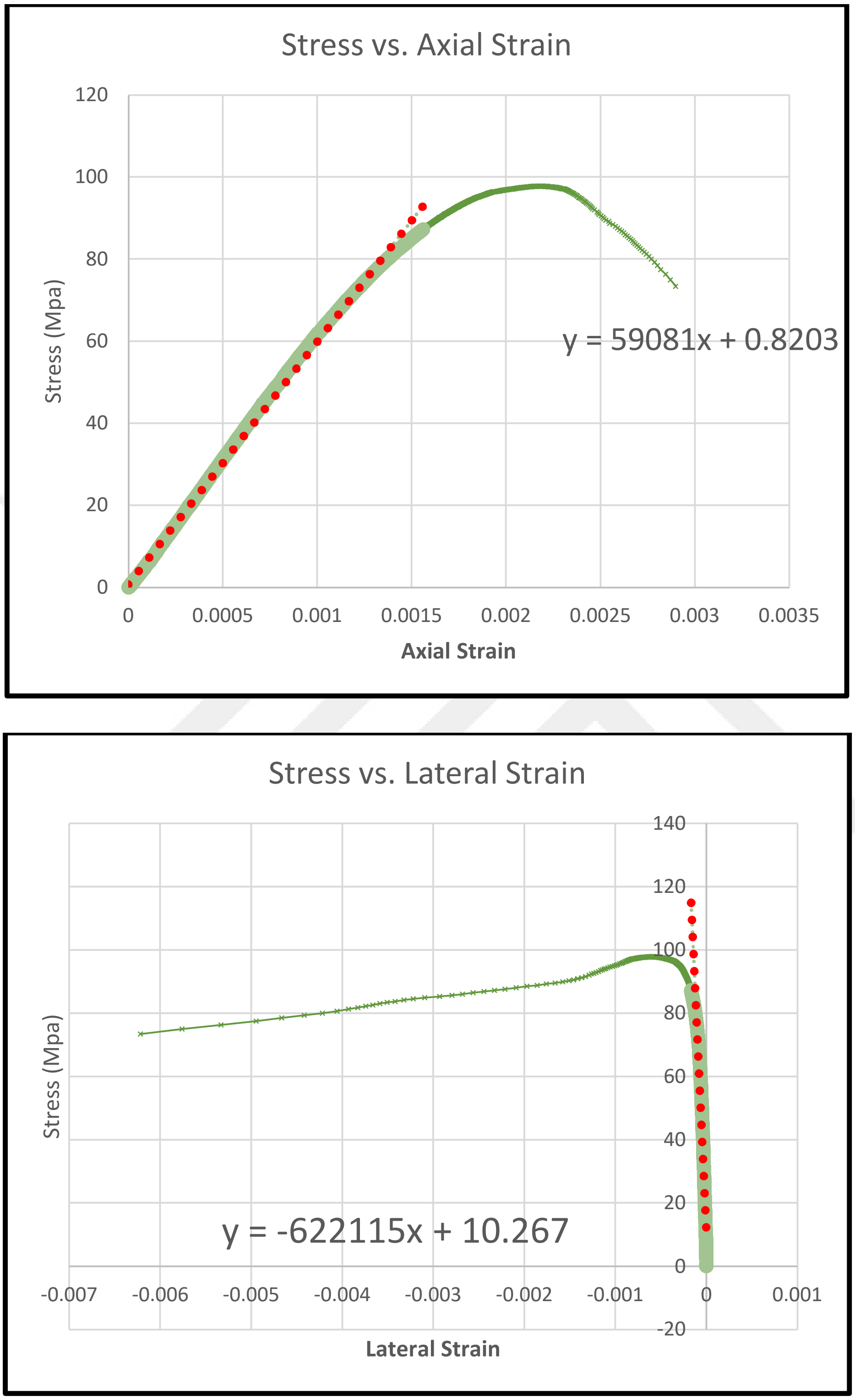

Figure 45. S8-1: Almacik Hill, Stress-related Axial and Lateral Strain

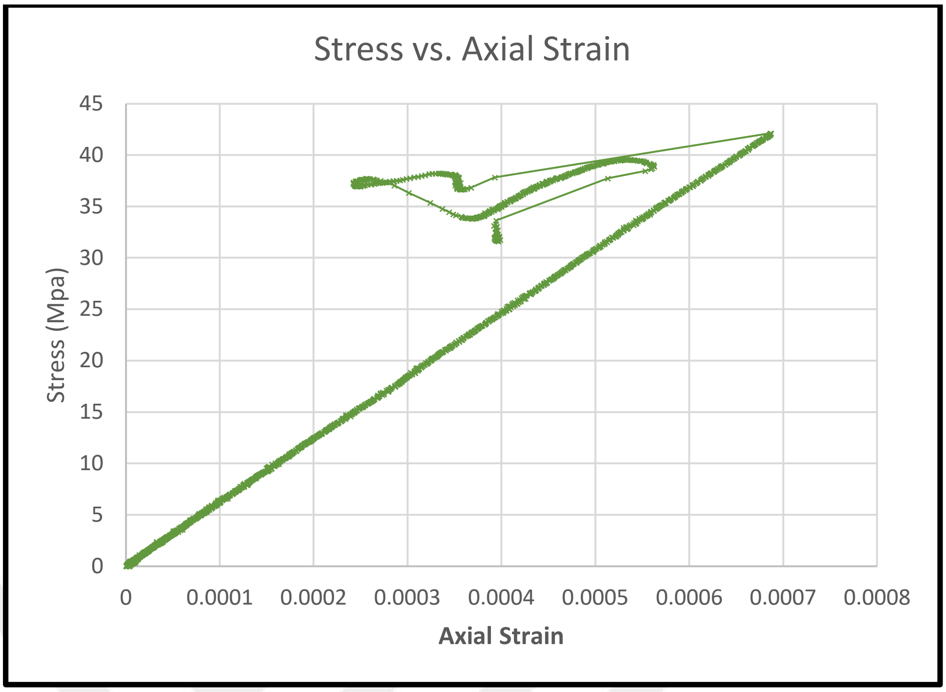

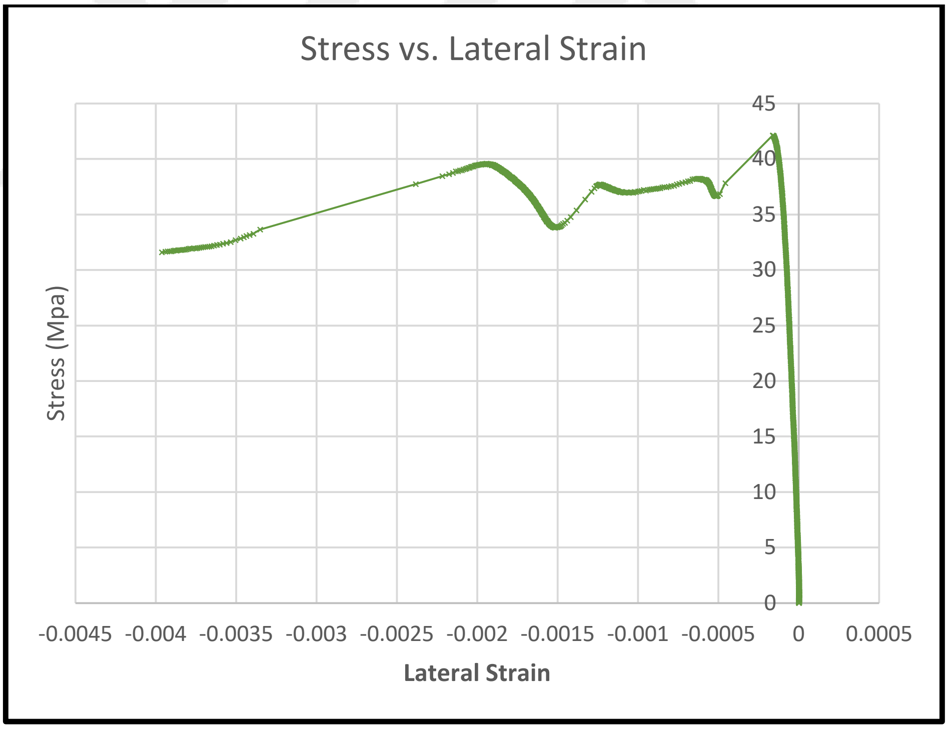

Figure 46. S8-4: Almacik Hill, Stress-related Axial and Lateral Strain

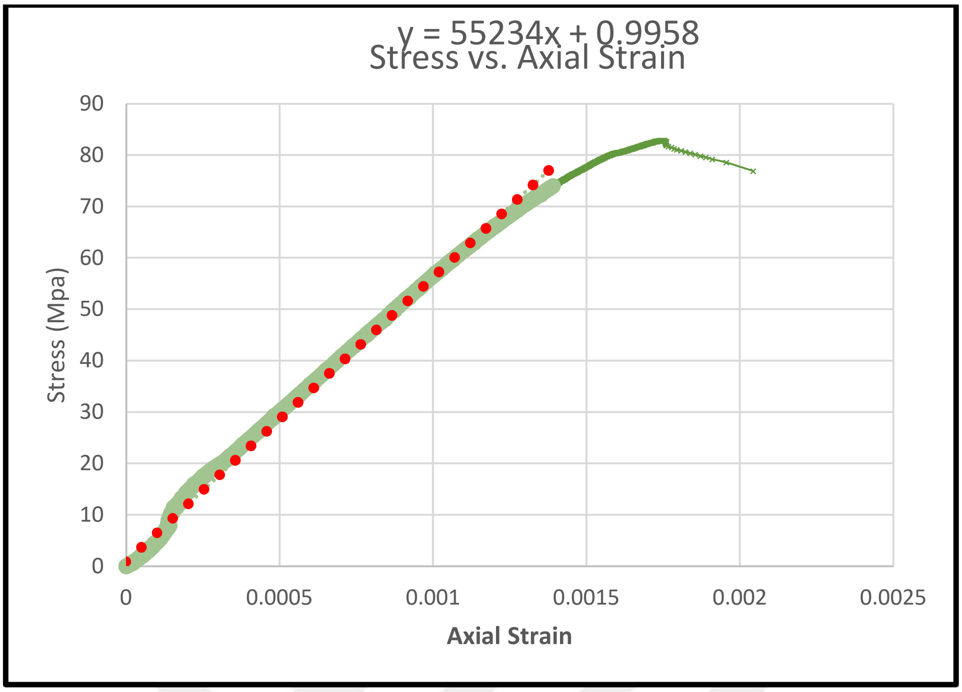

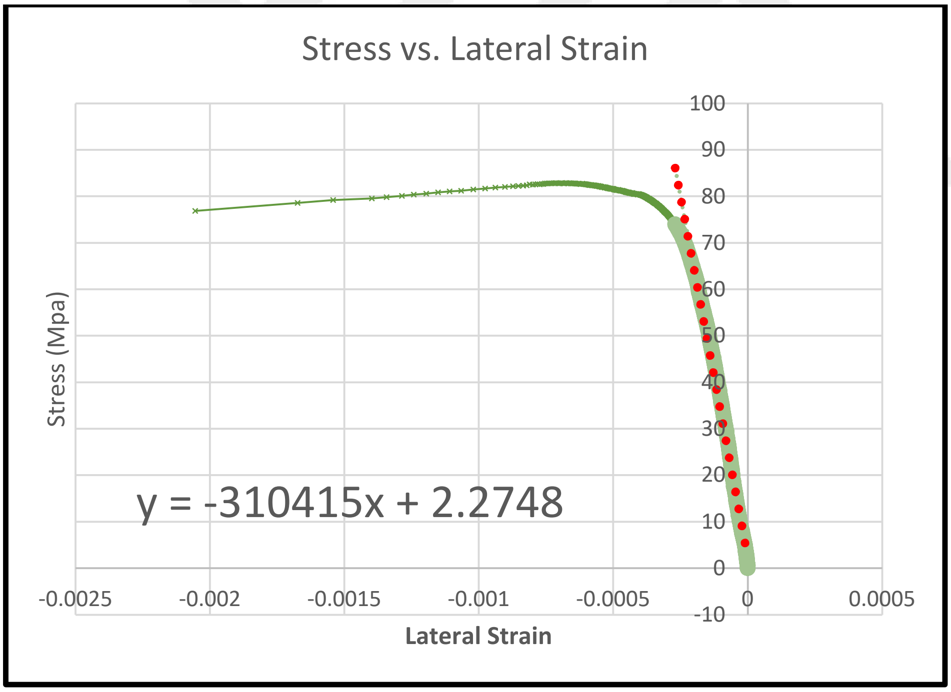

Figure 47. S8-5: Almacik Hill, Stress-related Axial and Lateral Strain

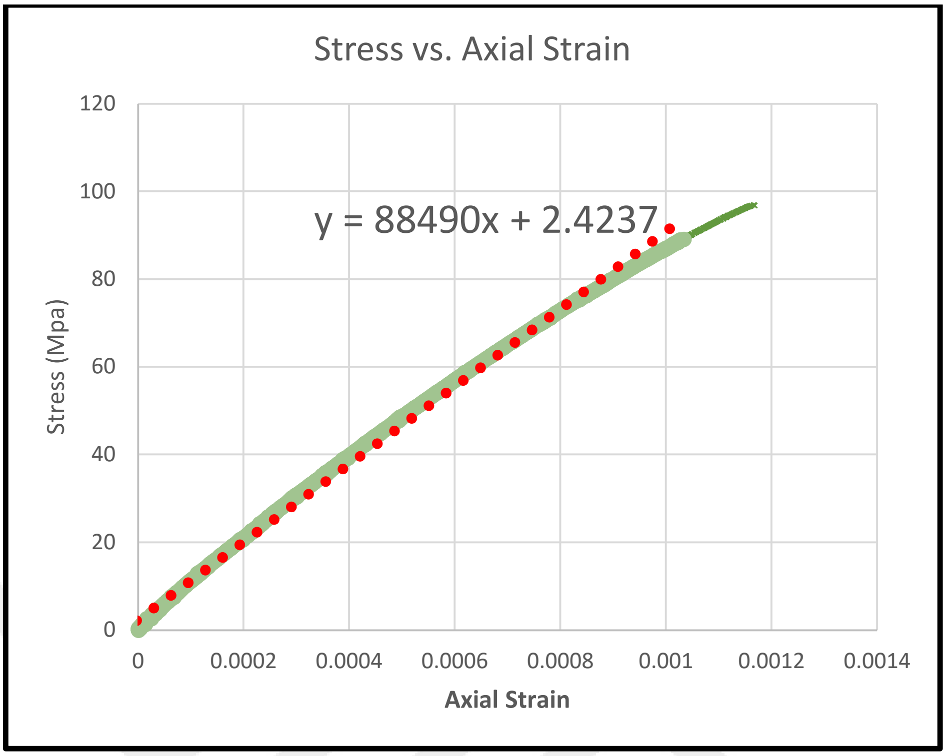

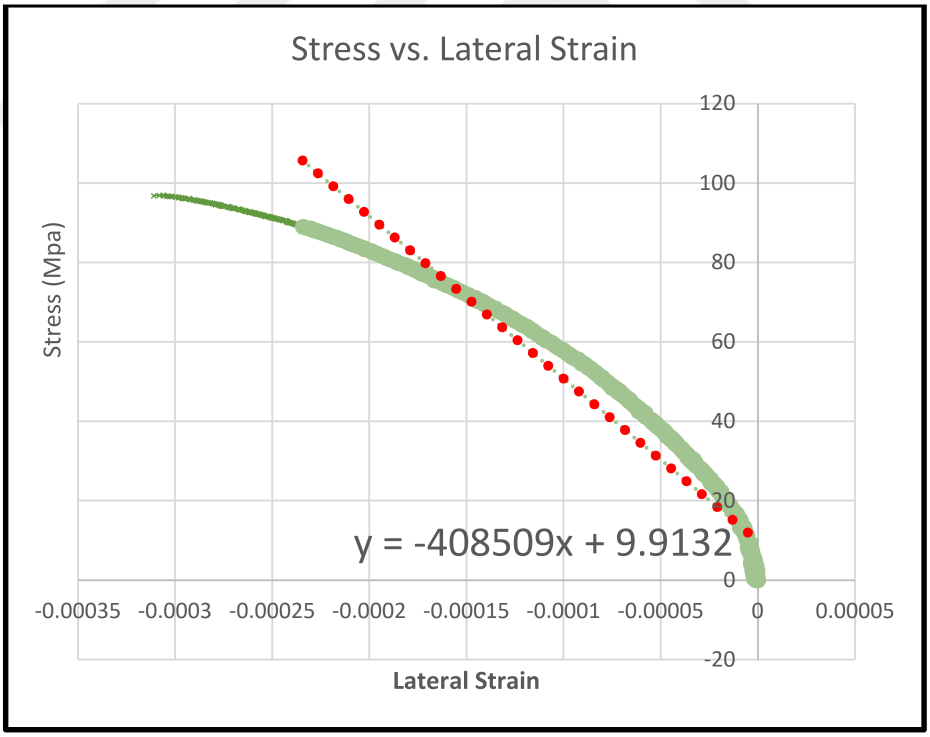

Figure 48. S1-1: Yukarıkayacık-Maden, Stress-related Axial and Lateral Strain

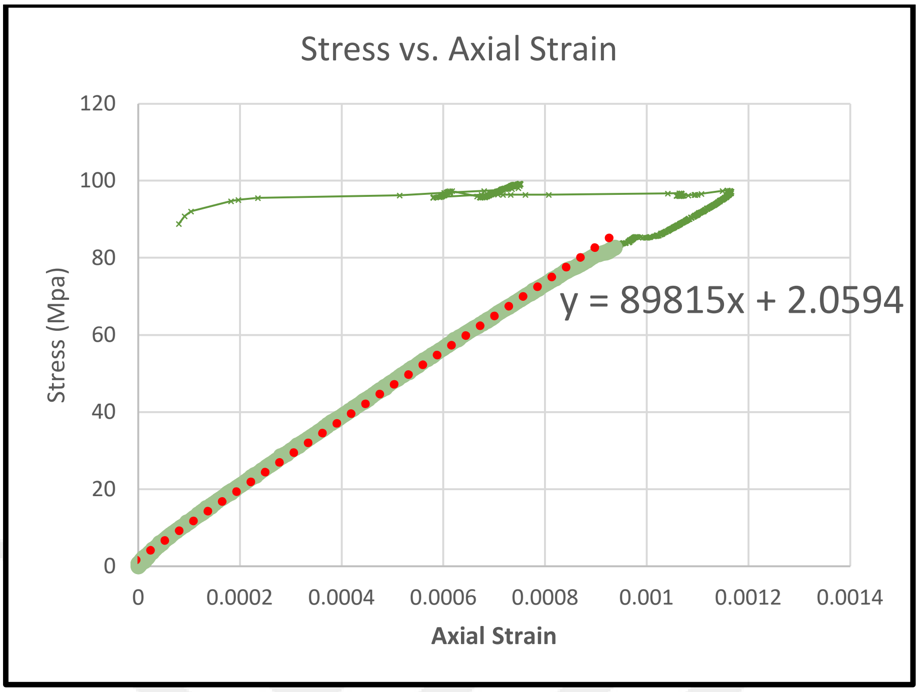

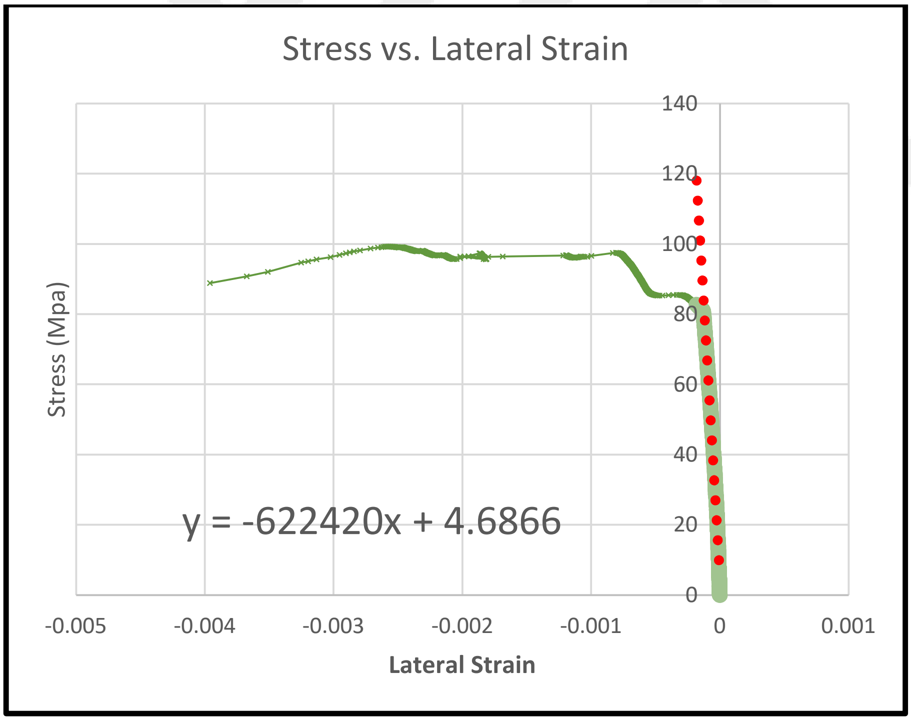

Figure 49. S1-2: Yukarıkayacık-Maden, Stress-related Axial and Lateral Strain

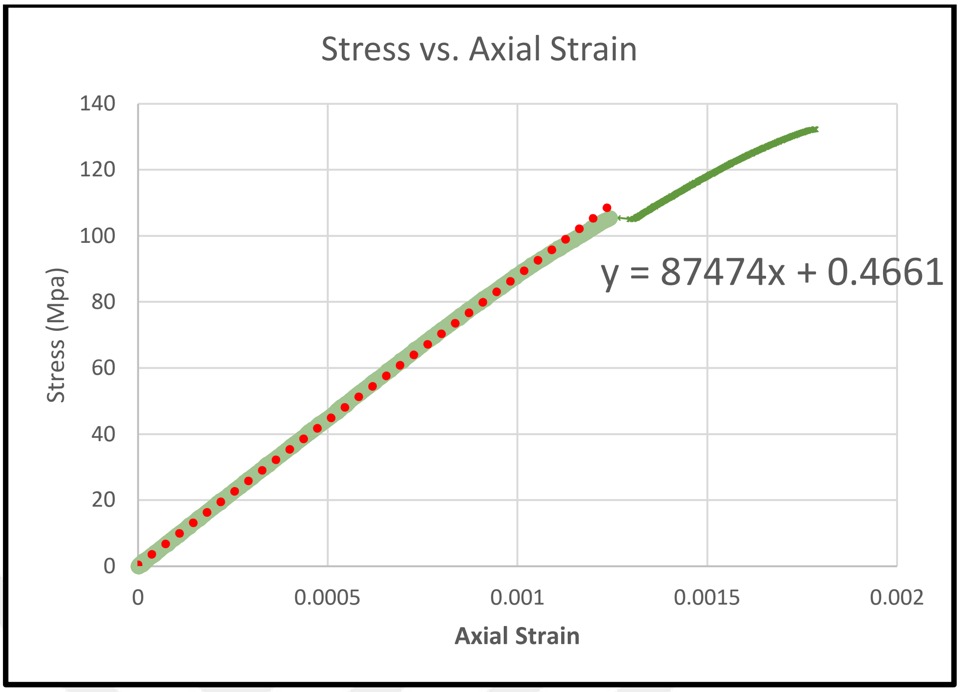

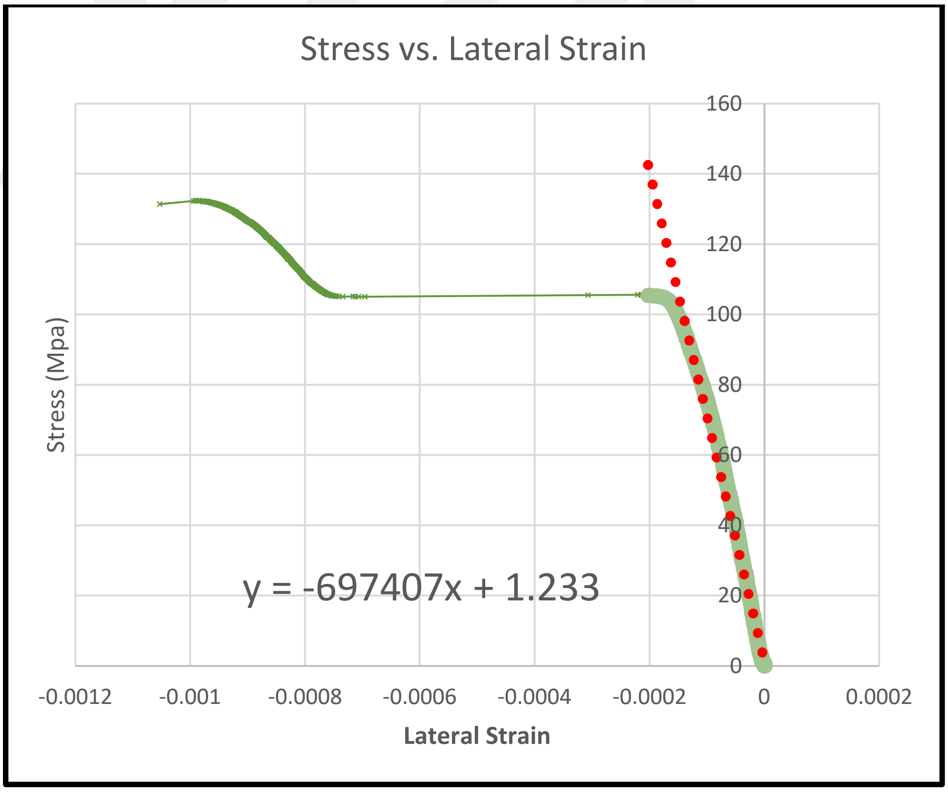

Figure 50. S1-5: Yukarıkayacık-Maden, Stress-related Axial and Lateral Strain

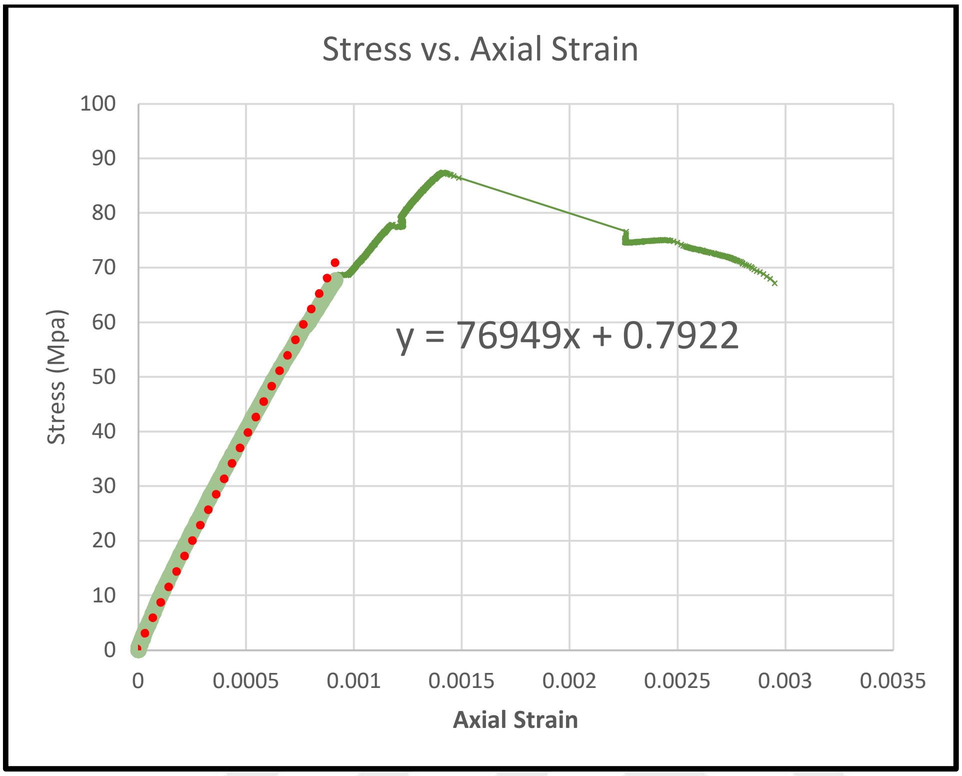

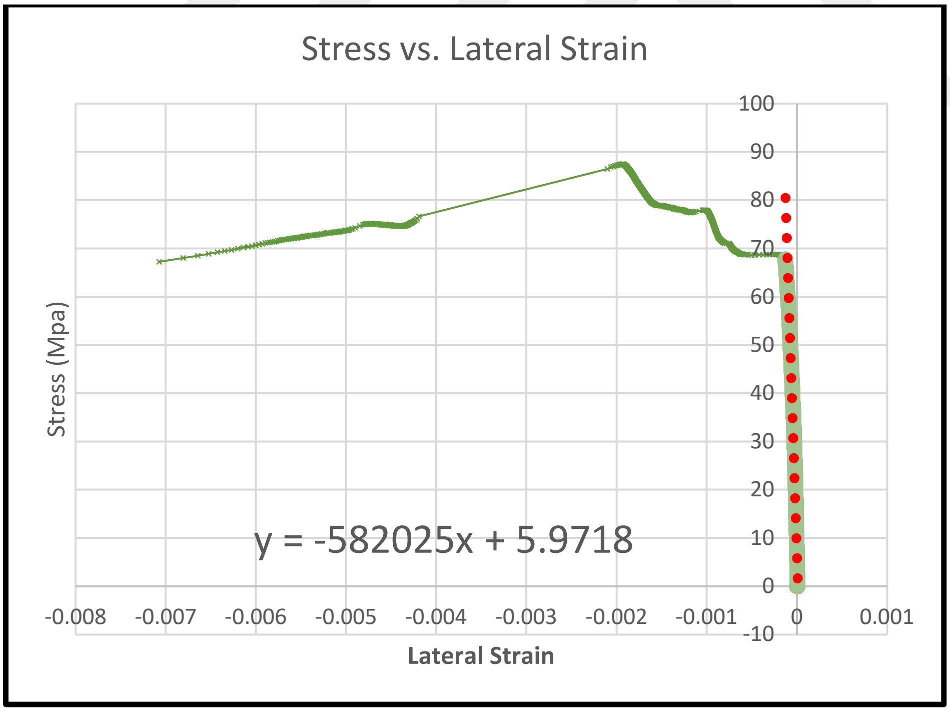

Figure 51. TY2-1: Terziler, Stress-related Axial and Lateral Strain

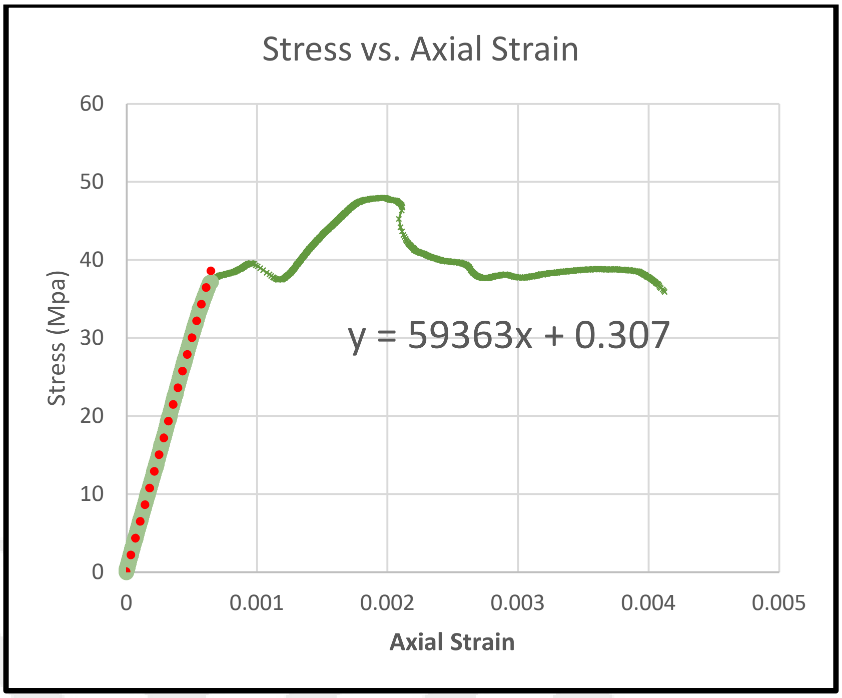

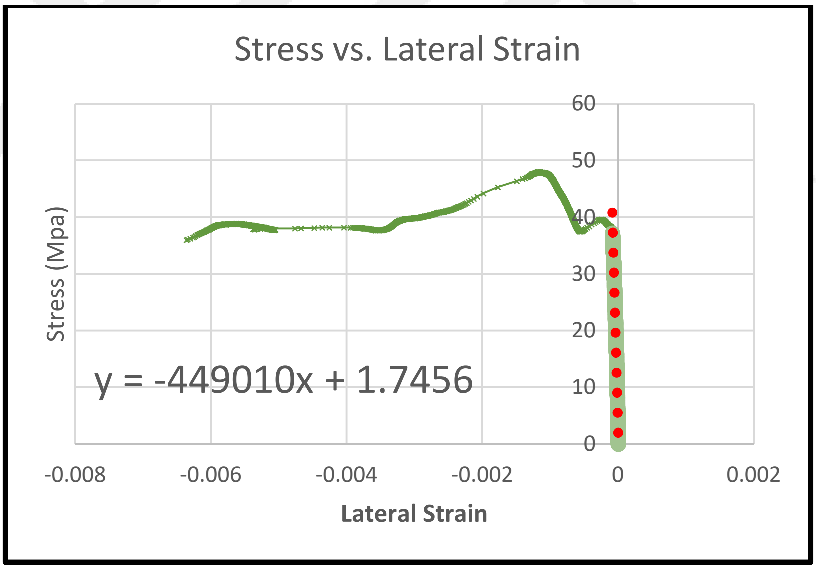

Figure 52. TY2-3: Terziler, Stress-related Axial and Lateral Strain Graphs of Static Deformability Experiments

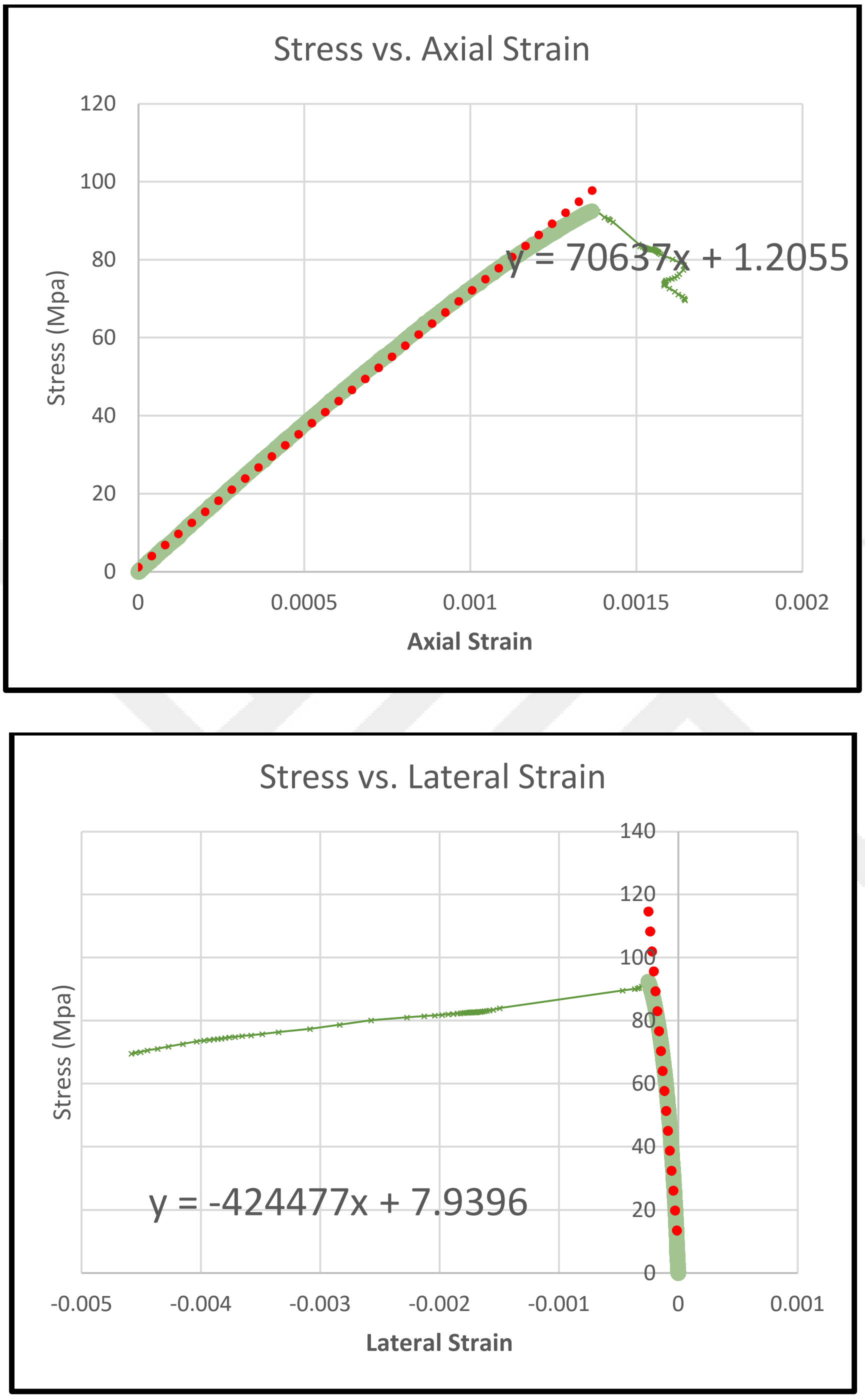

Figure 53. TY2-4: Terziler, Stress-related Axial and Lateral Strain

Table 3. Rock mechanics experiments Triaxial Compression (TCS) test results

Sample Name	Length (mm)	Diameter (mm)	Lateral Pressure (MPa)	Failure Load (kg)	Kg/cm^2	Sig 1 (MPa)	Cohesion (MPa)	Angel of Internal Friction (degree)
Gökkiriş-1	117.51	52.83	2.5	21751	992.27	97.34	26.86	27.87
Gökkiriş - 2	116.2	52.88	5	22476	1023.4	100.4		
Gökkiriş - 3	119.18	52.89	7.5	24888	1132.8	111.13		
Stop11-1	121.8	52.87	2.5	27113	1235.01	121.15	29.01	31.31
Stop11-2	121.21	52.83	5	22107	1008.51	98.93	2.93	61.24
Stop11-3	121.39	52.82	7.5	30596	1396.3	136.98		
İmamb. -1	121.75	52.7	4.5	16793	769.87	75.52	6.16	55.64
İmamb. -2	122.33	52.77	9	34933	1597.25	156.69		
İmamb. -3	121.68	52.6	13.5	37584	1729.58	169.67		
Halilb. -1	121.58	52.56	2.5	19481	897.86	88.08	8.82	57.08
Halilb. -2	121.56	52.5	5	25947	1198.61	117.58		
Halilb. -3	121.44	52.31	7.5	31848	1481.91	145.38		
S8-A	120.21	52.9	4	25100	1142.02	112.03	25.35	35.18
S8-B	119.54	52.93	8	28885	1312.74	128.78		
S8-C	119.9	52.86	12	31717	1445.27	141.78		
S11-A	120.02	52.94	5	25073	1139.07	111.74	21.06	40.99
S11-B	120.1	52.85	10	33555	1529.6	150.05		
S11-D	118.78	52.9	15	35818	1629.67	159.87		
S11-C	120.46	52.95	15	33061	1501.39	147.29	Dahil edilmedi	Dahil edilmedi
TY2-2	119.61	52.94	0			93.79	27.22	29.47
TY2-B	119.65	52.98	8	25909	1175.27	115.29		
TY2-C	120.86	52.93	12	29053	1320.38	129.53		
TY2-A	119.6	52.97	4	16567	751.79	73.75	Dahil edilmedi	Dahil edilmedi

Figure 54. Block 1: Gökkiriş and Block 3: Yukarikayacik-Maden (S11) core samples – Pre-experiment

Figure 55. Block 1: Gökkiriş and Block 3: Yukarikayacik-Maden (S11) core samples - post-experiment

Figure 56. B-4: İmambaba and B-5: Halilbeyli core samples – Pre-exp.

Figure 57. B- 4: İmambaba and B- 5: Halilbeyli core samples – Post-exp.

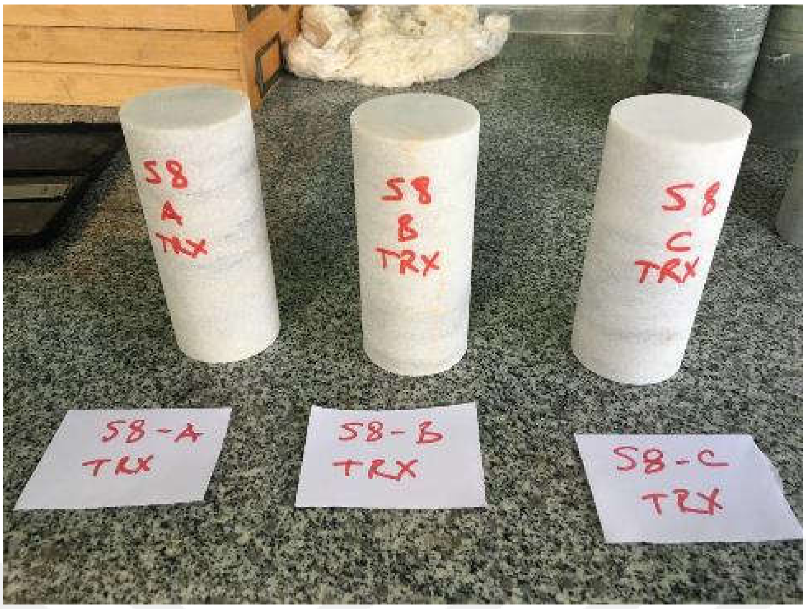

Figure 58. Almacık Hill (S8) core samples – Pre-exp.

Figure 59. Almacık Hill (S8) core samples – Post-exp.

Figure 60. Yukarıkayacık Maden (S11) core samples – Pre-exp.

Figure 61. Yukarıkayacık Maden (S11) core samples – Post-exp.

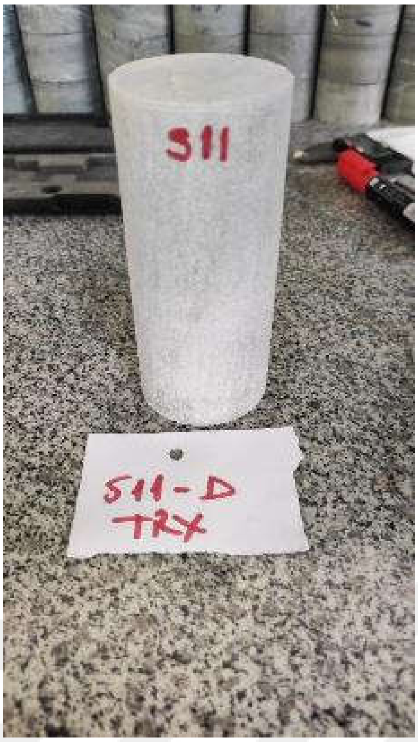

Figure 62. Yukarıkayacık-Maden (S11-D) core samples – Pre-exp.

Figure 63. Yukarıkayacık-Maden (S11-D) core samples – Post-exp.

Figure 64. Terziler (TY2) core samples – Pre-experiment

Figure 65. Terziler (TY2) core samples – Post-experiment

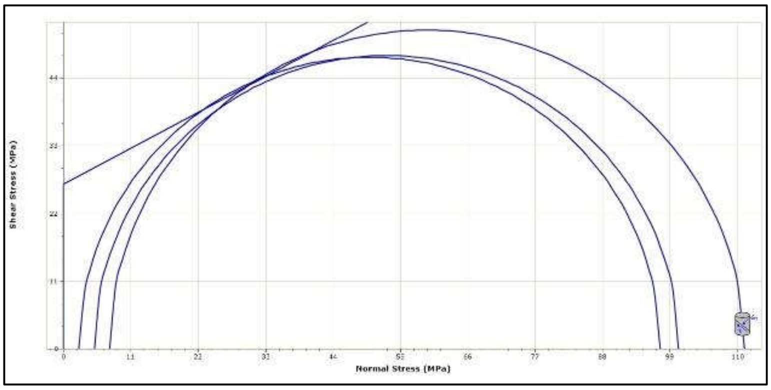

Figure 66. Gökkiriş, Mohr circles of B- 1

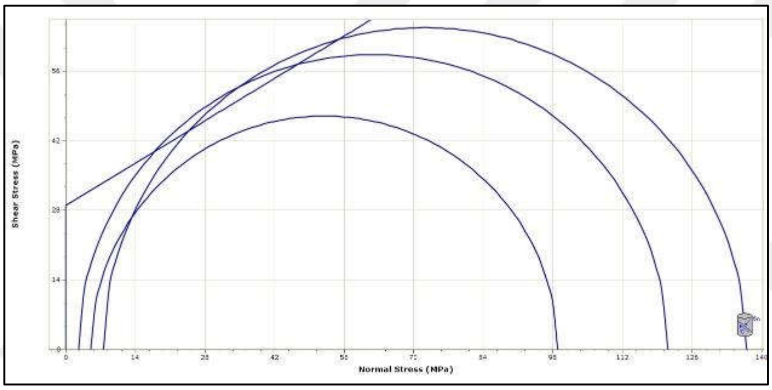

Figure 67. Yukarıkayacık-Maden Mohr circles of B- 3 (including 3 experiments)

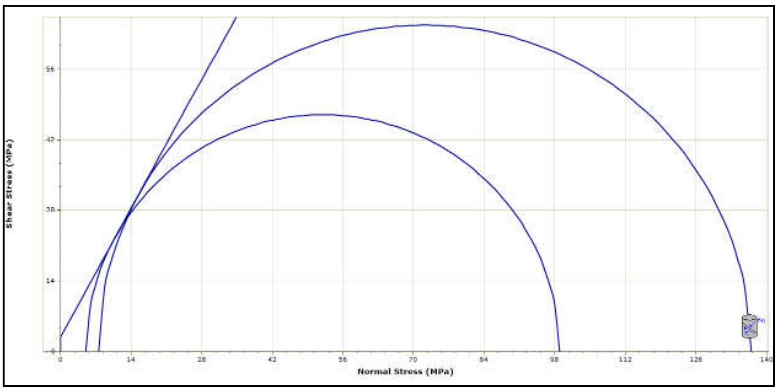

Figure 68. Yukarıkayacık-Maden: Mohr circles of B- 3 (excluding B -3-1)

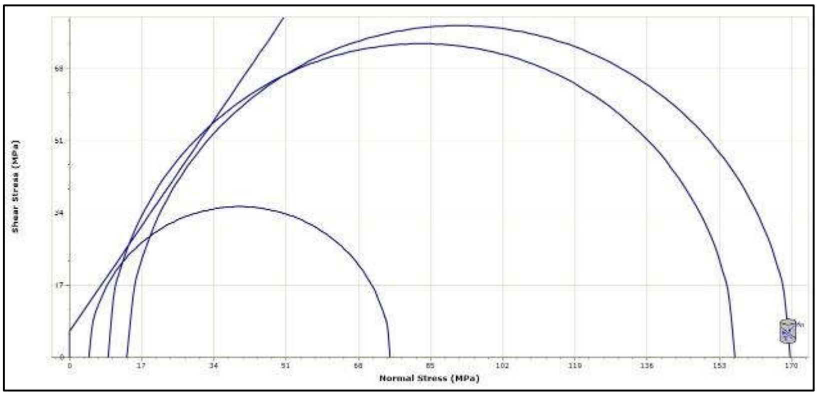

Figure 69. İmambaba: Mohr circles of B – 4

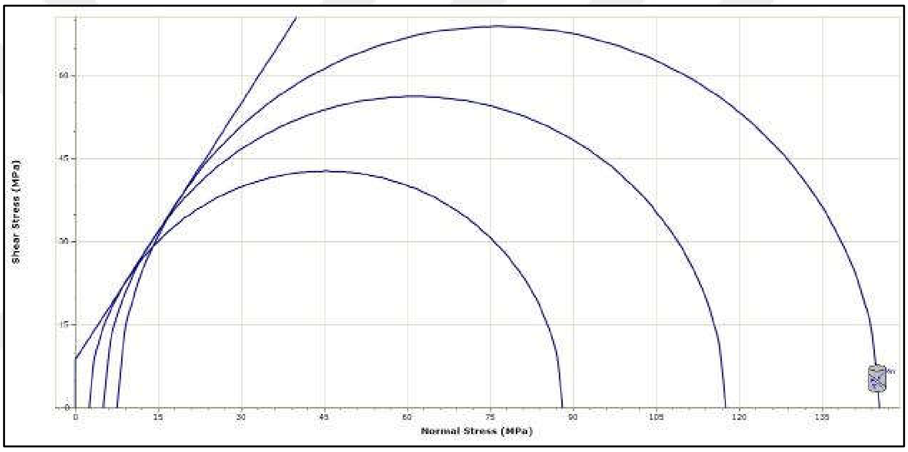

Figure 70.Halilbeyli Mohr circles of B - 5

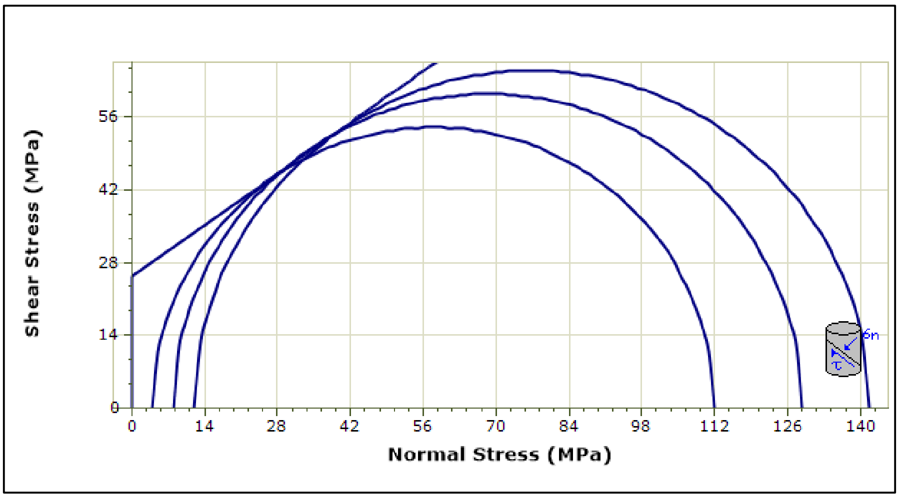

Figure 71. Almacık Hill: Mohr circles of S8

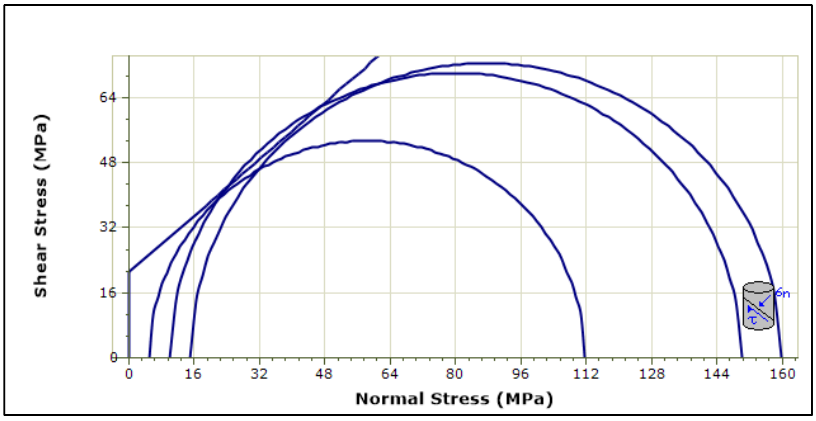

Figure 72. Yukarıkayacık-Maden: Mohr circles of S11

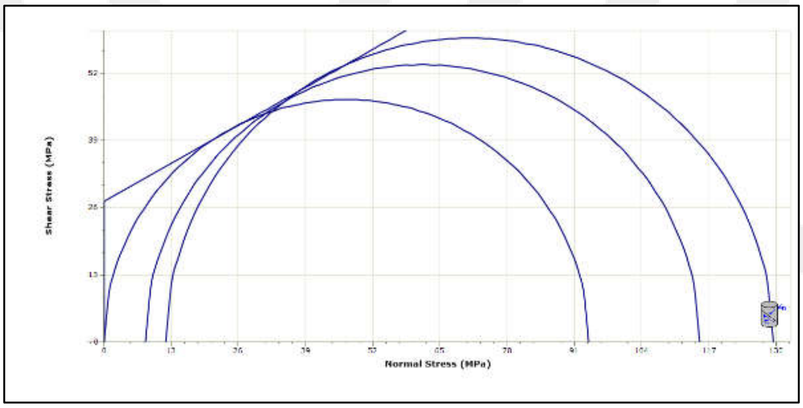

Figure 73. Terziler: Mohr circles of TY-2

C. MATLAB Mechanical Failure Code

```
% Load required MRST modules
mrstModule add hfm ad-core

% Load fracture data from Excel file
excelFilename = '04_All_1_2_3_NF.xlsx'; % Modify the filename
sheetName = 'Sheet1'; % Modify the sheet name
fractureData = readtable(excelFilename, 'Sheet', sheetName);

% Extract fracture data (start and end points, cohesion, friction angle)
SX = fractureData.EY;
SY = fractureData.EX;
EX = fractureData.SY;
EY = fractureData.SX;
cohesionValues = fractureData.Cohesion; % Cohesion values in Pa
frictionAngles = deg2rad(fractureData.FrictionAngle); % Friction angle in
radians
fractureIDs = fractureData.FractureID; % Fracture IDs

% Define grid dimensions and properties
celldim = [100, 100, 1]; % Define grid dimensions [Nx, Ny, Nz]
physdim = [100, 100, 1]; % Define physical dimensions [Lx, Ly, Lz] in
meters
G = cartGrid(celldim, physdim); % Create a Cartesian grid
G = computeGeometry(G); % Compute grid geometry
km = 1 * milli * darcy; % Define permeability in millidarcy
G.rock = makeRock(G, km, 0.25); % Define rock properties (permeability)

% Other constants
```

```
numFractures = size(fractureData, 1); % Number of fractures
sigma1 = 7e7; % Principal stress 1 (Pa)
sigma2 = 6e7; % Principal stress 2 (Pa)
sigma3 = 2.2e7; % Principal stress 3 (Pa)
initialPressure = 10 * barsa; % Initial reservoir pressure (Pa)
injectionWell = 1; % Index of the injection well
maxPressureIncrease = 500 * barsa; % Maximum allowed pressure increase (Pa)

% Define constants for pressure increment
pressureIncrement = 88 * barsa; % Incremental pressure increase (Pa)

% Initialize arrays to store results
failedFractures = false(numFractures, 1); % Initialize a failure flag for each fracture
failedFracturePressure = Inf(numFractures, 1); % Initialize failure pressure array with positive infinity
shearStressesAtFailure = nan(numFractures, 1); % Store shear stress at the time of failure

% Initialize a cell array to store failure statuses (F or N)
failureStatus = cell(numFractures, 1);

% Initialize a flag to track whether each fracture has previously failed
previouslyFailed = false(numFractures, 1);

% Calculate the number of cells based on grid dimensions
numCells = prod(celldim);

% Initialize pressure array
```

```
pressure = initialPressure * ones(numCells, 1); % Initialize pressure with
the initial value

% Create a figure before the loop to ensure all fractures are plotted
figure;

% Initialize step counter
step = 0;

% Iterate through the simulation steps
while max(pressure) < initialPressure + maxPressureIncrease
    % Print the current pressure for debugging
    fprintf('Step %d: Reservoir pressure = %f Pa\n', step,
pressure(injectionWell));

    % Inject fluid into the well cell
    pressure(injectionWell) = pressure(injectionWell) + pressureIncrement;

    % Iterate through fractures and calculate stress changes
    for f = 1:numFractures
        % If a fracture has previously failed, no need to check again
        if previouslyFailed(f)
            continue;
        end

        % Access fracture properties and calculate stress tensor
        fractureStart = [SX(f), SY(f)];
        fractureEnd = [EX(f), EY(f)];

        % Calculate the orientation (theta) for each fracture
```

```
        theta = atan2(fractureEnd(2) - fractureStart(2), fractureEnd(1) -
fractureStart(1));

        % Define orientations for sigma1 and sigma3 (in radians)
        sigma1Orientation = deg2rad(0); % Angle for sigma1
        sigma3Orientation = deg2rad(90); % Angle for sigma3

        % Calculate stress tensor for the fracture with orientations
        stressTensor = calculateStressTensor(sigma1, sigma2, sigma3, theta,
sigma1Orientation, sigma3Orientation, pressure(injectionWell));

        % Print stress tensor and failure check results for debugging
        fprintf('Fracture %d: Stress Tensor - Normal: %f Pa, Shear: %f Pa\n',
...
            fractureIDs(f), stressTensor.normalStress, stressTensor.shearStress);

        % Check for shear failure using the Mohr-Coulomb criterion
        if checkShearFailure(stressTensor.shearStress, cohesionValues(f),
frictionAngles(f))
            fprintf('Fracture %d failed at pressure %f Pa (Cohesion: %f Pa,
Friction Angle: %f radians)\n', ...
                fractureIDs(f), pressure(injectionWell), cohesionValues(f),
frictionAngles(f));
            failedFractures(f) = true; % Mark this fracture as having failed
            failureStatus{f} = 'F'; % Set failure status to 'F'
            previouslyFailed(f) = true; % Mark this fracture as having
previously failed

            % Update the lowest failure pressure if needed
            if pressure(injectionWell) < failedFracturePressure(f)
```

```
                failedFracturePressure(f) = pressure(injectionWell);
                shearStressesAtFailure(f) = stressTensor.shearStress; % Store
shear stress at failure
            end
        else
            fprintf('Fracture %d did not fail at pressure %f Pa\n', fractureIDs(f),
pressure(injectionWell));
            failureStatus{f} = 'N'; % Set failure status to 'N'
        end
    end

    % Clear the previous plot
    clf;

    % Plot fractures as lines
    for f = 1:numFractures
        if failedFractures(f) % Highlight failed fractures in red
            plot([SX(f), EX(f)], [SY(f), EY(f)], 'r-');
        else
            plot([SX(f), EX(f)], [SY(f), EY(f)], 'b-');
        end
        hold on;
    end

    xlabel('X Coordinate');
    ylabel('Y Coordinate');
    title('Fracture Network with Highlighted Failures');

    % Refresh the plot
    drawnow;
```

```
    % Increment step counter
    step = step + 1;
end

% Create a table with failure pressure and shear stress information
failureTable = table(fractureIDs(failedFractures),
failedFracturePressure(failedFractures),
shearStressesAtFailure(failedFractures), ...
    'VariableNames', {'FractureID', 'LowestFailurePressure_Pa',
'ShearStressAtFailure_Pa'});

% Display the table
disp(failureTable);

% Save the table to a CSV file
csvFilename = 'failure_data.csv'; % Specify the name of the CSV file
writetable(failureTable, csvFilename);

% Create a table with failure information
failureTableStatus = table(fractureIDs, failureStatus, 'VariableNames',
{'FractureID', 'FailureStatus'});

% Save the table to a CSV file
csvFilenameStatus = 'failure_status_data.csv'; % Specify the name of the
CSV file
writetable(failureTableStatus, csvFilenameStatus);

% Specify the name of the Excel file
excelFilename = 'failure_data.xlsx';
```

```
% Write the table to an Excel file
writetable(failureTable, excelFilename, 'Sheet', 'FailureData');
writetable(failureTableStatus, excelFilename, 'Sheet', 'FailureStatus');

% Display a message to confirm the save
disp(['Failure data saved to Excel file: ' excelFilename]);

% Function to calculate stress tensor based on principal stresses and
fracture geometry
function stressTensor = calculateStressTensor(sigma1, sigma2, sigma3,
theta, sigma1Orientation, sigma3Orientation, porePressure)
    % Initialize stressTensor as a struct with normalStress and shearStress
fields
    stressTensor = struct('normalStress', 0, 'shearStress', 0);

    % Adjust principal stresses for pore pressure
    adjustedSigma1 = sigma1 - porePressure;
    adjustedSigma3 = sigma3 - porePressure;

    % Rotate sigma1 and sigma3 by the orientations
    rotatedSigma1 = adjustedSigma1 * cos(2 * (theta - sigma1Orientation)) +
adjustedSigma3 * sin(2 * (theta - sigma1Orientation));
    rotatedSigma3 = adjustedSigma1 * sin(2 * (theta - sigma3Orientation)) +
adjustedSigma3 * cos(2 * (theta - sigma3Orientation));

    % Calculate normalStress and shearStress based on rotated principal
stresses
    stressTensor.normalStress = (rotatedSigma1 + rotatedSigma3) / 2;
    stressTensor.shearStress = (rotatedSigma1 - rotatedSigma3) / 2;
```

```
end

% Function to check shear failure using the Mohr-Coulomb criterion
function hasShearFailure = checkShearFailure(shearStress, cohesion,
frictionAngle)
    % Calculate the maximum shear stress (Mohr-Coulomb criterion)
    tauMax = cohesion * tan(frictionAngle);

    % Print the shearStress and tauMax for debugging
    fprintf('Shear Stress = %f Pa, Tau Max = %f Pa\n', shearStress, tauMax);

    % Check if shear stress exceeds the maximum shear stress
    hasShearFailure = shearStress > tauMax;
end
```

D. MATLAB Fluid Flow MRST Code

```
%% LOAD MRST MODULES
mrstModule add hfm ad-blackoil ad-core ad-props mrst-gui

%% Create an empty struct file to be populated
N = 282;
F2 = struct('points', cell(N, 1), ...
    'aperture', cell(N, 1), ...
    'poro', cell(N, 1), ...
    'perm', cell(N, 1), ..."
    'fractureID', cell(N, 1), ...
    'size', cell(N, 1));

% Initialize common values for all struct elements
aperture = 0.0014;
poro = 1;

%% Load Excel data using readtable
excelFilename = '04_All_1_2_3_NF.xlsx';
sheetName = 'Sheet1';
excelData = readtable(excelFilename, 'Sheet', sheetName);

for i = 1:N
    % Initialize each matrix
    points = zeros(4, 3);
    points(1, 1) = excelData.SX(i);  % Populate X-coordinate for point 1
    points(1, 2) = excelData.SY(i);  % Populate Y-coordinate for point 1
    points(2, 1) = excelData.EX(i);  % Populate X-coordinate for point 2
    points(2, 2) = excelData.EY(i);  % Populate Y-coordinate for point 2
```

```
    points(3, 1) = excelData.EX(i);  % Populate X-coordinate for point 3
    points(3, 2) = excelData.EY(i);  % Populate Y-coordinate for point 3
    points(4, 1) = excelData.SX(i);  % Populate X-coordinate for point 4
    points(4, 2) = excelData.SY(i);  % Populate Y-coordinate for point 4
    points(3, 3) = 1;
    points(4, 3) = 1;

    % Populate the struct element
    F2(i).points = points;
    F2(i).aperture = aperture;
    F2(i).poro = poro;
    F2(i).perm = excelData.Perm(i); % Assign perm from Excel data
    F2(i).fractureID = excelData.FractureID(i);
    F2(i).size = zeros();
end

%% Calculate the length of the fracture to populate size
for i = 1:N
    F2(i).size = 28571 * F2(i).aperture;
end

%% SETUP GRID
celldim = [200, 200, 1];
physdim = [150, 150, 1];
G = cartGrid(celldim, physdim);
G = computeGeometry(G);
km = 10000 * darcy; % Matrix permeability in Darcy

% Assign matrix permeability to the grid's rock property
G.rock = makeRock(G, km, 0.25);
```

```
%% EDFM PRE-PROCESSING
tol = 1e-5;
[G, F2] = EDFMgrid(G, F2, 'Tolerance', tol);
G = fracturematrixNNC3D(G, tol);
G = fracturefractureNNCs3D(G, F2, tol);

%% SETUP FLUID MODEL WITH OIL PROPERTIES
pRef = 260 * barsa;
fluid = initSimpleADIFluid('phases', 'W', ...
    'mu', 8 * centi * poise, ...
    'rho', 1000 * kilogram / meter^3, ...
    'pRef', pRef, ...
    'c', 1e-5 / barsa);

%% SETUP WATER MODEL
gravity reset off
model = WaterModel(G, G.rock, fluid);
model.operators = setupEDFMOperatorsTPFA(G, G.rock, tol);

%% PLOT GRID TO HELP DETERMINE APPROXIMATE WELL
LOCATION
figure;
[hm, hf] = plotEDFMgrid(G);
hm.EdgeAlpha = 0;
hold on
scatter(2.7, 1.15, 0.5, 'r', 'filled');
view(0, 90);
box on
xlabel('x [m]')
```

```
ylabel('y [m]')
title('Grid and Well Location');

%% modified locate (user) This locates the cell to start the flow that is
closest to the defined source location
fraccellcent = [80, 80, 0.5]; % Approximate location of well
fraccell = find(all(abs(G.cells.centroids - fraccellcent) < 0.5, 2));

if length(fraccell) == 1
    fprintf('One fraccell identified at centroid: [%f, %f, %f]\n',
G.cells.centroids(fraccell, :));
elseif length(fraccell) > 1
    fprintf('Multiple fraccells identified:\n');
    for i = 1:length(fraccell)
        fprintf('Fraccell %d centroid: [%f, %f, %f]\n', i,
G.cells.centroids(fraccell(i), :));
    end
    % Randomly select one of the identified fraccells
    randomIndex = randi(length(fraccell));
    fprintf('Randomly selected fraccell: [%f, %f, %f]\n',
G.cells.centroids(fraccell(randomIndex), :));

    % Set fraccell to the randomly selected index
    fraccell = fraccell(randomIndex);
else
    fprintf('No fraccell identified.\n');
end

assert(length(fraccell) == 1, 'more/less than one fraccell detected');
```

```
%% SET UP SINK
src = [];
src = addSource(src, fraccell, -100 * (meter^3) / day);
src.sat = ones(size(src.cell));

%% RUN SIMULATION
state = initResSol(G, pRef);
dt = diff(10.^(-8.5 + (1:60) * 0.25))'; % log-spaced timesteps
schedule = simpleSchedule(dt, 'src', src);
[~, states] = simulateScheduleAD(state, model, schedule);

%% WELL TEST DIAGNOSTIC PLOT
figure;
cellnum = src.cell;
pvalues = zeros(length(states), 1);

for i = 1:length(states)
   pvalues(i) = states{i}.pressure(cellnum);
end

tottime = cumsum(dt);

% Calculate pressure difference
deltaP = pRef - pvalues(end);

% Determine flux through the western boundary
westfaces = boundaryFaces(G, 'West');
waterflux = sum(abs(states{end}.flux(westfaces, 1)));

% Inverse Darcy's law for permeability
```

```
k_matrix = 0.1; % Example matrix permeability in Darcy
k_fracture = 1000; % Uniform fracture permeability assigned earlier

% Calculate overall permeability (parallel flow)
k_overall_parallel = 1 / (1/k_matrix + 1/k_fracture);

fprintf('Overall Permeability (Parallel Flow): %.6f Darcy\n',
k_overall_parallel);

%% PLOT MATRIX RESULTS
figure;
plotToolbar(G, states, 'lockCaxis', true, 'field', 'pressure');
caxis([50 100] * barsa);
colorbar('EastOutside');
[hm, hf] = plotEDFMgrid(G);
hm.EdgeAlpha = 0;
hf.EdgeAlpha = 0.25;
xlabel('x [m]')
ylabel('y [m]')
title('Matrix Pressure Distribution');

%% PLOT FRACTURE RESULTS
figure;
Gplot = createGplot(G, 1, F2);
plotToolbar(Gplot, states, 1 + G.Matrix.cells.num:G.cells.num, ...
   'lockCaxis', true, 'field', 'pressure');
caxis([50 100] * barsa);
colorbar('EastOutside');
xlabel('x [m]')
ylabel('y [m]')
```

```
title('Fracture Pressure Distribution');

%% PLOT DERIVATIVE RESULTS
% Assuming 'midtime' and 'dp_dlnt' based on assumed data
midtime = linspace(0, max(tottime), length(pvalues)); % Time array
dp_dlnt = -0.01 ./ (1 + exp(-0.1 * (midtime - 20))); % Example pressure
derivative data

figure;
loglog(midtime, dp_dlnt); % Plot the pressure derivative
grid on;
xlabel('Time (s)');
ylabel('Pressure derivative (Pa)');
title('Pressure Derivative vs. Time');

% Combine pressure values from both matrix and fracture regions
overall_pressure_accum = zeros(G.cells.num, 1);

for i = 1:length(states)
   overall_pressure_accum = overall_pressure_accum + states{i}.pressure;
end

% Calculate the average pressure over all time steps
overall_pressure = overall_pressure_accum / length(states);

% Create a figure for overall pressure distribution
figure;
scatter(G.cells.centroids(:, 1), G.cells.centroids(:, 2), 20, overall_pressure,
'filled');
colormap('jet');
```

```
colorbar;
axis equal tight;
xlabel('x [m]');
ylabel('y [m]');
title('Overall Pressure Distribution');

% Initialize a figure array to store the plots
pressure_figures = cell(length(states), 1);

for i = 1:length(states)
    overall_pressure = states{i}.pressure;

    % Create a figure for overall pressure distribution for each time step
    pressure_figures{i} = figure;
    scatter(G.cells.centroids(:, 1), G.cells.centroids(:, 2), 20,
overall_pressure, 'filled');
    colormap('jet');
    colorbar;
    axis equal tight;
    xlabel('x [m]');
    ylabel('y [m]');
    title(['Overall Pressure Distribution - Time Step ' num2str(i)]);
end

% Create a plot of the final pressure drawdown
figure;
plot(time(end), finalPressureDrawdown, 'b-', 'Marker', 'o', 'MarkerSize', 8,
'MarkerFaceColor', 'r');
grid on;
xlabel('Time (s)');
```

```
ylabel('Final Pressure Drawdown (Pa)');
title('Final Pressure Drawdown Near the Well');

% Display the final pressure drawdown value
fprintf('Final Pressure Drawdown: %.2f Pa\n', finalPressureDrawdown);

%% Locate cells near the source well
well_location = fraccellcent; % The approximate coordinates of the well
nearby_cells = find(all(abs(G.cells.centroids - well_location) < 100, 2)); %
Adjust tolerance as needed

% Initialize an array to store pressure values near the well at each time step
numTimeSteps = length(states);
nearby_pressures = zeros(numTimeSteps, length(nearby_cells));

%% Extract and store pressure values at each time step
for t = 1:numTimeSteps
   for j = 1:length(nearby_cells)
      nearby_pressures(t, j) = states{t}.pressure(nearby_cells(j));
   end
end

% If you want to calculate the average pressure near the well at each time
step:
average_pressure_near_well = mean(nearby_pressures, 2);

% Display the pressure values for each time step
for t = 1:numTimeSteps
   fprintf('Time Step %d, Average Pressure near Well: %.2f Pa\n', t,
average_pressure_near_well(t));
```

```
end

%% Plot the pressure near the well over time
figure;
plot(tottime, average_pressure_near_well, '-o', 'MarkerSize', 5);
xlabel('Time (s)');
ylabel('Average Pressure near Well (Pa)');
title('Pressure Near Well over Time');
grid on;

%% Define the folder path where figures will be saved
outputFolder = 'GeneratedFiguresALL';
if ~exist(outputFolder, 'dir')
    mkdir(outputFolder); % Create the folder if it does not exist
end

%% Loop through all open figures and save them
figHandles = findall(groot, 'Type', 'figure');
for i = 1:length(figHandles)
    % Set the figure as the current figure
    fig = figHandles(i);
    figure(fig);

    % Create a unique filename for each figure
    filename = fullfile(outputFolder, sprintf('Figure_%d.png', i));

    % Save the figure as a .png file
    saveas(fig, filename);

    % Optionally, save as .fig file for MATLAB format (editable later)
```

```
    % saveas(fig, fullfile(outputFolder, sprintf('Figure_%d.fig', i)));

    fprintf('Saved Figure %d to %s\n', i, filename);
end

%% Locate the Well Cell
% Define the approximate coordinates of the well
well_location = fraccellcent; % [x, y, z] coordinates of the well

% Locate the cell nearest to the well
nearby_cells = find(all(abs(G.cells.centroids - well_location) < 0.5, 2)); %
Adjust tolerance as needed

% If more than one cell is found, select the first one
if length(nearby_cells) == 1
    fraccell = nearby_cells;
    fprintf('Well location found at centroid: [%f, %f, %f]\n',
G.cells.centroids(fraccell, :));
else
    error('Well location is not uniquely identified or not found.');
end

%% Extract Pressure at Last Time Step
% Get the pressure at the well location at the last time step
final_pressure = states{end}.pressure(fraccell);

% Get the coordinates of the well cell
well_cell_coords = G.cells.centroids(fraccell, :);

%% Save Pressure Value to File
```

```
% Create a table to store the results
time_step_column = tottime(end);  % Time at the last step
pressure_table = table(time_step_column, well_cell_coords(1),
well_cell_coords(2), final_pressure, ...
    'VariableNames', {'TimeStep', 'X_Coordinate', 'Y_Coordinate',
'Pressure_Pa'});

% Define the output CSV file name
outputFilename = 'PressureAtWell_LastTimeStep.csv';

% Write the table to the CSV file
writetable(pressure_table, outputFilename);

% Display message confirming file save
fprintf('Pressure value at the well at last time step saved to %s\n',
outputFilename);
fprintf('Well cell found at (x=%.2f, y=%.2f) with pressure %.2f Pa at last
time step\n', ...
well_cell_coords(1), well_cell_coords(2), final_pressure);
```

CURRICULUM VITAE

Surname, Name: Yal, Gözde Pınar

EDUCATION

Degree	Institution	Year of Graduation
M.Sc	METU Geological Engineering	2010
M.Sc.	University of Utah, Environmental Science	2007
M.Eng	Cornell University, Ithaca, USA, Geological Engineering	2013
BS	Ankara University	2002
High School	TED Ankara College, Ankara	1998

FOREIGN LANGUAGES

Fluent in English

PUBLICATIONS

Cambazoglu, S., Yal, G.P., Eker, A.M., Sen, O. and Akgün, H., 2021, "Geothermal Favorability Assessment of the Gediz Graben Through Correlation and GIS Based MCDA Methodologies," World Geothermal Congress 2020+1, April-October 2021, Reykjavik, Iceland (Conference Presentation).

Yal, G.P., Cambazoglu, S., Eker, A.M., Sen, O. and Akgün, H., 2021, "Assessment of the Ability of GIS Based MCDA Methods to Reveal the Geothermal Potential of the Büyük Menderes Graben," World Geothermal Congress 2020+1, April-October 2021, Reykjavik, Iceland (Conference Presentation).

Cambazoglu, S., Yal, G.P., Eker, A.M., Sen, O. and Akgün, H., 2019, "Geothermal Resource Assessment of the Gediz Graben Utilizing TOPSIS Methodology," Geothermics, 80, 92-102.

Yal, G.P., Eker, A.M., Cambazoğlu, S., Akgün, H. and Şen, O., 2017, "Assessment of the Early Development Work for Kuyucak Geothermal Field, Turkey," 42nd Workshop on Geothermal Reservoir Engineering, February 13-15, 2017, Stanford, California, USA (Conference Presentation).

Cambazoğlu, S., Eker, A.M., Yal, G.P., Akgün, H., Dünya, H. and Şen, O., 2017, "Assessment of the Geothermal Potential of the Gediz Graben, Manisa, Turkey," 42nd Workshop on Geothermal Reservoir Engineering, February 13-15, 2017, Stanford, California, USA (Conference Presentation).

Eker, A.M., Yal, G.P., Cambazoğlu, S., Şen, O. and Dünya, H., 2017, "Enhancement of Geothermal Reservoir Through Varying Acidizing Operation Procedures in Aydın-Kuyucak Geothermal Field," 42nd Workshop on Geothermal Reservoir Engineering, February 13-15, 2017, Stanford, California, USA (Conference Presentation).

Hou, Z., Şen, O., Gou, Y., Eker, A.M., Li, M., Yal, G.P., Cambazoğlu, S. and Were, P., 2015, "Preliminary Geological, Geochemical and Numerical Study on the First EGS Project in Turkey," Environmental Earth Sciences, 73(11), 6747-6767.

Şen, O., Dünya, H., Yal, G.P., Cambazoğlu, S., Eker, A.M., 2015, "Spatial Assessment of Geothermal Potential with Current Geothermal Data and Geological Factors: Büyük Menderes Graben Example," 3rd Geothermal Resources Symposium and Exhibition, November 4-6, 2015, Ankara, Turkey, pp.479-492 [In Turkish] (Conference Presentation).

Şen, O., Eker, A.M., Cambazoğlu, S., Yal, G.P. and Hou, M.Z., 2015, "First Enhanced Geothermal Systems Project in Turkey, Dikili-İzmir," Geothermal Resources Symposium, May 6-7, 2015, İzmir [In Turkish] (Conference Presentation).

Cambazoğlu, S., Yal, G.P., Eker, A.M., Koçkar, M.K., Şen, O., Akgün, H., 2015, "Surface Temperature Mapping and Investigation of Geothermal Anomalies by Using Aster Images for Geothermal Exploration," 68th Geological Congress of Turkey, April 6-10, 2015, Ankara, Turkey [In Turkish] (Conference Presentation).

Yal, G.P., Cambazoğlu, S., Eker, A.M., Şen, O., Koçkar, M.K. and Akgün, H., 2014, "Thermal Anomaly and Alteration Mineral Mapping at İzmir-Dikili Region by Using Aster and Investigation of Geothermal Potential of the Region," 3rd Turkey National Geological Remote Sensing Symposium (JEOUZAL-3), pp.81-84 (Abstract only) (Conference Presentation).

Yal, G.P. and Akgün, H., 2013, "Landfill Site Selection and Landfill Liner Design for Ankara, Turkey," Environmental Earth Sciences, 70, 2729-2752.

Johnson, W.P., Li, X., and Yal, G.P., 2007, "Colloid Retention in Porous Media: Mechanistic Confirmation of Wedging and Retention in Zones of Flow Stagnation," Environmental Science and Technology Journal, 41(4), pp.1279-1287.

Yal, G.P., 2007, "Investigation of Hydraulic Properties of Subsurface in South Western Jordan Valley, Utah," MSc Thesis, Kennecott Copper Mine, Utah Detection of a Possible Groundwater Recharge to the Salars in an Arid Area- N. Chile, Atacama Desert; Cornell University, Ithaca, MS Thesis.